Silsesquioxanes and Silica Nanoparticles as Platforms for Fluorine and Gadolinium Based Contrast Agents for Magnetic Resonance Imaging

---

Silsesquioxane und Silika-Nanopartikel als Grundlagen für Fluor- und Gadolinium-basierte Kontrastmittel für die Magnetresonanz-Bildgebung

Dissertation

der Mathematisch-Naturwissenschaftlichen Fakultät

der Eberhard Karls Universität Tübingen

zur Erlangung des Grades eines

Doktors der Naturwissenschaften

(Dr. rer. nat.)

vorgelegt von

Filiz Kocak

aus Sulz a. N.

Tübingen

2014

Tag der mündlichen Qualifikation:	17.12.2014
Dekan:	Prof. Dr. Wolfgang Rosenstiel
1. Berichterstatter:	Prof. Dr. Hermann A. Mayer
2. Berichterstatter:	Prof. Dr. Reiner Anwander

Die vorliegende Arbeit wurde von Juni 2011 bis Dezember 2014 am Institut für Anorganische Chemie der Eberhard Karls Universität Tübingen unter Anleitung von Herrn Prof. Dr. Hermann A. Mayer durchgeführt.

Meinem Doktorvater, Herrn Prof. Dr. Hermann A. Mayer, danke ich herzlich für die Aufnahme in seinen Arbeitskreis, für die Bereitstellung des interessanten Themas und der hervorragenden Arbeitsbedingungen, seinem steten Interesse an meiner Arbeit, zahlreichen wertvollen Diskussionen und Anregungen sowie der Möglichkeit, Teile dieser Arbeit auf internationalen Konferenzen zu präsentieren.

Mein herzlicher Dank gilt

Meinen aktuellen und ehemaligen Arbeitskollegen Dr. Verena Feldmann, Dr. Cornelia Futter, Dr. Sophie Wernitz, Melike Baltaci, Fabian Deuring, Farzia Hossain, Farhad Jafarli, Dr. Wolfgang Leis, Johannes Maisch, Thomasz Misztal, Helene Strauch und Dr. Marc Stickel für das freundschaftliche Arbeitsklima, die gute Zusammenarbeit und die sehr schöne gemeinsame Zeit. Dr. Marc Stickel danke ich zusätzlich für das Korrekturlesen dieser Arbeit und Melike Baltaci für die Unterstützung meiner Arbeit in der Zeit als wissenschaftliche Hilfskraft. Meinem Arbeitskollegen Dr. Wolfgang Leis möchte ich außerdem sehr herzlich danken für die Einführung in spezielle NMR Messungen und seine hilfreichen Diskussionen.

Allen Kollegen im Arbeitskreis Wesemann für die schöne gemeinsame Zeit, insbesondere Michael Luick für das Korrekturlesen dieser Arbeit

Dr. Jörn Engelmann vom Max-Planck-Institut für biologische Kybernetik in Tübingen für die sehr schöne Kooperation, die hilfreichen Diskussionen und die zahlreichen Messungen, außerdem Dr. Ilgar Mamedov für seine Anregungen und Ratschläge sowie sämtliche Messungen der fluorierten Verbindungen, ebenso Dr. Phil. Gisela E. Hagberg für die Aufnahme der ^{19}F MR-Bilder, weiterhin Hildegard Schulz für die schöne Koorperation bei den Silika Partikeln und Dr. Aneta Keliris für ihre hilfreichen Diskussionen und ihre Hilfe bei der Koordination der ^{19}F Messungen.

Prof. Dr. Reiner Anwander für den Zugang zur ASAP 2020, Dr. Sonja König und Tatiana Spallek für die Einführung in die Messtechnik

Eva Lohmann vom Institut für angewandte Physik, für die Aufnahme der zahlreichen REM Bilder am Philips XL 30-FEG

Prof. Dr. Thomas Chassé und Elke Nadler für zahlreiche weitere REM und RTEM Aufnahmen am Hitachi SU8030

Dr. Klaus Eichele und Kristina Strohmaier für die Hilfe bei NMR relevanten Fragen

Brigitte Schindler für die Aufnahme der Festkörper-NMR Spektren

Prof. Dr. Rolf Daniels für den Zugang zum Zetasizer NanoZS und Klaus Weyhing für seine Hilfe und die Einführung in die Messtechnik

Dr. Markus Ströbele für die Aufnahme der thermogravimetrischen Messungen

Prof. Dr. Udo Weimar für die Mitbenutzung des Labors

Frau Dr. Dorothee Wistuba für die Anfertigung der hochaufgelösten ESI-TOF MS Messungen

Dr. Wolfgang Bock für die Anfertigung der Elementaranalysen

meinen Eltern, meinem Bruder und meiner Schwester sowie ihren Ehepartnern, für ihre unermüdliche Unterstützung.

Contributions and Posters

Contributions

Parts of this work are results from collaborations with Dr. Jörn Engelmann and Dr. Ilgar Mamedov (High-Field Magnetic Resonance Center, Max Planck Institute for Biological Cybernetics, Tübingen, Germany).

The ^{19}F *post mortem* images (chapter 3.1, Figure 7; chapter 3.6, Figure 27 and 28), *in vitro* experiments (chapter 3.6, Figure 26, Table 7) were performed, generated and provided by Dr. Ilgar Mamedov and Dr. Phil. Gisela E. Hagberg. The ^{19}F relaxation values (chapter 3.6, Table 6) were performed and provided by Dr. Ilgar Mamedov.
The ^{19}F relaxation values (chapter 3.6, Table 8), silica nanoparticle MRI experiments (chapter 4.2.10, Figure 55, Table 19 and 23) and relaxometry values of the leaching samples (chapter 4.2.11, Figure 56, Table 24) were performed, generated and evaluated by Dr. Jörn Engelmann.

Posters

ISACS13-Challenges in Inorganic and Materials Chemistry, Dublin, Ireland, 2014

5th EuCheMS Chemistry Congress, Istanbul, Turkey, 2014

Meinen Eltern

und

meinem Neffen Ensar

Table of Contents

Figures

Tables

Abbreviations and Symbols

A	specific surface area
ACN	acetonitrile
AIBN	azobisisobutyronitrile
APTES	(3-aminopropyl)triethoxysilane
B	magnetic field
BET	Brunauer-Emmet-Teller
CA	contrast agent
calc	calcinated
COSY	correlation spectroscopy
CP	cross polarisation
CPD	Composite Pulse Decoupling
CPMG	Carr-Purcell-Meiboom-Gill
d	doublet
d	diamagnetic
D	self-diffusion coefficient
d	day(s)
DCC	*N, N'*-dicyclohexylcarbodiimide
DCM	dichloromethane
DEE	diethylether
DEPT	distorsionless enhancement by polarisation transfer
d_H	hydrodynamic diameter
DIPEA	*N'N'*-diisopropylethylamine
DLS	dynamic light scattering
DMF	dimethylformamide
DMSO	dimethylsulfoxide
DO3A	1,4,7,10-tetraazacyclo-dodecane-1,4,7,10-triacetic acid
DOSY	diffusion-ordered spectroscopy
DOTA	1,4,7,10-tetraazacyclo-dodecane-1,4,7,10-tetraacetic acid
DOTA-BA	1,4,7,10-tetraazacyclododecane-1-(4-(carboxymethyl) benzoic)-4,7,10-triacetic acid

DOTA-GA	1,4,7,10-tetraazacyclododecane-1-glutaric-4,7,10-triacetic acid
DPAP	2,2-dimethoxy-2-phenylacetophenone
DRIFT	diffuse reflectance infrared spectroscopy
e.g.	exempli gratia
EA	elemental analysis
eq.	molar equivalents
ESI	electrospray ionization
Et	ethyl
EtOH	ethanol
FISP	fast imaging with steady state precession
FLASH	fast low angle shot
Gd	gadolinium
h	hour(s)
HEPES	4-(2-hydroxyethyl)-1-piperazineethanesulfonic acid
HMBC	heteronuclear multiple bond correlation experiment
HMQC	heteronuclear multiple-quantum correlation experiment
HPDEC	high power decoupling
HR	high resolution
HSQC	heteronuclear single quantum coherence experiment
Hz	Hertz
ICP	inductively coupled plasma
IR	infrared
J	coupling constant
K	Kelvin
k_B	Boltzmann constant
kDa	kilodalton
M	molar mass
m	mass
m	multiplet
M	molarity
m/z	mass to charge ratio
MAS	magic angle spinning

MeOD	deuterated methanol
min	minute(s)
mM	milli molar
MR	magnetic resonance
MRI	magnetic resonance imaging
MS	mass spectrometry
mV	milli Volt
N_A	Avogadro constant
NEt_3	triethylamine
NMR	nuclear magnetic resonance
NP	nanoparticle
O1	center frequency of spectrum
OAPh-POSS	octa(aminophenyl)-POSS
OAP-POSS	octa(3-chloroaminopropyl)-POSS
obs	observed
O_h	octahedral symmetry
OV-POSS	octavinyl-POSS
p	paramagnetic
p/p^0	relative pressure
PBS	phosphate buffered saline
PDI	polydispersity index
PEG	polyethylene glycol
PFC	perfluorocarbon
PFG	polyorganofluorinated group
PF-POSS	polyorganofluorinated POSS
pm	picometer
POSS	polyhedral oligomeric silsesquioxane
ppm	part per million
q	quartet
r_1	longitudinal relaxivity
r_2	transverse relaxivity
RARE	rapid acquisition relaxation enhancement
reh	rehydroxylated

r_H	hydrodynamic radius
rpm	rounds per minute
rt	room temperature
s	singlet
sep	septet
SNP	silica nanoparticle
SNR	signal-to-noise ratio
t	triplet
T	temperature
t	time
T	Tesla
T_1	longitudinal relaxation time
$t_{1/2}$	half life
T_2	transverse relaxation time
TBTU	O-(benzotriazol-1-yl)-*N,N,N′,N′*-tetramethyluronium tetrafluoroborate
TEOS	tetraethyl orthosilicate
THF	tetrahydrofurane
TOF	time-of-flight
V	volume
V_H	hydrodynamic volume
Γ	surface concentration
δ	chemical shift in ppm (NMR)
δ	bending vibration (IR)
η	viscosity
ν	stretching vibration (IR)
τ_R	rotational correlation time
ω	Larmor frequency

1 Introduction

The development of non-invasive diagnostic tools in order to analyze infections, injuries, tumors and many other diseases in an early stage is becoming increasingly important. Therein the magnetic resonance imaging (MRI) technique is one of the most important diagnostic tools for the visualization of the human soft tissue. The MRI technique was firstly developed by Lauterbur in the early 1970s. The measuring principles of MRI are based on the nuclear magnetic resonance (NMR). Nowadays, the MRI is an established diagnosis method in clinical medicine as well as in biomedical research. Most commonly, the ^{1}H MRI imaging technique is applied to obtain anatomical and soft tissue information. Furthermore the MR imaging is possible by detection of heteronuclear MRI atoms *inter alia* by the fluorine MRI (^{19}F MRI).

In order to enhance the sensitivity in MR images, so called contrast agents (CA) have become indispensable drugs in medical imaging. The CAs used in the ^{1}H or the ^{19}F MRI work in different ways. While the ^{1}H CA influences the water molecules present in living organisms, the signal in the ^{19}F MR image originates only from the fluorine atoms of the ^{19}F CA.

The mode of action of a ^{1}H CA is based on its paramagnetism, its unpaired electrons and the shortening of the longitudinal and/or transverse relaxation times (T_1 and/or T_2) of the surrounding water protons in tissues. These general paramagnetic metal based compounds can be divided into two groups, the positive agents (T_1 CAs) and the negative agents (T_2 CAs). Typical T_1 CAs are paramagnetic metal ion compounds of Mn^{2+}, Fe^{3+} and Gd^{3+} ions, which shorten the T_1 relaxation time significantly.[1–8] This results in an increase in brightness, which allows the discrimination between diseased and healthy tissue. In contrary, the T_2 agents lead to a decrease in the brightness by shortening of T_2 of the protons in the absorbing tissues. Typical T_2 agents are *e.g.* iron oxide (Fe_3O_4) nanoparticles.[9] Due to the positive signal enhancement the T_1 agents are thus often more preferred than the T_2 agents. Most of the currently used T_1 CA are based on a gadolinium(III) chelate complex.[10,11] Due to its seven unpaired electrons gadolinium has a large magnetic moment. By this way the effect of its paramagnetism is very efficient at low concentrations.

For the ^{19}F MRI the natural abundance of 100 % of the nucleus, the great similarity in the high magnetogyric ratio compared to ^{1}H, the broad chemical shift area as well as the lack

of background signals due to the absence of fluorine in human body outline the main advantages.[12,13] These properties render the ^{19}F MRI a very efficient alternative technique besides to the ^{1}H MRI which allow the detection of various diseases in their initial phase.[14] Recently reported research fields are for instance the *in vivo* inflammation imaging, fluorine labeled drugs, cell tracking studies and the application in nanotherapy.[14–18]

Furthermore, nanoparticular systems are gaining more and more importance in drug delivery and imaging techniques. [19–23] The immobilization of a contrast agent for ^{1}H or ^{19}F imaging any other targeting molecule or a drug molecule on a nano-sized material offers numerous benefits for a wide range of *in-vivo* applications. Besides the improved *in vivo* localization and longer half-live times due to longer circulation in organic systems, the implementation for instance as long term-tracking compounds or multimodal drug designs can be realized.[24–30] Furthermore the creation of second spot agents is realized by combined $^{1}H/^{19}F$ MRI, which profits from advantages of both MRI detectable nuclei.[31–33] For ^{1}H imaging the increased research on nanoparticle based T_1 contrast agents shows important features.[19] Especially silica based matrices offer great advantages due to their good biocompatibility and diverse surface modifications.[34–36] The porosity of a NP material influences the increasement of relaxivity. High relaxivities were reported before for mesoporous silica materials modified with high payloads of Gd(III) complexes.[37–44] However, in porous materials the water diffusion process is limited.[39,44,45] Conversely, nonporous particles ensure unhindered interaction with water protons. In consequence, high relaxivity efficiency with minimized amounts of Gd(III) is only guaranteed by the use of nonporous systems. Moreover the anchoring of CAs on nanoparticles reduces the rotational tumbling and leads to a higher rotational correlation time (τ_R) which increases the relaxivity.[1,28,46] Furthermore the immobilization, *e.g.* on a silsesquioxane or on a silica nanoparticle (SNP) shows an amplifying effect by significantly raising the number of bound CA molecules. In this way a high efficiency is obtained for ^{1}H and/or ^{19}F MRI by gaining high concentrations of CA molecules in a small volume.

The requirement of an intense, sharp signal in the ^{19}F MRI can be achieved by the synthesis of high symmetric structures. Especially, the utilization of molecular structures, like T_8-silsesquioxane cubes, has many advantages since the pharmacokinetics are easier to research for well-defined molecular structures.

Aim of the present work is the synthesis and investigation of new potential contrast agents for their application in ^{1}H and ^{19}F magnetic resonance imaging, respectively, which are generated by immobilization on silica matrices. Therefore two different lanthanoid(III) (Ln = Gd) DOTA chelate complexes will be anchored on nonporous SNPs to attain a high payload of Gd(III) complex, while the fluorinated CAs will be bound to cubic T_8-Silsesquioxanes in order to multiply the intensity of the ^{19}F NMR signal.

In the first part of this work a range of highly symmetrical, eightfold substituted polyorganofluorinated POSS cubes (PF-POSS) of different polarities each generating a sharp singlet in the ^{19}F NMR spectrum will be discussed. The PF-POSS cubes will be fully characterized by different analytical methods. The physicochemical properties of the obtained PF-POSS cubes in consideration of their solubilities, their molecular size and their hydrolytic stabilities will be examined. Furthermore, the T_1 and T_2 relaxation times for the ^{19}F nucleus of selected PF-POSS cubes will be determined. Finally *in vitro* and *post mortem* images will be measured to examine their suitability for ^{19}F MRI applications.

In order to evaluate an optimal particle size, particles with diameters of about 15, 50 and 130 nm will be examined in the second part of this work. For the immobilization of the Gd(III) chelate complexes nonporous silica particles will be used to offer the opportunity of unhindered water exchange by exclusively surface bound CA molecules. Since here the payload of the used SNPs will be securely defined by chemically bound Gd(III) chelate complexes and surface adsorbed or pores filled CA molecules without forming a chemical bond will be excluded. The synthesized SNPs will be fully characterized by different analytical methods after each synthetic step. Furthermore, the interparticle interactions and the influence of surface charges on the relaxivity will be investigated by repeated conjugation of Gd(III) complexes after the primary coupling of Gd(III), as well as by modification of residual functional groups on the SNP surface. The longitudinal and transverse relaxation rates (r_1 and r_2) of all modified SNPs will be investigated by MRI at 3 Tesla in agar phantoms. Finally leaching tests of the twice reacted SNPs will be carried out with respect to the release of free Gd(III) ion.

2 General Basics

2.1 Nanoparticular Silica

2.1.1 Silsesquioxanes

The silsesquioxanes are a class of nanostructured hybrid organosilicon compounds, which were first discovered by *D. W. Scott* in 1946.[47] Their empirical formula can be described as $[R\text{-}SiO_{3/2}]_n$, where R can be a variety of organofunctional moieties, like alkyl, alkene, aryl or arylene groups. Generally, their synthesis is performed by hydrolysis of organotrichlorosilanes ($RSiCl_3$) or organotrialkoxysilanes $[RSi(OR')_3]$. The structure of silsesquioxanes varies depending on the synthetic method, the precursors and the catalysts used for the reaction. By this way random polymeric structures, polymer chains as well as diverse silsesquioxane cages, either fully or partially condensed, can be produced.[48–50] The so called Polyhedral Oligomeric Silsesquioxanes (POSS), which own a fully condensed structure, are characterized by the nomenclature T_n. The index n corresponds to the number of silicon atoms or Si-OR functions which form the cage (Figure 1).[51] The designation T refers to the number of oxygen atoms the silicon is connected to. Especially, due to its high symmetry and defined nanosized structure the T_8-POSS cage offers an ideal core for further functionalization with organic moieties.

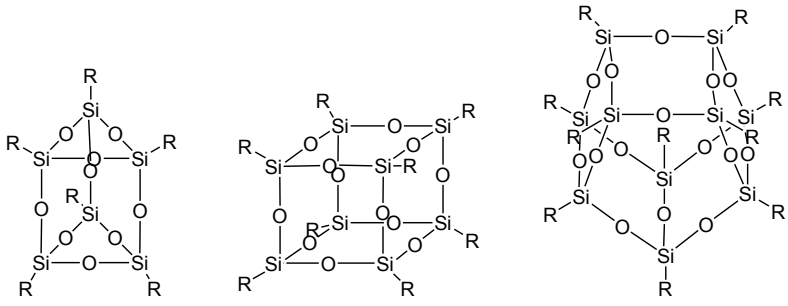

Figure 1: Structures of fully condensed POSS cages.

The excellent characteristics like electric insulation, thermal and photo stability and the non-toxicity of silicon offer the possibility of using the silsesquioxanes in several fields like in material sciences or biomedical applications to target biomolecules and in medicinal diagnostic agents.[48,50,52–59] In previous works, the T_8-POSS cage served as a

nanocomposite, core for dendrimers as well as for the functionalization with gadolinium chelates as contrast agents.[60–63]

2.1.2 Stöber Particles

Stöber particles are synthesized *via* the sol-gel process. The synthetic pathway of the sol-gel process provides the opportunity to construct inorganic networks from precursor molecules, like alkoxysilane or metal monomers, by condensation or hydrolysis reactions. Prime examples for sol-gel precursors are alkoxides of silicon, boron, aluminium, titanium and zirconium. The advantage of using alkoxides of metals and metalloids is their eager reactivity with water. The sol-gel process creates inorganic networks by the formation of a colloidal suspension of solid particles and polymers (sol) and the gelation of this sol to give a three dimensional, continuous matrix (gel) in a liquid phase. Different morphologies can be achieved by using additives and modifying the drying process. In this way, by utilizing the sol-gel process a wide material range can be produced like powders, fibers, non-porous ceramics and glasses, thin film coatings, monoliths and non-porous nanoparticles. Various applications, *e.g.* in the fields of catalysis, coating, chromatography, optical and electronics, medicinal industries and health care, benefit from sol-gel materials. The silicon sol-gel procedure runs through five different stages; the hydrolysis, condensation, gelation, ageing and drying. To produce branched structures in the sol-gel matrix, the precursor alkoxides have to be hydrolyzed and the partially hydrolyzed species connected again by condensation. These both reactions take place simultaneously and sol-particles with diameters of about 0.05-2 μm are formed.[64] There are various parameters which can influence the reactions and result in different sol-gel products. By modifying those parameters, targeted controlling of the desired product can be achieved. The hydrolysis and condensation reaction can result in monomeric, oligomeric and polymeric sols. The first case occurs when secondary and tertiary alkoxy groups are used for the reaction, while oligomers and polymers result by using primary alkoxy groups. The sol-gel process can either be catalyzed by an acid or by a base.[65,66]

The precursors for the synthesis of Stöber particles are mostly tetraalkoxysilanes like, methyl-, ethyl-, *n*-propyl- or *n*-butylalkoxysilanes. The reaction is performed in alcohols (methanol, ethanol, *n*-propanol, *n*-butanol) in the presence of ammonia and water. The size of the particles is determined by the temperature, the solvent (alcohol), the kind of

precursor (alkoxysilanes), the concentration ratio of the alcohol and water as well as the concentration of the tetraalkoxysilane.[67]

According to the moieties which are bound to the silicon atom, a nomenclature of M-, D-, T- and Q-groups was established. The superscript number reflects the quantum of siloxane bonds. By ^{29}Si solid state NMR spectroscopy the different groups can be detected due to their different chemical shifts. The most important ones are assigned in Figure 2. [51]

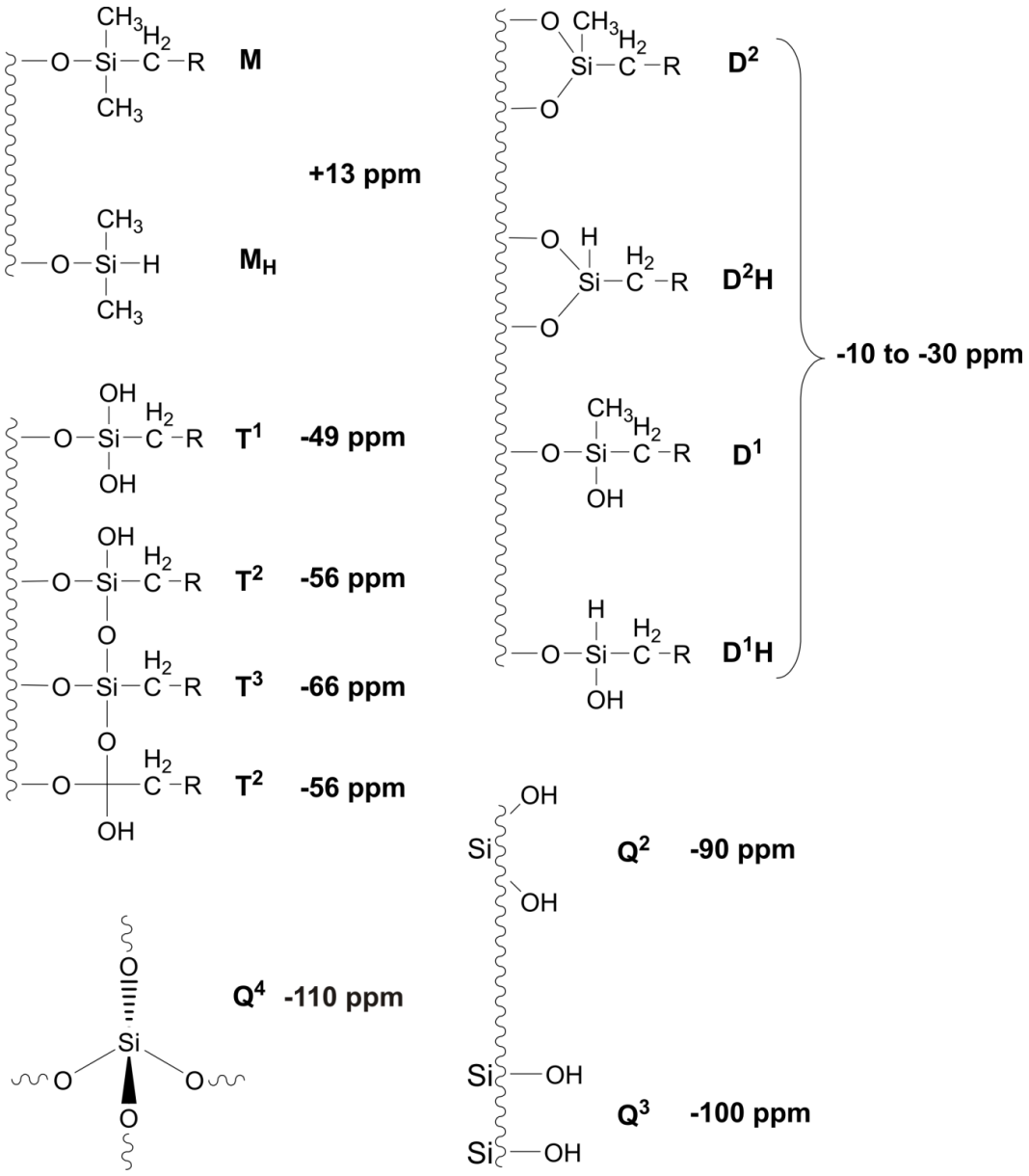

Figure 2: Nomenclature and ^{29}Si NMR shifts of different silica groups.

2.2 Characterization Methods

2.2.1 Dynamic Light Scattering (DLS)

Dynamic light scattering (DLS), also known as Photon correlation spectroscopy (PCS), is a common method to determine the hydrodynamic size of a species dispersed in a liquid. The typical application fields are measurements of micelles, emulsions, nanoparticles, colloids, proteins and polymers. The diffusion of a component in solution, the so called Brownian motion, is determined by the temperature and viscosity of the liquid as well as by the size of the suspended species. The DLS measures the speed of the diffusion due to the Brownian motion and relates it to the size, *e.g.* of the particles.[68,69] This is performed by the irradiation of the suspension by a laser beam and the subsequent detection of fluctuations of the scattered light, which are caused by the motion of the particles. The smaller particles cause fast fluctuations, while larger particles cause slow fluctuations. The diffusion velocity of the Brownian motion is defined by the translational diffusion coefficient (D). The obtained optical signal can be interpreted in terms of an autocorrelation function by the application of a cumulant method. The decay rate of this function is proportional to the diffusion coefficient. Applying the Stokes-Einstein equation the hydrodynamic diameter (d_H) of a suspended species can be calculated from the determined diffusion coefficient D.

$$d_H = \frac{k_B T}{3\pi\eta D}$$

d_H = hydrodynamic diameter k_B = Boltzmann constant D = translational diffusion coefficient

T = temperature η = viscosity of the liquid

Equation 1: Stokes Einstein equation.

Furthermore the translational diffusion coefficient is affected by the shape, surface structure and surface charge of the particles as well as by the ionic concentration of the liquid. For the latter two cases the diffusion speed can vary by changes of the thickness of the electric double layer, the so called Debye length (K^{-1}). Consequently, a low conductivity results in a thicker double layer, which minimizes the diffusion coefficient D due to slower motion of the suspended species. This results in a larger apparent

hydrodynamic diameter (d_H). On the contrary, higher conductivity of the fluid results in a smaller apparent d_H by a thinner electric double layer.

The hydrodynamic diameter (d_H), defined by the so called Z-average (d_z), results from the fit of a single exponential (cumulant analysis) of the correlation function. The Z-average is used for monodisperse particles with narrow size distributions. However, this technique is very sensitive to the presence of larger particles. In this case the fit by a multiple exponential results in an intensity weighted distribution (d_i). By using the Mie theory, this distribution can be transformed into the volume (d_v) or number weighted size (d_n) characterization.[69,70] This method is used for broad or multimodal distributions. In Figure 3 different size distributions (d_i, d_v and d_n) are compared.

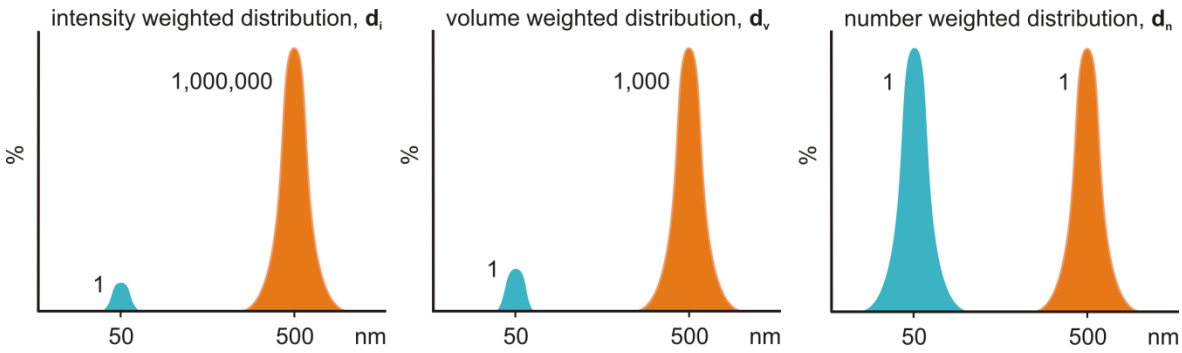

Figure 3: Different weighted distributions of a bimodal mixture of equal numbers of 50 nm and 500 nm particles.

2.2.2 Zeta Potential

In general the zeta potential (ζ) is the charge, which arises at the interface of a solid surface and the surrounding liquid.[69] A suspended solid, *e.g.* a particle, is surrounded by a solvent shell consisting of two layers. The inner layer (Stern layer) consists of ions, which are bound tight to the particle surface, the other is a diffuse layer with loosely bound ions. The potential of the diffuse region decreases with the distance from the particle surface. With the motion of a particle induced in an electric field the boundary with closely associated ions moves along with it through the liquid. The potential which arises with the motion of the particle between the shear layer and the surrounding liquid, the so called shear plane, is defined as the zeta potential. The determined zeta potential displays the effective surface charge of the particles and furthermore gives an indication for the stability of a colloidal system, *e.g.* by strong electrostatic repulsion of the particles due to a high negative surface

charge. Zeta potentials <-30 mV or >+30 mV indicate the stability of a particle suspension or any other colloidal system.

2.3 Magnetic Resonance Imaging (MRI)

2.3.1 ^{1}H MRI

The magnetic resonance imaging (MRI) is used as a standard diagnostic technique for the imaging of soft tissues of the human body.[11,71] The measuring principles are based on the nuclear magnetic resonance (NMR). For high quality images the human body's natural magnetic properties are used. As the human body consists of a high proportion of water (55 %) mostly the ^{1}H nucleus is applied for the MR imaging. In order to generate images from a NMR measurement, the ^{1}H NMR signals have to be depicted in dependence of their location. This is accomplished by linear, time dependent magnetic field gradients along all three spatial directions (x,y,z). The relation of the magnetic field strength B(z,t) in the z-axis direction is given according to Equation 2.

$$B(z,t) = B_0 + G_z(t)z$$

B_0 = external magnetic field z = spatial coordinate in z-direction

$G_z(t)$ = gradient strength

Equation 2

The Equation 2 is also valid for the x and y directions, which in all results in a Larmor frequency ω depending on the location r and the time t. This mathematical relationship is given by Equation 3, with the magnetogyric ratio γ.

$$\omega(r,t) = -\gamma B(r,t) \qquad r = \begin{bmatrix} x \\ y \\ z \end{bmatrix}$$

Equation 3

The resonance frequency of the water protons is dependent on the magnetic field strength (G). Hence due to the localization-dependency the excitation of protons in a certain region in the body is accomplishable. The assignment of a signal to a definite imaging unit, the

voxel, is achieved by the application of all three field gradients. The implementation of the measurements by different pulse sequences gives a dependency of the signal intensity on the spin density (ρ), the longitudinal relaxation time (T_1) and the transverse relaxation time (T_2). Importantly, these parameters depend on the different chemical environments of the excited water protons, this is *e.g.* the case for various types of tissues and furthermore the difference between healthy and diseased tissue. Using diverse pulse sequences, the image intensity can be weighted with respect to the T_1 or T_2 relaxation. To obtain an image by the resulting resonances, the signal intensity of each voxel is converted into the brightness of a gray-level scale.[2]

2.3.1.1 Contrast Agents

Contrast agents (CA) are employed to improve the discrimination of soft tissue or fluid in the human body. The signal intensity of NMR active nuclei, like water protons, can be influenced by shortening the spin-lattice (T_1) and spin-spin relaxation time (T_2), respectively. Generally paramagnetic metal based compounds act as CAs, which influence the T_1 and/or T_2 relaxation times of the protons in the surrounding tissue. An ideal CA should obtain a high number of unpaired electrons which causes a large magnetic moment. This is ensured for paramagnetic metal ions. However, a further condition must be fulfilled to attain an effective relaxation agent. Despite a high number of unpaired electrons, the electron spin relaxation time must be close to the Larmor frequency (ω) of the measured protons to obtain an ideal CA.[1,72] Those conditions are met best for Mn^{2+}, Fe^{3+} and Gd^{3+} ions.[1,2] Most commonly, the Gd(III) ion is used as a CA metal due to its seven unpaired electrons and thus the consequential long electron spin relaxation time, which results in a strong effect on the longitudinal relaxation time (T_1). Furthermore, the dwell time of water protons on the gadolinium aqua complex are very short.[73] Consequently, the high exchange rate of water leads to a higher influence of larger amounts of surrounding bulk water molecules. The major difficulty in using Gadolinium is its toxicity in the human body, due to the similar ionic radius compared to the calcium(II) ion.[74,75] In order to circumvent this disadvantage, inert and stable complexes of chelating ligands of Gd(III) are used.[74,76,77] Generally most CAs are based on a 1,4,7,10-tetraazacylododecane framework (cyclen) (Figure 4). Examples based on this structure are the commercially available contrast agents Dotarem™ and Magnevist™.[78]

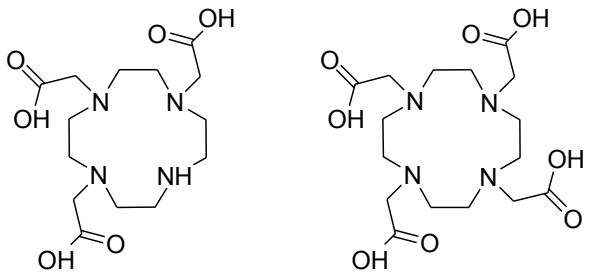

Figure 4: Examples of cyclen based structures for CA molecules.

The influence of paramagnetic compounds on the relaxation of surrounding water is given for the observed relaxation rate ($1/T_{1,2obs}$) by the sum of the diamagnetic ($1/T_{1,2d}$) and the paramagnetic term ($1/T_{1,2p}$).

$$\frac{1}{T_{1,2obs}} = \frac{1}{T_{1,2d}} + \frac{1}{T_{1,2p}}$$

Equation 4

The paramagnetic part is induced by the fluctuating local magnetic field caused by the unpaired electrons. The paramagnetic relaxation term is linearly proportional to the concentration of the paramagnetic metal ion ([M], usually in $mmolL^{-1}$).

$$\frac{1}{T_{1,2obs}} = \frac{1}{T_{1,2d}} + r_{1,2}[M]$$

Equation 5

The efficiency of a contrast agent is given by its relaxivity ($r_{1,2}$). The proportionality constant $r_{1,2}$ given in $mM^{-1}s^{-1}$, is the direct measured magnitude, which determines the capability of a contrast agent to enhance the proton relaxation rate. The relaxivity can also be defined as the paramagnetic relaxation which is normalized to a 1 mM concentration of the metal ion.[79] Commercial CAs generate a longitudinal relaxivity of 4-5 $mM^{-1}s^{-1}$ at a 20 MHz field (25 °C).[78]

For the water exchange, one or two coordination sites of the complex must be uncoordinated, since the relaxation rate ($1/T_{1,2}$) is influenced by the interaction of the Gd(III) ion with the water protons. The total proton relaxivity by paramagnetic compounds is the sum of the inner-sphere, the second sphere and the outer sphere relaxivity (Figure 5).

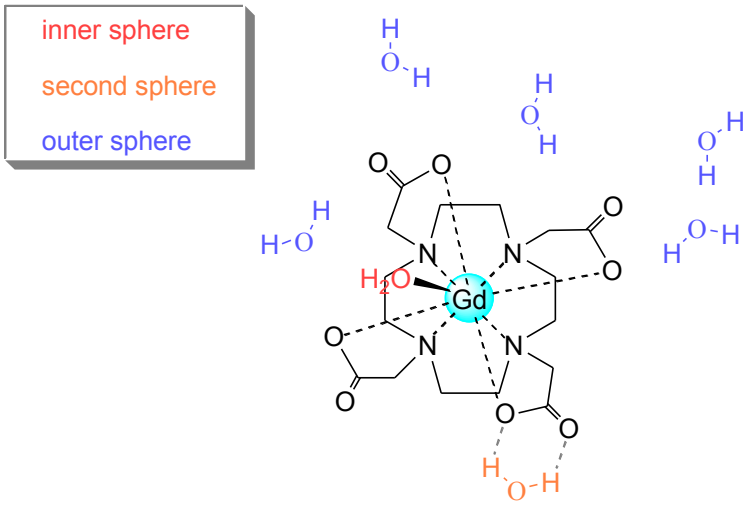

Figure 5: Schematic interactions of water molecules with Gd(III) based CAs.

In the inner sphere the relaxation is generated by the interaction of coordinated water molecules with the electron spins of the metal ion. In the second sphere the water molecules are bound to the ligands. With the exchange of influenced water molecules with bulk molecules by random translational diffusion, the relaxation effect affects a large amount of water. Each exchange depicted in Figure 5 contributes to the relaxation, where the inner sphere has the greatest influence.[2,72,80] The second and outer sphere contribute 40-50 % to the overall relaxivity.[78,80,81]

2.3.2 ^{19}F MRI

Nowadays nearly all contrast agents are based on the influence of the ^{1}H nucleus. An important alternative diagnostic technique is the use of the ^{19}F nuclei. Recently several groups have been using the ^{19}F nuclei as diagnostic and drug delivery tools.[17,31,82–84] Already in the early 1970s, shortly after the introduction of the ^{1}H MRI technique, first experiments with fluorinated molecules have been tested as contrast agents for the ^{19}F MR imaging.[85] In a broad range of biomedical applications, like infectious diseases, anesthetics and anticancer drugs, fluorinated substances are used, due to their nontoxicity

and chemical inertness.[86] The ^{19}F MRI is an especially promising technique owing to the 100 % natural abundance and the ½ spin of ^{19}F. Furthermore the magnetogyric ratio of the ^{19}F isotope is very close to that of hydrogen. This leads to a remarkably high MRI sensitivity of 83 % related to the hydrogen nucleus.[85,87] In addition, the possibility to measure ^{19}F MR images at low field strength without the re-fitting of a clinical device, due to the slight deviation of the ^{19}F frequency from the proton frequency, presents a great advantage considering the clinical application and the cost issue.[88,89] Moreover, due to the broad chemical shift area (> 350 ppm) of the ^{19}F nucleus a high resolution of the resonance lines is achieved with clinical MR scanners. Actually, fluorine in the human tissues only exists in teeth and bone matter (> 10^{-6} M). The short spin-spin relaxation times (T_2) of those ^{19}F containing body parts are not visible with conventional MRI techniques since the signal is below the MRI detection limit.[12] Hence, due to the lack of endogenous fluorine in living organisms no disturbing background signal is present, which leads to a better signal-to-noise ratio and offers an exact anatomic localization of the ^{19}F signal of injected substances by the combination of $^{1}H/^{19}F$ MRI *in vivo* techniques. The combined $^{1}H/^{19}F$ imaging was first demonstrated in 1977.[85] The suitability of ^{19}F MRI for several quantitative applications was shown and the linear relationship between the ^{19}F content and the generated signal intensity was demonstrated.[83] Special attention must be paid to inflammatory processes, which can be detected in high resolution by ^{19}F MRI. Since in the initial phase of the disease no great differences between the diseased tissue and the healthy tissue are observed, the early identification by *in vivo* ^{19}F MRI attains therefore more and more attention for illnesses such as cardiovascular disease, multiple sclerosis or different types of cancer.[14,17] For medicinal researches generally perfluorocarbons (PFCs, *e.g.* perfluoro-15-crown-ether, C_2F_6) or SF_6 are used.[82,90] Because, those compounds are not water soluble and significantly lipophobic they have to be injected as emulsions, inhaled or administered as nanocapsules.[82,91,92] This causes a high retention time in the body. The ideal ^{19}F tracer should fulfill *inter alia* the following conditions: The compound has to contain a large amount of chemically equivalent ^{19}F atoms and should own a facile synthesis and formulation.[12] Furthermore definite chemical properties, as well as low *in vitro* and *in vivo* toxicity are required. Lastly the compound should show a simple ^{19}F spectrum, if procurable with a sharp and intense singlet and further should be characterized by a short T_1 as well as a long T_2 relaxation time.[12]

3 Polyfluoroorganofunctionalized T_8-Silsesquioxanes (POSS)

3.1 Review and Aim of the Work

As part of this work a series of different precisely defined highly symmetrical polyorganofluorinated T_8-silsesquioxanes (PF-POSS) were synthesized to study their chemical characteristics and suitability as building blocks for contrast agents (CA) in the ^{19}F magnetic resonance imaging (^{19}F MRI). In this context, solubilities, hydrodynamic radii, hydrolytic stabilities as well as relaxivities of several PF-POSS were determined.

In a previous work two different PF-POSS were synthesized as possible CA building blocks for ^{19}F MRI (**I** and **II**) by the addition reaction of the amino function to the corresponding isothiocyanate (Figure 6).[60]

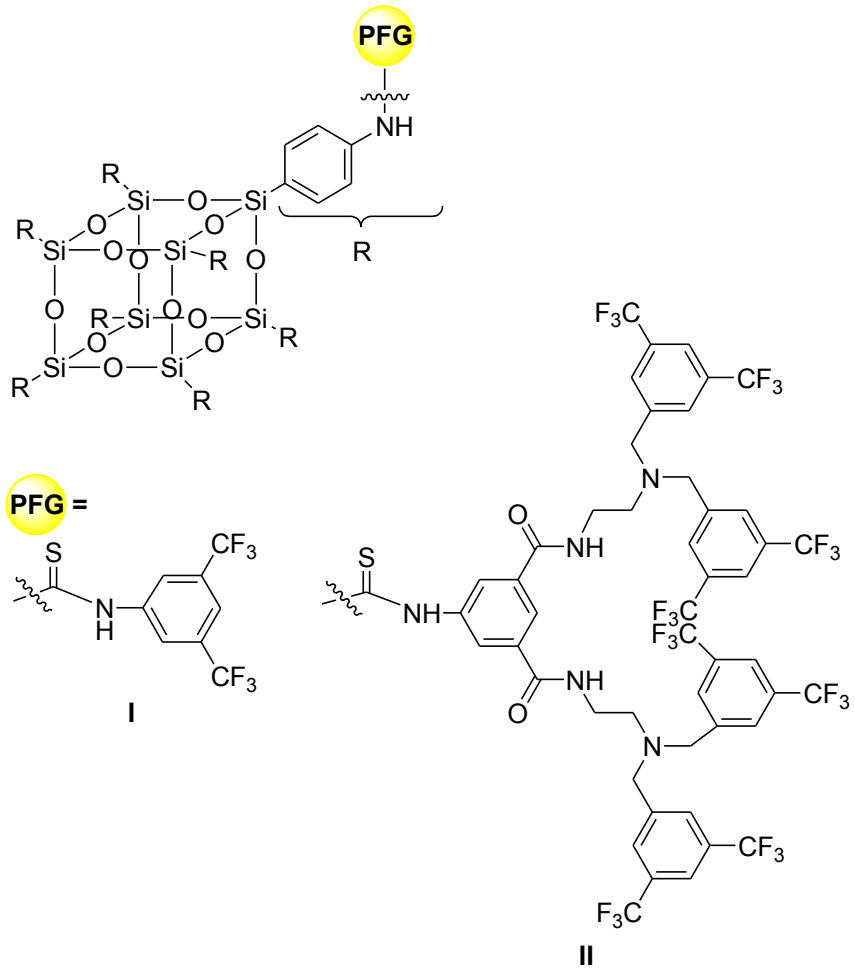

Figure 6: Chemical structures of PF-POSS **I** and **II**.

The great advantage of the addition reaction by forming a thiourea bond lies in the fact of not forming by-products and not requiring any reagents which could cause difficulties in

the purification of the compound. Each of the reactions was carried out in dry THF, while the reactants were stirred at room temperature for 3 h. In the first case octaaminophenyl-POSS (OAPh-POSS) was functionalized with a monomeric polyorganofluorinated group (PFG), 3,5-bis(trifluoromethyl)phenyl isothiocyanate, to give the PF-POSS **I** (Figure 6). In the latter case an isothiocyanate functionalized PFG of a dendrimeric structure was synthesized and bound to the OAPh-POSS to give Cube **II** (Figure 6). By this design a remarkable increase in the number of fluorine atoms from 24 up to 48 per POSS was achieved (Figure 6).[60] Both of the syntheses resulted in successful eightfold POSS substitution and generated a sharp singlet in the ^{19}F NMR spectrum for each substance.[60] Due to the high number of ^{19}F atoms and to the high symmetry the NMR signal of the compounds showed one sharp intense signal. However, the solubility of both compounds turned out to be insufficient for *in vivo* applications.

For ^{19}F magnetic resonance imaging (MRI) of **I** *in vitro* solutions of 40 µg substance per 100 µl solution related to the concentration of ^{19}F atoms were used. A signal-to-noise ratio (SNR) of about 1000 in 1 min measurement time (without Rayleigh correction) was obtained. The best signal was achieved with the ^{19}F-RARE pulse sequence (Figure 7, **B**).[93,94] The MRI *post mortem* images 1 h after insertion of the sample into the brain showed no signal neither with the ^{19}F-RARE nor the ^{19}F-FISP sequence (Figure 7, **F** and **H**).[95] Thus no additional ^{19}F-FLASH pulse sequence experiments were performed.[96] Eight days after insertion of the sample, further measurements with the reference compound in a vial placed on the top of the *post mortem* rat head were performed. The reference vial was readily visible in the upper slice with SNR of 500 within 5 min (Figure 7, **J**). However no signal for compound **I** was detectable for the middle and lower slices (Figure 7, **K** and **L**). From this it must be concluded that no distribution of **I** into the brain tissue takes place. Hence a *post mortem* measurement of **II** has not been carried out.

sequences

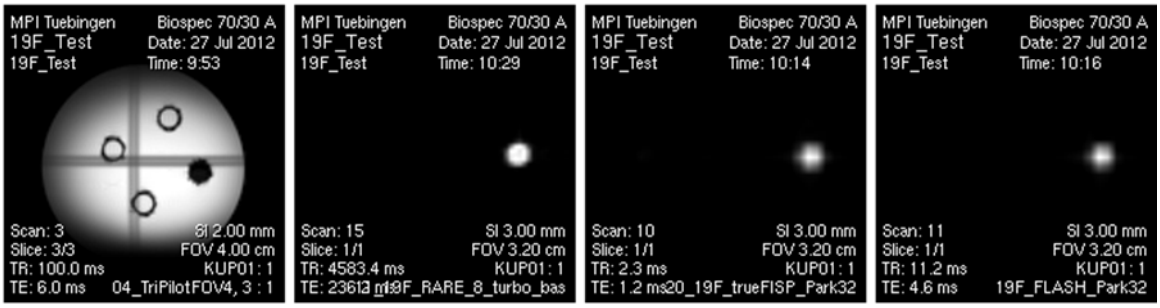

A ^{1}H localizer | **B** ^{19}F RARE | **C** ^{19}F FISP | **D** ^{19}F FLASH

***post mortem* 1 h after insertion**

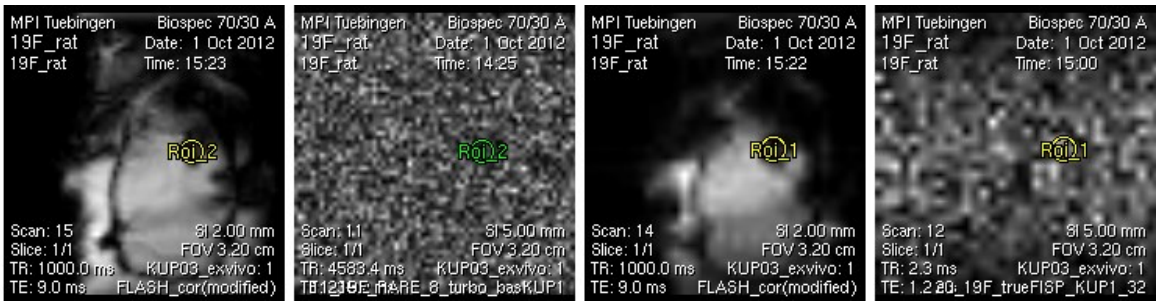

E ^{1}H localizer for RARE | **F** ^{19}F RARE | **G** ^{1}H localizer for FISP | **H** ^{19}F FISP

***post mortem* 8 days after insertion**

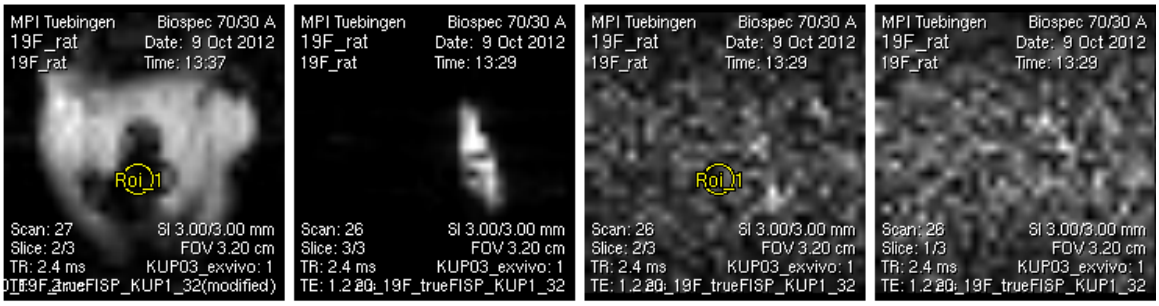

I ^{1}H localizer | **J** ^{19}F FISP upper slice | **K** ^{19}F FISP middle slice | **L** ^{19}F FISP lower slice

Figure 7: ^{19}F MRI experiments of **I**.

In order to vary the chemical properties of cube **I** (Typ **C** in Figure 8), modifications of the POSS were carried out in two directions. First by decreasing the polarity of compound **I** by the insertion of aliphatic parts (Typ **A/B**) and second by increasing the polarity as much as possible to achieve partial or complete water solubility (Figure 8, Typ **D/E**). In the first instance the polarity of **I** was decreased to investigate the behavior in non-polar media like in the brain tissue. Therefore initially, the POSS-bound aromatic structure was displaced by an aliphatic linker, by using octa(3-chloroammoniumpropyl)-POSS (OAP-POSS) as

core structure (Figure 8, Typ **B**).

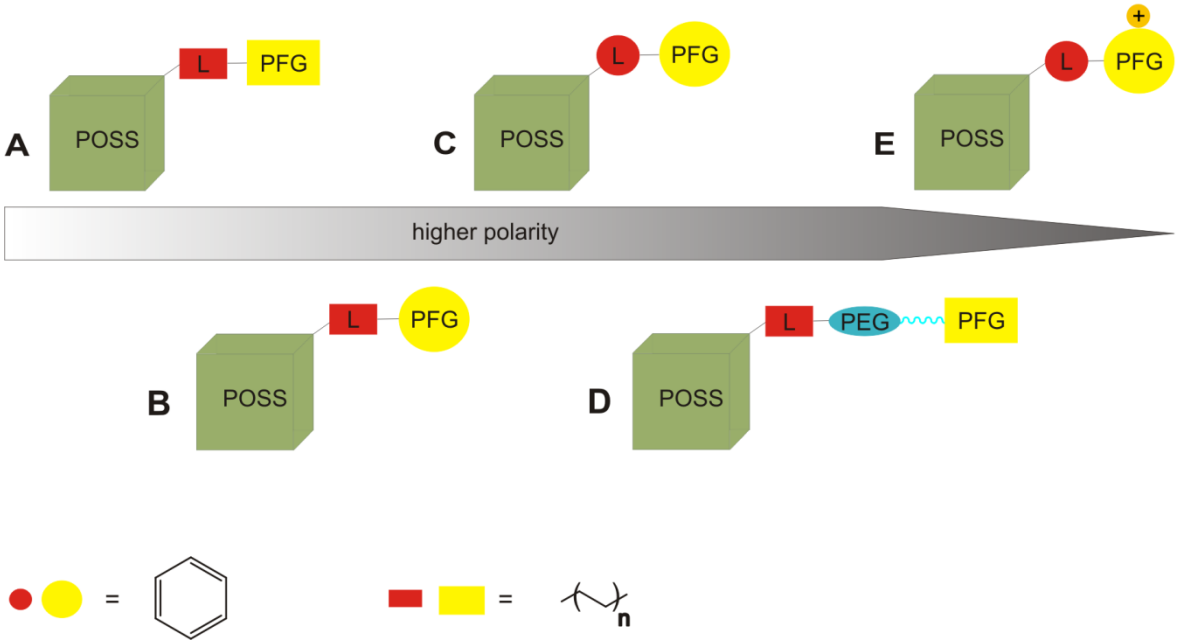

Figure 8: Modification types of PF-POSS cubes; Rectangles symbolize the aliphatic structures, circles symbolize the aromatic structures.

In the next step, a further reduction of polarity was aimed by replacing each, the POSS-bound and PFG-bound spacers, through aliphatic groups (Figure 8, Typ **A**). In contrast to this, a higher polarity of PF-POSS materials was obtained by coupling of polar functions to the POSS cages. Therefore the coupling of two different polyethyleneglycol (PEG) groups to octavinyl-POSS (OV-POSS) and chemical bonding of a positively charged PFG to OAPh-POSS was carried out, respectively (Figure 8 , Typ **D** and **E**). For all PF-POSS an ideal sharp singlet in the ^{19}F NMR spectrum was aimed. Physicochemical properties of the PF-POSS with diverse polarities and flexibilities of their linkers were investigated concerning their suitability as possible building blocks for ^{19}F MRI.

3.2 Results and Discussion

3.2.1 Syntheses

3.2.1.1 Synthesis of PF-POSS 3

In order to decrease the polarity compared to cube **I**, the POSS-bound aromatic structure was replaced by an aliphatic component according to modification type **B** (Figure 8). Therefore octa(3-chloroammoniumpropyl)-POSS (OAP-POSS, **2**) was used as the starting material.[61] Because the OAP-POSS decomposes rapidly, the compound has to be isolated as an octaammonium chloride salt to avoid a nucleophilic attack of the amino nitrogen at the silicon atom.[61,97] Furthermore, decomposition of the cage occurs by the presence of traces of water and thus the formation of hydroxide ions *via* reaction with the free amine of the POSS. Hence to generate a thiourea bond with 3,5-bis(trifluoromethyl)phenyl-isothiocyanate (**1**) the ammonium salt had to be activated by a base. The reaction was carried out at room temperature with an excess of **1** in anhydrous dimethyl sulfoxide for 16 h.

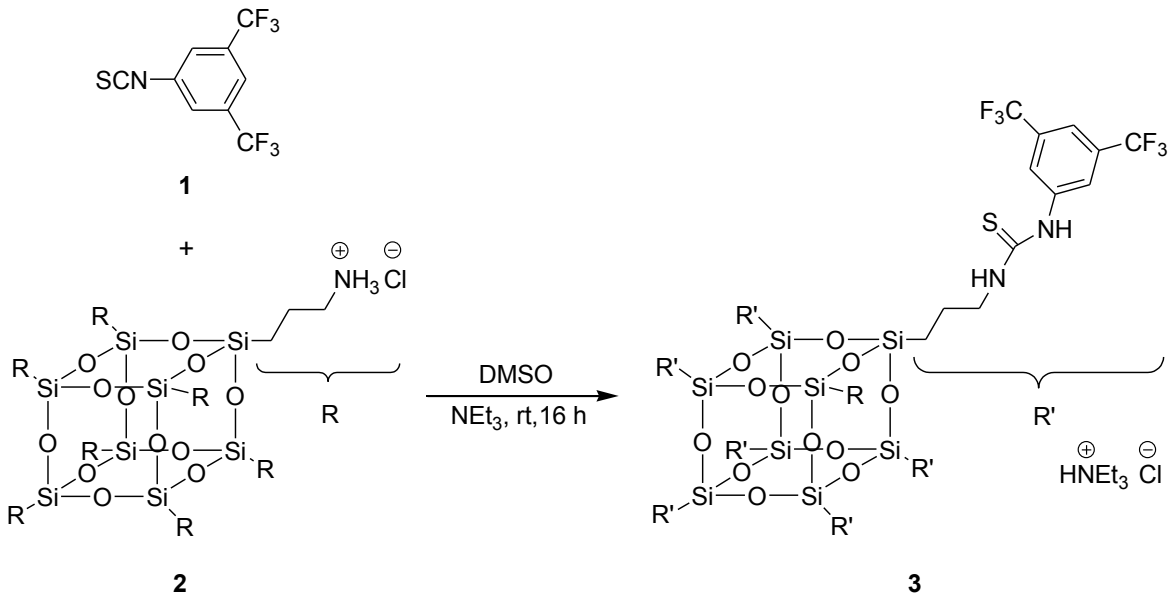

Scheme 1 Synthesis of PF-POSS **3**.

The implementation of the reaction with *N,N*-diisopropylethylamine (DIPEA) preferred as a non-nucleophilic hindered base resulted in an incomplete reaction both at room temperature (for 8 h) and at 60 °C (for 5 h). Precipitation of **1** from toluene yields incomplete substituted POSS resulting in a broad ^{19}F NMR signal for both reactions. A

higher conversion of the POSS amino groups to thiourea was observed for the reaction at room temperature. The purification by silica gel chromatography provides substituted POSS edges of about 89% (determined from the ^{1}H NMR spectrum) for the isolated product. Moreover complete conversion was obtained by the application of triethylamine (NEt_3) as base (Scheme 1).

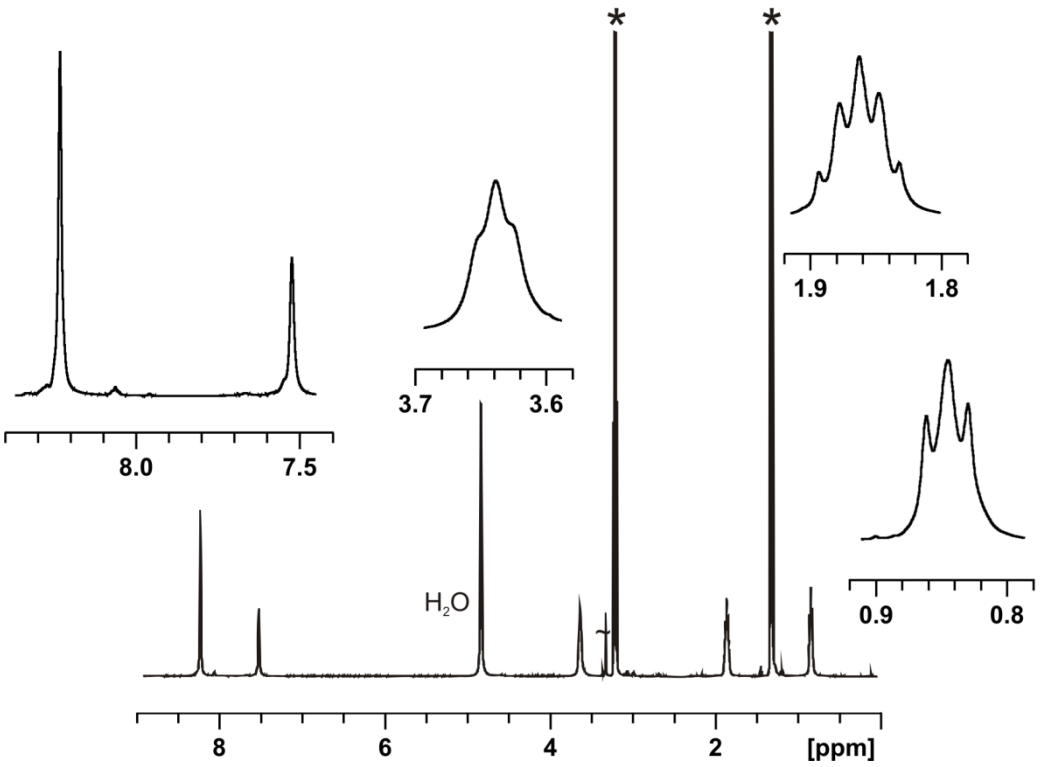

Figure 9: ^{1}H NMR spectrum of **3** in MeOD solution; *$HNEt_3^+$ salt.

After precipitation of unreacted **2** from methanol and the excess of **1** from acetone, further purification was implemented by column chromatography using silica gel. Remaining **1** was eluted with dichloromethane and the isolation of cube **3** was finally accomplished by elution using methanol. The isolated PFG-POSS **3** shows a sharp singlet at -64.30 ppm in the ^{19}F NMR spectrum and one signal at -67.8 ppm in the ^{29}Si DEPT-45 NMR spectrum, which indicates an intact and fully substituted POSS cage. The ^{1}H NMR spectrum in MeOD solution reveals the signals of residual triethylammonium salt at 1.31 and 3.20 ppm (Figure 9).The multiplet of the $SiCH_2$ protons displays a characteristic chemical shift of 0.84 ppm. The signal of the methylene protons next to the thiourea bond is observed at 3.64 ppm. The thiourea protons are not observed in the spectrum most probably due to fast

water exchange. The $^{13}C\{^1H\}$ NMR spectrum of **3** shows all signals of the desired product, as well as expected couplings of carbon atoms next to the CF_3 groups. However, complete separation of the triethylammonium salt from PF-POSS **3** could not be achieved *via* additional elution from an Amberlite XAD1600 resin column using acetonitrile.

3.2.1.2 Synthesis of PF-POSS 5

Another synthetic way to functionalize OAP-POSS (**2**) according to modification type **B** (Figure 8) was performed by an amidation reaction. The Schotten-Baumann method, a nucleophilic acylic substitution, is based on the reaction of amines with acid chlorides forming an amide bond. During the acylation of the amine an acidic proton is formed. Hence the addition of an additional equivalent base is required to continue the reaction by deprotonation of created ammonium ions. The reaction of **2** with 3,5-(bistrifluoromethyl)benzoyl chloride (**4**) according to the Schotten-Baumann method gives octafunctionalized PF-POSS **5** using NEt_3 as base (Scheme 2).

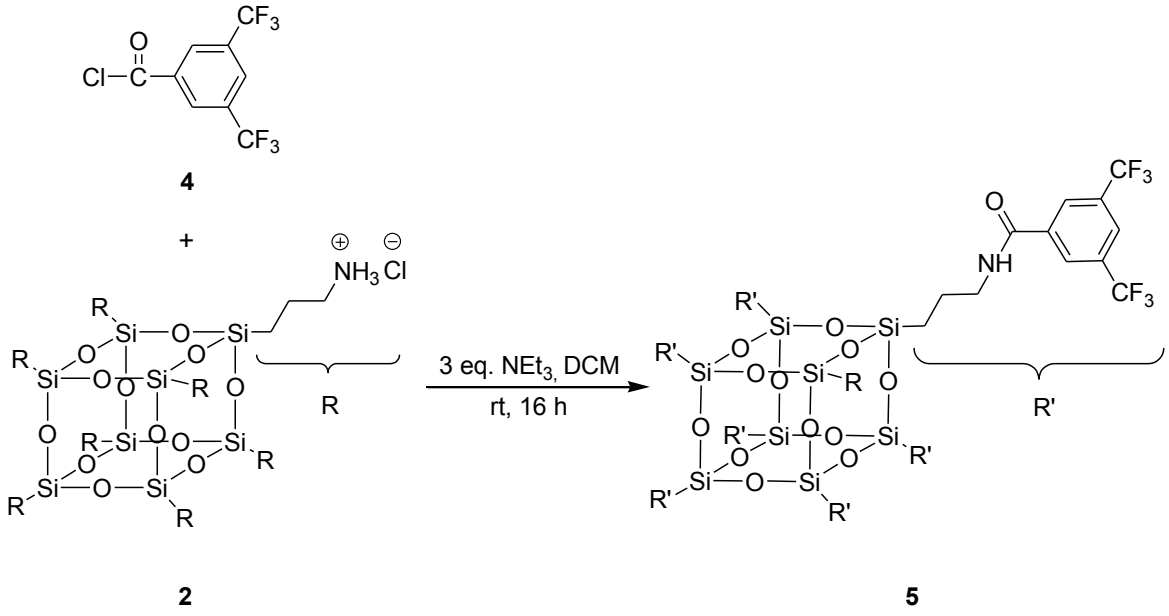

Scheme 2: Synthesis of PF-POSS **5**.

The ^1H NMR spectrum in MeOD solution of the PF-POSS **5** shows the expected signals at high field with the same multiplet structure as obtained for **3**. Both silica neighboring methylene groups exhibit signals at 0.75 and 1.78 ppm, respectively. The proton signal next to the amide bond occurs as a broadened triplet at 3.39 ppm with a coupling constant of 7.3 Hz. Signals of residual educt **4** appear in the aromatic region. To remove the

remaining salt the mixture in DCM was extracted with brine. However, NMR spectra of the organic phase showed a degradation of the PF-POSS cage. An alternative way of the extraction with DCM and hydrochloric acid (0.1 M) led to the same result. To investigate a more suitable purification by using another base the reaction was repeated with DIPEA. Interestingly, using DIPEA under identical reaction conditions resulted in partially substituted POSS. Prolonging the reaction time to 6 d still showed residual non-reacted POSS edges. Since the first synthetic way using NEt_3 base could not be combined with a suitable purification method another synthetic pathway than the Schotten-Baumann method was chosen to synthesize a PF-POSS according to type **B**. It is to be noted that a similar reaction as shown above by common peptide synthesis techniques and an acid functionalized PFG at room temperature (4 h) resulted in several ^{19}F resonances. Furthermore, the peptid coupling reagent (TBTU) could not be removed by extraction or column chromatography and generated a second ^{19}F NMR signal. Hence methods which do not require any additional reagents were considered as more suitable pathways to obtain the desired PF-POSS cubes.

3.2.1.3 Synthesis of PF-POSS Cubes via Thiol-ene Reactions

Alternative reactions to obtain PF-POSS of the type **B** with POSS-bound aliphatic frameworks were performed using thiol functionalized PFGs (**6-8**).

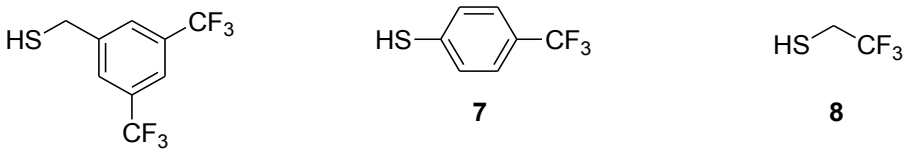

6 **7** **8**

Figure 10: Thiol functionalized PFGs.

Divergent from the strategy used above the following reactions are based on a radical mechanism. The so called thiol-ene reaction was preferred in this work to minimize the formation of by-products and the requirement of further reagents.[98–111] The reaction of the octavinyl-POSS (OV-POSS, **9**) with the PFG **6** delivers the desired PF-POSS **10** by using azobisisobutyronitrile (AIBN) as radical initiator (Scheme 3).[101] The reaction at 80 °C for 24 h in toluene shows incomplete substitution of **9**.

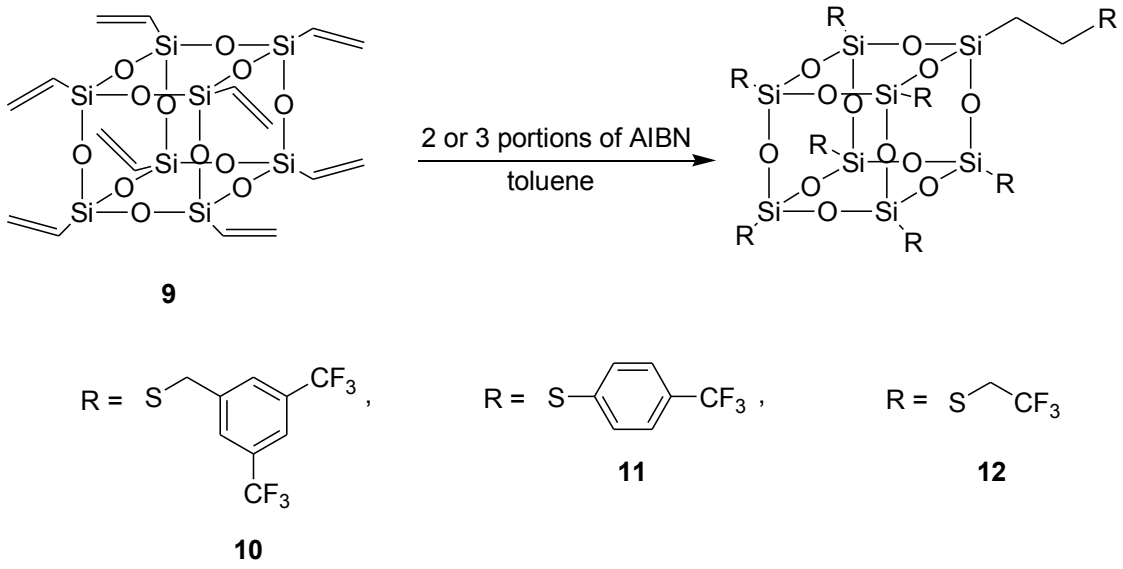

Scheme 3: Syntheses of the PF-POSS **10**, **11** and **12** *via* radical thiol-ene reaction.

The half-life time of AIBN of about 75 min at 80 °C and the additional steric effect of **6** which probably slows down the reaction was considered as the reason for only partial substitution of **9**.[112,113] Therefore, the reaction was continued for further 22 h after addition of a new portion of AIBN. The ^{1}H NMR spectrum in MeOD solution of the desired PF-POSS **10** verified the signals of the methylene groups at 0.88, 2.42 and 3.80 ppm which are shifted to lower field the more distant they are with respect to the POSS cage (Figure 11 a). The aromatic resonances were observed at 7.33 and 7.49 ppm in the correct integral ratio to the signals of the methylene protons. Investigation of the ^{1}H NMR spectrum reveals an almost complete substitution of **9**.

Quantification of the less intense signals of residual vinyl groups reveals a good conversion of 96 % for all POSS cage edges. Both in the ^{29}Si DEPT-45 NMR spectrum at -68.49 ppm and in the ^{19}F NMR spectrum at -64.21 ppm a singlet is observed and emphasizes the intactness of the PF-POSS **10**. Similarly the reaction with 4-(trifluoromethyl)thiophenol (**7**) results, after two portions of AIBN, in almost exclusively octafunctionalized PF-POSS (**11**) (Scheme 3 and Figure 11 b). Quantification from the ^{1}H NMR measurement leads to a good conversion of 97 % for all POSS edges.

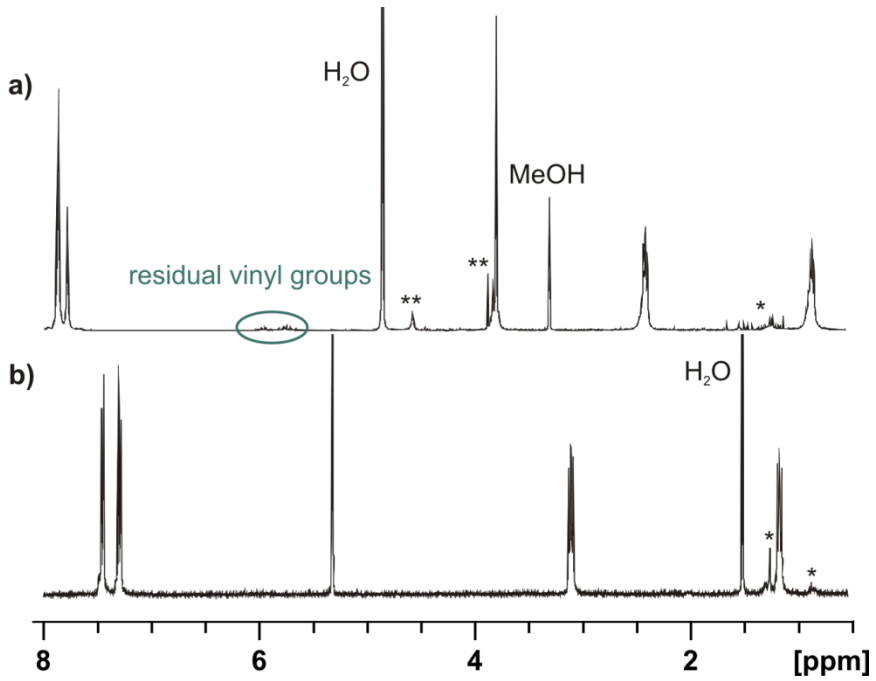

Figure 11: ^{1}H NMR spectra of a) **10** in MeOD (*H grease, **impurity) and b) **11** in CD_2Cl_2 (*H grease).

The aromatic protons, of an AA'BB' system, show a characteristic roof effect for the signals at 7.29 and 7.45 ppm (Figure 11 b). The resonances of the aliphatic protons display multiplet structures and integrate in the expected ratio to the aromatic protons. For both compounds **10** and **11** multiplets in the ^{13}C NMR spectra are generated by coupling with the ^{19}F nuclei. The expected septet for the aryl-CH of **10** at 7.78 ppm displays a coupling constant of 4.8 Hz ($^{3}J_{C\text{-}F}$). The quartets of the carbon atoms for the CF_3 groups result in coupling constants of 272.0 Hz ($^{1}J_{C\text{-}F}$) and for the neighboring quarternary carbon atoms of 33.1 Hz ($^{2}J_{C\text{-}F}$).[114,115] The PF-POSS cubes **10** and **11** are soluble in dichloromethane, chloroform, dimethyl sulfoxide and methanol.

For further reduction of polarity and the investigation of solubility properties and relaxivity effects the POSS-bound aromatic structures of **10** and **11** were changed into an aliphatic function according to the modification type **A** (Figure 8). The thiol-ene reaction was therefore performed with 2,2,2-trifluoroethanethiol (**8**) and three portions of AIBN at 80 °C in toluene. Upon completion of the reaction a final conversion of the initial OV-POSS groups by 96 % was achieved for **12** (Scheme 3 and Figure 12 a). The ^{1}H NMR spectrum reveals the signals of the aliphatic protons next to the POSS at 1.02 and 2.74 ppm (Figure 12 a). Furthermore, a quartet structure for the CF_3 neighbored methylene group at 3.06 ppm is observed, which results from the $^{3}J_{H\text{-}F}$ coupling of 10.0 Hz.

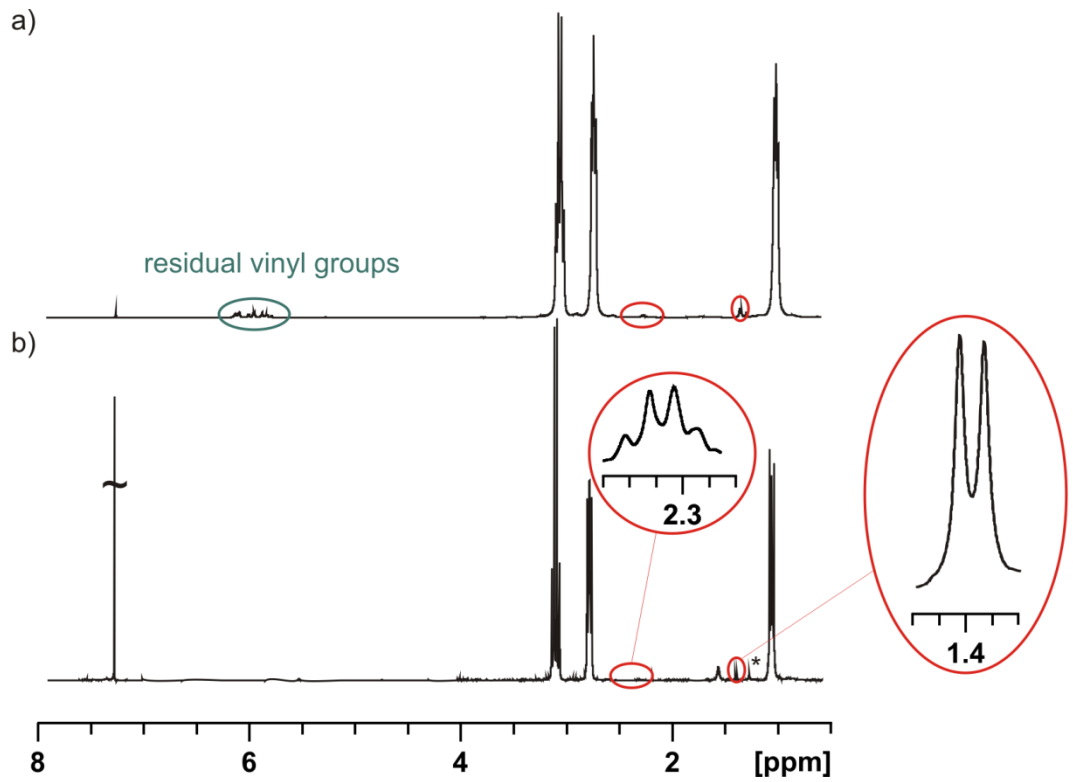

Figure 12: ^{1}H NMR spectra of **12** in $CDCl_3$ solution a) reaction with AIBN, b) reaction with UV light; (*H grease); multiplets of the Markovnikov product are highlighted in red.

The same reaction of OV-POSS **9** with **8** was performed using a 700 W medium pressure mercury lamp. The reaction mixture was dissolved in dry THF and irradiated for 3 h after the addition of 2,2-dimethoxy-2-phenylacetophenone (DPAP) as photoinitiator (Scheme 4).[98]

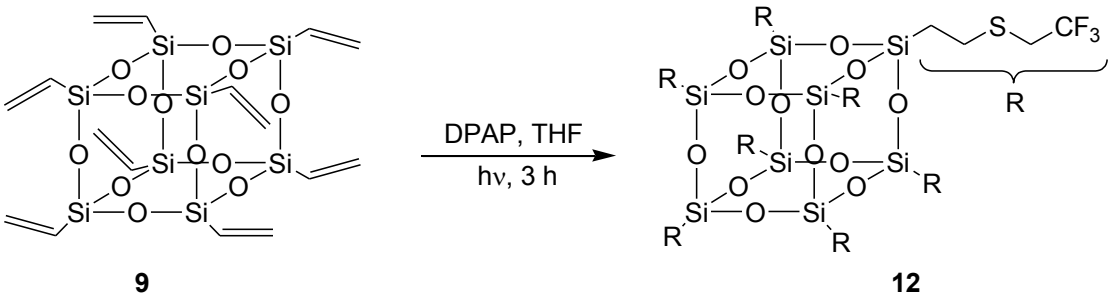

Scheme 4: Synthesis of **12** *via* UV radiation.

Evaporation of the solvent and precipitation of the residue from methanol results in the desired octafunctionalized cube **12**. In contrast to the reaction with AIBN (Scheme 3) no traces of unreacted POSS edges are observed in the proton NMR spectrum (Figure 12 b). Due to faster molecule rotation and lower molecular mass of **12** sharper lines are observed

in the proton NMR spectra and the coupling structures are more distinct in contrast to the aromatic substituted compounds **10** and **11**. Furthermore, the ^{1}H and ^{13}C NMR spectra provide prove of the formation of the Markovnikov product in small quantities (1 %) (Figure 12 and 13) in both reaction procedures (Scheme 3 and 4).

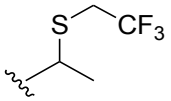

Figure 13: Markovnikov isomer of **12**.

The signals of the Markovnikov product appear at 1.40 ppm as doublet for the methyl group and as quartet at 2.31 ppm for the methine proton. In the ^{13}C NMR spectrum the resonances for the Markovnikov product appear at 15.5 and 21.9 ppm, where the latter belongs to the methine carbon atom. The signal of the carbon atom next to the CF_3 group is nearly identical to that of the anti-Markovnikov product. The corresponding signal of the CF_3 group is not observed for the Markovnikov isomer or is probably obscured by the signals of the main product **12**. In contrast to **12** the reactions with the sterically more demanding thiols **10** and **11** show no evidence for the formation of Markovnikov products. The coupling structures (for **12**) apparent in the ^{13}C NMR spectrum for coupling into quartets over one and two bounds ($^{1}J_{C\text{-}F}$ and $^{2}J_{C\text{-}F}$) are of the same order as for the aromatic compounds **10** and **11**. The PF-POSS cube is soluble in chloroform, dichloromethane and dimethyl sulfoxide.

3.2.1.4 Synthesis of PEGylated PF-POSS Cubes

Polyethylene glycol is used on a broad range in the food, cosmetic and pharmaceutical industry. The PEG shows low toxicity and is eliminated from the body *via* the kidneys for PEGs < 30 kDa (and in feces for PEGs > 20 kDa).[116,117] In the so called PEGylation technique, which is widely used in drug chemistry, a polyethylene glycol chain is attached to a protein or peptide, nanoparticle or any other drug molecule.[99,118–123] The PEGylation is a common method to improve the effectiveness and safety of drugs. By higher molecular mass and higher protease stability by shielding from enzymes, better pharmacokinetics were reported before.[118,124] Besides, the attachment of PEG molecules can affect the biological activity in a positive way by changes in the molecular size, weight and conformation. Furthermore, the PEGylated counterparts of pharmaceutical drugs were

reported to show increased half-life, lowered renal clearance and a better distribution in diseased tissue.[125] Additionally, higher drug solubility by changed hydrophilicity and a higher stability over a range of temperature and pH changes could be observed for PEGylated drugs in contrast to their unPEGylated analogs.[126–128]

Consequently, in order to gain higher polarity polyethyleneglycol spacers according to modification type **D** (Figure 8) were considered as suitable building blocks to generate new PF-POSS systems. The radical reaction of OV-POSS (**9**) with thiol PEG derivatives enables favorable conditions to achieve octafunctionalization as a simple and less to by-products tending method.[99,129] The following reactions were performed with the two different PEG linkers **13** and **14** (Figure 14).[130]

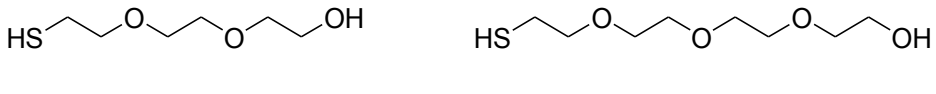

13 **14**

Figure 14: Thiol polyethyleneglycol spacers.

However, longer PEG chains were avoided in order to prevent the diminishing influence of the POSS cage with lengthening of the PEG chain. In addition it was considered that longer chains may broaden the ^{19}F singlet.

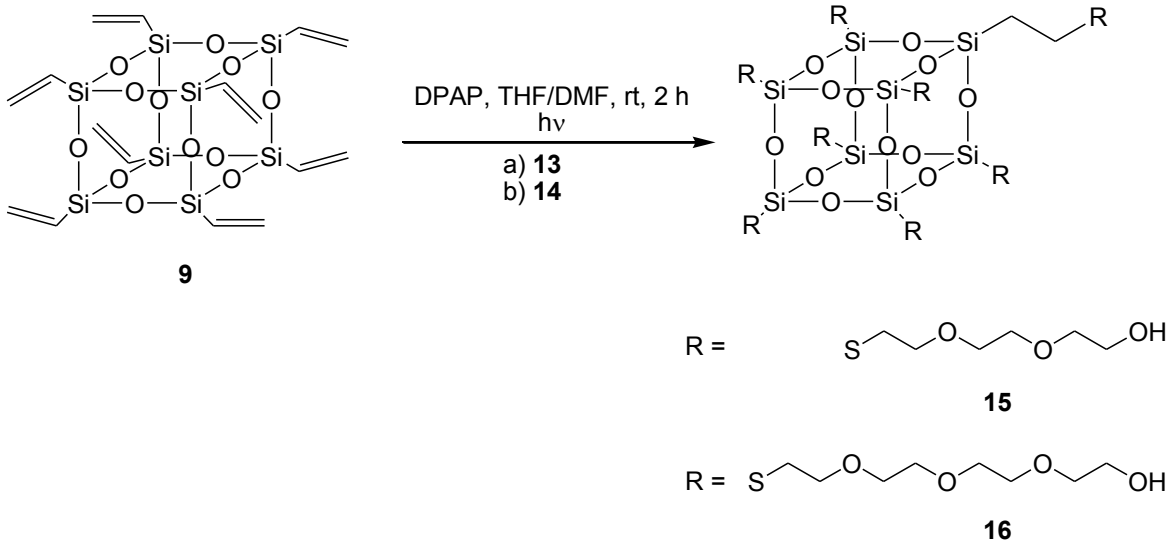

9 **15** **16**

Scheme 5: Syntheses of PEGylated POSS cubes **15** and **16**.

The thiol functionalized PEG derivatives (**13** and **14**) were anchored to **9** by irradiation of a

THF/DMF solution of the reactants in the presence of the photoinitiator DPAP (Scheme 5). The crude product was purified by column chromatography to give the PEGylated POSS cubes **15** and **16**, respectively (Scheme 5). As column material Sephadex LH-20 was used, which is a hydroxypropylated cross linked dextran matrix for gel filtration. The semi-rigid gel allows size exclusion chromatography using water or alcohol as mobile phase. Resonances in the ^{1}H NMR and ^{29}Si NMR spectra of the isolated PEGylated POSS cube **15** are compatible with those reported earlier.[99] The protons of the additional methylene groups of **16** show resonances with the expected integration ratios. The multiplets of the POSS neighbored methylene groups were observed at 1.06 and 2.67 ppm, respectively, shifting to higher field with increasing distance from the POSS core. Accordingly, the triplet of the sulfur neighbored methylene group is observed at 2.74 ppm. The PEG methylene groups resonate from 3.58 to 3.69 ppm, whereas the proton of the OH group is detected at 2.83 ppm as a singlet. The single resonance at -68.6 ppm of the ^{29}Si nuclei underlines the complete substitution of **16**. The high resolution ESI-TOF MS spectrum reveals the characteristic isotopic pattern of the two-times positively charged $[M+2Na]^{2+}$ ion. The obtained POSS cage **16** is well soluble in water, methanol, dichloromethane and chloroform.

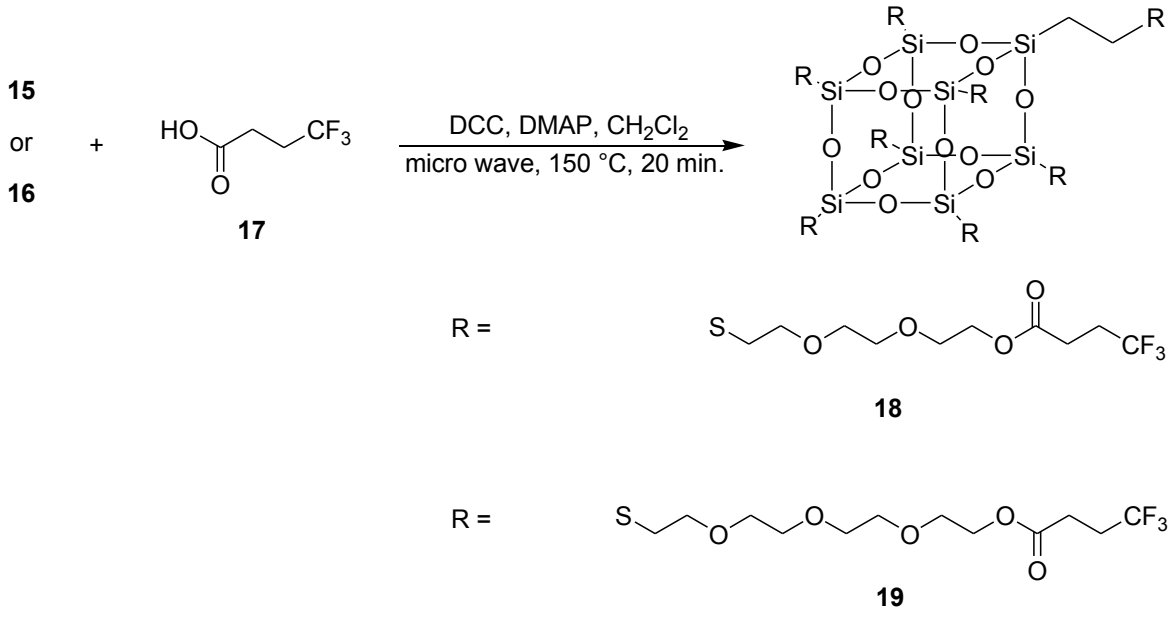

Scheme 6: Syntheses of the PEGylated PF-POSS **18** and **19**.

For the polyorganofluorination of the PEG-POSS cubes **15** and **16** the small aliphatic group, 4,4,4-trifluorobuyric acid (**17**), was considered as ideal PFG (Scheme 6). The so called Steglich esterification was performed by irradiation of the corresponding PEG cube

(**15**, **16**) with **17** in dichloromethane by a micro wave irradiation at 150 °C for 20 min.[131] After precipitation from diethylether, the crude product was purified by Sephadex-LH20 chromatography with MeOH as eluent to give PF-POSS **18** and **19**, respectively (Scheme 6). The compounds (**18**, **19**) were obtained as slightly yellow oils in good quantities. The obtained PF-POSS **18** and **19** are soluble in dichloromethane, chloroform and methanol. Furthermore, PF-POSS **18** is soluble in DMSO/water (80 : 20) mixtures, while the PF-POSS **19** is soluble in DMSO/water (70 : 30) mixtures.

Each of the PEGylated PF-POSS, **18** and **19**, reveals a sharp singlet in the ^{29}Si-DEPT-45 and ^{19}F NMR spectra, which confirms the octafunctionalization and intactness of the obtained cages. Furthermore, the high resolution ESI-TOF MS spectra reveal for each of the compounds **18** and **19** the two-times positively charged $[M+2Na]^{2+}$ ion.

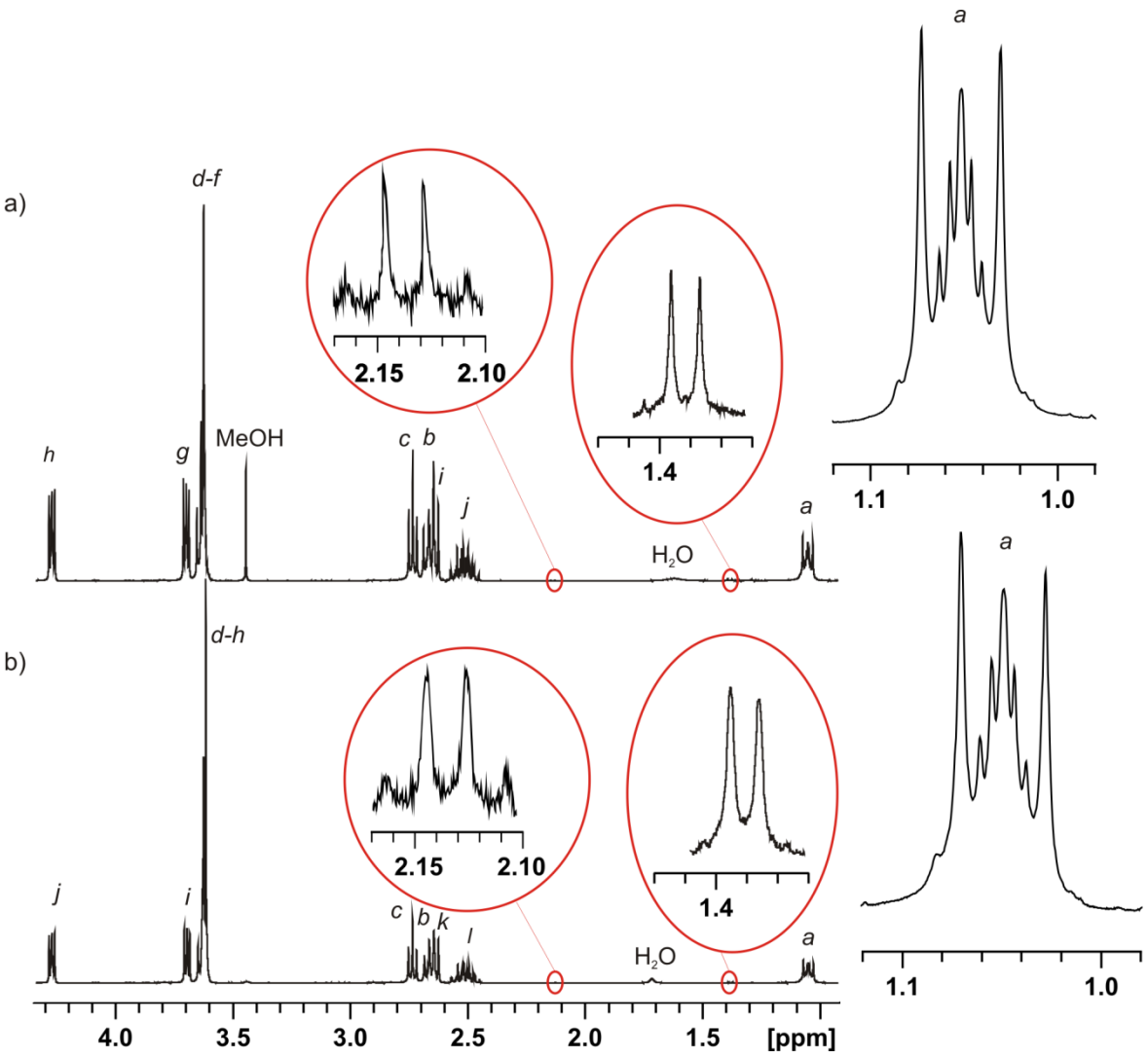

Figure 15: ^{1}H NMR spectra of PEG functionalized PF-POSS a) **18** and b) **19** in CD_2Cl_2 solution; multiplets of the Markovnikov product are highlighted in red.

The NMR assignments for **18** and **19** are shown in Figure 16. The ^{1}H NMR spectra of both compounds (**18** and **19**) display the resonances of the silica bound methylene protons in the high field at 1.02 (*a*) and 1.05 ppm (*a*), respectively, (Figure 15 and 16) and confirm complete substitution of the precursor **9**. Interestingly, compared to **18** the lines are more broadened for **19** due to the longer PEG chain of one C_2 unit. With increased distance to the POSS core the signals of the PEG methylene groups shift into the lower field. For **18** the single triplet in the spectrum belongs to the first PEG protons (*c*) next to the sulphur atom at 2.70 ppm ($^{2}J_{H\text{-}H}$ = 6.9 Hz).The multiplets of the middle PEG units (*d-f*) of **18** are obtained in the area from 3.56 to 3.64 ppm, where the methylene PEG protons next to the ester group split into multiplets at 3.67 (*g*) and 4.24 ppm (*h*). Furthermore, the methylene protons of **18** at 2.63 ppm belong to the ester neighbored CH_2 protons (*i*) and to the CF_3 neighbored protons (*j*) at 2.42 ppm (Figure 16). For the CH_2 protons (*j*) a multiplet pattern is obtained by the coupling to the CF_3 group.

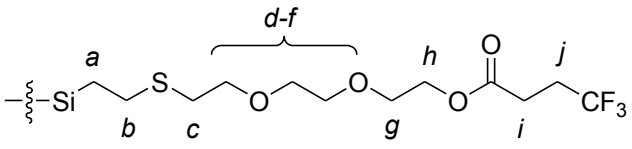

18

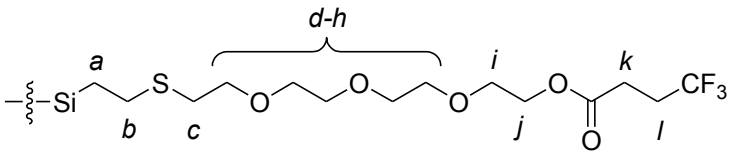

19

Figure 16: Assignments of NMR resonances for PF-POSS **18** and **19**.

Moreover, due to slow rotation in solution the resonances of the methylene protons *i*, *j* (**18**) and *k*, *l* (**19**) show a higher order of splitting. The shifts of the ^{1}H NMR resonances for **19** are in the same order as for **18** and show the same multiplet structures, while the middle PEG methylene protons (*d-h*) from 3.62 to 3.66 ppm own a higher integral due to the longer PEG linker. For both PEGylated PF-POSS **18** and **19** less intense signals of the Markovnikov product (2 %) are detected (highlighted in red in Figure 15 a and b). The Markovnikow isomer (for **18** and **19**) shows a doublet at 1.38 ppm and a quartet at 2.13 ppm with a coupling constant of 7.4 Hz ($^{2}J_{H\text{-}H}$) (Figure 15 a and b). The ^{13}C NMR spectra of both compounds (**18** and **19**) indicate the successful esterification with **17** by the observed coupling pattern with the fluorine atoms. In the following the ^{13}C NMR spectrum

is shown for cube **19** (Figure 17). The resonances of the carbon atoms (*a*/*b* and *c*) next to the POSS core appear in the high field (Figure 16 and 17), while the signals *i* and *j* are revealed at higher frequencies (Figure 17). Five ^{13}C resonances for the middle PEG groups (*d-h*) are arising in the region from 70.7 to 71.5 ppm as broad singlets. The quartets resulting from couplings over various bonds with the ^{19}F nuclei are shown magnified in Figure 17. The smallest coupling constant of 3.2 Hz ($^4J_{C-F}$) appears for the resonance at 27.4 ppm (*k*), while the carbon atom (*l*) next to the CF_3 group shows a coupling of 29.9 Hz ($^3J_{C-F}$) at 29.6 ppm. For the CF_3 carbon atom the quartet reveals the largest coupling of 275.9 Hz ($^1J_{C-F}$) at 127.1 ppm. Resonances in the same order and with similar multiplet patterns are observed for the POSS cube **18**.

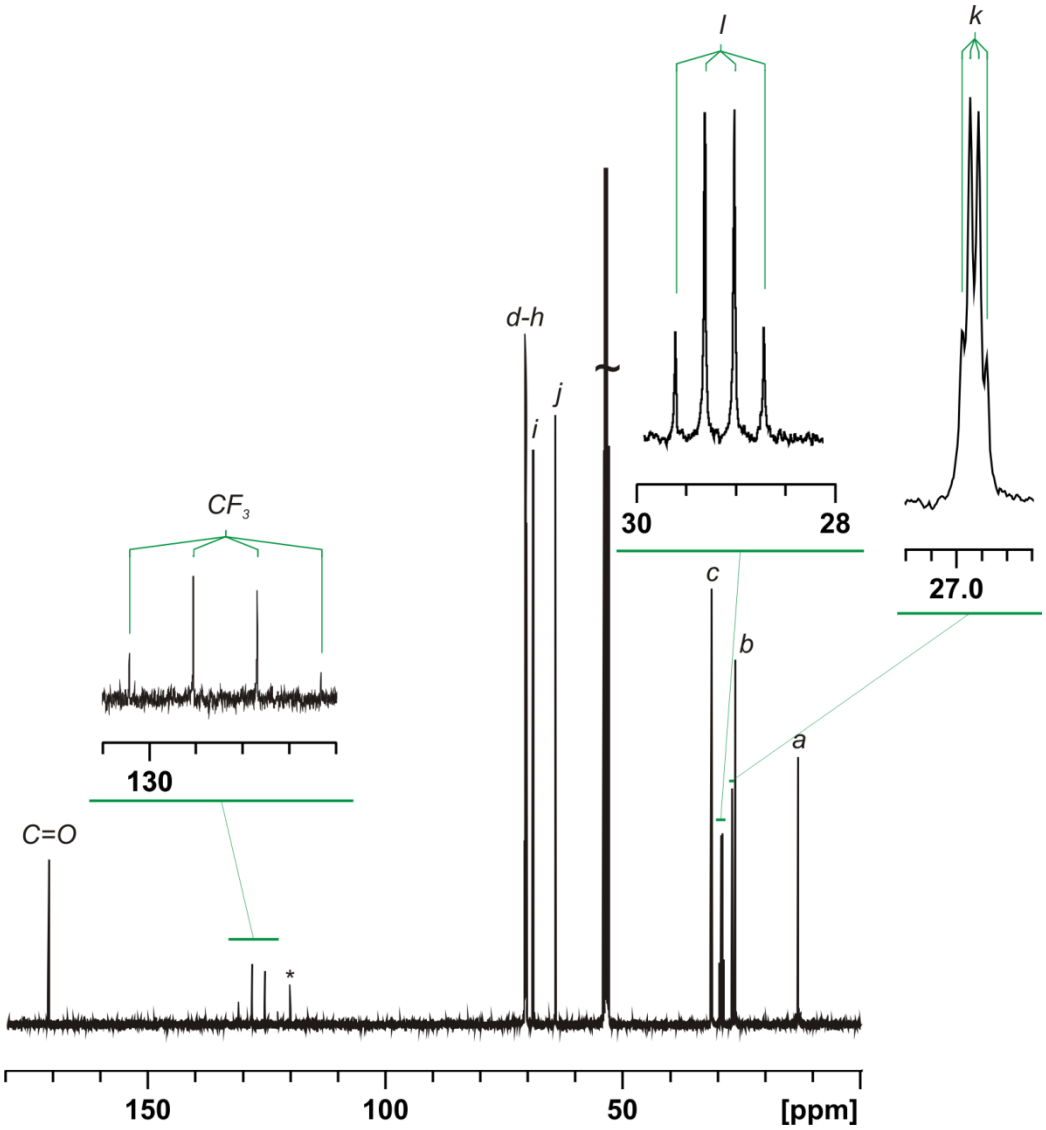

Figure 17: ^{13}C NMR spectrum of PF-POSS **19** in CD_2Cl_2 solution; (*offset artefact).

3.2.1.5 Synthesis of a charged PF-POSS

Perfluorocarbons (PFCs) are the contrast agents, most commonly used for ^{19}F MRI. Since these compounds are highly hydrophobic and significantly lipophobic they have to be injected as emulsions.[12] Perfluorocarbons are cleared *via* the reticuloendothelial system and excreted by exhalation through the lungs.[132] Hence water soluble ^{19}F CAs may present a promising alternative to conventional perfluorocarbon emulsions.[133,134]

To achieve water solubility and investigate physiochemical properties, a synthesis was planned for a charged PF-POSS according to the modification type **E** (Figure 8). To attain a charged compound the creation of a quarternary nitrogen atom was considered as a suitable element for the introduction of a positive charge into the PF-POSS. Therefore a synthetic way was exerted by using bis(trifluorethyl)amine **20** (Figure 18) and its nucleophilic attack of **23** (bromoisothiocyanate) to form an isothiocyanate functionalized PFG **22**.

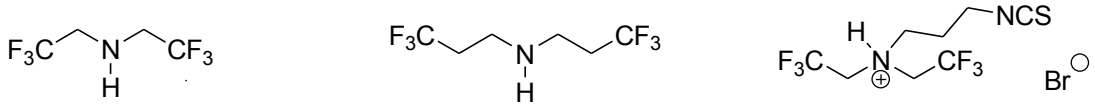

20 **21** **22**

Figure 18: PFGs with amine function **20** and **21** and of the desired product **22**.

The reaction of **20** with **23** in dry ACN at 75 °C with different reaction times up to 3 d and at 105 °C with reaction times up to 2 d did not deliver the desired substituted product **22**. Proton and ^{19}F NMR measurements showed that no reaction took place and **20** could be recovered from the reaction mixture. The same reaction above was repeated with the addition of K_2CO_3 as base at different temperatures (75 and 105 °C) with reaction times up to 3 d and showed no reaction affording **22**. The proximity of the CF_3 group was considered for the non-reactivity of the nitrogen atom of **20**.

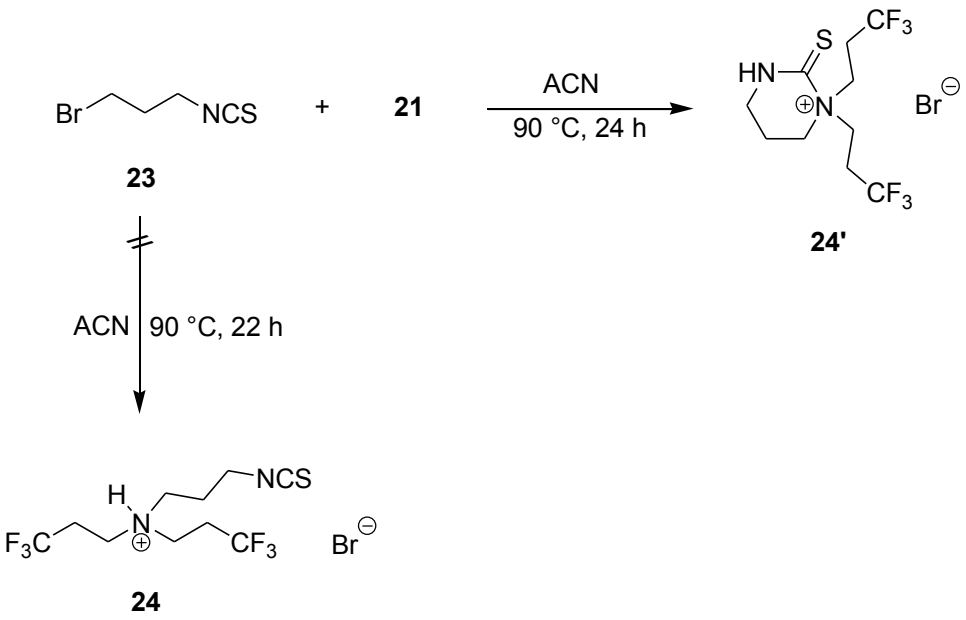

Scheme 7: Reaction schemes of the obtained product **24'** and the desired product **24**.

Hence, the reaction was carried out with PFG **21** in ACN at 90 °C for 22 h and new signals were verified by ^{1}H NMR spectroscopy (Scheme 7). A fluffy white powder was obtained after precipitation of the crude product from toluene, which was very well soluble in water and polar organic solvents. However, the structure determination by NMR spectra did not result in the desired target molecule **24** but its cyclic isomer **24'**. Interestingly, the ^{13}C NMR chemical shift for the quarternary carbon atom (C=S) was observed at 165.3 ppm, whereas the NMR frequency of an isothiocyanate is expected in the higher field. Furthermore, the cyclic structure of **24'** was proven by ^{1}H-^{13}C HMBC NMR spectroscopy, which yield a $^{4}J_{C\text{-}H}$ coupling between the methylene protons *c* and *d* underlining the formation of the cyclic structure **24'** (Scheme 7 and Figure 19). The DRIFT spectrum confirmed the result by the absence of the vibrations belonging to an isothiocyanate function, while the stretching vibration of the thiocarbonyl bond was observed at 1024 cm^{-1} [ν (C=S)] for **24'**. The mass spectrometry and elemental analysis of the obtained product confirmed the composition of **24'**.

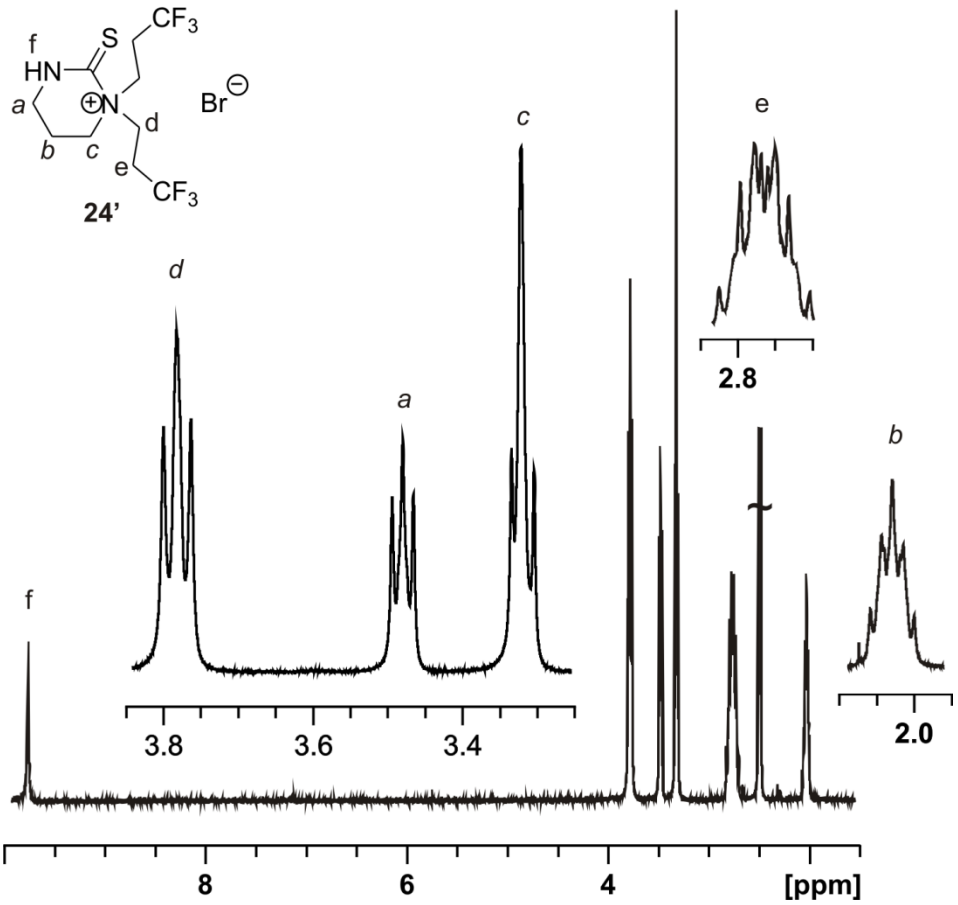

Figure 19: ^{1}H NMR spectrum of **24'** in CD_3CN solution.

The ^{1}H NMR spectrum shows the multiplet structures of the pyrimidinethiol protons at 2.04 (*b*) and 3.49 ppm (*a*), while the signal at 3.33 ppm occurs for the protons (*c*) adjacent to the cation. The methylene resonances neighbored to the CF_3 groups show a coupling pattern of higher order at 2.77 ppm (*e*) and in the low field at 3.79 ppm (*d*) by the deshielding effect of the nitrogen cation. The singlet for the nitrogen proton is detected at higher frequencies (9.77 ppm).

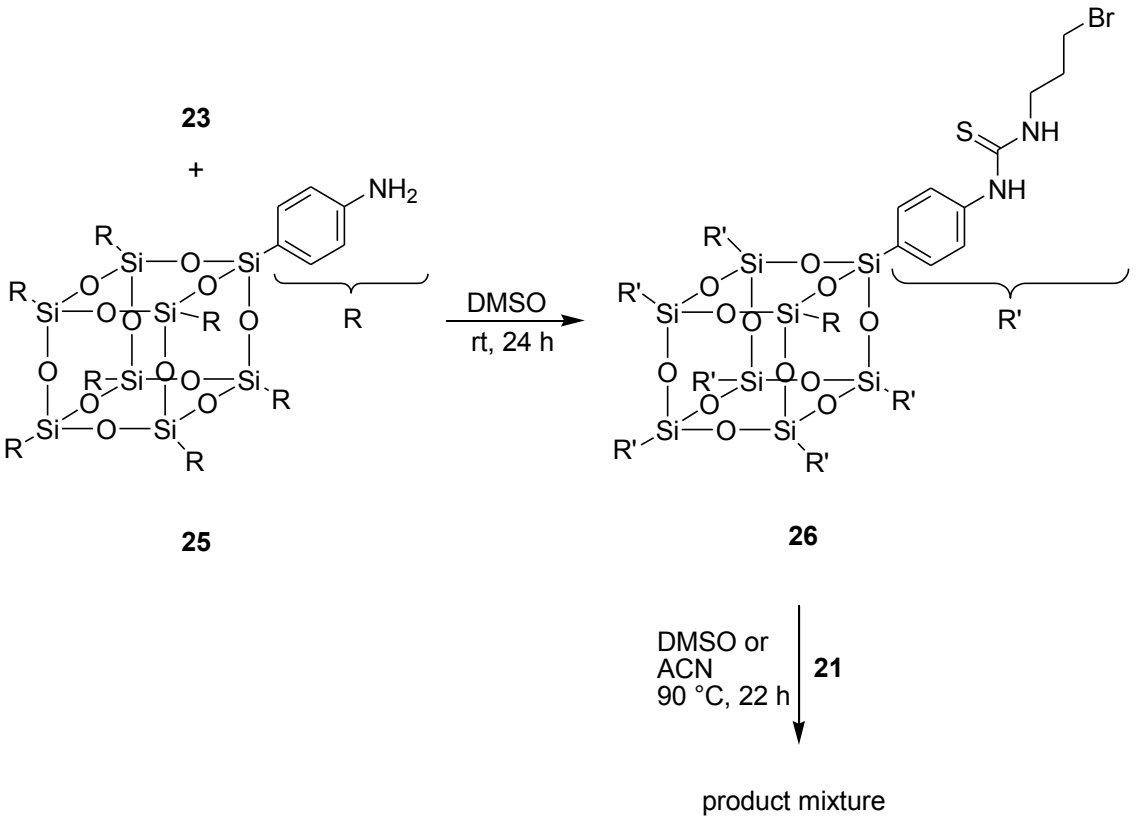

Scheme 8: Synthesis of the Bromo-POSS **26** and reaction with PFG **21**.

To avoid the intramolecular cyclization reaction of **24**, an alternative synthetic way was performed by first anchoring the linker to the POSS core. Therefore, the Bromo-POSS **26** was synthesized according to Scheme 8. A yellowish powder was obtained, which is soluble in DMSO. The ^{1}H, ^{13}C and ^{29}Si NMR spectra reveal the signals of the desired Bromo-POSS **26**. The thiourea carbon atom could not be detected due to broad lines in the ^{13}C NMR spectrum. However, the availability of the thiourea function could be confirmed by the DRIFT spectrum. The reaction of the isolated Bromo-POSS **26** with PFG **21** at 90°C in a DMSO or ACN solution each resulted in broad lines in the ^{19}F NMR spectrum. It can be assumed, that due to the solubility of the desired PF-POSS cube the reaction does not offer favorable conditions for the complete substitution of **25**. Since the reactions resulted in product mixtures, the next step of alkylation of the amine function to obtain a charged POSS could not be performed. Because PFG **21** could not be used for a suitable synthetic way to obtain a charged POSS structure, the consideration was given to find a different appropriate PFG.

In order to circumvent any cyclization as in the case of **24'**, an aromatic PFG was considered as a more suitable framework. Accordingly, 3,5-bistrifluormethylpyridine (**27**)

was used as precursor and reacted with **23** to give an isothiocyanate functionalized PFG (**28**). The reaction was carried out by refluxing the reaction mixture in dry ACN for 4 d (Scheme 9). The crude product was precipitated from toluene to give a slightly yellowish powder. Resonances of the methylene protons of the propyl chain integrate in the correct ratio to the resonances of the aromatic protons. The alkyl signals of **28** are observed at 2.43, 3.89 and 4.86 ppm, while the signals of the pyridine protons are detected at 9.73 and at 10.09 ppm in the ratio 1:2. The DRIFT spectrum reflects the stretching vibration of the intact isothiocyanate bonding at 2186-2126 cm^{-1}. However, the yield of the synthesis is very low. This is most likely based on the presence of two CF_3 groups and their very strong electron withdrawing effect.[135] Due to this the pyridine nitrogen is strongly reduced in its nucleophilicity, which results in the poor yield.

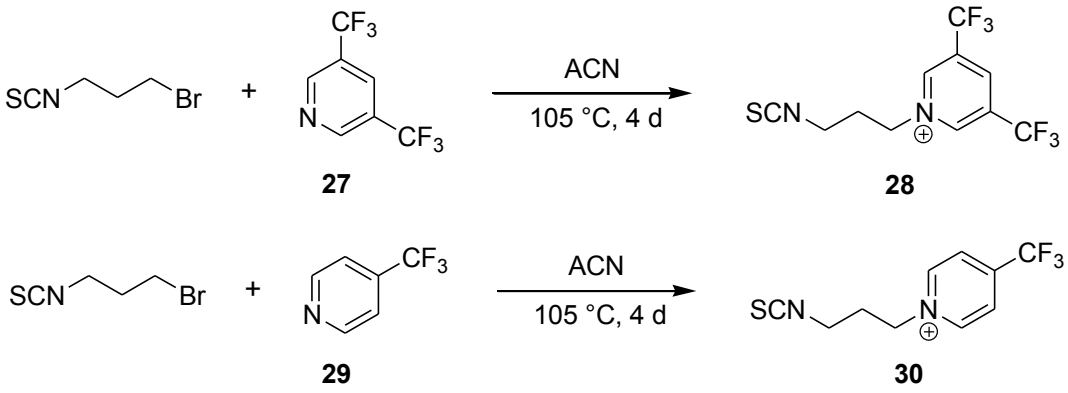

Scheme 9: Syntheses of charged isothiocyanate functionalized PFGs **28** and **30**.

Consequently an analogous reaction was exerted by reducing the number of CF_3 groups while using 4-trifluoromethylpyridine (**29**) (Scheme 9). The reaction mixture was refluxed for 4 d and the crude product was precipitated with toluene. A slightly yellowish powder was obtained in very good yield (94 %). The ^{1}H NMR spectrum of **30** displays the signals of the propylene chain at 2.42 (*b*), 3.85 (*a*) and 4.95 ppm (*c*) as well as the resonances of the pyridine ring, an AA'XX'-system, at 8.40 (*e*) and 9.40 ppm (*d*) in the correct integration ratio to the propyl signals (Figure 20). The ^{13}C NMR data verify the presence of the isothiocyanate group (127.8 ppm) and display the quartets, which result from the coupling of the aromatic carbon atoms to the fluorine nuclei.

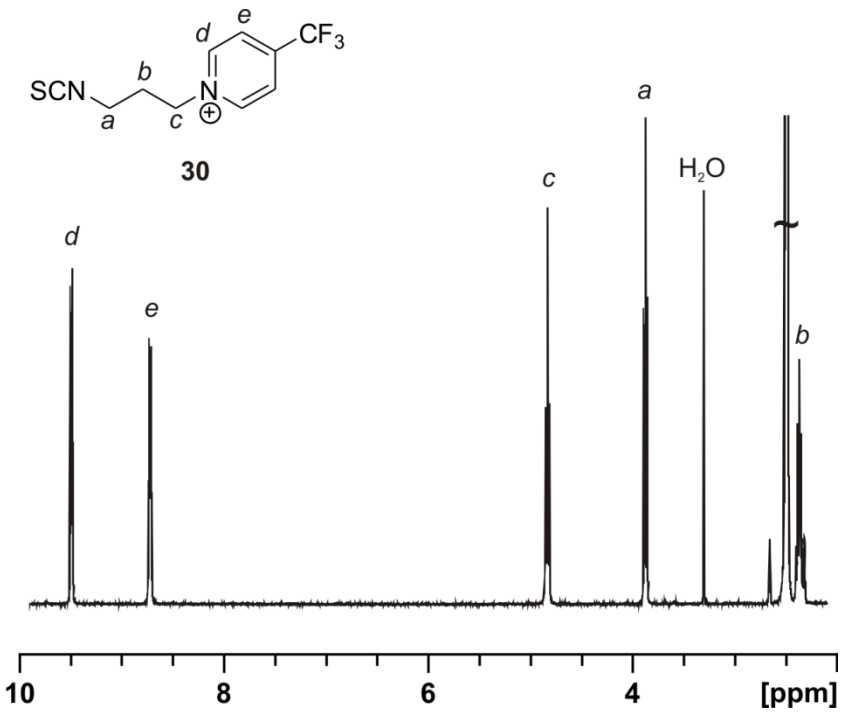

Figure 20: ^{1}H NMR spectrum of PFG **30** in $(CD_3)_2SO$.

In order to anchor the PFG **30** to a POSS cube, OAPh-POSS (**25**) was selected. The connection *via* a thiourea bond offers a fast and simple way without the requirement of any additional reagents. According to this **30** and **25** were reacted in an ACN/THF solution mixture. Since the substituted PF-POSS **31** is poorly soluble in ACN, a stepwise heating was performed to ensure a maximum dwell time of the reacting POSS to complete the reaction. After refluxing at 98 °C for 16 h a yellow precipitate was formed. The solid was washed with an ACN/THF solution mixture and finally with diethyl ether to give an off-white powder. NMR measurements prove the successful synthesis of the PF-POSS **31**. Compound **31** is soluble in (hot) water or water/DMSO (2 %) mixtures and polar organic solvents. The ^{1}H-^{29}Si HBMC NMR spectrum reveals one single cross peak at -65.0 ppm. Furthermore a singlet in the ^{19}F NMR spectrum at -63.86 ppm confirms the intactness of the cube **31**.

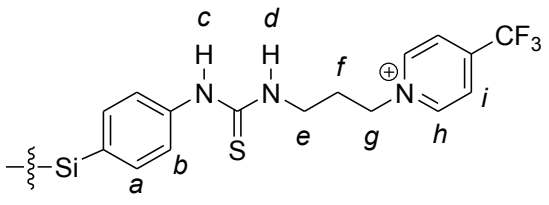

Figure 21: Assignments of ^{1}H NMR signals of PF-POSS **31**.

In the ^{1}H NMR spectrum of **31** the methylene frequencies of the propyl chain are detected at 2.27 (*f*), 3.56 (*e*) and 4.80 ppm (*g*) as broad signals with non-resolved multiplets (Figure 21, 22). It can be assumed that the long rotational correlation time, as well as rotation and conformation isomers of **31** cause the broad lines and lead to poorly resolved multiplets.

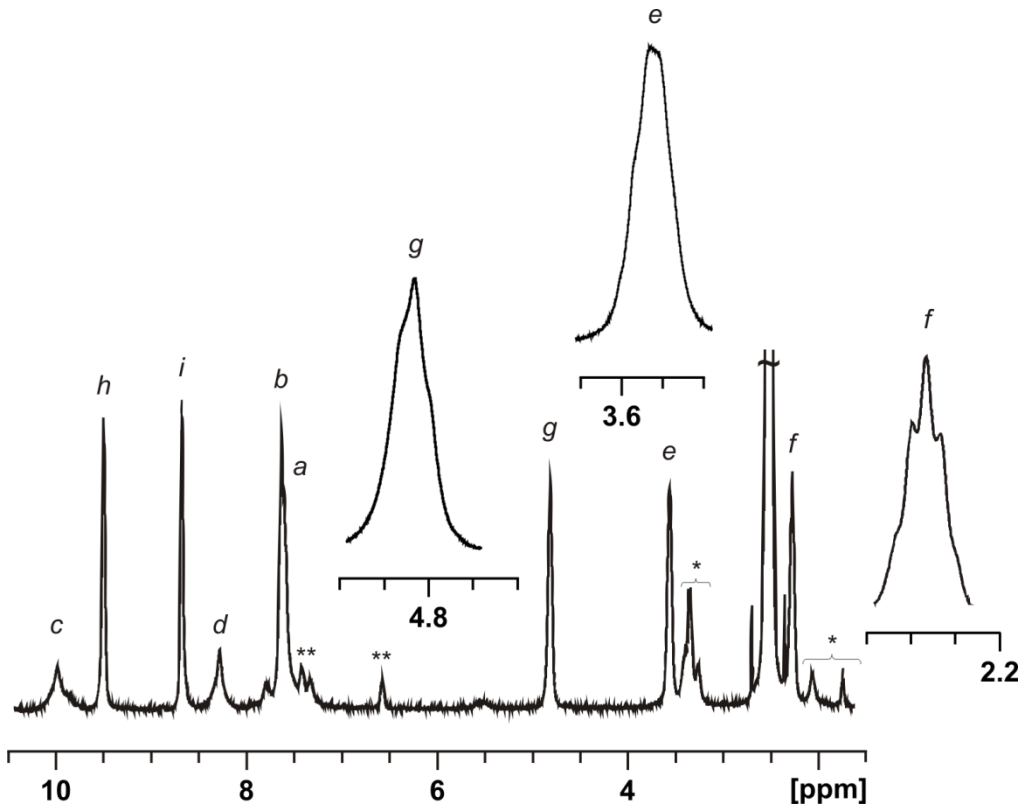

Figure 22: ^{1}H NMR spectrum of PF-POSS **31**; (*solvents, **impurity).

The multiplet signal of the A-part of an AA'BB' system for the POSS phenyl protons is detected at 7.59 ppm (*a*), while the multiplet of the B-part (*b*) is observed at 7.64 ppm. The signals of the pyridine protons are detected more at the lower field with the typical pattern of an AA'XX' system. The A-part at 9.49 ppm belongs to the nitrogen neighbored protons (*h*), while the resonance for the protons of the X-part emerges at 8.68 ppm (*i*). Due to slow water exchange in deuterated DMSO solution the protons of the thiourea bonding occur as singlets in the low field at 8.24 ppm for the PFG-bound thiourea proton (*d*), while the POSS-bound proton (*c*) experiences a stronger shift to 9.96 ppm. Due to line broadening the thiourea carbonyl could not be detected by ^{13}C NMR spectroscopy. However, DRIFT measurements showed the expected stretching vibrations of the thiourea group in the region from 1599 to 1464 cm^{-1} [ν (NH-C=S)] and at 1094 cm^{-1} [(ν (C=S)]. Analysis by ESI-MS spectrometry detects the completely substituted sodium adduct $[M+8Na]^{8+}$ at

430.24 m/z. Furthermore, the elemental analysis of **31** is in accordance to the composition of the molecule. Interestingly the cube **31** is not stable in the solid state at temperatures above 80 °C.

3.2.2 ^{1}H NMR Diffusion Spectroscopy of POSS Cubes

The molecular size of the synthesized POSS cubes is not only important for biomedical applications but also to investigate the influence on the size by the structural orientation of different POSS linkers. In medicinal applications the molecular size of a substance determines the nature and manner of the distribution in the body. As an example the penetration of a compound into a cell or their extracellular activity as well as excretion from the body depends on the size and the nature of the functional groups. The ^{1}H NMR diffusion spectroscopy enables to determine the size and agglomeration behavior of a molecule which dominates in solution, as well as the mobility of a compound in solution. Hence this method allows for the investigation of the influence on the overall size of the POSS cube by the length and structure of the respective linker. The physical parameter that is determined by diffusion NMR is the translational self-diffusion coefficient (D). With the Stokes-Einstein equation the hydrodynamic radius (r_H) is calculated (Equation 6). This equation is valid for spherical molecules and gives the relation of the diffusion coefficient to the molecular size in solution. In this equation k_B is the Boltzmann constant, T the temperature in Kelvin and η the viscosity of the solvent.

$$D = \frac{k_B T}{6\pi\eta r_H}$$

Equation 6

$$V_H = \frac{4}{3}\pi r_H^3$$

Equation 7

$$\tau_R = \frac{4\pi\eta r_H^3}{3k_B T}$$

Equation 8

The data determined by ^{1}H NMR diffusion spectroscopy are listed in Table 1. From the calculation of the hydrodynamic radius (r_H) an estimation of the hydrodynamic volume (Equation 7) and the evaluation of the rotational correlation time τ_R (Equation 8) was performed. Results of the hydrodynamic radii r_H (Table 1) verify the importance of the flexibility of the used linkers. The replacement of an aliphatic chain by an aromatic ring results in a more rigid structure, which leads to a significant increase in r_H (**11**, **26**, **31** Table 1).[28] Interestingly, the additional methylene group in PF-POSS **10** is the reason for the smaller hydrodynamic radius, since the linker gets more flexible and is able to kink. The

PEG-POSS **15** indicates the presence of some agglomerates, which is displayed by the slightly increased hydrodynamic radius of 1.16 nm. Obviously, the more flexible PEG chain in **16** folds around the POSS core since the r_H of 0.67 nm is much smaller as it would be expected for an outwardly oriented linker. After functionalization with the non-polar PFG the hydrodynamic radius of **19** is increased. However, the increase is not as large as it would be for outstretched linkers, which further indicates that the PEG chains fold around the cube core. Generally the obtained values show the right tendency of r_H for all POSS cubes according to the length of the linker, the aliphatic or aromatic structure as well as the polarity of the functional groups. In the case of biomedical application the compounds must be able to pass the quite small pores of the kidneys of the so called glomerular filter. These pores sizes are in the range of 3 to 5 nm.[136] If the hydrodynamic volumes V_H are considered of all PFG-POSS cubes, the excretion *via* the kidneys is possible, since the sizes of all PF-POSS cubes are significantly smaller. This provides a good basis for a fast clearance from the body.

Table 1: Translational diffusion coefficients D, calculated hydrodynamic radii r_H, the hydrodynamic volume V_H and rotational correlation times τ_R determined at 25 °C of different POSS cubes.

compound	deuterated solvent	D [$\times 10^{-10}$ m^2s^{-1}]	r_H [nm]	v_H [nm^3]	τ_R [ps]
10	$CDCl_3$	7.41	0.53	0.62	84
11	$CDCl_3$	4.36	0.90	3.05	412
12	$CDCl_3$	6.77	0.58	0.82	110
15	CD_2Cl_2	4.58	1.16	6.60	657
16	CD_2Cl_2	7.95	0.67	1.26	126
18	CD_2Cl_2	9.03	0.59	0.86	86
19	CD_2Cl_2	7.11	0.75	1.76	176
26	DMSO	0.73	1.50	14.07	6790
31	DMSO	0.68	1.61	17.59	8489
I[60]	THF	3.5	1.3	9.2	1200
II[60]	THF	3.1	1.55	15.6	1730

3.2.3 Hydrolysis of the Synthesized POSS Cubes in Aqueous Media

The synthesis of POSS cubes is obtained by the hydrolytic condensation of alkoxysilanes. Hence the reverse reaction, the hydrolysis, may occur in aqueous media. In former works studies of the decomposition of silsesquioxanes in aqueous media were reported.[28,97] The hydrolysis of the POSS cage by the addition of water is initiated by the opening of one POSS edge. Consequently, the symmetry of the POSS cube (O_h) decreases drastically by formation of different primary hydrolysis species. At the hydrolysis endpoint, high and low molecular weight species, like monomers, dimers and trimers are in an equilibrium by re-condensation and hydrolysis processes (Scheme 10). The linear isomers **32** and **33** could be detected by ESI-MS spectrometry and no evidence for the cyclic isomers could be found (Table 2). In a former work the hydrolysis of POSS cubes functionalized with Y-chelate complexes was studied by ^{1}H , ^{29}Si NMR and ^{1}H NMR diffusion spectroscopy as well as mass spectrometry.[61]

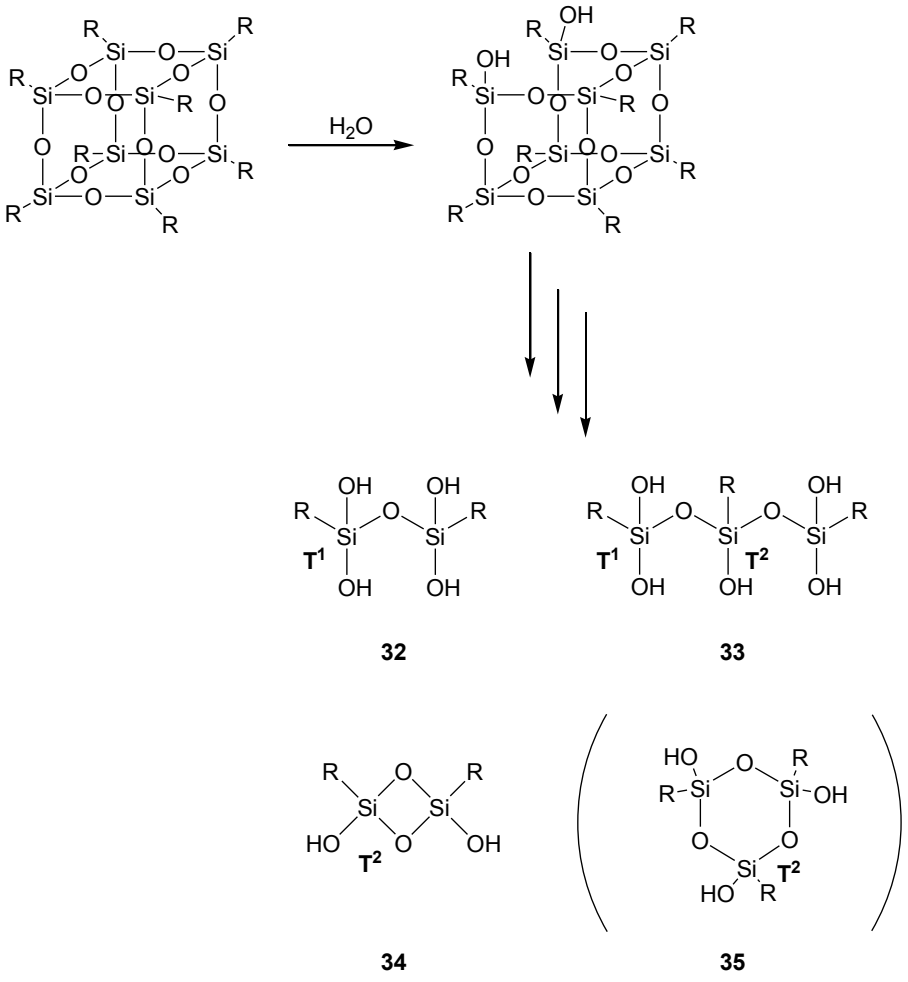

Scheme 10: Hydrolysis of the POSS framework in an aqueous media.

The study of the hydrolysis stability of each PF-POSS is essential for the determination of their suitability for ^{19}F imaging. Generally a stability of the compound for at least 3 h is required for the time between injection of the compound and performing the measurement. For ^{19}F MRI imaging a sharp intense signal of the ^{19}F resonance correlates with a good contrast. As the intensity of the signal should be maintained during the data acquisition, the stability of the highly symmetrical PF-POSS cubes becomes an important criterion for MRI applications. The hydrolysis of the PF-POSS disrupts the symmetry of the cube which results in broad or multiple ^{19}F resonances, lowers the intensity of the signal and consequently reduces the MRI contrast. Thus the knowledge of the hydrolysis of the PF-POSS cubes is significant for potential MRI applications. To investigate the hydrolytic stability and the kind of hydrolysis products, DMSO-d6/D_2O solutions of the respective POSS (**10**, **12**, **15**, **16**, **18**, **19** and **31**) were prepared. A pD of 7.4 was maintained by a HEPES buffer to ensure a constant pD throughout the measurement.[137] The DMSO-d6/D_2O ratio was varied for each sample to achieve a good solution of the respective PF-POSS. The least amount of D_2O (of 10 % volumetric quantity), which was used for the experiments corresponds to a 72 fold excess of water in relation to one edge of the PF-POSS cube. Thus, for each solution enough water is provided to enable a complete hydrolysis of the POSS framework. Time dependent NMR spectra were recorded at 37 °C for the ^{1}H, ^{19}F and ^{29}Si nuclei for each sample. 2D experiments (^{29}Si-^{1}H HSQC or HMBC NMR) were used to detect the consecutively arising silicon resonances.

As an example time dependent ^{1}H NMR spectra of PF-POSS **12** are depicted in Figure 23. They show the same behavior as those reported before.[61] Generally the hydrolysis of the POSS cube is indicated by the drop in intensity of the multiplet of the $SiCH_2$ protons accompanied by new resonances, which grow in at high field (Figure 23). These new signals are rather broad due to the low symmetry of the hydrolysis products, many different species or condensation products of high molecular weight. After prolonged hydrolysis new multiplets are observed at a chemical shift typically for low molecular weight species. This and the narrow lines of the detected new $SiCH_2$ multiplets indicate, that the hydrolysis is complete. In all cases this behavior was confirmed by ^{1}H-^{29}Si HSQC or HMBC NMR spectra. Likewise during the stepwise hydrolysis, the single resonance of the T^3-groups of the intact cube decreases in intensity, while new singlets of the T^2 and T^1 groups arise at low field (Scheme 10).

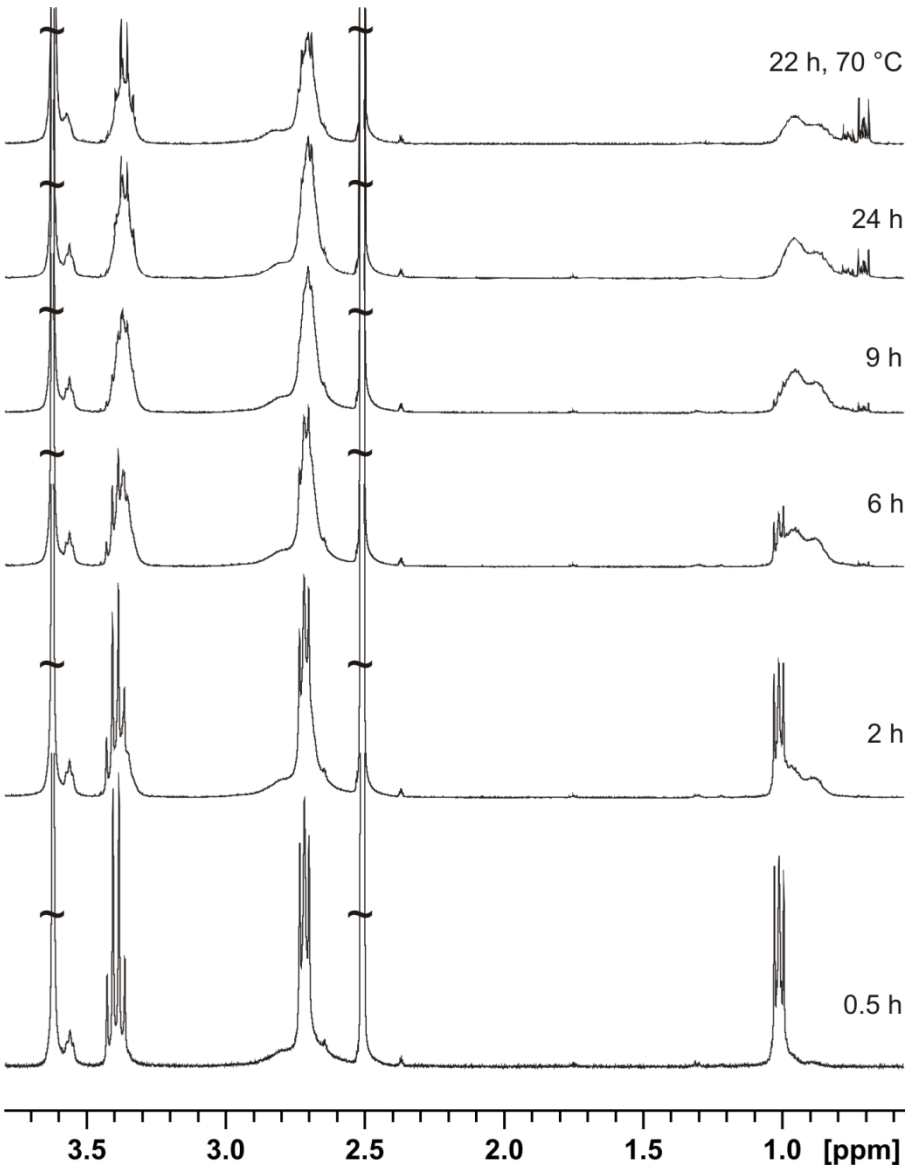

Figure 23: Time dependent ^{1}H NMR spectra of PF-POSS **12**, in DMSO-d6/D_2O-HEPES solution with pD 7.4.

The stability towards hydrolysis of the different cubes **10**, **12**, **15**, **16**, **18**, **19** and **31** depends strongly on the steric effects of the linker as well as the polarity of the functional group.

Two hours after starting the hydrolysis of PF-POSS **12** the initial hydrolysis of the POSS framework is apparent (Figure 23, trace 2 h). For PF-POSS **12** the signal of low molecular hydrolysis products is observed after 6 h at 37 °C (Figure 23), while no new signals are detected for **10** after stirring the sample at 37 °C for seven weeks. Only after heating the solution of **10** to 70 °C for 24 h, shows the start of decomposition of the POSS framework. The hydrolysis of **10** proceeds at temperatures ≥100 °C. High temperatures over several

weeks (70 °C for **12** and 100 °C for **10**), show that an equilibrium of condensation and hydrolysis is achieved between high and low molecular hydrolysis products. Moreover the addition of further D_2O/HEPES solution does not show changes in the spectra and confirms this conclusion. For both solutions of PF-POSS **10** and **12** the MS-ESI spectrometry reveals the pattern of the hydrolysis products, which can be assigned to different charged species of monomers, dimers or trimers, respectively (Table 2). Interestingly after heating the solution of **10** at 130 °C (for 15 weeks) the ^{29}Si NMR spectrum indicates the presence of Q^2 groups at -87 ppm, which shows that high temperatures shift the equilibrium more to re-condensation and cross-linking after breaking the Si-O bond. In conclusion it can be assumed, that the higher stability of PF-POSS **10** compared to **12** is most probably due to a hindered access of water molecules to the silica core. The much smaller and less fluorinated PFG of **12**, offers a higher accessibility for D_2O molecules, hence hydrolysis starts already after 2 h at 37 °C. Similar stability as in the case of **10** was observed for the PF-POSS cube **31**. Stirring the solution at 37 °C for seven weeks shows no signals of the low weight hydrolysis products. The new signals which arise in the high field are detected only after heating the sample to 70 °C (Table 3).

Table 2: MS-ESI measurements of hydrolysis products of POSS cubes **10**, **12**, **15**/**16** and **18**/**19**.

	MS-ESI spectrometry		
	monomers	dimers	trimers
10		236.83 $[M-3H]^{3-}$	530.72 $[M-2H]^{2-}$ 353.92 $[M-3H]^{3-}$ 264.88 $[M-4H]^{4-}$
12	110.83 $[M-2H]^{2-}$	212.68 $[M-2H]^{2-}$	
15			381.15 $[M-2H]^{2-}$ 254.03$[M-2H]^{3-}$
16			439.90 $[M-2H]^{2-}$ 293.14 $[M-3H]^{3-}$
18		372.10 $[M-2H]^{2-}$	
19			310.14 $[M-4H]^{4-}$

Interestingly the new $SiCH_2$ multiplets are broader than those obtained for the other POSS cubes (**10**, **12**, **15**/**16**, **18**/**19**). The shielding effect, which depends on the amount of CF_3

groups, as well as limited accessibility for water molecules by the sterically more demanding aromatic linkers, inhibit the rapid hydrolysis of PF-POSS **10** and **31** in comparison to the aliphatic structured PF-POSS **12**.

Table 3: ^{29}Si NMR resonances of time dependent measurements during hydrolysis of **15**/**16** and **18**/**19** and **31**.

sample	NMR resonance shift [ppm]			
10	-45 (T^1)	-55 (T^2)		
12	-45(T^1)	-54 (T^2)		
15	-42 (T^1)	-51 (T^2)		
16	-41 (T^1)	-51 (T^2)	-61 (T^3)	-69 (T^3)
18	-45 (T^1)	-53 (T^2)		-69 (T^3)
19	-45 (T^1)		-61 (T^3)	-70 (T^3)
31	-46 (T^1)**(1)**	-52 (T^2)	-62 (T^3)	

[1] very low intensity

According to the observations above, the PEG-POSS cubes **15** and **16** are nearly completely hydrolyzed (at 37 °C) in contrast to their fluorinated counterparts. The ^{29}Si NMR signals of the hydrolysis products of **15** and **16** are listed in Table 3. For the PF-POSS cubes the first arising resonances obtained by the hydrolysis products could be detected after heating the solutions at temperatures ≥ 70 °C. The ^{29}Si HMQC NMR spectra of PF-POSS **18** reveal the signals of the hydrolysis products after heating the sample additionally to 70 °C for 2 d (Figure 24). The MS-ESI spectra of the POSS cubes **15** and **16** as well as **18** and **19** reveal isotopic patterns of the hydrolysis products, which can be assigned to the dimers and trimers of the low molecular weight species.

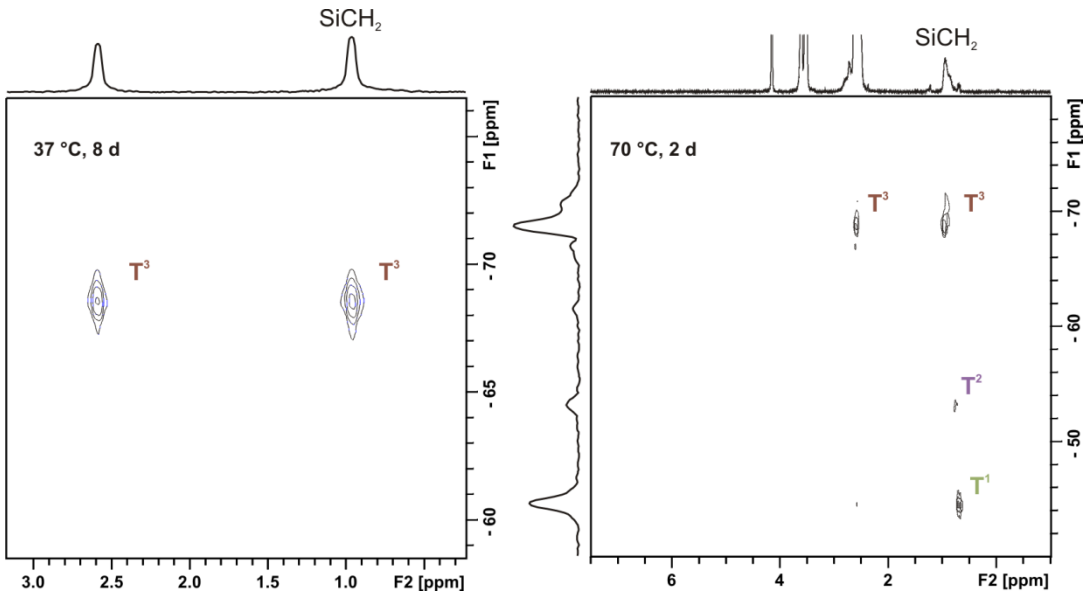

Figure 24: Time dependent ^{29}Si HMQC NMR spectra of the hydrolysis sample of **18**. ^{29}Si NMR shifts in ppm (F1), ^{1}H NMR shifts in ppm (F2).

3.2.4 Time Dependent ^{1}H NMR Diffusion Spectroscopy

The degradation of the silica cube can be tracked during the process of hydrolysis by diffusion NMR spectroscopy. This technique allows the determination of the self-diffusion coefficient (D) of the fragments generated by hydrolysis. All ^{1}H DOSY NMR experiments were recorded at 37 °C. The diffusion coefficients of the hydrolysis products were determined from the spectra, in which the sharp multiplet of the hydrolysis product reaches its maximum intensity. The key fragments were determined as follows: The first key component was determined from the signal of the intact POSS cage in the respective DMSO-d6/D_2O-HEPES solution. All further key components were determined from the most intense signal of the sharp multiplet, which belongs to the hydrolysis product. The diffusion coefficients at the start of the hydrolysis ($D_{initial}$) and after reaching the hydrolysis equilibrium (D_{final}) for the cubes **15**, **16** and **18**, **19** are summarized in Table 4. The hydrodynamic radii of the main hydrolysis products of the PEG-POSS cubes **15** and **16**, as well as of the PF-POSS cubes **18** and **19** are depicted in Figure 25.

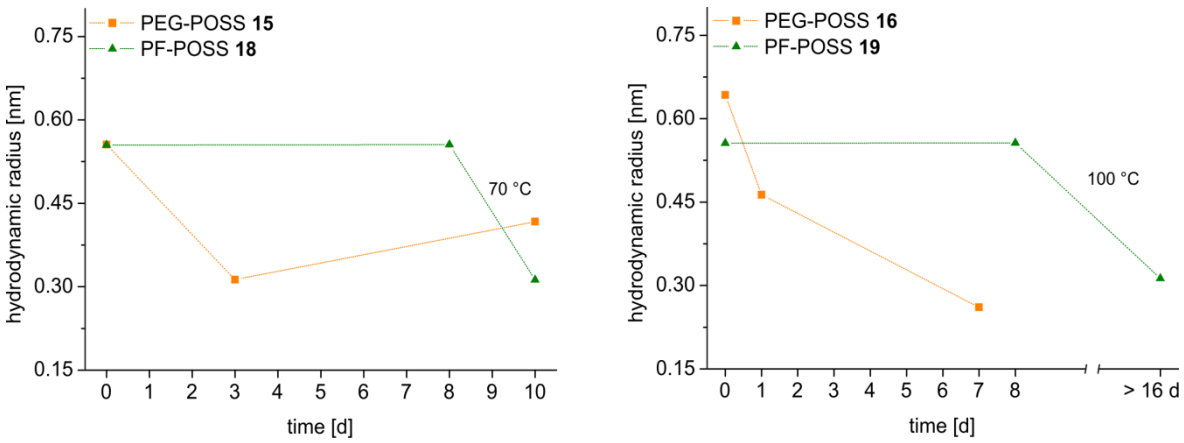

Figure 25: Time dependent measurement of the hydrodynamic radii of **15**, **18** and **16**, **19**.

Interestingly the PEG-POSS **15** reaches a minimal radius of 310 pm after three days followed by a re-condensation which resulted in hydrodynamic radii of about 420 pm (10 d). The heating of the sample to 70 °C for more than seven days shows no further changes. Thus it must be assumed that an equilibrium is achieved and the formations of re-condensed compounds like dimers or trimers are more favored than monomers.

Table 4: Diffusion coefficients of the key hydrolysis products.

compound	$D_{initial}$ [$\times 10^{-10}$ m^2s^{-1}]	D_{final} [$\times 10^{-10}$ m^2s^{-1}]	$\eta_{solvent}$ [1] [mPas]
15	3.65	4.87	1.12
18	2.74	4.87	1.49
16	2.37	6.49	1.49
19	2.74	4.87	1.49

[1] the viscosity of the samples were approximated by using the diffusion coefficient D_{DMSO} in the respective sample and $r_{H,DMSO}$ (176 pm, consistent with the averaged, geometrical size) derived from a self-diffusion measurement of DMSO (T=25 °C, η_{DMSO}=1.987 mPas).

For **16** r_H at the starting point (time 0) is slightly increased due to agglomeration of the compound. Similar to **15** a fast hydrolysis (after 2.5 h) takes place for **16** at 37 °C, whereas a hydrodynamic radius of 310 pm is calculated. The second major component reveals a hydrodynamic radius of 420 pm, which indicates similar hydrolyzed species as of **15**. After achieving the equilibrium the main hydrolysis products with r_H of 240 and 310 pm are smaller than those for **15**. This indicates, that the re-condensation of smaller compounds is slow which might be an effect of the longer PEG chain. While the hydrolyze of the PEG cages **15** and **16** were largely progressing at 37 °C, each of the fluorinated counterparts **18**

and **19** mainly maintain the initial hydrodynamic radii of about 560 pm after 8 days. Hence to obtain the products of the proceeded hydrolysis of **18** and **19**, the hydrolyzing process was accelerated by heating the samples to 70 °C and 100 °C, respectively. The key compounds obtained from these solutions revealed hydrodynamic radii of about 310 pm for the hydrolyzed PF-POSS cubes **18** and **19**, respectively.

The obtained diffusion coefficients of the PF-POSS **10**, **12** and **31** are summarized in Table 5. The hydrodynamic radius calculated for **10** at the beginning of the hydrolysis reveals some agglomeration of the compound in solution. The main hydrolysis product of **10** exhibits a radius r_H of 200 pm, while the main hydrolysis product of the PF-POSS **12** with the aliphatic linker shows a higher hydrodynamic radius of about 420 pm. From this it can be concluded, that the sterically demanding linker of **10** hinders the re-condensation of smaller species. The PF-POSS **31**, shows a stability at 37 °C over the course of seven weeks. After heating the solution at 70 °C for eight days the first hydrolysis product with a hydrodynamic radius of 470 pm is observed. In general for all PF-POSS with sterically demanding linkers a slower hydrolysis occurs due to hindered access of water. Consequently the nucleophilic attack on the silicon atom is restricted. Furthermore a diminished re-condensation of this compounds results in larger hydrolysis products.

Table 5: Diffusion coefficients (D) and hydrodynamic radii (r_H) of the main hydrolysis products of **10**, **12** and **31**.

compound	$D_{initial}$ [$\times 10^{-10}$ m^2s^{-1}]	r_H [pm]	D_{final} [$\times 10^{-10}$ m^2s^{-1}]	r_H [pm]	$\eta_{solvent}$[1] [mPas]
10	1.33	1106	7.46	200	1.54
12	2.74	560	3.65	420	1.49
31	2.55	890	4.87	470	1.00

[1] the viscosity of the samples were approximated by using the diffusion coefficient D_{DMSO} in the respective sample and $r_{H,DMSO}$ (176 pm, consistent with the averaged, geometrical size) derived from a self-diffusion measurement of DMSO (T=25 °C, η_{DMSO}=1.987 mPas).

In conclusion, the PF-POSS **10**, **12**, **15**, **16**, **18**, **19** and **31** resist hydrolysis under physiological conditions for the period of time, which is required to perform ^{19}F MRI experiments. This is an important finding as already the first hydrolysis step would reduce the symmetry of the cube and increase the number of ^{19}F resonances which attenuates the contrast. The sterically more demanding aromatic linkers lead to a much slower hydrolysis process of the POSS cage as the aliphatic groups in case of the PF-POSS **10** and **31**. Also the strongly decelerated hydrolysis process caused by the hydrophobicity of the

polyfluorine groups has hardly any effect on the ^{19}F NMR spectra. Furthermore, even despite their incomplete hydrolysis to smaller fragments, each of the compounds **10**, **12**, **18**, **19** and **31** obtains a molecular size which can be easily eliminated *via* the kidneys. Because of their solubility the PF-POSS cubes **12** and **31** are of particular interest for their behavior in organic tissue. Since PF-POSS **12** possess a less polar structure the suitability for application in brain tissue is of great interest. In the case of PF-POSS **31** the water solubility may offer an excellent advantage compared to commercially available non soluble fluorinated compounds, which have to be injected as emulsions.

3.2.5 ^{19}F Magnetic Resonance Imaging

In order to assess the potential of the PF-POSS **10**, **11** and **12** as ^{19}F contrast agents for brain tissue, MR images were performed *in vitro*. Initially the ^{19}F spin-lattice (T_1) and spin-spin (T_2) relaxation times were determined in solutions (0.9 mM) for each of the PF-POSS **10**, **11** and **12**, respectively (Table 6).

Table 6: ^{19}F T_1 and T_2 relaxation times of the PF-POSS **10**, **11** and **12**.

sample	T^1 [ms]	T^2 [ms]
10	966.0	578.2
11	999.6	565.3
12	853.6	570.3
$\mathbf{I}^{[60]}$	1200.0	728.0

The ^{19}F MRI *in vitro* measurements were executed with two different concentrations related to the amount of ^{19}F nuclei (260 mM and 26 mM) (Figure 26).

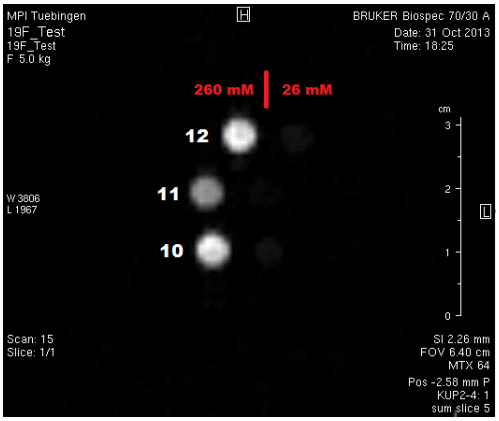

Figure 26: *In vitro* ^{19}F image of PF-POSS **10**, **11** and **12** with concentrations of 260 mM and 26 mM related to the ^{19}F amount.

The obtained signal-to-noise ratios (SNRs) after 40 min of measurement of the respective concentration are listed in Table 7. Each of the PF-POSS shows a good contrast for the 260 mM concentrated solution (Figure 26). Interestingly, the contrast in the images is strongest for PF-POSS cube **12**. Besides **12** possesses the lowest polarity among the three PF-POSS cubes, which is a good basic for the application in brain tissue. Hence for **12** a *post mortem* measurement by injection of the substance into the rat brain was performed visualized by the turbo-spin echo experiment (Figure 27).

Table 7: Signal-to-noise ratio (SNR) after 40 min measurement time.

concentration related to the ^{19}F amount	**10**	**11**	**12**
260 mM	78	50	68
26 mM	8	5	8

Figure 27: ^{1}H MR images of sagittal (left) and coronal (right) sections to show injection site of **12**.

The injection site into the rat brain is depicted in Figure 27. Two hours after injection of **12** two clearly visible spots are detected in the ^{19}F MR image (Figure 28). According to the time dependent ^{19}F NMR spectra of **12** in DMSO-d6/D_2O-HEPES buffer, the hydrolysis process can be excluded as reason for the second spot in the MR image. The ^{19}F NMR spectra show a slight line broadening of the original triplet (Figure 28). A second ^{19}F NMR resonance at higher frequencies is first observed after 25 h of hydrolysis. Hence it can be assumed that solubility properties cause the two spots. In this aspect, even though the PF-POSS **12** shows some solubility in the brain tissue, the compound is insufficient for *in vivo* applications due to the loss of the single ^{19}F signal after 2 hours. However, **12** shows potential chances to serve as basic structure for further functionalization to achieve higher stability and solubility. Since the aliphatic structure of **12** delivers the best contrast among the PF-POSS **10**-**12** in the organic tissue more detailed investigations in the brain tissue, can be worthwhile. In order to improve the nonpolar PF-POSS compounds even higher ^{19}F contents seem to be necessary.

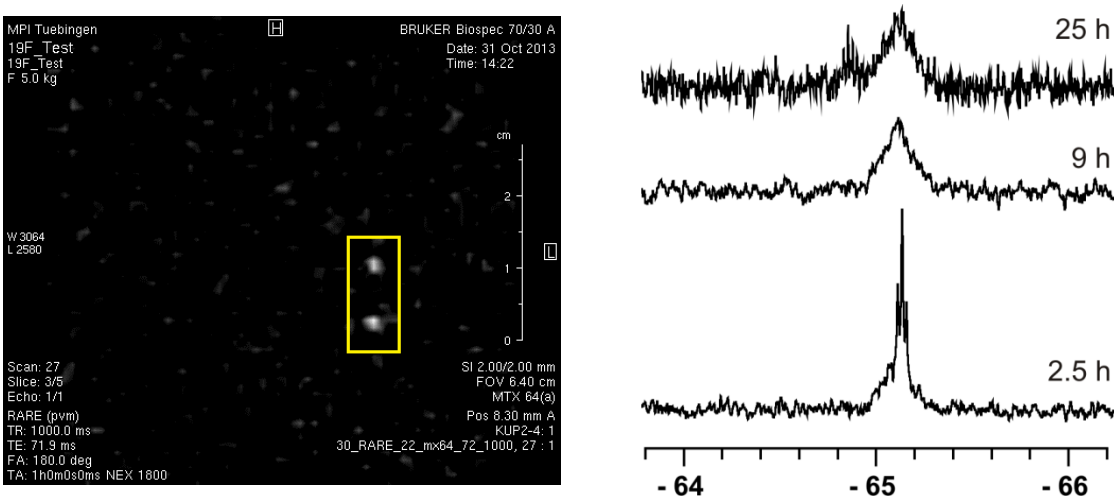

Figure 28. ^{19}F MR Image of **12** and time dependent ^{19}F-^{1}H NMR spectra of the hydrolysis sample of **12** in DMSO-d6/D_2O-HEPES buffer.

In order to estimate the suitability of the polar PF-POSS cubes **18**, **19** and **31** their respective T_1 and T_2 relaxation times were determined in DMSO solution. The evaluated relaxation times are listed in Table 8. Interestingly the PEG functionalized PF-POSS **18** and **19** deliver higher T_1 and T_2 values compared to the charged PF-POSS **31**. Due to the higher molecular mass of **31** the expected low T_2 value compared to **18** and **19** is observed.

Table 8: ^{19}F T_1 and T_2 relaxation times of PF-POSS **18**, **19** and **31**.

sample	T^1 [ms]	T^2 [ms]
18	1864.3	901.0
19	1806.3	944.0
31	1011.3	480.7

However, the water solubility of PF-POSS **31** compared to the partial solubility in water of the PF-POSS cubes **18** and **19** makes the PF-POSS **31** a better candidate for further examinations, like ^{19}F *in vitro*, *post mortem* and *in vivo* experiments.

In conclusion several high symmetrical PF-POSS cubes, which generate a single sharp signal in the ^{19}F NMR spectra were successfully synthesized. Furthermore, the syntheses of the PF-POSS cubes were obtained by favorable fast synthetic steps. The study revealed that the T_8-silsesquioxane core is a suitable amplifier for an intense ^{19}F signal, sufficient for MRI detection. Furthermore, each of the synthesized PF-POSS cubes shows an

adequate stability of the ^{19}F signal for the required period of time which is required for a MRI image. Besides the intact POSS cages as well as low weight hydrolysis products should be easily excreted *via* the kidneys due to the small molecular sizes. Moreover, the full range of PF-POSS cubes of different polarities was achieved successfully. At that the synthesis of nonpolar PF-POSS cubes for application in brain tissue as well as the synthesis of partial or fully water soluble PF-POSS cubes show the wide variety for potential fields of applications using PF-POSS cubes as building blocks for ^{19}F imaging agents.

4 Synthesis and characterization of Ln[DOTA-BA] and Ln[DOTA-GA] functionalized silica nanoparticles

4.1 Aim of the Work

Size dependent properties of spherical and monodisperse silica nanoparticles (SNPs) with diameters of about 15, 50 and 130 nm will be examined as a platform for the application as potential contrast agents (CAs) for magnetic resonance imaging (MRI). Therefore the SNPs will be covalently functionalized with two different lanthanoid(III) (Ln = Y, Gd) 1,4,7,10-tetraazacyclododecane-1,4,7,10-tetraacetic acid (DOTA) chelate complexes *via* an aminopropyl linker. In order to evaluate an optimal particle size, the expected increase in relaxivity due to Gd(III) surface payloading will be examined. Therefore, relaxation phenomena based on various parameters, like particle diameter, water exchange, surface charge and Gd(III) surface loading will be analyzed for a series of SNPs.

4.2 Results and Discussion

The properties of the $\mathbf{M0_{130}}$ SNPs series, which were reported before, are compared with those of smaller particles which are presented here.[25] The bare SNPs of 50 nm ($\mathbf{M0_{50}}$) and 130 nm ($\mathbf{M0_{130}}$) were synthesized by a modified Stöber process. Bare SNPs of 15 nm in solid state were not accessible, due to their agglomeration during isolation. Hence SNPs of 15 nm diameters with an already aminofunctionalized surface ($\mathbf{M1_{15}C_3NH_2}$) were purchased for further functionalization.

4.2.1 Syntheses

For the synthesis of the $\mathbf{M0_{50}}$ particles, a mixture of water and ethanol was equilibrated at 35 °C for at least 30 minutes and aqueous ammonia and TEOS were added quickly under strong stirring (Scheme 11).[64,67] After stirring for 20 h, the resulting particles were separated by centrifugation. The particles were dried *in vacuo* at 100 °C for at least 15 h.

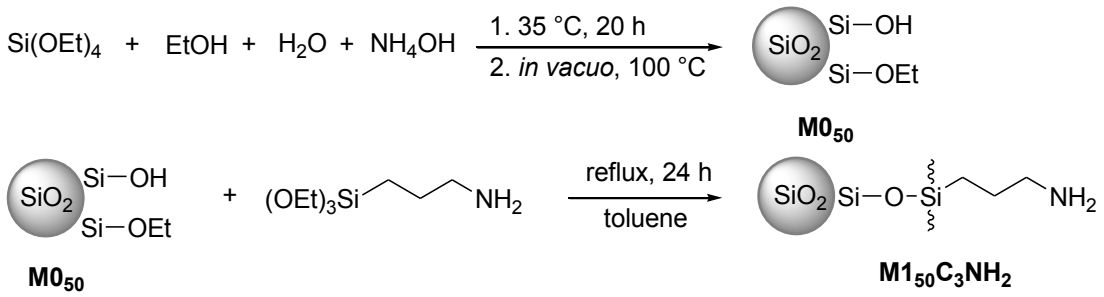

Scheme 11: Synthesis and silanisation of Stöber particles $\mathbf{M0_{50}}$.

The step of calcination, which is usually performed with particles > 100 nm, was avoided to prevent irreversible agglomeration of the quite small particles ($\mathbf{M0_{50}}$).[67,138–140] Due to this workup modification, residual ethoxy groups remain on the silica surface (Scheme 11). This is in contrast to the larger particles $\mathbf{M0_{130}}$ which were calcinated at 600 °C to give $\mathbf{M0_{130calc}}$ (Scheme 12). [25] The formed surface siloxane bonds were rehydroxylated in a second step to generate surface OH groups exclusively ($\mathbf{M0_{130reh}}$).

For the coupling of Gd(III) chelate complexes to the particle, the surface SiOH groups need to be modified with a functional linker.[24,141,142] The silanisation of the surface silanol groups with functionalized alkoxysilanes provides the opportunity for obtaining different functional groups on the surface.[51,143–150] Thus Stöber particles $\mathbf{M0_{50}}$ and $\mathbf{M0_{130reh}}$ were reacted with 3-aminopropyl-triethoxysilane (APTES) to attain an amino functionalized spacer (Scheme 11 and 12).[139,151,152]

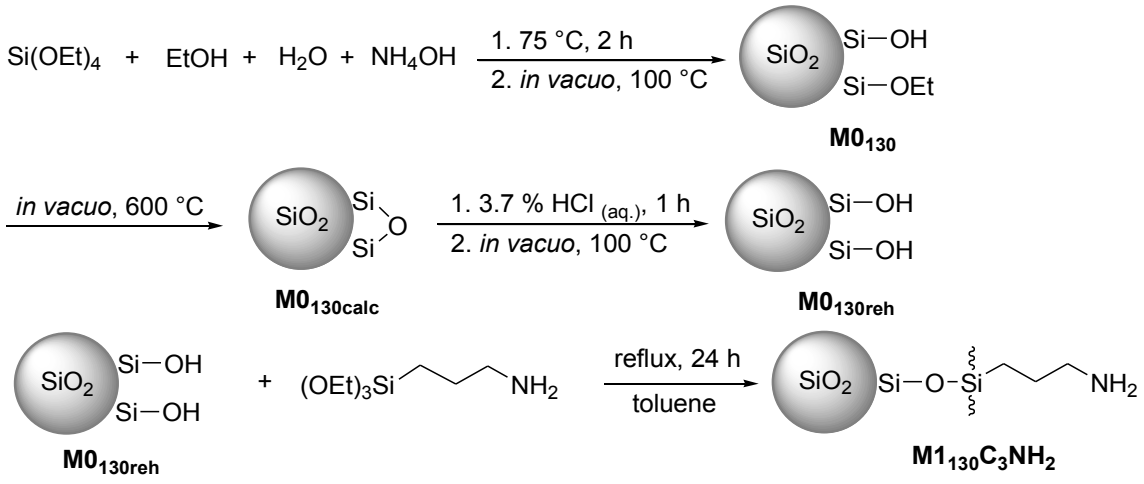

Scheme 12: Synthesis and silanisation of Stöber particles $\mathbf{M0_{130reh}}$.

4.2.2 Surface Modification of Amino Functionalized Silica Particles with Ln[DOTA] Derivatives

The **Ln[DOTA]** derivatives with a carboxylic acid group (**[Gd-BA]** and **[Gd-GA]**) were covalently bound to the amino groups of the functionalized particles $\mathbf{M1_{50}C_3NH_2}$ and $\mathbf{M1_{15}C_3NH_2}$ by common peptide synthesis techniques. The same procedure was reported for $\mathbf{M1_{130}C_3NH_2}$ SNPs.[25] For NMR spectroscopic investigations the corresponding [**Y-BA**] and [**Y-GA**] derivatives were synthesized in an analogous way (Scheme 13).[28]

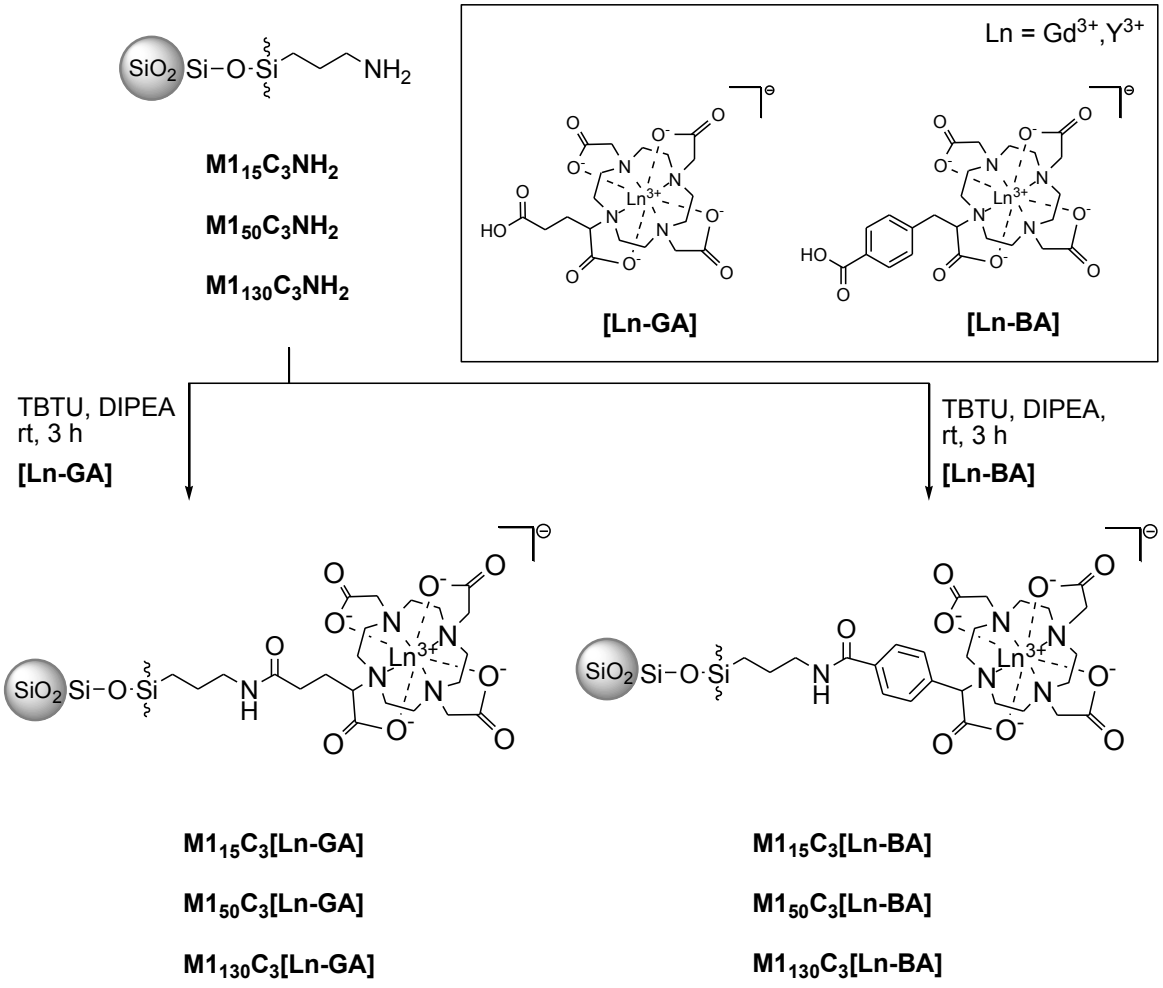

Scheme 13: Syntheses of $\mathbf{M1_{15/50/130}C_3}$**[Ln-BA]** and $\mathbf{M1_{15/50/130}C_3}$**[Ln-GA]**.

For the coupling reactions of the amino moiety and the carboxylic acid groups, the peptide coupling reagent O-(benzotriazol-1-yl)-N,N,N',N'-tetramethyluronium tetrafluoroborate (TBTU) was applied and the deprotonation of the carboxylic functions was achieved by diisopropylethylamine (DIPEA). Typically the amino functionalized silica particles

$M1_{15}C_3NH_2$ and **$M1_{50}C_3NH_2$,** respectively, were suspended in DMSO. The carboxylic acid groups of the **[Ln-DOTA]** derivatives (**[Ln-BA]**, **[Ln-GA]**) were activated with DIPEA and TBTU and subsequently added to the particles. After stirring the mixtures **$M1_{15/50}C_3$[Gd-BA]** and **$M1_{15/50}C_3$[Gd-GA]**, respectively, the particles were separated from the solution by centrifugation, washed and dried at 60 °C. The same procedure was used to synthesize **$M1_{130}C_3$[Gd-BA]** and **$M1_{130}C_3$[Gd-GA]** particles.[25] The absence of non-coordinated Gd(III) ions was verified by the xylenol test.[153] In order to investigate higher surface coupling of the **$M1_{15}C_3$[Gd-GA]** and **$M1_{50}C_3$[Gd-GA]** silica particles, this procedure was repeated with the **[Gd-GA]** complex resulting in the particles **$M1_{15}C_3$[Gd-GA]*** and **$M1_{50}C_3$[Gd-GA]***.

For acetyl group protection of the residual surface amino groups, the **$M1_{15/50/130}C_3$[Gd-BA]** and **$M1_{15/50/130}C_3$[Gd-GA]** SNPs, respectively, were suspended in DMF and treated with acetic anhydride.[154] After their reaction each of the materials **$M1_{15/50/130}C_3$[Gd-BA]ac** and **$M1_{15/50/130}C_3$[Gd-GA]ac** was separated by centrifugation, washed and dried at 60 °C.

4.2.3 Spectroscopic Characterization

4.2.3.1 Nuclear Magnetic Resonance Spectroscopy

Solid state NMR spectroscopy offers the opportunity to investigate the successful synthesis and surface modification of SNPs. For NMR spectroscopic characterization different methods like ^{29}Si CP/MAS and ^{29}Si HPDEC/MAS NMR as well as ^{13}C CP/MAS measurements were performed.

High resolution ^{29}Si CP/MAS NMR (cross polarization magic angle spinning NMR) is an efficient method for elucidation of solid silica materials. With this method different silica groups existing on the particle surface and in the bulk material can be assigned (Figure 29). The ^{29}Si CP/MAS spectrum of bare **$M0_{50}$** silica particles shows a signal at -110 ppm for Q^4-groups and a stronger signal for Q^3-groups at -101 ppm (Figure 30a). The Q^4-groups result from bulk material and surface siloxane bonds. The Q^3-groups are revealed by internal silanol groups and isolated SiOH moieties on the particle surface (Figure 29).[138]

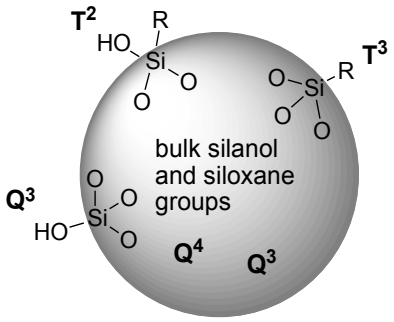

Figure 29: Silanol groups and siloxane bridges on the SNP surface and in the bulk material.

After APTES functionalization the ^{29}Si CP/MAS spectra of $\mathbf{M1_{50}C_3NH_2}$ silica particles exhibit next to the Q^3- and Q^4-resonances the signals of T^3-groups at -66 ppm (Figure 30 a). The appearance of only a small resonance, visible as a shoulder at -60 ppm for the T^2-groups proves a good binding of the linker. The minor intensity results from coupling of APTES over one or two of the three ethoxy groups to the surface of the particles. Based on the small surface to bulk ratio the T^2- and T^3-group signals are less intense. A similar effect is visible in the ^{29}Si CP/MAS spectra of $\mathbf{M1_{130}C_3NH_2}$, which reveals the signals of the T^2-group at -58 ppm and those of the T^3-group at -66 ppm (Figure 31).

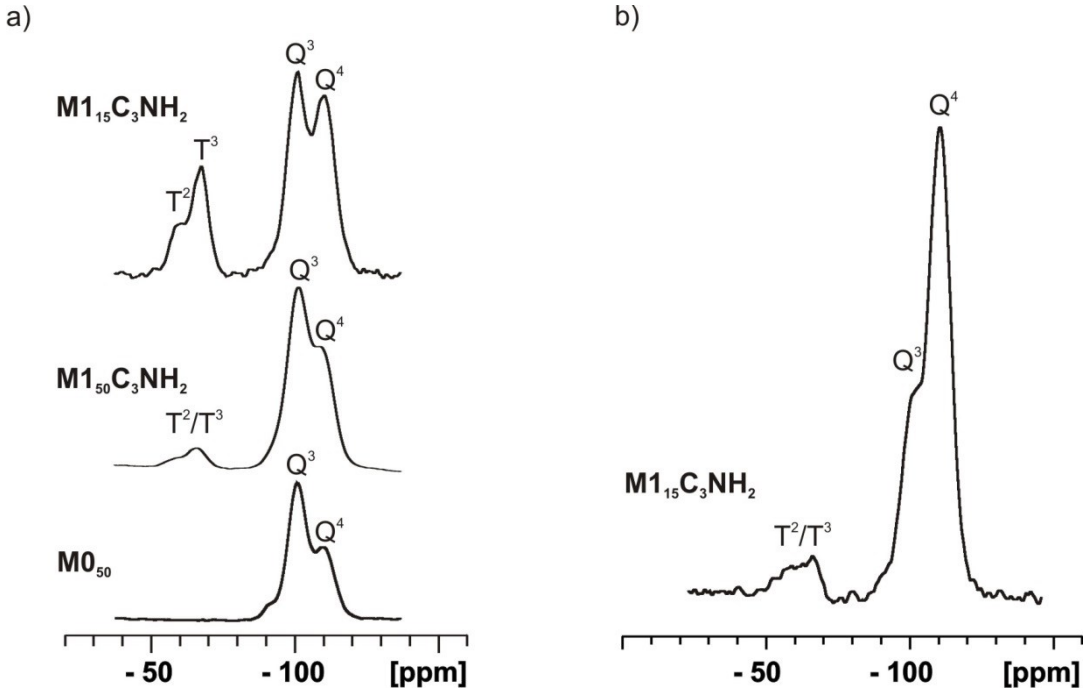

Figure 30: a) ^{29}Si CP/MAS NMR spectra of $\mathbf{M1_{15}C_3NH_2}$, $\mathbf{M1_{50}C_3NH_2}$ and $\mathbf{M0_{50}}$, b) ^{29}Si HPDEC/MAS NMR spectrum of $\mathbf{M1_{15}C_3NH_2}$.

The peak of the Q^3 group and a shoulder for Q^4 group are observed at -100 and -108 ppm, respectively (Figure 31).[25] In contrast to the larger particles, the spectrum of **$M1_{15}C_3NH_2$** shows a higher intensity in the signals of T^3- and T^2-groups at -68 ppm and -60 ppm (Figure 30 a). This may be an evidence for a higher surface modification by APTES groups, which is consistent with the high carbon content measured by the elemental analysis (see below, chapter 4.2.7).

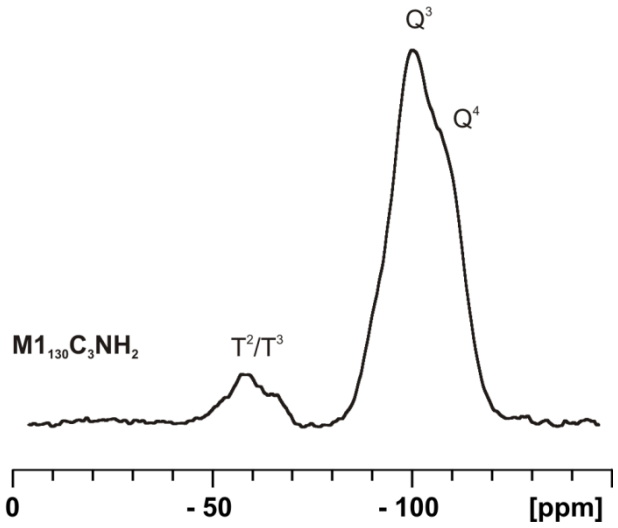

Figure 31: ^{29}Si CP/MAS NMR spectrum of **$M1_{130}C_3NH_2$**.

^{29}Si High Power Decoupling/MAS NMR (HPDEC/MAS NMR) is a method, which allows for the quantification of the different species. The ^{29}Si HPDEC/MAS spectrum of **$M1_{15}C_3NH_2$** renders a Q^4/Q^3 group ratio of 73 % (Q^4) to 27 % (Q^3) (Figure 30 b). The signals of T^3- and T^2-groups can be found at -68 ppm and -60 ppm, respectively. However, a quantitative analysis by HPDEC/MAS NMR is not possible for particles with small surface to bulk ratios (T^3/Q^4). This results from the small amount of T^3-groups which become undetectable in an appropriate time without the gain of cross-polarization. Therefore, in the case of **$M1_{50}C_3NH_2$** and **$M1_{130}C_3NH_2$** only ^{29}Si CP/MAS NMR spectra with qualitative information were recorded to characterize the chemical shifts of the different silica groups (Figure 30 a and Figure 31).

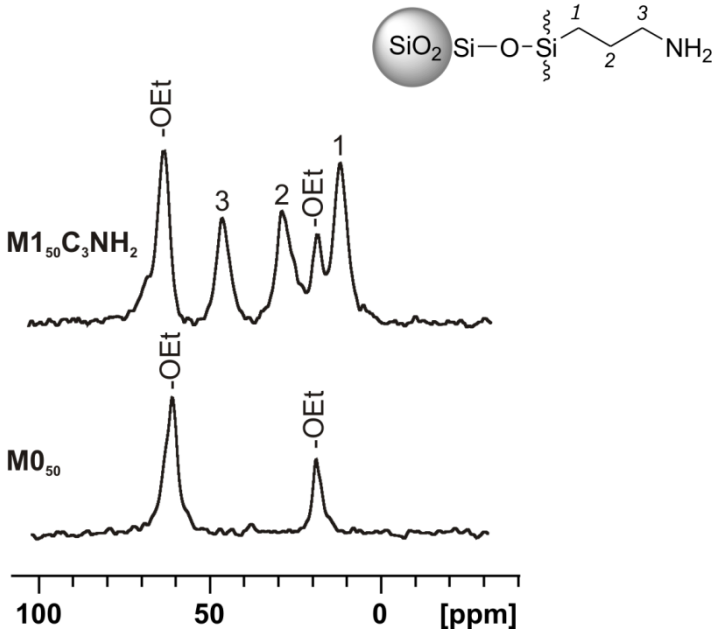

Figure 32: ^{13}C CP/MAS spectra of **M0$_{50}$** and APTES modified **M1$_{50}$C$_3$NH$_2$** particles.

In the ^{13}C CP/MAS NMR spectrum of bare **M0$_{50}$** silica particles, signals of residual ethoxy groups on the surface can be found at 19 and 61 ppm (Figure 32). After coupling of the APTES linker the ^{13}C CP/MAS spectrum of **M1$_{50}$C$_3$NH$_2$** shows three additional signals at 12, 29 and 46 ppm which result from the propylene chain of the linker.[155] In the same way the ^{13}C CP/MAS spectrum of **M1$_{130}$C$_3$NH$_2$** gives evidence for the successful surface modification by silanisation (Figure 33).[25] For NMR investigations the Y(III) ion was used for the complexation of the ligands **[DOTA-BA]** and **[DOTA-GA]**, since evaluable NMR measurements are not possible with the Gd(III) ion due to its paramagnetism.

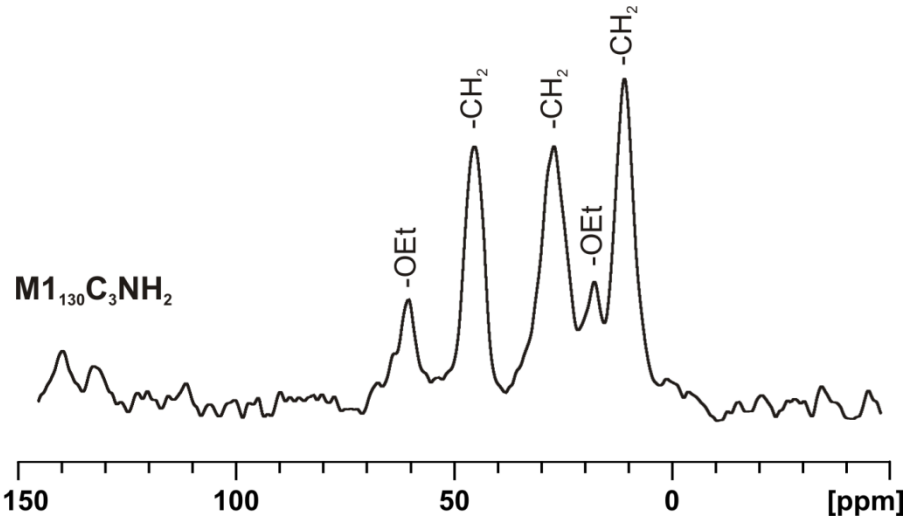

Figure 33: ^{13}C CP/MAS spectrum of **M1$_{130}$C$_3$NH$_2$** particles.

The successful coupling of the **[Y-GA]** complex to the surface of $\mathbf{M1_{50}C_3NH_2}$ is indicated by signals originating from the alkyl groups of the ligand (51 to 85 ppm) and signals of the carbonyl groups (179 ppm) (Figure 34).

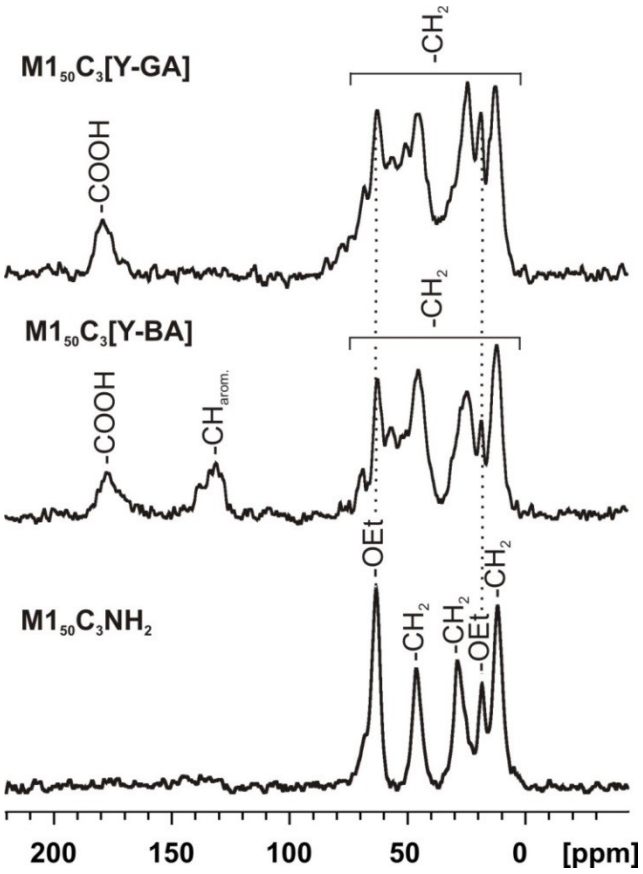

Figure 34: ^{13}C CP/MAS spectra of the modified particles $\mathbf{M1_{50}C_3NH_2}$, $\mathbf{M1_{50}C_3}$**[Y-BA]** and $\mathbf{M1_{50}C_3}$**[Y-GA]**.

Similarly the coupling of the **[Y-BA]** complex displays resonances for the alkyl groups of the ligand (51 to 72 ppm) and for the carbonyl groups (178 ppm). Additionally, the signals of the aromatic carbon atoms appear at 131 ppm (Figure 34).

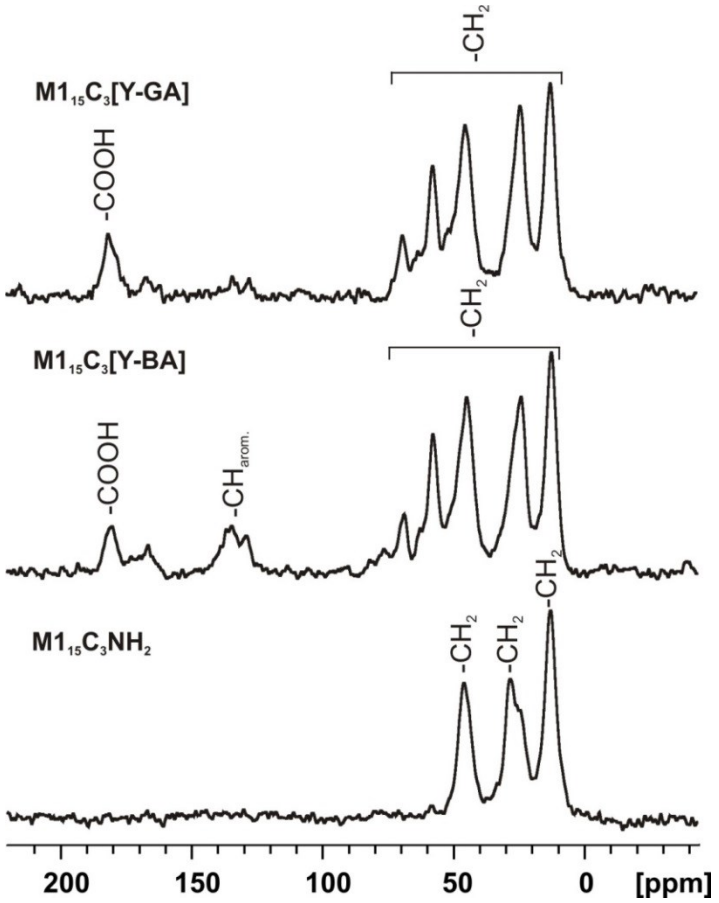

Figure 35: ^{13}C CP/MAS spectra of the modified particles **M1$_{15}$C$_3$NH$_2$, M1$_{15}$C$_3$[Y-BA]** and **M1$_{15}$C$_3$[Y-GA]**.

The ^{13}C CP/MAS characterization of **M1$_{15}$C$_3$NH$_2$** displays three signals resulting from the propyl chain of APTES (13, 28 and 46 ppm) whereas no resonances resulting from ethoxy groups appear (Figure 35). Thus the alkyl signals after coupling of the **Y-DOTA** derivatives with **M1$_{15}$C$_3$NH$_2$** are more apparent. The ^{13}C CP/MAS spectrum shows alkyl carbon signals between 48 to 73 ppm for **M1$_{15}$C$_3$[Y-GA]** and the carbonyl signals around 181 ppm. After coupling of [**Y-BA**] the alkyl carbon signals for **M1$_{15}$C$_3$[Y-BA]** appear between 53 to 74 ppm, the aromatic carbon atoms at 134 ppm and the signals of the carbonyl atoms are detected down-field around 181 ppm.

4.2.3.2 DRIFT Spectroscopy

After each synthetic step DRIFT spectra of the respective SNPs were recorded to confirm the successful synthesis. The assignments of all IR frequencies are summarized in Table 9. For all materials strong bands are observed for the vibration of interior siloxane bonds [ν (Si-O-Si)] around 1984, 1864 and from 1279 to 995 cm^{-1}. Additionally, Si-OH stretching frequencies appear at 945 cm^{-1}. In the DRIFT spectrum of **M0$_{50}$** the stretching vibrations of the residual ethoxy groups [ν $(CH)_x$] can be detected at 2975 cm^{-1} as well as the vibrations of adsorbed water at 1629 cm^{-1} due to the hydrophilic particle surface (Figure 36a). In contrast to **M0$_{50}$** no vibrations for residual ethoxy groups [ν $(CH)_x$] are visible for **M0$_{130reh}$** (Figure 37).[25] Due to the formation of siloxane bonds during calcination the vibrations of internal Si-OH bonds are also absent.

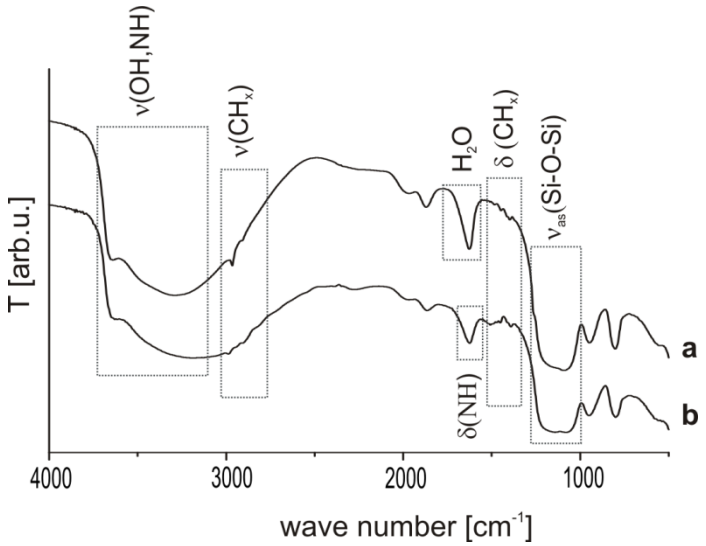

Figure 36: DRIFT spectra of a) **M0$_{50}$** and b) **M1$_{50}$C$_3$NH$_2$**.

After reaction with the aminopropyl linker there is no significant stretching vibration of the propyl groups visible (Figure 36 b). Only stronger bending vibrations of the methylene groups [δ $(CH)_x$] can be observed from 1395 to 1371 cm^{-1}. Additionally the deformation vibration [δ (NH)] of the amino groups at 1628 cm^{-1} is noticed. The detected vibration bands are in accordance to those described earlier.[156] The vibration band at 1628 cm^{-1} is close to reported values for the $–NH_2$ bending mode when water molecules are weakly bonded to the NH_2 groups and consequently allow the protonation of the amine.[149,157] These vibrations reported above are in accordance with frequencies stated for **M1$_{130}$C$_3$NH$_2$** SNPs (Figure 37).[25]

Table 9: Assignment of IR vibrations in wave numbers [cm^{-1}].

$M0_{50}$	**$M0_{130reh}$**	**$M1_{15}C_3NH_2$**	**$M1_{50}C_3NH_2$**	**$M1_{130}C_3NH_2$**	**$M1_{15}C_3$[Gd-BA]**	**$M1_{15}C_3$[Gd-GA]**	**$M1_{15}C_3$[Gd-GA]***	**$M1_{50}C_3$[Gd-BA]**	**$M1_{50}C_3$[Gd-GA]**	**$M1_{50}C_3$[Gd-GA]***	**$M1_{15}C_3$[Gd-BA]ac**	**$M1_{15}C_3$[Gd-GA]ac**	**$M1_{50}C_3$[Gd-BA]ac**	**$M1_{50}C_3$[Gd-GA]ac**	**$M1_{130}C_3$[Gd-BA]ac**	**$M1_{130}C_3$[Gd-GA]ac**	assignment
3640-3015	3655-3125	3761-2987	3787-3011	3652-3151	3767-2965	3764-2959	3770-3004	3784-3016	3775-3013	3741-3010	3719-2989	3757-2978	3743-3021	3758-3012	3769-2969	3766-2966	ν (Si-OH) ν (OH), ν (NH)
2975 2911	2927 2855	2937-2879	2989-2899	2941 2871	2934-2871	2937-2876	2937-2871	2984-2884	2984-2907	2984-2855	2937-2882	2937-2879	2987-2939	2983-2940	2940-2862	2934-2858	ν (CH_x)
1984	1988	2003	1977		1994	1988	1995	1974	1983	1987	1982	1988	1982	1980	1982	1986	ν (Si-O-Si)
1864	1863	1864	1866		1864	1864	1870	1866	1867	1872	1872	1872	1869	1869	1866	1866	
1629	1631																H_2O
		1628	1628	1619													δ (NH)
					1628	1628	1623	1622	1625	1629	1630	1636	1629	1628	1622	1622	ν (NHC=O)
											1558	1558	1552	1551	1561	1547	ν ($CO-CH_3$)
1396		1383	1395	1482	1386	1384	1393	1386	1392	1390	1374	1371	1380	1383	1371	1371	δ,γ (CH_x)
1279-995	1309-924	1252-982	1252-991	1275-975	1253-982	1253-982	1250-979	1250-999	1251-1002	1265-989	1253-993	1261-990	1259-999	1245-996	1276-973	1273-981	skeletal Si
948		953	953		956	956	951	950	953	946	950	946	944	946			ν (Si-OH)
802	817	796	802	812	799	802	802	802	805	802	798	801	798	798	810	813	δ (O-Si-OH)

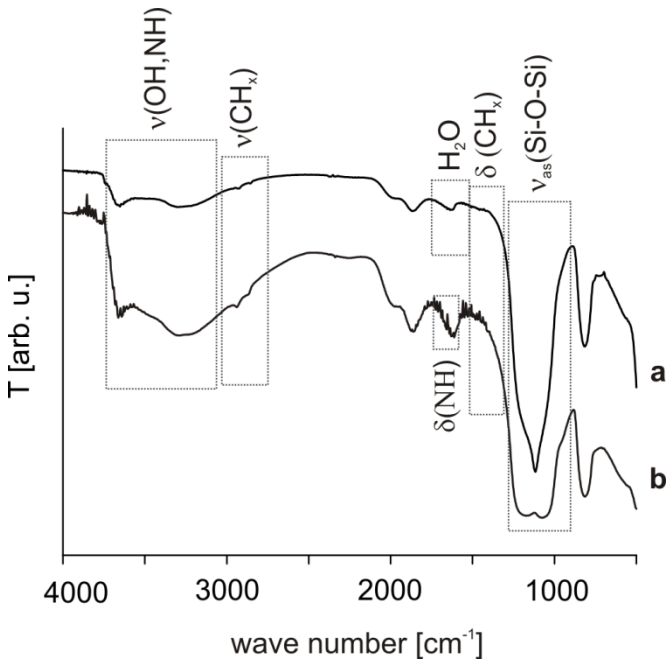

Figure 37: DRIFT spectra of a) $\mathbf{M0_{130reh}}$ and b) $\mathbf{M1_{130}C_3NH_2}$.

After successful coupling of the complex [**Gd-BA**] and [**Gd-GA**], respectively, to $\mathbf{M1_{50}C_3NH_2}$, the acid amide vibrations appear at 1622 and 1625 cm^{-1} (Figure 39 b and c). The slightly more pronounced acid amide vibration band in Figure 39 b indicates that the coupling with [**Gd-BA**] is more complete than the coupling with [**Gd-GA**], which is also confirmed by ICP-measurements (see chapter 4.2.8, Table 16). The improved coupling with [**Gd-BA**] also becomes noticeable by the stronger vibrational bands of the CH_2 groups from 2984 to 2884 cm^{-1}. Additionally the enhancement of the bending vibrations (1386 cm^{-1}) is more distinct. The IR frequencies of the Gd(III) chelate functionalized SNPs of the $\mathbf{M0_{130}}$ series present comparable vibrations as reported previously.[25] The DRIFT spectra of the $\mathbf{M1_{15}C_3NH_2}$ particles show more signals at 1628 to 1491 cm^{-1} (Figure 38 a). These vibrations result from ulterior alkyl moieties due to altered preparation conditions. They are more distinct because of the higher number of functional groups per amount of silica. After the reactions with the **[Gd-BA]** and **[Gd-GA]** complexes, respectively, the vibrations of their acid amide groups are detectable at 1628 cm^{-1} (Figure 39 b and c). The coupling with **[Gd-GA]** seems to work better than the coupling with **[Gd-BA]**, which is certified by ICP-measurements (Table 16).

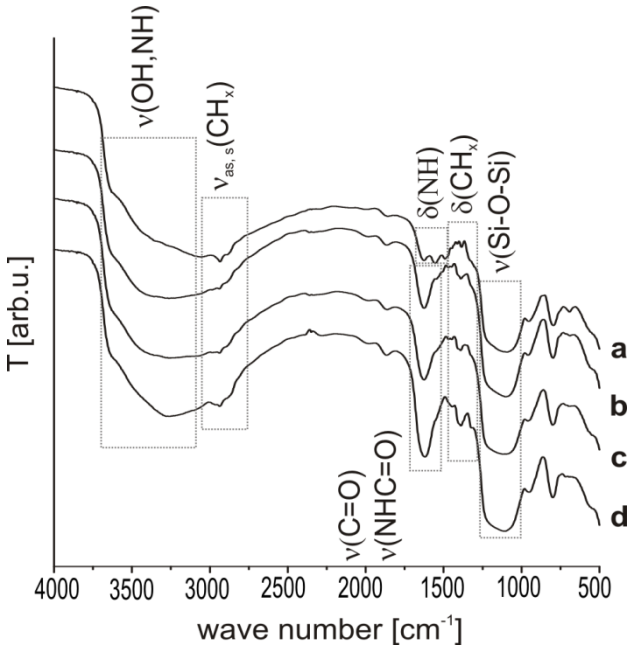

Figure 38: DRIFT spectra of a) $\mathbf{M1_{15}C_3NH_2}$, b) $\mathbf{M1_{15}C_3}$**[Gd-BA]**, c) $\mathbf{M1_{15}C_3}$**[Gd-GA]** and d) $\mathbf{M1_{15}C_3}$**[Gd-GA]***.

The bending vibrations of the carbon groups appear at 1386 and 1384 cm^{-1}. Further increase of the vibrational bands of the acid amide bond as well as the carbon bending vibrations are distinguishable after reacting $\mathbf{M1_{50}C_3}$**[Gd-GA]** and $\mathbf{M1_{15}C_3}$**[Gd-GA**], respectively, with additional Gd(III) complexes (Figure 38 and 39).

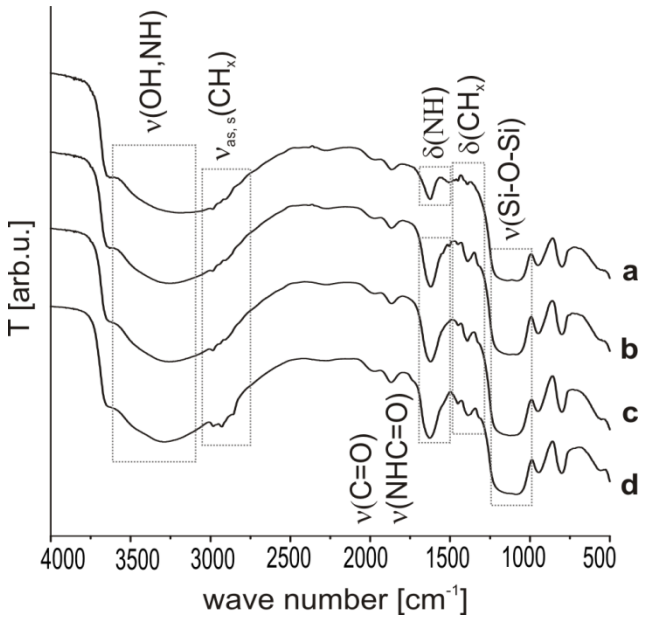

Figure 39: DRIFT spectra of a) $\mathbf{M1_{50}C_3NH_2}$ b) $\mathbf{M1_{50}C_3}$**[Gd-BA]** c) $\mathbf{M1_{50}C_3}$**[Gd-GA]** and d) $\mathbf{M1_{50}C_3}$**[Gd-GA]***.

Moreover, the stretching vibrations of the CH-groups are clearly observed from 2984 to 2855 cm^{-1} and from 2937 to 2871 cm^{-1}, respectively (Figure 38 d and Figure 39 d). In order to examine how the residual amino groups interact with the solvent and influence the water exchange process and consequently also the relaxivities, the amino moieties were protected with acetyl groups.

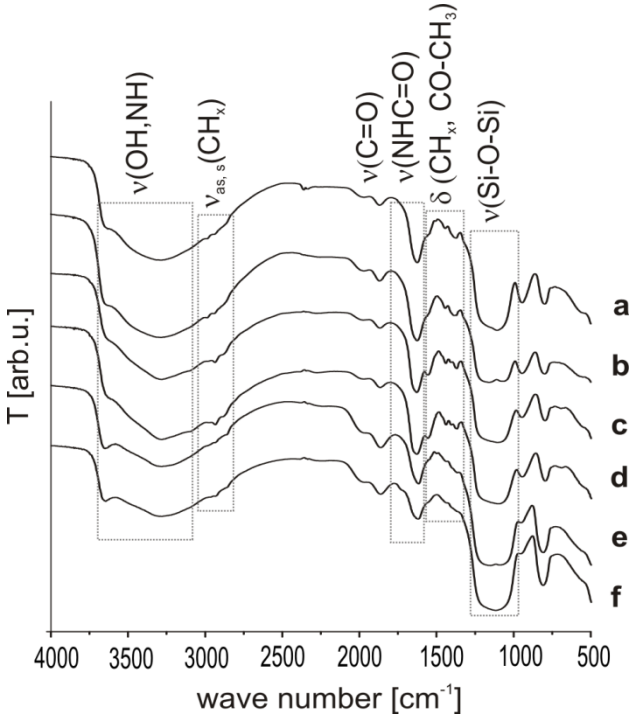

Figure 40: DRIFT spectra of a) **$M1_{50}C_3$[Gd-BA]ac**, b) **$M1_{50}C_3$[Gd-GA]ac**, c) **$M1_{15}C_3$[Gd-BA]ac**, d) **$M1_{15}C_3$[Gd-GA]ac**, e) **$M1_{130}C_3$[Gd-BA]ac** and f) **$M1_{130}C_3$[Gd-GA]ac**.

The DRIFT spectra verify the reaction of the surface amino groups with acetic anhydride (Figure 40). The signals for the bending vibrations of the methylene groups (1371-1383 cm^{-1}) are increased. Additionally, vibrations of the CH_3 unit of the acetyl group are observed. While the additional vibrations of the acid amide groups are detected as an almost separate signal for **$M1_{15}C_3$[Gd-BA]ac** and **$M1_{15}C_3$[Gd-GA]ac** (Figure 40 c and d), the signal is seen as a shoulder for **$M1_{50}C_3$[Gd-BA]ac** and **$M1_{50}C_3$[Gd-GA]ac** (Figure 40 a and b) and as an even smaller shoulder for **$M1_{130}C_3$[Gd-BA]ac** and **$M1_{130}C_3$[Gd-GA]ac** (Figure 40 e and f). The ratio of the surface groups to bulk is larger for the smaller particles than for larger particles in a defined volume, therefore the vibrations are less intense for the larger particles (**$M1_{130}$[Gd-BA]ac** and **$M1_{130}C_3$[Gd-GA]ac**).

4.2.4 Sizes of Particles and Particle Particle Interaction

The efficiency of a CA depends on its relaxivity. With higher relaxivity the CA offers the opportunity of improved contrast in MR images. The relaxivity of a CA is influenced by several parameters, such as electronic relaxation effects and molecular parameters like the water exchange rate, as well as the local and global rotation.[81,158] The silica particle is able to provide a high payload of Gd(III) chelate complexes for a high relaxivity effect. Therefore knowledge of size, size distribution as well as dispersion properties are of great importance. The agglomeration behavior of the SNPs not only changes the mobility of the material, but also determines the accessible particle surface. Limited accessibility of the chelate complexes on the surface for water molecules results in reduced exchange with bulk water and in a decrease of the relaxivity. Smaller particles, like $\mathbf{M1_{15}C_3NH_2}$ and $\mathbf{M1_{50}C_3NH_2}$ SNPs, own due to their smaller diameters much larger total surfaces per amount of silica than their larger counterparts. However, dynamic light scattering (DLS), scanning electron microscopy (SEM) and scanning transmission electron microscopy (STEM) measurements of all modified particles display different agglomeration behaviors depending on the particle size and surface modification as well as the medium.

Scanning electron microscopy reveals information about the size of the silica particles as well as their arrangement in the solid state. Different size and surface functionalization of SNPs result in altered interparticle interactions. The arrangements in the solid state can differ from those in the suspended state, as here the hydrate shell of the particles is missed and no interaction with ionic compounds of the solution takes place. The flexibility of surface molecules is also diminished. However, particle surface groups can interact *via* Coulomb forces. Changing surface charges by modifying the functional groups on the surface can influence the arrangement of the SNPs, accordingly. Moreover, the interfaces between the different particle sizes play an important role. With larger contact surface areas between the SNPs, as in the case of smaller particles, the strength of interaction increases. The clumping of several particles, the so called agglomeration, therefore is typically observed for small particles and increases with attractive interactions of surface groups. The following chapter summarizes the important influence of the particle size and surface functionalization on the physiochemical properties of dry and dispersed materials. Size distribution and agglomeration behavior of the particles were analyzed by SEM, STEM and DLS measurements.[159]

The SEM and STEM images of **M0$_{50}$** and **M0$_{130reh}$** reveal the successful syntheses of the desired particle sizes of 50 and 130 nm in diameter (Figure 41 and 42). Due to insufficient resolution of the particle boundary size measurements by SEM and STEM, image acquisitions of the purchased very small particles **M1$_{15}$C$_3$NH$_2$** were not possible. In contrast to this, average diameters d_{SEM} vary within the narrow range of 49-54 nm and 130-132 nm for the **M0$_{50}$** and **M0$_{130reh}$** particles and their modified counterparts, respectively (Table 10). The diameters determined from SEM images d_{SEM} of the amino coated, **[Gd-BA]** or **[Gd-GA]** functionalized and acetyl protected SNPs do not differ significantly from the starting materials **M0$_{50/130}$** (Figure 44, 46, 47).

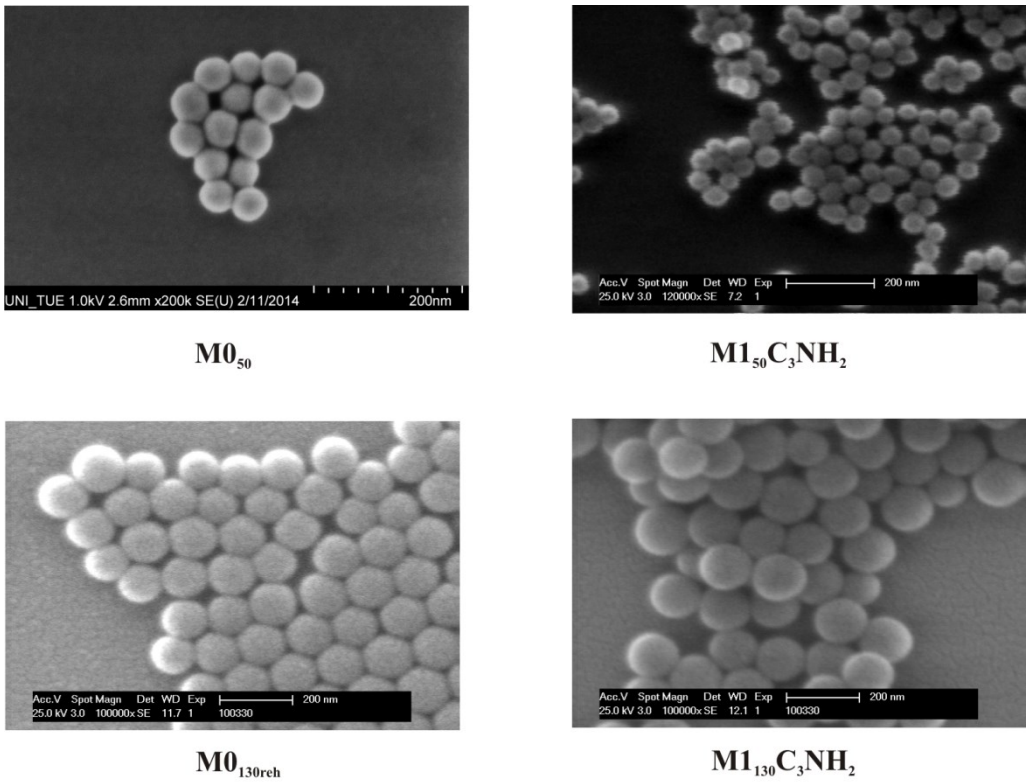

M0$_{50}$ **M1$_{50}$C$_3$NH$_2$**

M0$_{130reh}$ **M1$_{130}$C$_3$NH$_2$**

Figure 41: Scanning electron micrographs of **M0$_{50}$**, **M1$_{50}$C$_3$NH$_2$**, **M0$_{130reh}$** and **M1$_{130}$C$_3$NH$_2$**.

An evaluation of the scanning electron micrographs of all prepared particles shows that the agglomeration behavior strongly depends on the size and surface modification of the particles. In general smaller particles tend to form larger three dimensional agglomerates than their bigger counterparts (Figure 43). Interestingly APTES functionalized particles are even more inclined to form agglomerates.

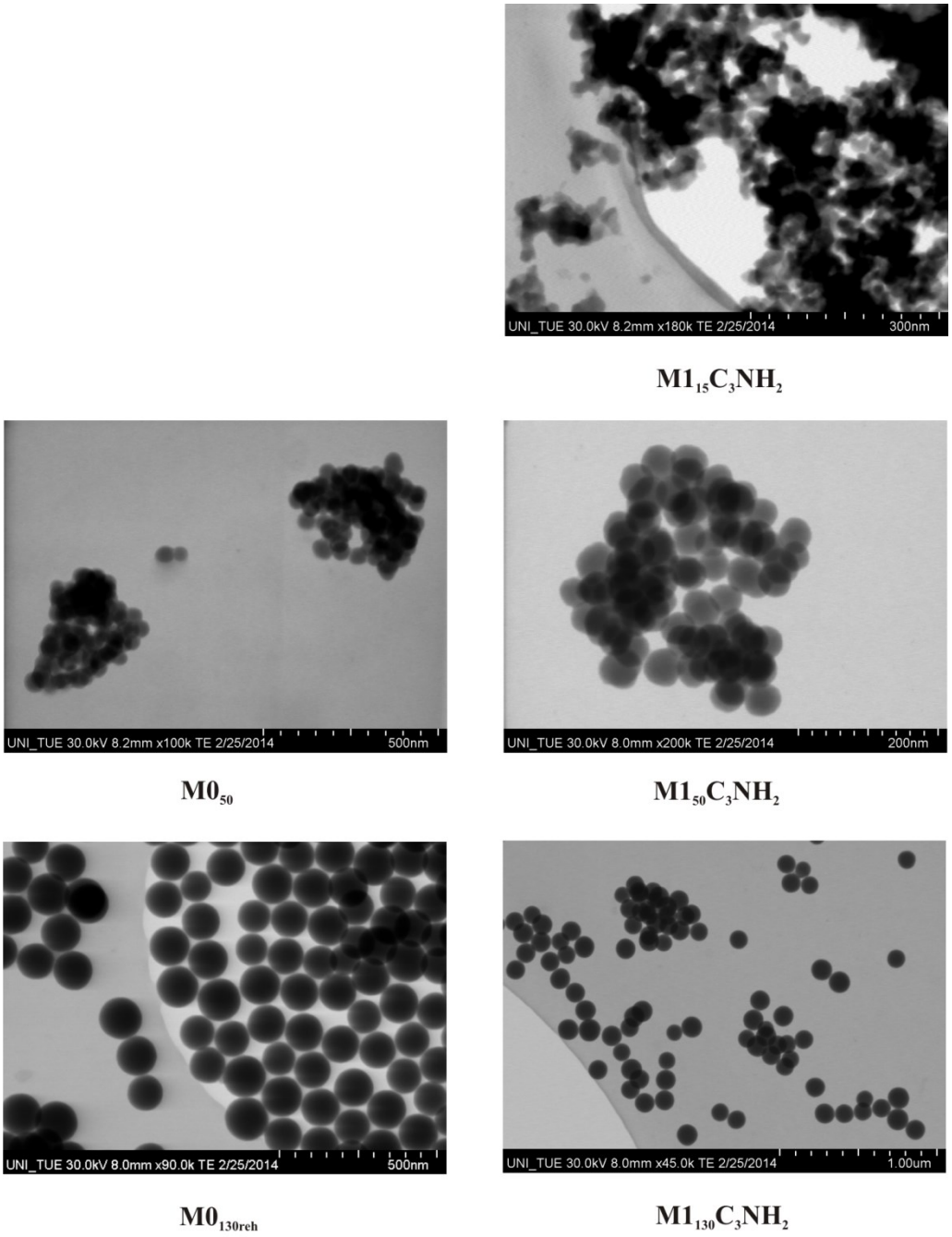

Figure 42: Scanning transmission electron micrographs of Stöber particles $\mathbf{M1_{15}C_3NH_2}$, $\mathbf{M0_{50}}$, $\mathbf{M1_{50}C_3NH_2}$, $\mathbf{M0_{130reh}}$ and $\mathbf{M1_{130}C_3NH_2}$.

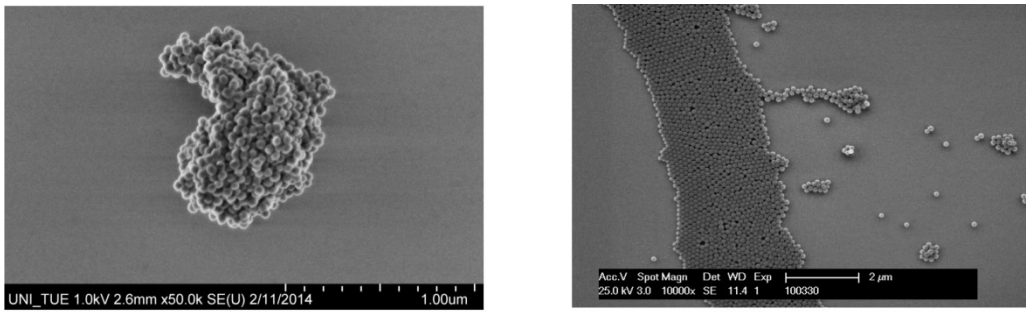

M0$_{50}$ **M0$_{130reh}$**

Figure 43: Scanning electron micrographs of **M0$_{50}$** and **M0$_{130reh}$**.

When the surface of the particles is covered with negatively charged Gd(III) chelate complexes, agglomerates are only observed for the small **M1$_{15}$C$_3$[Gd-BA]** and **M1$_{15}$C$_3$[Gd-GA]** materials (Figure 45). The **M1$_{50}$C$_3$[Gd-BA]** and **M1$_{50}$C$_3$[Gd-GA]** particles tend to agglomerate less and rather arrange in monolayers (Figure 46). All larger Gd(III) modified particles (**M1$_{130}$C$_3$[Gd-BA**] and **M1$_{130}$C$_3$[Gd-GA**]) extensively arrange in monolayers (Figure 47). If the conversion of original silanol groups into Gd(III) complexes (α_{Gd}/α_{OH}, see below Table 16) is considered for all SNPs, it must be assumed, that the particle size probably dominates the remaining agglomeration behavior of the smaller SNPs. Acetyl modified particles behave in a similar way as the Gd(III) modified particles at each particle size. **M1$_{15}$C$_3$[Gd-BA]ac** and **M1$_{15}$C$_3$[Gd-GA]ac** particles even tend to form smaller less compact agglomerates than **M1$_{15}$C$_3$[Gd-BA]** and **M1$_{15}$C$_3$[Gd-GA]** particles (Figure 45). The protected SNPs prevent the interaction of residual amino functions with Gd(III) complexes,[40] which results in an increase of repulsive effects. The least influence on the agglomeration behavior is noticeable for the **M1$_{130}$C$_3$[Gd-BA]ac** and **M1$_{130}$C$_3$[Gd-GA]ac** particles by still forming monolayers like their non-acetylated precursors **M1$_{130}$C$_3$[Gd-BA]** and **M1$_{130}$C$_3$[Gd-GA]**.

All observations of SEM images are in accordance with DLS data in suspended state and show similar agglomeration tendencies (Table 10).

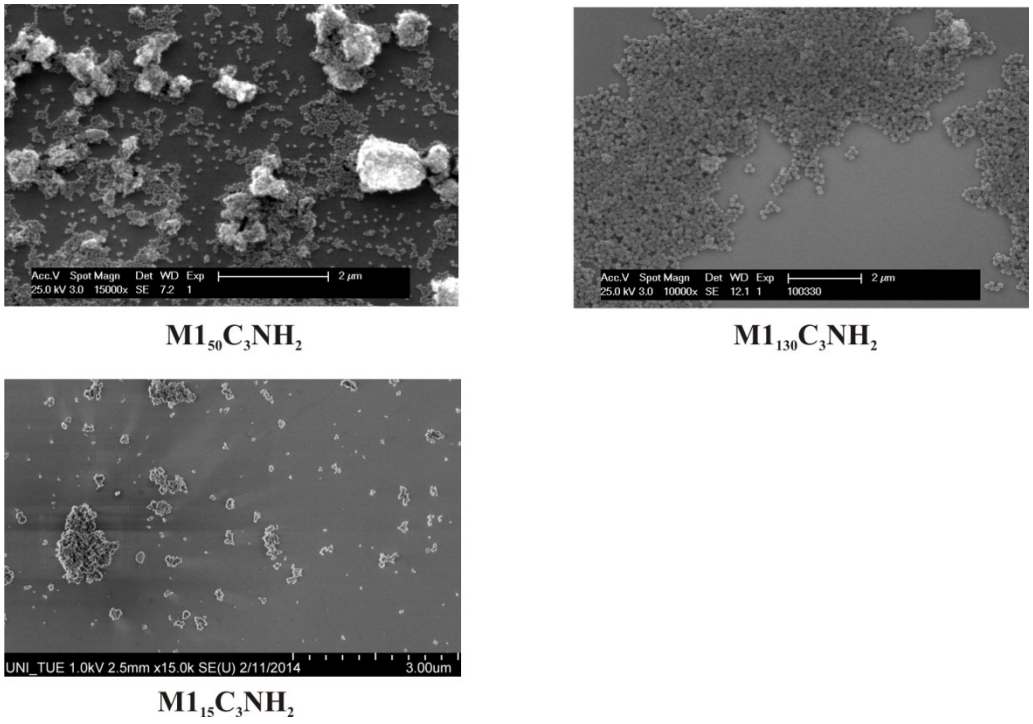

$M1_{50}C_3NH_2$ $M1_{130}C_3NH_2$ $M1_{15}C_3NH_2$

Figure 44: Scanning electron micrographs of $M1_{15/50/130}C_3NH_2$.

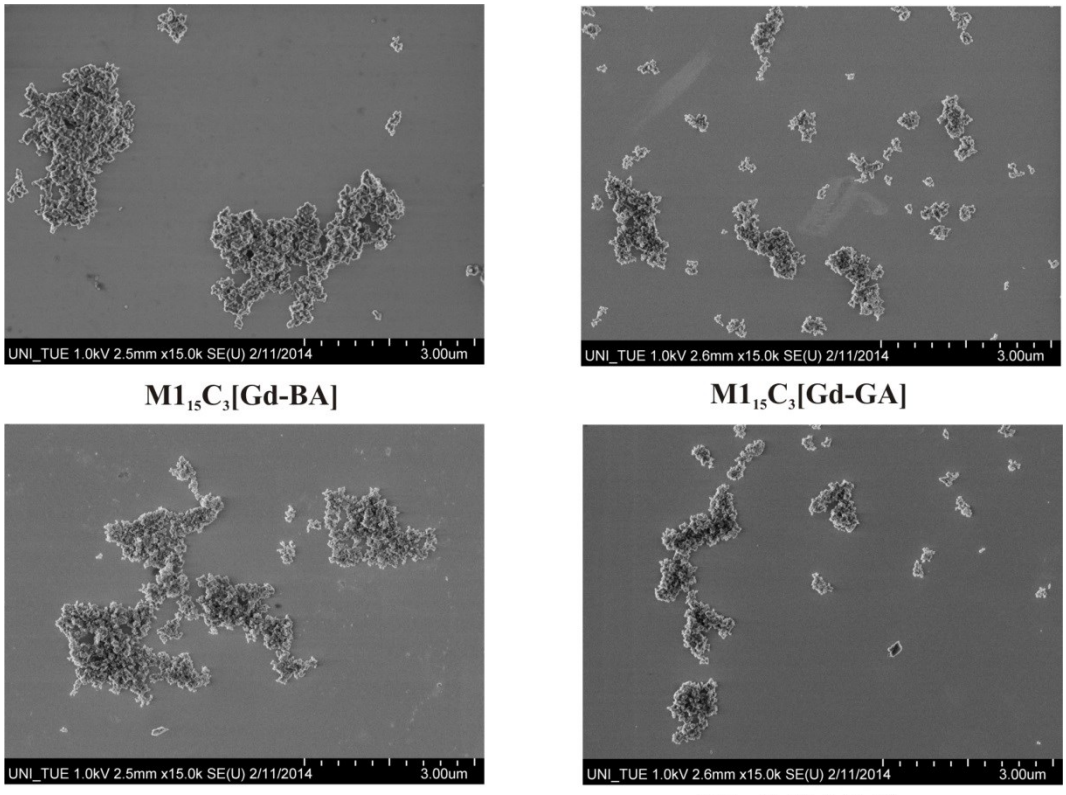

$M1_{15}C_3$[Gd-BA] $M1_{15}C_3$[Gd-GA] $M1_{15}C_3$[Gd-BA]ac $M1_{15}C_3$[Gd-GA]ac

Figure 45: Scanning electron micrographs of **$M1_{15}C_3$[Gd-BA], $M1_{15}C_3$[Gd-GA]** and their acetylated modifications **$M1_{15}C_3$[Gd-BA]ac, $M1_{15}C_3$[Gd-GA]ac**.

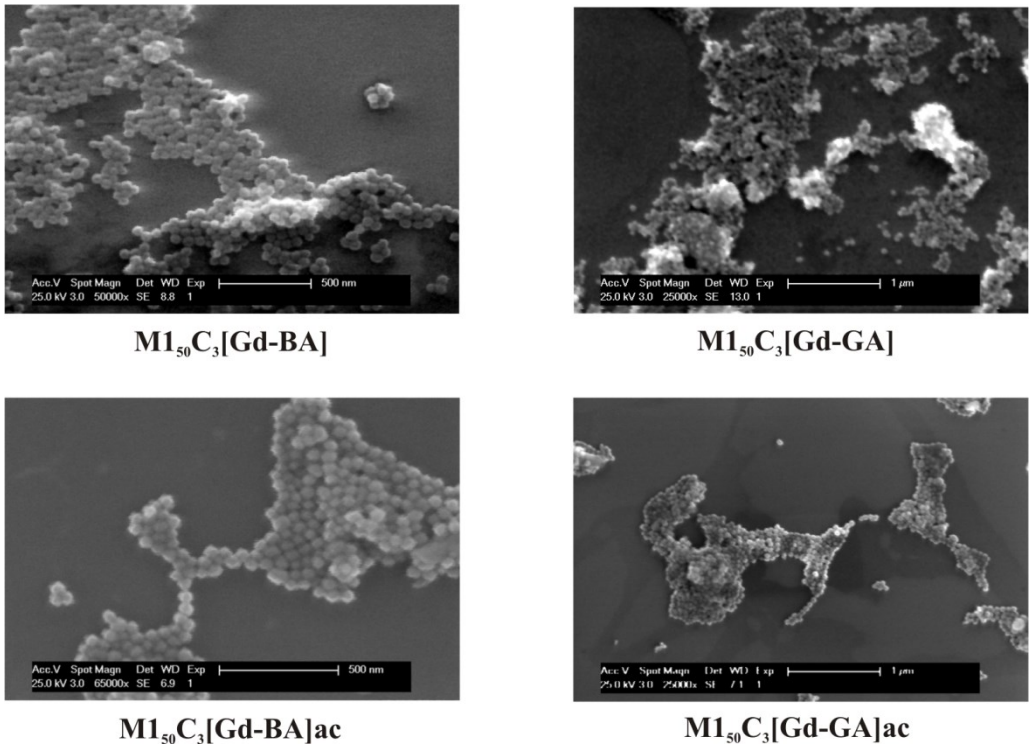

$M1_{50}C_3$[Gd-BA] **$M1_{50}C_3$[Gd-GA]**

$M1_{50}C_3$[Gd-BA]ac **$M1_{50}C_3$[Gd-GA]ac**

Figure 46: Scanning electron micrographs of **$M1_{50}C_3$[Gd-BA], $M1_{50}C_3$[Gd-GA]** and their acetylated modifications **$M1_{50}C_3$[Gd-BA]ac**, **$M1_{50}C_3$[Gd-GA]ac**.

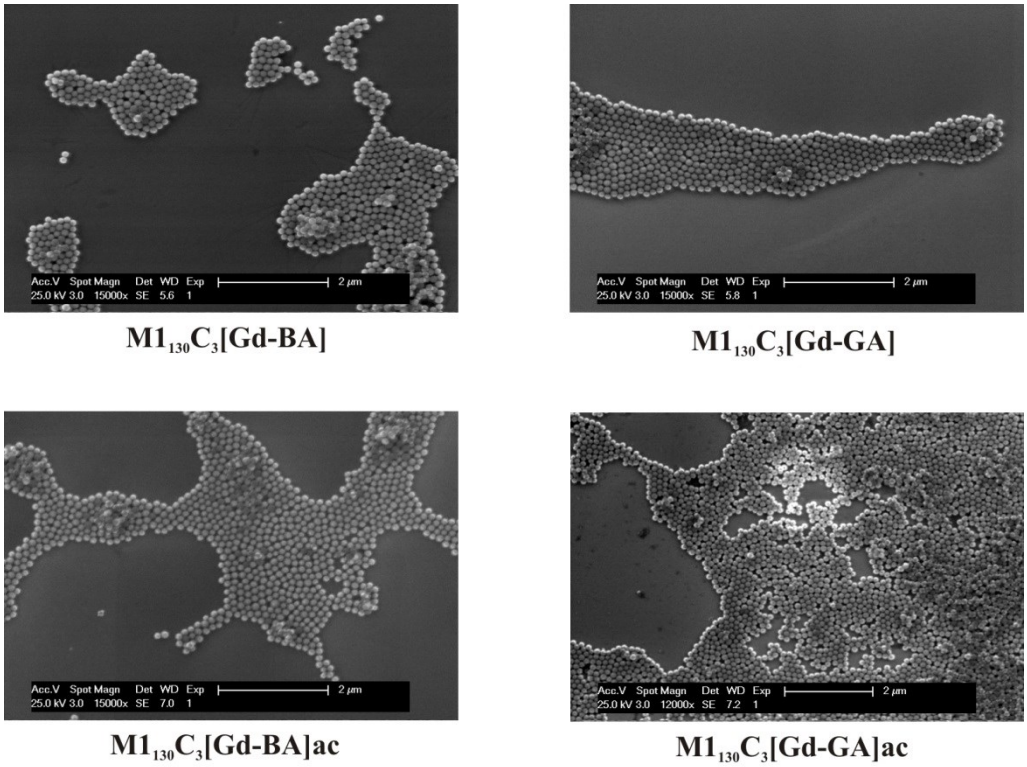

$M1_{130}C_3$[Gd-BA] **$M1_{130}C_3$[Gd-GA]**

$M1_{130}C_3$[Gd-BA]ac **$M1_{130}C_3$[Gd-GA]ac**

Figure 47: Scanning electron micrographs of **$M1_{130}C_3$[Gd-BA]**, **$M1_{130}C_3$[Gd-GA]** and their acetylated modifications **$M1_{130}C_3$[Gd-BA]ac**, **$M1_{130}C_3$[Gd-GA]ac**.

For DLS measurements, a suspension of each material (ρ = 1-2 mg/ml) was prepared in water or phosphate buffered saline (PBS) at pH 7.4 and filtered through a 0.25 μm nylon filter before measurement to remove larger agglomerates. Compared to the diameters obtained by SEM images, which represent mainly the naked particle diameter, the DLS values (d_{DLS}) are often larger as here the hydrodynamic radius is measured. Besides that larger average diameters result from agglomeration of the particles and become visible by higher standard deviations and a higher polydispersity index (PDI). The PDI is dimensionless with values between 0 and 1; values smaller than 0.05 indicate a highly monodisperse suspension in contrast to values > 0.7 confirming a broad size distribution (Table 10).

DLS size measurements offer the possibility to represent different average values. The most applied method by measuring Z-average intensity weighted radii is obtained by the cumulant analysis of the autocorrelation function of the scattered light (see also chapter 2.2.1). The resulting size distribution is given by a plot of the relative intensity of the light scattered by various sized particles. Generally the Z-average (d_z) is more suitable for monomodal distributions. In the case of multimodal (or very broad monomodal) distributions, the obtained results may not represent the real sizes in suspension. Reason for this is that scattering of bigger particles or agglomerates is much stronger than for little particles. In this case the intensity distribution can be misleading, hence only a small amount of aggregates can dominate the distribution.[160] Therefore it is important to measure multimodal distributions additionally with the number weighted mode, especially to compare with results measured by microscopy. Usually the former multimodal distributions (if not otherwise mentioned) become monomodal distributions, hence the number of agglomerates are vanishingly small (Table 10). For the following measurements with multimodal distributions the number weighted size measurements (d_n) result in expected values.

Especially the smaller particles **$M1_{15}C_3NH_2$, $M0_{50}$, $M1_{50}C_3NH_2$** and their Gd(III) chelate modified products tend to reflect multimodal distributions, hence the values rather represent approximations.

In water, bare particles **$M0_{50}$** and **$M0_{130reh}$** show hydrodynamic diameters (d_z) of about 128 and 134 nm, respectively (Table 10). Here the hydrodynamic radii of the smaller particles (**$M0_{50}$**) lead to larger values due to the presence of some aggregates, which is also displayed by the higher PDI. The size measurement weighted by number (d_n) represents a

monomodal distribution of 54 nm of the hydrodynamic diameter for **M0$_{50}$** particles, which is consistent with SEM measurements. For very small silica particles (10 nm) a high agglomeration with a broad size distribution was reported before.[161] In water all APTES coated particles **M1$_{15/50/130}$C$_3$NH$_2$** yield high PDI values and display a stronger agglomeration behavior the smaller the particles are. The **M1$_{50}$C$_3$[Gd-BA]** and **M1$_{50}$C$_3$[Gd-GA]** each show a less agglomeration tendency, while significantly stronger agglomeration and thus larger diameters are obtained for **M1$_{15}$C$_3$[Gd-BA]** and **M1$_{15}$C$_3$[Gd-GA]**, respectively, compared to the APTES coated precursors. Low PDI indices and no agglomeration tendency is observed for the **M1$_{130}$C$_3$[Gd-BA]** and **M1$_{130}$C$_3$[Gd-BA]** particles, respectively. Interestingly, the DLS measurement of the **M1$_{15}$C$_3$[Gd-GA]*** material reveals large hydrodynamic diameters and a broad size distribution in water. These small particles still agglomerate despite their higher surface loading with Gd(III). Compared to **M1$_{15}$C$_3$[Gd-GA]**, however, the agglomeration behavior is reduced most likely due to the presence of more negative charges on the surface. This observation is consistent with the measurements in the number weighted mode delivering smaller hydrodynamic radii of 80 nm (d_n). The **M1$_{50}$C$_3$[Gd-GA]*** material shows similar hydrodynamic radii as for **M1$_{50}$C$_3$[Gd-GA]**. From the presence of more single particles and some agglomerates, the distribution becomes multiple in intensity weighted mode. Similar hydrodynamic radii of both materials **M1$_{50}$C$_3$[Gd-GA]** and **M1$_{50}$C$_3$[Gd-GA]*** is a result of fewer increase of the surface loading in comparison to the materials **M1$_{15}$C$_3$[Gd-GA]** and **M1$_{15}$C$_3$[Gd-GA]***. Probably the presence of less residual APTES groups (see below, chapter 4.2.7, Table 15) is a reason for this.

Table 10: Size characterization of bare and surface modified silica particles.

	SEM	**DLS in water**			
		number weighted	intensity weighted		
sample	d_{SEM} [nm]	DLS_{H_2O} d_n[(1)] [nm]	Modality of distribution[(2)] [m_{I, H_2O}]	DLS_{H_2O} d_Z[(3)][nm]	PDI
$M0_{50}$	49 ± 5	54 ± 20	mono (br)	128	0.288
$M0_{130reh}$	130 ± 11	112 ± 29	mono	134	0.052
$M1_{15}C_3NH_2$	-	165 ± 54	multi	216	0.209
$M1_{50}C_3NH_2$	52 ± 5	300 ± 63	mono (br)	536	0.548
$M1_{130}C_3NH_2$	131 ± 13	172 ± 49	mono (br)	256	0.334
$M1_{15}C_3$[Gd-BA]	-	254 ± 94	multi	483	0.438
$M1_{15}C_3$[Gd-GA]	-	391 ± 64	mono	947	0.682
$M1_{15}C_3$[Gd-GA]*	-	80 ± 26	mono	121	0.122
$M1_{50}C_3$[Gd-BA]	54 ± 3	68 ± 21	mono (br)	104	0.126
$M1_{50}C_3$[Gd-GA]	52 ± 4	68 ± 25	mono (br)	132	0.258
$M1_{50}C_3$[Gd-GA]*	-	62 ± 19	multi	133	0.379
$M1_{130}C_3$[Gd-BA]	132 ± 11	120 ± 29	mono	140	0.016
$M1_{130}C_3$[Gd-GA]	129 ± 10	120 ± 28	mono	138	0.021
$M1_{15}C_3$[Gd-BA]ac	-	110 ± 36	mono	150	0.132
$M1_{15}C_3$[Gd-GA]ac	-	111 ± 33	mono	149	0.184
$M1_{50}C_3$[Gd-BA]ac	52 ± 5	59 ± 18	mono	100	0.187
$M1_{50}C_3$[Gd-GA]ac	52 ± 3	57 ± 18	mono	96	0.135
$M1_{130}C_3$[Gd-BA]ac	130 ± 10	126 ± 30	mono	145	0.014
$M1_{130}C_3$[Gd-GA]ac	130 ± 13	126 ± 31	mono	145	0.014

(1) Measured size by number weighted mode d_n. **(2)** Modality in intensity weighted mode m_I. **(3)** Measured size by intensity weighted mode Z-average d_z.

Table 11: Size characterization of bare and surface modified silica particles in PBS.

	SEM		**DLS in PBS**		
		number weighted	intensity weighted		
sample	d_{SEM} [nm]	DLS_{PBS} d_n[(1)] [nm]	Modality of distribution[(2)] [$m_{I,PBS}$]	DLS_{PBS} d_Z[(3)] [nm]	PDI
M0$_{50}$	49 ± 5	53 ± 14	multi	73	0.144
M0$_{130reh}$	130 ± 11	116 ± 27	mono	135	0.023
M1$_{15}$C$_3$NH$_2$	-	344 ± 77	mono (br)	728	0.687
M1$_{50}$C$_3$NH$_2$	52 ± 5	300 ± 67[(4)]	multi	3192	0.872
M1$_{130}$C$_3$NH$_2$	131 ± 13	132 ± 71	multi	233	0.268
M1$_{15}$C$_3$[Gd-BA]	-	254 ± 94	multi	531	0.480
M1$_{15}$C$_3$[Gd-GA]	-	117 ± 35[(5)]	multi	444	0.454
M1$_{15}$C$_3$[Gd-GA]*	-	35 ± 8[(6)]	multi	188	0.389
M1$_{50}$C$_3$[Gd-BA]	54 ± 3	69 ± 22	mono	96	0.363
M1$_{50}$C$_3$[Gd-GA]	52 ± 4	61 ± 24	multi	139	0.289
M1$_{50}$C$_3$[Gd-GA]*	-	55 ± 16	mono	86	0.129
M1$_{130}$C$_3$[Gd-BA]	132 ± 11	128 ± 35	mono	151	0.046
M1$_{130}$C$_3$[Gd-GA]	129 ± 10	117 ± 31	mono	140	0.053
M1$_{15}$C$_3$[Gd-BA]ac	-	105 ± 36	mono	147	0.113
M1$_{15}$C$_3$[Gd-GA]ac	-	100 ± 35	mono	144	0.131
M1$_{50}$C$_3$[Gd-BA]ac	52 ± 5	51 ± 15	mono	81	0.148
M1$_{50}$C$_3$[Gd-GA]ac	52 ± 3	52 ± 14	mono	77	0.137
M1$_{130}$C$_3$[Gd-BA]ac	130 ± 10	120 ± 30	mono	141	0.022
M1$_{130}$C$_3$[Gd-GA]ac	130 ± 13	118 ± 28	mono	77	0.018

(1) Measured size by number weighted mode d_n. **(2)** Modality in intensity weighted mode m_I. **(3)** Measured size by intensity weighted mode Z-average d_Z. **(4)** Bimodal distribution Peak 1 (80.0 %), Peak 2 (20.0 %) 60 ± 7 nm. **(5)** Bimodal Distribution Peak 1 (80.4 %), Peak 2 (19.6 %) 331 ± 103 nm. **6** Bimodal Distribution Peak 1(53.8 %), Peak 2 (46.2 %) 89 ± 43 nm.

Opposed charges of the Gd(III) complexes and the residual protonated amino groups of other particles may cause a strong attractive interaction between particles. Consequently, the repulsive strength becomes overcompensated in water (Figure 48). Most likely this effect is stronger for smaller particles (*e.g.* **M1$_{15}$C$_3$[Gd-GA]**) because of the higher number of particles in a defined volume of a suspension and for this reason a further enhanced particle-particle interaction. Agglomeration based on opposed charges on particle surface has already been investigated for the so called heteroagglomeration of particles, by interaction of two different surface modified particles.[162,163] The relation of the particle number to the number of counterions may also play a role for agglomeration behavior.[164]

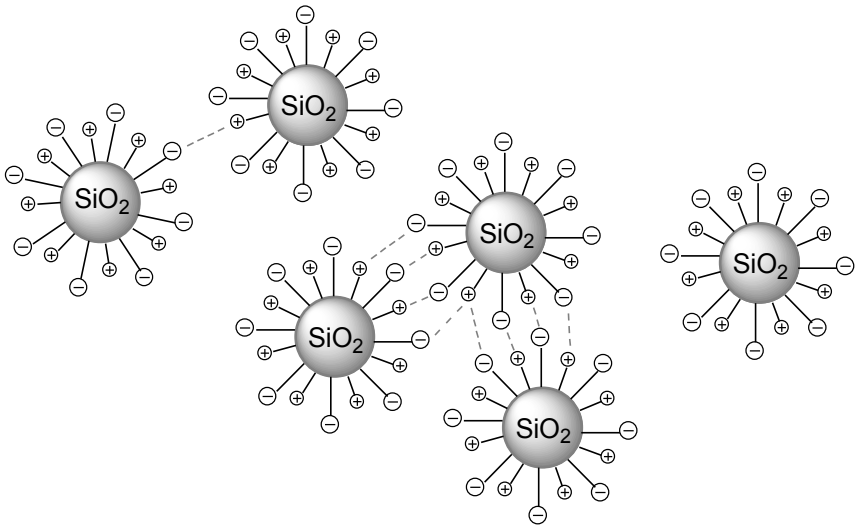

Figure 48: Interactions of opposed charges on the silica particle surface.

The DLS values in water for all acetyl protected materials **M1$_{15/50/130}$C$_3$[Gd-BA]ac** and **M1$_{15/50/130}$C$_3$[Gd-GA]ac** display a narrow monomodal size distribution. Moreover smaller agglomerates are found for the **M1$_{15}$C$_3$[Gd-BA]ac** and **M1$_{15}$C$_3$[Gd-GA]ac** silica particles compared to the non-protected amino functions. Especially the larger particles (**M1$_{50/130}$C$_3$[Gd-BA]ac** and **M1$_{50/130}$C$_3$[Gd-GA]ac**) appear to form hardly any agglomerates. Both **M1$_{15}$C$_3$[Gd-BA]ac** and **M1$_{15}$C$_3$[Gd-GA]ac** materials show size distributions of about 150 nm in water, while the small PDI index indicates an extensive consistent agglomerate size distribution. Reduced agglomeration is probably induced through neutralization of the amino groups *via* acetyl protection and therefore extensive removal of opposed charges on the particle surface. Consequently, the repulsive

interactions become stronger whereas agglomeration decreases. This observation is consistent with the interactions proposed in Figure 48.

Phosphate buffered saline is a solution which contains sodium chloride and potassium phosphate. This buffer is commonly used for the investigation of materials for medical or biological applications because the solution is consistent in its isotonicity with liquids in the human body. Due to the presence of high concentrations of ionic components, the dispersion behavior of the SNP deviates from those which were measured in water. In PBS the DLS values for the bare nanoparticles $\mathbf{M0_{50}}$ and $\mathbf{M0_{130reh}}$ result in sizes of 73 and 135 nm (d_z), respectively (Table 11). The hydrodynamic radii in PBS for all amino modified particles $\mathbf{M1_{15/50/130}C_3NH_2}$ indicate agglomerates with broadened size distributions of 728, 263 and 233 nm, respectively. In the case of $\mathbf{M1_{15}C_3NH_2}$ the suitability for DLS measurements reaches the limit of the analytical methodology owing to the very high polydispersity. All acetyl protected silica nanoparticles show a narrow size distribution (Table 11). The suspensions of $\mathbf{M1_{50/130}C_3}$**[Gd-BA]ac** and $\mathbf{M1_{50/130}C_3}$**[Gd-GA]ac** particles are highly monodisperse with smaller PDI indices in comparison to the non-acetylated particles $\mathbf{M1_{50/130}C_3}$**[Gd-BA]** and $\mathbf{M1_{50/130}C_3}$**[Gd-GA]**. The $\mathbf{M1_{15}C_3}$**[Gd-BA]ac** and $\mathbf{M1_{15}C_3}$**[Gd-GA]ac** particles form much smaller agglomerates with good PDI indices in contrary to the unprotected analogs.

In summary the acetyl protected silica nanoparticles, especially the Gd(III) modified smaller particles $\mathbf{M0_{15/50}}$ display a less or no agglomeration tendency due to their changed surface and consequently resulting charge differences. Probably the negatively charge of the used Gd(III) complexes is less compensated by the positively charged amino groups. Consequently due to stronger repulsion effects fewer agglomerates are formed.

4.2.5 Zeta Potential

The electrostatic potential at the electrical double layer (consisting of ions and counterions), which surrounds a nanoparticle in a colloidal dispersion causes the so called zeta potential (ζ). With the movement of a nanoparticle in an electric field the zeta potential arises at the shear plane. For examination of suitability for different desired applications of any naked or modified particles, the investigation of the stability of the suspension as well as the determination of the surface charge of the nanoparticles, given by the zeta potential, is necessary. Generally a high zeta potential of positive or negative

charge (<-30 mV or >+30 mV) indicates the stability of a particle suspension. Moreover the values represent an anionic (negative ζ) or cationic (positive ζ) nanoparticle surface in the respective medium.[165] The stability of particle suspensions depends among others on various factors like particle size, surface charge, interparticle interactions as well as interactions with species present in the respective solution. There are already different studies relating to amorphous silica particles.[166–169] In the following chapter the zeta potential is discussed for all silica particles at a physiological pH of 7.4 in phosphate buffered saline (PBS) and cell culture medium with 10 % serum. Furthermore, changes in the potentials by modification of the particles with Gd(III) chelate complexes as well as after functionalization with acetyl protection group was analyzed. The following zeta potentials depict an average within a monomodal distribution and in the case of multimodal distributions, the zeta potential is given as an average across all peaks and additionally for each peak (Table 12 and 13).

In PBS the bare SNPs **M0$_{50}$** and **M0$_{130reh}$** display more negative zeta potentials than the amino modified analogs with their positive charge on the surface (Table 12). The stability of the suspension of **M0$_{130reh}$** and **M0$_{50}$** particles is in accordance with the agglomeration behavior observed by DLS measurements (Table 10). Beyond that, the zeta potentials are most notably lower for the **M0$_{50}$** particles caused by additional ethoxy moieties on the surface. The Si-OH bonds of the **M0$_{130reh}$** particles are deprotonated in water and therefore contribute to more negative charges on the surface. Smaller zeta potentials were reported for silica particles of about 20 nm at pH 7.4.[170] There the ζ values of -30 and + 38 mV are obtained for unmodified and APTES modified particles, respectively. After modification of the particles **M0$_{15/50/130}$C$_3$NH$_2$** with Gd(III) complexes the zeta potential becomes again more negative based on additional negative charges of the Gd(III) complexes in both media (Table 12).

Table 12: Zeta potentials at a physiological pH of 7.4 in phosphate buffered saline (PBS) and cell culture medium with 10 % serum.

sample	ζ PBS [mV]	ζ medium+ 10 % serum [mV]	Distribution PBS/Medium
$M0_{50}$	-46.3 ± 1.1	-39.0 ± 0.3	monomodal/monomodal
$M0_{130reh}$[(1)]	-55.7 ± 1.5	-45.3 ± 0.6	monomodal/monomodal
$M1_{15}C_3NH_2$	-55.1 ± 3.89	-20.9 ± 2.23	multimodal/monomodal
$M1_{50}C_3NH_2$	-16.1 ± 1.2	-26.8 ± 4.9	monomodal/monomodal
$M1_{130}C_3NH_2$[(1)]	23.9 ± 0.8	-32.2 ± 0.4	monomodal/monomodal
$M1_{15}C_3$[Gd-BA]	-60.2 ± 2.6	-22.6 ± 11.4	monomodal/monomodal
$M1_{15}C_3$[Gd-GA]	-53.2 ± 1.5	-46.8 ± 3.1	monomodal/monomodal
$M1_{15}C_3$[Gd-GA]*	-55.3 ± 1.5	-34.4 ± 1.5	monomodal/multimodal
$M1_{50}C_3$[Gd-BA]	-34.9 ± 2.6	-43.8 ± 0.9	monomodal/monomodal
$M1_{50}C_3$[Gd-GA]	-37.5 ± 5.4	-36.0 ± 1.0	multimodal/multimodal
$M1_{50}C_3$[Gd-GA]*	-28.4± 1.5	-26.2 ± 1.7	monomodal/monomodal
$M1_{130}C_3$[Gd-BA][(1)]	-51.3 ± 1.9	- 45.7 ± 0.4	monomodal/monomodal
$M1_{130}C_3$[Gd-GA][(1)]	-55.0 ± 0.9	-48.6 ± 1.4	monomodal/monomodal
$M1_{15}C_3$[Gd-BA]ac	-41.7 ± 0.9	-39.0 ± 2.8	monomodal/monomodal
$M1_{15}C_3$[Gd-GA]ac	-40.0 ± 2.9	-37.5 ± 0.2	monomodal/monomodal
$M1_{50}C_3$[Gd-BA]ac	-44.2 ± 1.1	-38.3 ± 0.5	monomodal/monomodal
$M1_{50}C_3$[Gd-GA]ac	-43.9 ± 0.5	-36.4 ± 1.2	monomodal/monomodal
$M1_{130}C_3$[Gd-BA]ac	-55.3 ± 0.7	-48.5 ± 1.3	monomodal/monomodal
$M1_{130}C_3$[Gd-GA]ac	-56.7 ± 0.3	-46.8 ± 1.2	monomodal/monomodal

(1) [25]

In PBS values between -60.2 and -28.4 mV were measured for the Gd(III) functionalized SNPs. The zeta potential rises with increasing particle diameter, and Gd(III) modified particles form more stable suspensions than those of APTES functionalized particles.[160] In consideration of the DLS values, the stronger agglomeration and following sedimentation of smaller particles may cause lower zeta potentials. Furthermore smaller values in the range between -10 and -15 mV were reported for their Gd-DTPA (gadolinium-diethylenetriaminepenta- aceticacid)chelate complex functionalized modifications.[170] The

zeta potentials obtained from the particles **M1$_{15/50}$C$_3$NH$_2$** as well as **M1$_{15/50}$C$_3$[Gd-BA]** and **M1$_{15/50}$C$_3$[Gd-GA]**, respectively, present based on their strong agglomeration behavior, rather an average zeta value by formation of multimodal distributions or broad monomodal distributions. In medium, generally the zeta potentials are lower for all bare and modified particles than in PBS. Re-conjugated SNPs own due to a higher payload of Gd(III) complexes an increased negative charge on their surface. Interestingly, zeta measurements do not significantly display the higher negative charge. For **M1$_{15}$C$_3$[Gd-GA]*** the zeta potentials are increased in PBS compared to **M1$_{15}$C$_3$[Gd-GA]**, whereas the potential in medium is lower. A similar effect is represented by the zeta potential of **M1$_{50}$C$_3$[Gd-GA]*** particles. From this it follows that the higher occupancy with **[Gd-GA]** is not strong enough to antagonize the strong agglomeration behavior of these small particles. However the repeated conjugation of Gd(III) complex seems to improve the dispersion properties, especially for **M1$_{50}$C$_3$[Gd-GA]*** particles by forming a monomodal distribution.

After coupling the chelate complexes to SNPs free amino groups still remain on the particle surface. To investigate the strength of the interaction between the free amino groups and the environment, the zeta potentials were measured again after protecting these amino groups with acetic anhydride. In comparison to the unprotected materials the zeta potentials are reduced, but the potentials are defined by a more narrow and consistent monomodal distribution. The effects of both, higher stability and lower agglomeration, can also be noticed in the DLS values (Table 10) as well as in the relaxivities of the compounds, especially in water (Table 19 and 23).

In summary, the Gd(III) functionalized particles show very high zeta potentials under given conditions even for the smaller particles **M1$_{15/50}$C$_3$[Gd-BA]** and **M1$_{15/50}$C$_3$[Gd-GA]**, whereas the zeta potentials of the acetyl protected silica particles are lower. However, the suspensions of the acetylated particles are more stable due to a better defined particle size distribution and therefore continuously represent a more stable and defined zeta potential. Multimodal distributions change into mainly monomodal distributions with larger particle sizes and the prevention of opposed charges on the particle surfaces. For the **M1$_{15}$C$_3$[Gd-BA]** and **M1$_{15}$C$_3$[Gd-GA]** particles, respectively it is very difficult to guarantee a defined primary particle structure, because the agglomeration behavior influences more the smaller the particles are.

Table 13: Multimodal distributions of zeta potential measurements.

sample	ζ fluid	Z-Average [mV]	Peak 1 [mV]	Peak 2 [mV]
$M1_{15}C_3NH_2$	ζ_{PBS}	-55.1	-60.3 (90%)	-24.2 (10%)
$M1_{50}C_3$[Gd-GA]	$\zeta_{Med.}$	-36.0	-37.1 (87%)	-17.4 (13%)
$M1_{50}C_3$[Gd-GA]	ζ_{PBS}	-37.5	-36.7 (85%)	-6.3 (15%)

ζ_{Med}; measured zeta potential in medium+ 10% serum [mV]. ζ_{PBS}; measured zeta potential in phosphate buffered saline [mV].

4.2.6 Specific Surface Area and Porosity of the Particles

Specific surface areas (A_{BET}) and pore sizes (d_P) were determined by nitrogen adsorption isotherms by means of the Brunauer-Emmet-Teller (BET) model.[171–173] The specific surface area of the silica particles can be determined by adsorption of gas (Adsorbate) on the surface of the silica powder (Adsorbent) at a given pressure by calculating the amount of adsorbed gas on the surface. The measurements of all samples indicate the typical curves for non-porous materials type II Isotherms and mesoporous materials type IV Isotherms (after classification by IUPAC) (Figure 49). The determined A_{BET} for all samples are summarized in Table 14. After functionalization of **$M0_{50}$** with APTES to **$M1_{50}C_3NH_2$**, the surface area becomes substantially smaller (61 m^2/g). Similarly the **$M1_{15}C_3NH_2$** particles indicate a small surface area (69 m^2/g). Probably the strong agglomeration behavior provides only a small surface for the nitrogen absorption. The hystereses of the isotherms are more pronounced with decreasing particle diameters. Especially the isotherm curves of the particles **$M0_{50}$** and **$M1_{50}C_3NH_2$** show a characteristic hysteresis as reported for particles sizes < 200 nm and reflect the form of the isotherm typ IV (Figure 49). This results when capillary condensation of N_2 occurs for mesoporous materials with pore diameters between 2 - 50 nm. The BET characterization curves (typ II) of **$M1_{15}C_3NH_2$**, **$M0_{130reh}$** and **$M1_{130}C_3NH_2$** show a multilayer adsorption after reaching the monolayer adsorption and the capillary condensation at higher pressure. The pore diameters determined by BET measurements show values of 11.8 up to 27.2 nm (Table 14). These obtained pore diameters are in fact the interstices between the particles. With decreasing particle size they also become smaller, so the smallest values are obtained for **$M0_{50}$** with diameters of about 11.8 nm and the biggest interstices for **$M0_{130reh}$** with 27.2

nm. The difference in the isotherms between the materials **$M0_{50}$** and **$M0_{130reh}$** arises from the calcination of the **$M0_{130reh}$** SNPs, while the smaller particles **$M0_{50}$** were not calcinated (see chapter 4.2.1).

Table 14: Specific surface area (**A_{BET}**) and pore diameter (**d_P**) of the Stöber particles.

sample	A_{BET} [m^2/g]	d_P [nm]
$M0_{50}$	106	11.8
$M0_{130reh}$	30	27.2
$M1_{15}C_3NH_2$	69	15.7
$M1_{50}C_3NH_2$	61	16.5
$M1_{130}C_3NH_2$	26	20.6

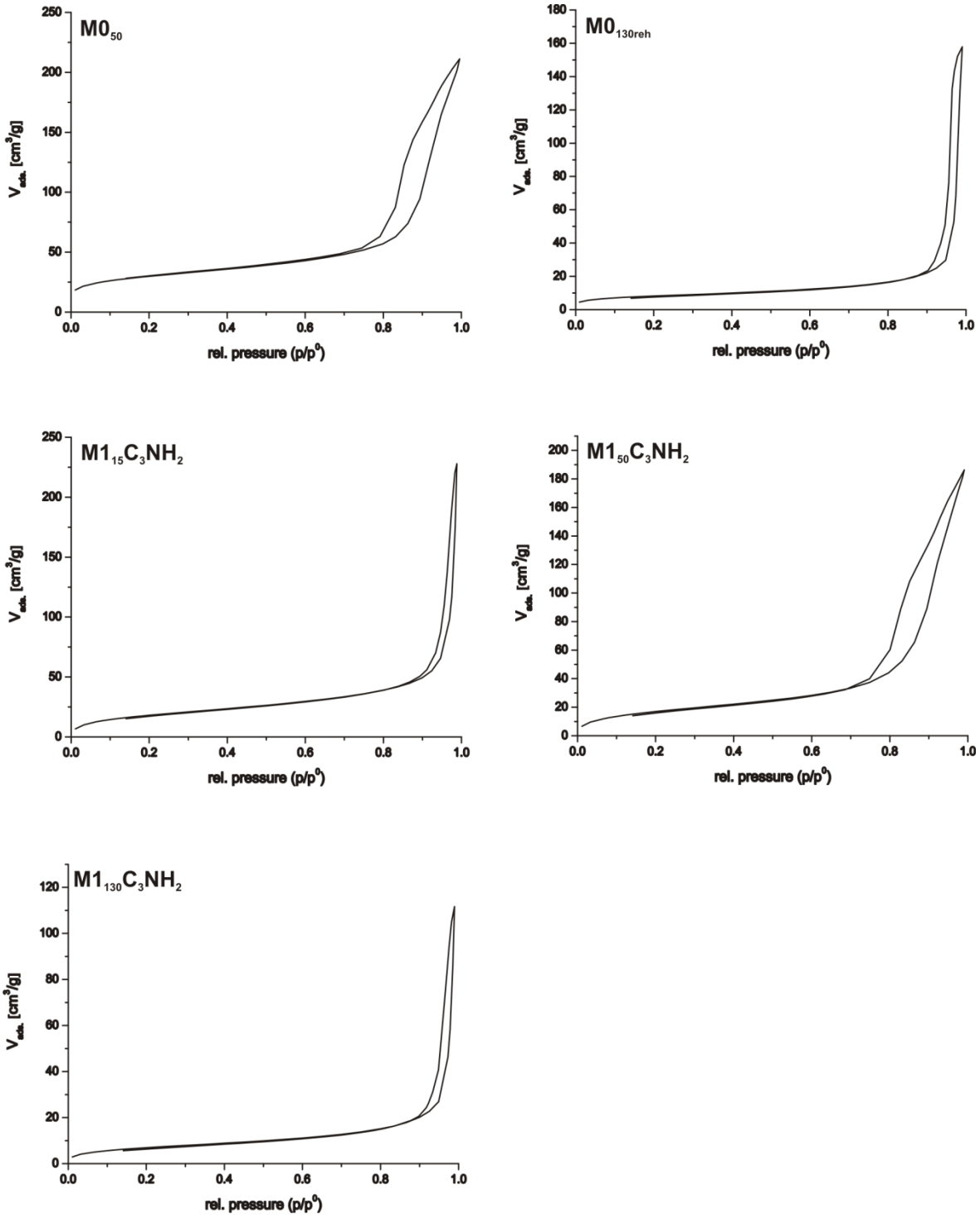

Figure 49: BET adsorption and desorption isotherms for **M0$_{50}$**, **M0$_{130reh}$** and **M1$_{15/50/130}$C$_3$NH$_2$**.

4.2.7 Surface Concentration of Coupled Molecules

The quantity of surface modifications was determined by means of elemental analysis (EA) for the amino functionalized material **$M1_{50}C_3NH_2$**. Therefore, the initial state has to be known and the amount of silanol groups on the surface of the particles (α_{OH}) has to be determined. An average value of α_{OH} = 4.9 OH functions per nm^2 has been reported.[138] The specific surface area was determined by BET measurements. To determine the quantity of the surface concentration of the coupled ligand (Γ_{Ligand}) the percentage of carbon (%C) of the respective material obtained by EA was used. The values were corrected by the percentage of carbon (%$C_{corr.}$) of the **M0** precursor. With Equation 9 (n_C = number of carbon atoms in the ligand, M_C = molecular weight of carbon) the surface concentration of the ligand (Γ_{Ligand}) can be calculated.

$$\Gamma_{Ligand} = \frac{\%C_{corr.}}{100 * n_C * M_C} \left[\frac{mol}{g}\right]$$

Equation 9

From the surface concentration, the number of coupled ligands per area (α_{Ligand}) can be determined by Equation 10, where N_A is the Avogadro constant and A_{BET} the specific surface area measured by BET.

$$\alpha_{Ligand} = (\Gamma_{Ligand} * N_A)/(A_{BET} * 10^{-21}) \left[\frac{1}{nm^2}\right]$$

Equation 10

For **$M1_{50}C_3NH_2$** the calculation yields 2.26 ligands per nm^2 and consequently a ratio of $\alpha_{Ligand}/\alpha_{OH}$ of 0.46 (Table 15). That means that 46 % of the surface silanol groups did react with aminopropyltriethoxysilane and were transformed into amino groups. In relation to the surface concentration of the silanol groups (Γ_{OH}) the surface concentration of the amino groups can be ascertained (Γ_{NH2}). Hence, with an original surface concentration α_{OH} of 862 µmol/g, the surface concentration Γ_{NH2} can be estimated to 400 µmol/g (Table 15).

In the entire calculation the coupling with the reagent is considered as a reaction with only one single silanol surface group. Actually the bond coupling can also be formed by two or rather unlikely three bonds which is not considered in the calculation.[152] Additionally, the ethoxy groups, which remain on the particle surface due to preparation conditions, are not considered in the evaluation. Therefore the calculated number should be seen more as an estimation of the surface concentration than an accurately determined number.

Table 15: Evaluation of elemental analyses based on % of carbon (%C).

	A_{BET} [m^2/g]	%C (EA)	$\%C_{corr.}$(EA)	Γ_{Ligand} [mmol/g]	α_{Ligand} [nm^{-1}]	$\alpha_{Ligand}/\alpha_{OH}$
$M1_{15}C_3NH_2$	69	5.60	n.d.			
$M0_{50}$	106.4	2.51				
$M1_{50}C_3NH_2$	106.4[(1)]	3.95	1.44	0.400	2.26	0.46
$M0_{130reh}$[(2)]	30	0.08				
$M1_{130}C_3NH_2$[(2)]		0.54	0.46	0.13	2.59	0.53

%C (EA), percentage of carbon corrected by the percentage of carbon [$\%C_{corr.}$ (EA)] of the precursor; Γ_{Ligand}, coupled ligand surface concentration.
1 following from a reversible agglomeration the BET value of the precursor **$M0_{50}$** is used for calculation.
2 [25]

4.2.8 Surface Concentration of Gadolinium

The surface concentration $\Gamma_{Gd(III)}$ of Gd(III) ions was determined with an atomic emission (ICP-AES) spectrometer. The absence of free Gd(III) ions in the samples was confirmed prior to the measurement by the xylenol test of suspended materials in water.

For the **$M1_{15}C_3NH_2$** material the coupling with [**Gd-GA**] is slightly more efficient than the coupling with [**Gd-BA**] (Table 16). In contrast to this, a higher coupling with the [**Gd-BA**] ligand is detected for both the **$M1_{50}C_3$[Gd-BA]** and **$M1_{130}C_3$[Gd-BA]** particles which is in accordance with the data from the DRIFT spectra (Figure 38, 39).

If the reaction conversion is considered for the total amount of silanol groups available on the particle surface of **$M0_{50}$**, a coverage of Gd-chelate complexes of about 7 % is achieved for **$M1_{50}C_3$[Gd-BA]** and 6 % for **$M1_{50}C_3$[Gd-GA]**. The smaller particles have even smaller values, only 4 % for **$M1_{15}C_3$[Gd-BA]** and 5 % for **$M1_{15}C_3$[Gd-GA]** in ligand coverage has been obtained. The twice with [**Gd-GA**] reacted material **$M1_{15}C_3$[Gd-GA]*** demonstrates a better coverage with 125 µmol/g Gd(III) and consequently a conversion of 12 %. A comparatively smaller increase by 71.5 µmol/g Gd(III) coverage of **$M1_{50}C_3$[Gd-GA]*** particles corresponds to a conversion of 8 % of the original silanol groups. Similar to

the 50 nm particles the connection of [**Gd-BA**] exhibits better coupling rates for the **M1$_{130}$C$_3$[Gd-DOTA]** derivatives (11 %) than for [**Gd-GA**] (4 %). If the maximum coverage by reaction of each amino function is considered, a conversion of 46 % could be achieved for the **M1$_{50}$C$_3$[Gd-DOTA]** derivatives, whereas for **M1$_{130}$C$_3$[Gd-DOTA]** derivatives a maximal coverage of 53 % could have been obtained (Table 15).

Table 16: Coupling efficacy of Gd(III) complexes to the surface of modified particles

sample	$\Gamma_{Gd(III)}$ [µmol/g]	α_{Gd}/α_{OH}	n_{Gd} per NP	$n_{Gd}/n_{Gd,geo}$ [%]
M1$_{15}$C$_3$[Gd-BA]	47.4	4	155	17
M1$_{15}$C$_3$[Gd-GA]	55.6	5	182	20
M1$_{15}$C$_3$[Gd-GA]*	125.0	12	409	45
M1$_{50}$C$_3$[Gd-BA]	63.0	7	2799	28
M1$_{50}$C$_3$[Gd-GA]	54.4	6	2417	24
M1$_{50}$C$_3$[Gd-GA]*	71.5	8	3178	32
M1$_{130}$C$_3$[Gd-BA]	27.0	11	36792	49
M1$_{130}$C$_3$[Gd-GA]	10.7	4	15023	20
M1$_{15}$C$_3$[Gd-BA]ac	47.7	-	-	-
M1$_{15}$C$_3$[Gd-GA]ac	51.8	-	-	-
M1$_{50}$C$_3$[Gd-BA]ac	59.5	-	-	-
M1$_{50}$C$_3$[Gd-GA]ac	52.2	-	-	-
M1$_{130}$C$_3$[Gd-BA]ac	26.7	-	-	-
M1$_{130}$C$_3$[Gd-GA]ac	10.8	-	-	-

$\Gamma_{Gd(III)}$, surface concentration of Gd complexes per gram NP, determined by ICP-MS.
α_{Gd}/α_{OH} percentage of coupled Gd complexes by reaction with OH surface groups.
n_{Gd} per NP, number of Gd complexes per nanoparticle.
$n_{Gd}/n_{Gd,geo}$ [%], percentage of coupled Gd complexes in the geometrical possible number of Gd complexes per NP.

If the spatial dimensions of one single Gd(III) chelate complex is considered under ideal conditions, an area of 7.9×10^{-19} m^2 can be calculated with an assumed hydrodynamic radius of 0.5 nm. Then a maximum number $n_{Gd,geo}$ of 900 Gd complexes fits on the surface of one single particle of **M0$_{15}$**. In the case of **M0$_{50}$** particles the maximal number amounts to 10000 complexes, whereas the **M0$_{130reh}$** particles can carry up to 76000 Gd(III) complexes. Table 16 depicts the amount of Gd(III) complexes per NP and also the percentage of the actual number of Gd(III) complexes in the maximal number of chelate complexes based on geometrical considerations (n_{Gd}/n_{geo}).

Pertaining the convertions to geometrical considerations, a high coverage of the surface area in the case of **M1$_{130}$C$_3$[Gd-BA]** (49 %) and of **M1$_{15}$C$_3$[Gd-GA]*** (45 %) has been achieved, whereas lower values are obtained for the single-time reacted particles (20 % and 17 %, respectively.).

After protecting the unreacted amino groups at the particle surface with acetyl groups, no significant difference in the Gd(III) concentration values is expected based on the small

mass difference of the particles. The Gd(III) concentrations are slightly decreasing for the **M1$_{15}$C$_3$[Gd-GA]** and the **M1$_{50}$[Gd-DOTA]** derivatives, whereas there is no significant change in the values for the **M1$_{15}$C$_3$[Gd-BA]** and for the **M1$_{130}$C$_3$[Gd-DOTA]** derivatives (Table 16).

4.2.9 Thermogravimetric Analysis (TGA)

The TGA measurement offers the opportunity to quantify weight loss and to investigate the process of weight loss of the material as a function of the temperature. This allows for a good way to draw conclusions about the composition of the material and its thermal behavior. In the following the TGA measurement of the 50 nm particle series **M0$_{50}$**, **M1$_{50}$C$_3$NH$_2$** and **M1$_{50}$C$_3$[Gd-BA]** is compared as representative for the rest of the materials of the **M1$_{15}$C$_3$NH$_2$** and **M0$_{130}$** series (Figure 50). The measurements were performed starting from room temperature up to 1250 °C. The determined weight losses for **M1$_{50}$C$_3$NH$_2$** and **M1$_{50}$C$_3$[Gd-BA]** are corrected by the weight losses of the **M0$_{50}$** particles (Table 17).

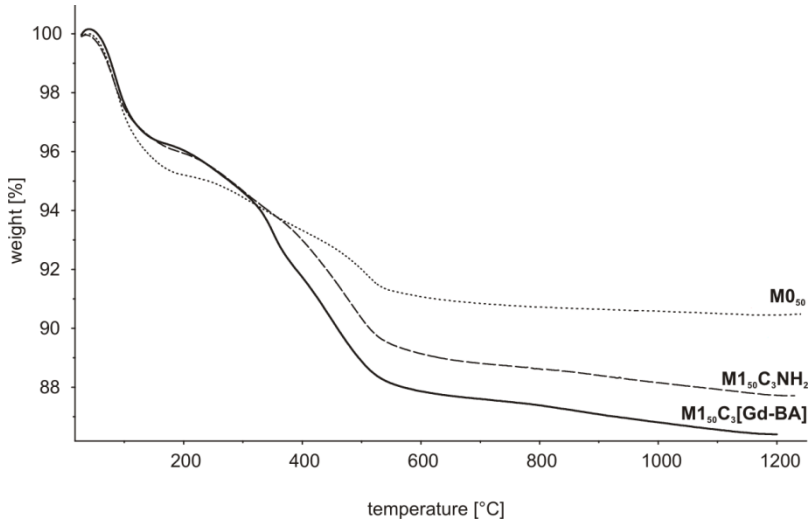

Figure 50: TGA measurements of bare **M0$_{50}$, M1$_{50}$C$_3$NH$_2$** and **M1$_{50}$C$_3$[Gd-BA]** particles.

The TG curve of M**0$_{50}$** shows the complete desorption of physically absorbed water up to 200 °C. The following weight loss until 600 °C in two stages is assigned to the loss of chemically bound water and ethanol which arises from residual ethoxy groups on the surface. Further condensation by the formation of siloxane bonds occurs. Similarly the **M1$_{50}$C$_3$NH$_2$** particles lose adsorbed water until 200 °C and in the second stage the loss of

organic moieties on the particle surface takes place (≤ 600 °C).

Table 17: Weight loss of the materials from 35-1200 °C (determined by TGA analysis).

	weight loss mass percentage (w/w)%				corrected weight loss mass percentage (w/w)%
	1.	2.	3.	total loss	
$M0_{50}$	-4.80	-2.03	-2.10	8.93	
$M1_{50}C_3NH_2$	-3.95	-2.04	-4.80	10.79	1.86
$M1_{50}C_3$[Gd-BA]	-3.87	-4.31	-4.05	12.23	1.44

Higher mass loss with further functionalization of the particle surface is demonstrated on the example of **$M1_{50}C_3$[Gd-BA]**. The trend of the curve of **$M1_{50}C_3$[Gd-BA]** describes the successful coupling with the Gd(III) complexes by a higher mass loss of organic moieties in comparison to the **$M1_{50}C_3NH_2$** precursor (Figure 50). However the resulting weight losses gained by TGA measurements are lower compared to the surface concentrations determined by ICP measurements (Table 16 and 18).[141] The reason for this based on the formation of Gadoliniumoxide, -carbonates and -oxycarbonates which seal the particle surface and disturb the measurements. The quantitative determination of surface molecules is therefore not measurable by TGA analysis for these Gd(III) chelate complex functionalized SNPs. Therefore further measurements of other particles were omitted.

Table 18: Gd(III) content determination by TGA measurements.

	m (sample)	mass %	m (Gd-BA)	n (Gd-BA)	
	[mg]	(Gd-DOTA)	[mg]	[µmol]	[µmol/g]
$M1_{50}C_3$[Gd-BA]	46.832	1.44	0.67438	0.97629	26.99

4.2.10 Relaxivities

The relaxivity (r_1 and r_2) of a contrast agent is the ability to enhance the paramagnetic longitudinal or transverse relaxation rate, which is caused by one millimolar concentration of the respective contrast agent (CA). For high relaxation the Larmor frequency of the CA molecule should be similar to the frequency of the magnetic field of a clinical scanner. One way to achieve this is the immobilization of CAs on SNPs. After immobilization the decreased tumbling rate of the CAs is closer to the Larmor frequency of the protons, increasing the efficiency of relaxation.[38] Moreover, the silica particle delivers a high payload of the Gd(III) chelate complexes in a small volume offering a high local relaxivity effect.

Further factors for the enhancement of the relaxivity are the molecular properties of the immobilized compounds. Generally there is the inner sphere and the outer sphere relaxation of water protons which contribute to the entire paramagnetic relaxation rate enhancement. The paramagnetic relaxation of the water protons arise mainly from dipol-dipol interactions between the proton nuclear spins and on the paramagnetism of Gd. The inner sphere relaxation origins from interactions between Gd(III) spins and the protons from water in the inner sphere and outer sphere relaxation arises by interaction with bulk water protons. Various parameters among others like water exchange rate and local rotational dynamics of the surface bound Gd(III) chelates influence the inner sphere relaxivity. High water exchange influences larger amounts of bulk water. Moreover, a slower local rotational correlation time τ_R by more rigid systems contributes also to high relaxivities.

The two different Gd(III) chelate complexes **[Gd-BA]** and **[Gd-GA]**, which were investigated in this work, differ in flexibility of the linker. The aromatic ring in the linker of **[Gd-BA]** introduces a rigid barrier, which has an impact on the relaxivity.[28] The relaxivities of all materials presented in this work are listed in Table 19 and visualized in Figure 51-55. The relaxation phenomena of all prepared materials strongly depend on the diameter of the particle, the Gd(III) chelates (**[Gd-BA]** vs. **[Gd-GA]**), the Gd(III) surface loading, the medium and the surface activity. Thus the immobilization of the **[Gd-GA]** to any of the silica particles leads to an increase of the relaxivity r_1 in water as well as in medium (Table 19 and Figure 51, 52).

Table 19: Longitudinal and transverse relaxivities (r_1 and r_2) of Gd(III) modified particles at 3 T and room temperature.

		relaxivity per mM Gd		
sample	fluid	r_1 [$mM^{-1}s^{-1}$]	Δr_1 [%]	r_2 [$mM^{-1}s^{-1}$]
Gd[DOTA-BA]	water	7.6 ± 0.3		10.5 ± 0.3
Gd[DOTA-GA]	water	3.9 ± 0.1		4.2 ± 0.0
$M1_{15}C_3$[Gd-BA]	water	6.9 ± 1.5	-9	44.8 ± 2.1
$M1_{15}C_3$[Gd-GA]	water	5.9 ± 1.1	51	37.3 ± 10.6
$M1_{15}C_3$[Gd-GA]*	water	7.8 ± 1.7	100	39.7 ± 9.0
$M1_{50}C_3$[Gd-BA]	water	6.1 ± 0.6	-20	37.6 ± 7.1
$M1_{50}C_3$[Gd-GA]	water	6.0 ± 1.2	54	32.1 ± 8.2
$M1_{50}C_3$[Gd-GA]* [(1)]	water	8.8 ± 1.3	126	76.7 ± 9.9
$M1_{130}C_3$[Gd-BA]	water	10.2 ± 1.2	34	41.2 ± 16.3
$M1_{130}C_3$[Gd-GA]	water	13.1 ± 2.1	236	46.2 ±0.8
$M1_{15}C_3$[Gd-BA]ac	water	9.7 ± 1.1	28	62.0 ± 11.0
$M1_{15}C_3$[Gd-GA]ac	water	10.6 ± 1.0	172	58.9 ± 18.7
$M1_{50}C_3$[Gd-BA]ac	water	8.0 ± 1.3	5	90.5 ± 15.6
$M1_{50}C_3$[Gd-GA]ac	water	7.8 ± 0.6	100	81.4 ± 2.3
$M1_{130}C_3$[Gd-BA]ac	water	11.8 ± 0.7	55	91.6 ± 1.5
$M1_{130}C_3$[Gd-GA]ac	water	14.8 ± 0.9	280	201.6 ± 152.3
Gd[DOTA-BA]	medium	4.6 ± 0.7		7.1 ± 1.4
Gd[DOTA-GA]	medium	3.0 ± 0.1		3.9 ± 0.5
$M1_{15}C_3$[Gd-BA]	medium	7.2 ± 1.7	57	47.0 ± 12.2
$M1_{15}C_3$[Gd-GA]	medium	6.2 ± 2.0	107	25.2 ± 0.8
$M1_{15}C_3$[Gd-GA]*	medium	8.6 ± 1.8	187	23.4 ± 6.9
$M1_{50}C_3$[Gd-BA]	medium	6.3 ± 1.0	37	31.7 ± 7.0
$M1_{50}C_3$[Gd-GA]	medium	7.7 ± 2.8	157	27.8 ± 4.0
$M1_{50}C_3$[Gd-GA]*[(1)]	medium	5.6 ± 0.1	87	64.7 ± 11.0
$M1_{130}C_3$[Gd-BA]	medium	8.0 ± 1.3	74	22.5 ± 11.7
$M1_{130}C_3$[Gd-GA]	medium	11.7 ± 0.6	290	27.0 ± 2.85
$M1_{15}C_3$[Gd-BA]ac	medium	9.5 ± 0.6	107	50.8 ± 7.4
$M1_{15}C_3$[Gd-GA]ac	medium	9.3 ± 1.4	210	44.8 ± 10.2
$M1_{50}C_3$[Gd-BA]ac	medium	6.7 ± 0.2	47	68.5 ± 7.4
$M1_{50}C_3$[Gd-GA]ac	medium	7.8 ± 0.3	160	65.7 ± 33.8
$M1_{130}C_3$[Gd-BA]ac	medium	10.8 ± 0.9	135	86.18 ± 7.3
$M1_{130}C_3$[Gd-GA]ac	medium	12.1 ± 3.3	303	123.8 ± 41.1

Values represent mean ± SD. For comparison the relaxivities of the two Gd complexes, **Gd[DOTA-BA]** and **Gd[DOTA-GA]**, used for coupling to the nanoparticles are given for both solvent systems. Δr_1 values for the nanomaterials are given in respect to the longitudinal relaxivities of the corresponding free complexes.

[1] different batch of particles **$M1_{50}C_3$[Gd-GA]** ($\Gamma_{Gd(III)}$ = 52.8 µmol/g) doubly reacted with **[Gd-GA]** (resulting in $\Gamma_{Gd(III)}$ = 71.5 µmol/g).

Interestingly, in the case of **[Gd-BA]** an increase in water is only observed for the **$M1_{130}C_3$[Gd-BA]** particles as well as for all acetylated materials (Table 19 and Figure 51). For the smaller particles (**$M1_{15}C_3$[Gd-BA]** and **$M1_{50}C_3$[Gd-BA]**) a decrease in relaxivity is detected. Obviously, the more rigid linker in **[Gd-BA]** allows for a better interparticle interaction, which leads to agglomerates in water and hinders the access of water molecules to the Gd center. This agrees with the increase in relaxivity after protection of the residual amino groups on the silica surface as well as in medium where additional ions hinder the interparticle interactions. This is also consistent with observations made by DLS and SEM studies (Table 10, Figure 45, 46).

Thus compared to the free complexes in medium, both of the materials present an increase in their relaxivities by 57 % in the case of **$M1_{15}C_3$[Gd-BA]** (r_1 = 7.2 $mM^{-1}s^{-1}$) and 107 % in the case of **$M1_{15}C_3$[Gd-GA]** (r_1 = 6.2 $mM^{-1}s^{-1}$) (Table 19 and Figure 52).

The growth in the payload of Gd(III) chelate complexes on the surface of **$M1_{15}C_3$[Gd-GA]*** and **$M1_{50}C_3$[Gd-GA]*** leads to an increase in relaxivity which is less pronounced in medium (Table 19 and Figure 52). The higher coverage with Gd(III) complexes may result in hindered local rotation of the complexes, as well as heightened negative charges on the surface. Therefore less agglomeration and a better water exchange lead to an increase of the r_1 values. Simultaneously the remaining agglomeration of the particles probably antagonizes a possibly even higher relaxivity value. In comparison to material **$M1_{15}C_3$[Gd-GA]** the relaxivity of **$M1_{15}C_3$[Gd-GA]*** is nearly twofoldly increased in water. In medium the relaxivity of **$M1_{15}C_3$[Gd-GA]*** (r_1 = 8.6 $mM^{-1}s^{-1}$) increases by 187 %, whereas residual surface functions might interact with the ions in medium. The absolute value for the longitudinal relaxivity of the **$M1_{15}C_3$[Gd-GA]*** particles shows no significant differences between water and medium. Compared to **$M1_{15}C_3$[Gd-GA]** the relaxivity of **$M1_{15}C_3$[Gd-GA]*** is enhanced by 75 % concomitant with the higher surface loading of 125 % (Table 19).

The longitudinal relaxivities of **$M1_{50}C_3$[Gd-BA]** in water (r_1 = 6.1 $mM^{-1}s^{-1}$) indicate a debilitating effect by -20 % in comparison to the free Gd(III) chelate. The **$M1_{50}C_3$[Gd-GA]** particles (r_1 = 6.0 $mM^{-1}s^{-1}$) demonstrate a relaxivity similar to the smaller **$M1_{15}C_3$[Gd-GA]** particles (+54 % compared to the free chelate).

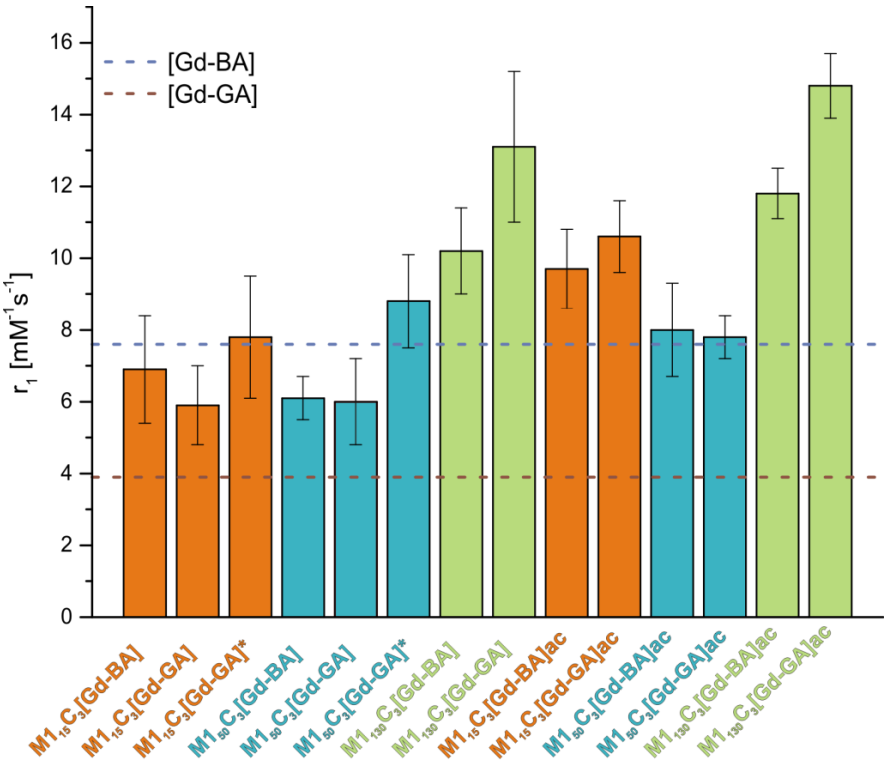

Figure 51: Longitudinal relaxivities (r_1) of Gd(III) modified particles in water.

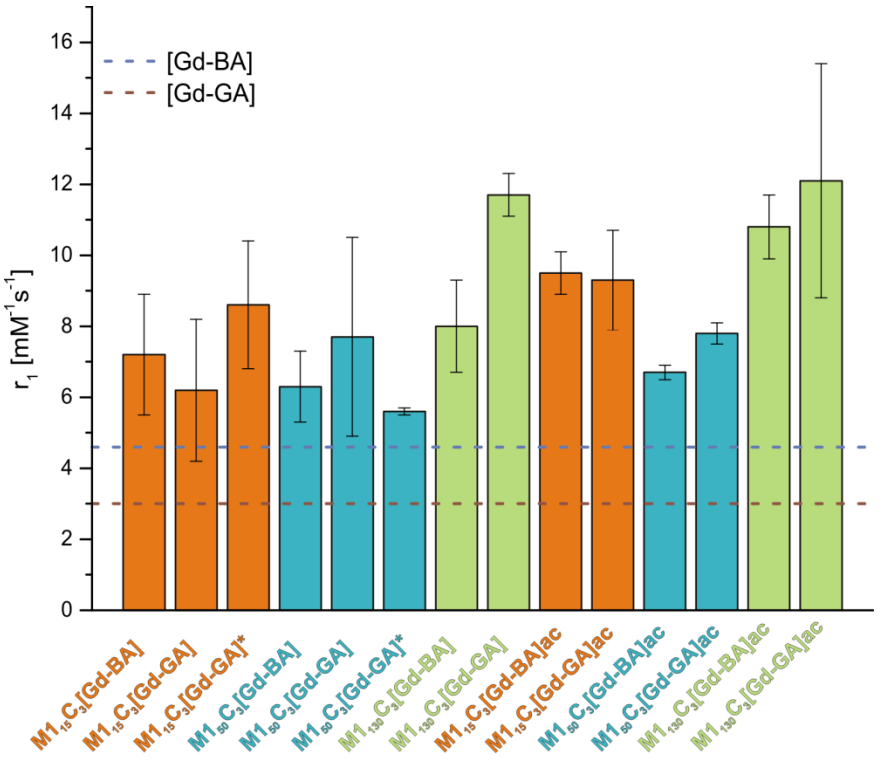

Figure 52: Longitudinal relaxivities (r_1) of Gd(III) modified particles in medium.

Due to the reasons discussed above the relaxivity decreasing effect for **M1$_{50}$C$_3$[Gd-BA]** (r_1 = 6.3 $mM^{-1}s^{-1}$) disappears in medium (+37 %), while a further increase for **M1$_{50}$C$_3$[Gd-GA]** (r_1 = 7.7 $mM^{-1}s^{-1}$) by 157 % compared to the single Gd(III) complex is obtained (Table 19 and Figure 52). The material with the higher payload **M1$_{50}$C$_3$[Gd-GA]*** shows less high relaxivities (+87 %) in medium. This effect is consistent with the lower zeta potential compared to **M1$_{50}$C$_3$[Gd-GA]** (Table 12). Interestingly, the relaxivity in water is higher for **M1$_{50}$C$_3$[Gd-GA]*** than for **M1$_{50}$C$_3$[Gd-GA]** particles, probably based on better dispersion (Table 10) and can also be noticed in the zeta values which are lower compared to **M1$_{50}$C$_3$[Gd-GA]** but show a monomodal distribution with smaller standard deviation (Table 12).

The highest relaxivities are obtained for the **M1$_{130}$** samples, especially the **M1$_{130}$C$_3$[Gd-GA]** material (r_1 = 13.1 $mM^{-1}s^{-1}$) which show an increase by 236 % in water (Table 19 and Figure 51). For **M1$_{130}$C$_3$[Gd-BA]** (r_1 = 10.2 $mM^{-1}s^{-1}$) the effect with 34 % is not as high as for the **[Gd-GA]** analog. In agreement with the smaller particles the relaxivities become higher in medium compared to the respective free Gd(III) complexes with a gain of relaxivity for **M1$_{130}$C$_3$[Gd-BA]** (r_1 = 8.0 $mM^{-1}s^{-1}$) of 74 % and for **M1$_{130}$C$_3$[Gd-GA]** (r_1 = 11.7 $mM^{-1}s^{-1}$) of 290 %.

For studying the influence of the residual amino functions on the surface on the relaxivity each sample was treated with acetic anhydride to protect the amino groups. In water the attenuation of the longitudinal relaxivity of **M1$_{15}$C$_3$[Gd-BA]** is inhibited with an enhancement for **M1$_{15}$C$_3$[Gd-BA]ac** (r_1 = 9.7 $mM^{-1}s^{-1}$) by 28 % (Figure 19 and Figure 51). The relaxivity is higher for **M1$_{15}$C$_3$[Gd-GA]ac** (r_1 = 10.6 $mM^{-1}s^{-1}$) by 172 % which in comparison with the **M1$_{15}$C$_3$[Gd-GA]** particles (+51 %) is more than threefold of the enhancement effect (Table 19). In comparison to the particles **M1$_{15}$C$_3$[Gd-GA]***, nearly a double enhancement for **M1$_{15}$C$_3$[Gd-GA]ac** in relation to the single Gd(III) complex is detected for r_1. The relative enhancement of r_1 of the acetyl protected materials in relation to the corresponding unprotected materials displays a size dependency, which is in accordance with the agglomeration tendency (Table 20). Therefore the relative enhancement achieved by the protection of the amino groups becomes most apparent for the smallest particles **M1$_{15}$C$_3$[Gd-DOTA]ac** (**Gd-DOTA = [Gd-BA]** and **[Gd-GA]**). By protecting the amino functions, the positive charge of those by protonation is abolished and less interaction occurs with the negative charge of the Gd(III) chelate complexes. This may

be the reason for less agglomeration of the small particles in water (Table 10). The effect is similar for **M1$_{50}$C$_3$[DOTA]ac**.

The decreasing effect in the r_1 value for **M1$_{50}$C$_3$[Gd-BA]** in comparison to the free Gd(III) complex vanishes and **M1$_{50}$C$_3$[Gd-BA]ac** (r_1 = 8.0 $mM^{-1}s^{-1}$) undergoes a gain by 31 %, alike for the **M1$_{50}$C$_3$[Gd-GA]ac** particles (r_1= 7.8 $mM^{-1}s^{-1}$) by 31 % (Table 20).
The positive effect of the amino protection of **M1$_{130}$C$_3$[DOTA]ac** is not as strong as for the smaller particles, which is most likely due to the already less agglomeration (Table 10). The relaxivity of the **M1$_{130}$C$_3$[Gd-BA]ac** material (r_1 = 11.8 $mM^{-1}s^{-1}$) increases by 16 % while **M1$_{130}$C$_3$[Gd-GA]ac** (r_1 = 14.8 $mM^{-1}s^{-1}$) indicates an additional gain of 13 %. Furthermore a higher relaxivity by a probably faster water exchange rate by protection of the $–NH_2$ groups is achieved.[40]

Table 20: Enhancement of r_1 of acetyl protected materials in water in relation to the correspondent unprotected materials.

	relaxivity enhancement per mM Gd in water
sample	$\Delta\Delta r_1$ [%]
M1$_{15}$C$_3$[Gd-BA]ac	41
M1$_{15}$C$_3$[Gd-GA]ac	80
M1$_{50}$C$_3$[Gd-BA]ac	31
M1$_{50}$C$_3$[Gd-GA]ac	30
M1$_{130}$C$_3$[Gd-BA]ac	16
M1$_{130}$C$_3$[Gd-GA]ac	13

$\Delta\Delta r_1$ [%] values for the nanomaterials are given in respect to the longitudinal relaxivities of the corresponding unprotected complexes.

In medium each of the unprotected samples holds nearly the same absolute value for r_1 as in water (Table 19). Each of the acetyl group protected materials show the same effect and exhibit nearly the same absolute values for r_1 in water and in medium. Interestingly, the relaxivities in medium are enhanced for the acetyl protected materials compared to the unprotected materials (Figure 52). The increase is strongest for **M1$_{15}$C$_3$[BA]ac** and **M1$_{15}$C$_3$[GA]ac** (Table 19). Presumably the small particles own larger amounts of residual amino groups on the surface, therefore their protection causes more significant changes compared to the larger particles. While the materials **M1$_{15}$C$_3$[Gd-BA]ac** (r_1 = 9.5 $mM^{-1}s^{-1}$) and **M1$_{15}$C$_3$[Gd-GA]ac** (r_1 = 9.3 $mM^{-1}s^{-1}$) show an enhancement by 32 % and 50 %, the gain for **M1$_{50}$C$_3$[Gd-BA]ac** (r_1 = 6.7 $mM^{-1}s^{-1}$) and **M1$_{50}$C3[Gd-BA]ac** (r_1 = 7.8 $mM^{-1}s^{-1}$) with 6 % and 1 %, respectively, is less pronounced (Table 21). For **M1$_{130}$C$_3$[Gd-BA]ac** (r_1 = 10.8 $mM^{-1}s^{-1}$) a stronger increase by 35 % and for **M1$_{130}$C$_3$[Gd-GA]ac** (r_1 = 12.1 $mM^{-1}s^{-1}$) a slight increase by 3 % is obtained. In general the effect of the protection of the

materials is not as strong as in water due to the higher ion concentration. The strongest enhancement is obtained for **$M1_{15}C_3$[Gd-DOTA]ac** materials, similar to those obtained in water (Table 20). Except for **$M1_{130}C_3$[Gd-BA]ac** the values before and after protection are nearly the same for **$M1_{130}C_3$[Gd-GA]ac**, **$M1_{50}C_3$[Gd-BA]ac** and **$M1_{50}C_3$[Gd-GA]ac** materials, probably based on already reduced agglomeration and perturbing interactions (Table 21).

Table 21: Enhancement of r_1 of acetyl protected materials in medium in relation to the correspondent unprotected materials.

	relaxivity enhancement per mM Gd in medium
sample	$\Delta\Delta r_1$ [%]
$M1_{15}C_3$[Gd-BA]ac	32
$M1_{15}C_3$[Gd-GA]ac	50
$M1_{50}C_3$[Gd-BA]ac	6
$M1_{50}C_3$[Gd-GA]ac	1
$M1_{130}C_3$[Gd-BA]ac	35
$M1_{130}C_3$[Gd-GA]ac	3

$\Delta\Delta r_1$ [%] values for the nanomaterials are given in respect to the longitudinal relaxivities of the corresponding unprotected complexes.

The transverse relaxivities r_2 for all materials are significantly increased in ascending order with bigger particle size, compared to the corresponding single complex in water and medium, respectively (Table 19, 22). A longer rotational correlation time τ_R by immobilization of the Gd(III) complexes on the particle surface leads to a sharp increase of the transverse relaxivities r_2. After protection with the acetyl group a further heightening of the r_2 relaxivities is observed both in water and in medium (Table 19, 22 and Figure 53, 54).

Table 22: Enhancement of transverse relaxivities r_2 in water and medium after protection with the acetyl group.

	relaxivity enhancement per mM Gd	
	in water	in medium
sample	$\Delta\Delta r_2$ [%]	$\Delta\Delta r_2$ [%]
$M1_{15}C_3$[Gd-BA]ac	38	8
$M1_{15}C_3$[Gd-GA]ac	58	78
$M1_{50}C_3$[Gd-BA]ac	141	116
$M1_{50}C_3$[Gd-GA]ac	154	136
$M1_{130}C_3$[Gd-BA]ac	122	283
$M1_{130}C_3$[Gd-GA]ac	336	359

$\Delta\Delta r_2$ [%] values for the nanomaterials are given in respect to the transverse relaxivities of the corresponding unprotected complexes.

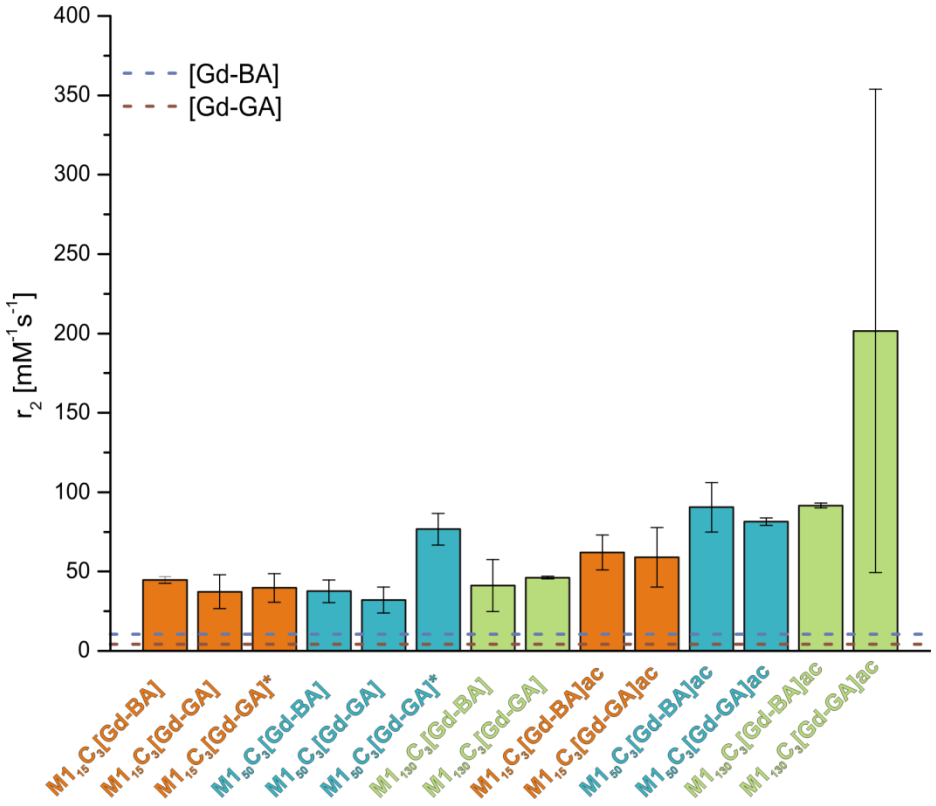

Figure 53: Transverse relaxivities (r_2) of Gd(III) modified particles in water.

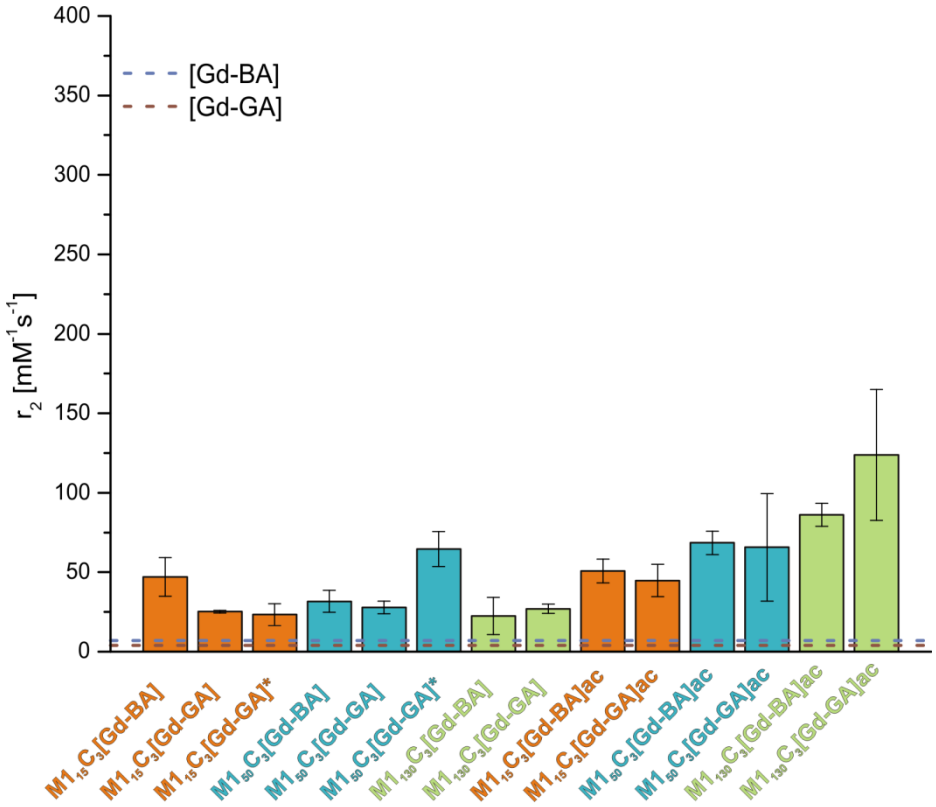

Figure 54: Transverse relaxivities (r_2) of Gd(III) modified particles in medium.

The increase of r_2 is stronger the bigger the particles are, sequentially with a maximum for the **$M1_{130}C_3$[Gd-BA]ac** and **$M1_{130}C_3$[Gd-GA]ac** particles (Table 22). After protection the values of r_2 for all **$M1_{15/50/130}$[Gd-GA]ac** functionalized particles are higher than for the **$M1_{15/50/130}$ [Gd-BA]ac** modified SNPs in relation to the corresponding single complex. Most likely the interaction of the more flexible linker **[Gd-GA]** is more affected by protecting the amino groups. If the effect of heightening of r_2 by acetyl protection is considered for both media, especially for **$M1_{130}C_3$[Gd-BA]ac** and **$M1_{130}C_3$[Gd-GA]ac** the influence in medium seems to be stronger (+283 % and +359 %) (Table 19). In contrast regarding the influence of acetylation for the smaller particles, despite **$M1_{15}C_3$[Gd-GA]ac**, r_2 is more enhanced in water.

The longitudinal and transverse relaxivities (r_1 and r_2) of Gd(III) per NP are summarized in Table 23. The longitudinal relaxivities r_1 per particle are higher the larger the particles are, due to a larger surface area per particle and consequently larger amounts of chelate complexes on the surface (Table 23). So the highest values in water are obtained for **$M1_{130}C_3$[Gd-BA]** ($r_1 = 4.21\times10^5$ $mM^{-1}s^{-1}$) and for **$M1_{130}C_3$[Gd-GA]** ($r_1 = 1.95\times10^5$ $mM^{-1}s^{-1}$). Due to reasons discussed above further heightening of the longitudinal relaxivities for all samples after protection delivers the highest values for **$M1_{130}C_3$[Gd-BA]ac** and **$M1_{130}C_3$[Gd-GA]ac** of 4.89×10^5 $mM^{-1}s^{-1}$ and 2.21×10^5 $mM^{-1}s^{-1}$ per mM NP, respectively. In medium the longitudinal relaxivities are higher for the unprotected materials than in water. For the protected analogs values up to 4.49×10^5 $mM^{-1}s^{-1}$ for **$M1_{130}C_3$[Gd-BA]ac** are obtained and r_1 is decreased in comparison to water.

In summary each of the samples indicate higher longitudinal relaxivities in medium compared to the respective free Gd(III) complex, **[Gd-BA]** or **[Gd-GA]**. The total relaxivity of the smaller particles results from the average of the directly opposed effects of the higher surface coverage and the extent to agglomerate. Agglomeration attenuates r_1 of these particles through smaller accessible surface areas and thus hindered water access. If the absolute values of relaxivities of all particle sizes are compared between water and medium there is no remarkable difference observed. However, if the relaxivities are compared to the respective single complex, the gain in relaxivity is higher for measurements in medium. Interestingly a reverse effect is shown for Gd-DO3A-hexylamine (M_xC_n[Gd-HA]) modified particles.[141] Hence the ligand systems **[Gd-BA]**

Table 23: Longitudinal and transverse relaxivities (r_1 and r_2) of Gd(III) per NP of modified particles at 3 T and room temperature.

			relaxivity per mM NP	
sample	fluid	number Gd per NP	r_1 [$mM^{-1}s^{-1}$]	r_2 [$mM^{-1}s^{-1}$]
$M1_{15}C_3$[Gd-BA]	water	155	1.07×10^3	6.98×10^3
$M1_{15}C_3$[Gd-GA]	water	182	9.72×10^2	6.57×10^3
$M1_{15}C_3$[Gd-GA]*	water	409	3.20×10^3	1.62×10^4
$M1_{50}C_3$[Gd-BA]	water	2799	1.66×10^4	1.02×10^5
$M1_{50}C_3$[Gd-GA]	water	2417	1.43×10^4	7.59×10^4
$M1_{50}C_3$[Gd-GA]*	water	3178	2.80×10^4	2.44×10^5
$M1_{130}C_3$[Gd-BA]	water	36792	4.21×10^5	1.70×10^6
$M1_{130}C_3$[Gd-GA]	water	15023	1.95×10^5	6.87×10^5
$M1_{15}C_3$[Gd-BA]ac	water	155	1.51×10^3	9.46×10^3
$M1_{15}C_3$[Gd-GA]ac	water	182	1.86×10^3	1.04×10^4
$M1_{50}C_3$[Gd-BA]ac	water	2799	2.16×10^4	2.46×10^5
$M1_{50}C_3$[Gd-GA]ac	water	2417	1.85×10^4	1.93×10^5
$M1_{130}C_3$[Gd-BA]ac	water	36792	4.89×10^5	3.80×10^6
$M1_{130}C_3$[Gd-GA]ac	water	15023	2.21×10^5	3.00×10^6
$M1_{15}C_3$[Gd-BA]	medium	155	1.12×10^3	7.30×10^3
$M1_{15}C_3$[Gd-GA]	medium	182	1.10×10^3	4.43×10^3
$M1_{15}C_3$[Gd-GA]*	medium	409	3.50×10^3	9.56×10^3
$M1_{50}C_3$[Gd-BA]	medium	2799	1.72×10^4	8.61×10^4
$M1_{50}C_3$[Gd-GA]	medium	2417	1.82×10^4	6.58×10^4
$M1_{50}C_3$[Gd-GA]*	medium	3178	1.88×10^4	2.06×10^5
$M1_{130}C_3$[Gd-BA]	medium	36792	3.30×10^5	9.33×10^5
$M1_{130}C_3$[Gd-GA]	medium	15023	1.74×10^5	4.02×10^5
$M1_{15}C_3$[Gd-BA]ac	medium	155	1.48×10^3	7.91×10^3
$M1_{15}C_3$[Gd-GA]ac	medium	182	1.64×10^3	7.88×10^3
$M1_{50}C_3$[Gd-BA]ac	medium	2799	1.83×10^4	1.86×10^5
$M1_{50}C_3$[Gd-GA]ac	medium	2417	1.85×10^4	1.56×10^5
$M1_{130}C_3$[Gd-BA]ac	medium	36792	4.49×10^5	3.57×10^6
$M1_{130}C_3$[Gd-GA]ac	medium	15023	1.80×10^5	1.84×10^6

and **[Gd-GA]** seems to be more suitable as CAs. Furthermore, in contrast to former works with silsesquioxanes a higher relaxivitiy of the more rigid system **[Gd-BA]** after attachment to the SNPs could not be observed. Probably the huge mass of the SNPs surpresses the rigidity difference between the complexes **[Gd-BA]** and **[Gd-GA]**.

Interestingly, the twofold reacted materials **$M1_{15}C_3$[Gd-GA]*** and **$M1_{50}C_3$[Gd-GA]*** exhibit a noteworthy higher surface concentration, hence the agglomeration behavior may reduce the effect of relaxivity. Despite the smaller particles of the **$M1_{50}$** and **$M1_{15}$** series obtaining higher Gd(III) surface loadings, the expected positive effect of higher concentrations of Gd related to the amount of substance (Gd/g) could not be observed as for the larger particles of the **$M1_{130}$** series.

In water all acetyl protected materials show a much higher difference in longitudinal relaxivities relative to the single complex due to charge changes on the surface and abating interactions between positively charged amino groups and negatively charged Gd(III) complexes and hence prevention of agglomeration. Consequentially, the gain of relaxivity is maximized for **$M1_{15}C_3$[Gd-BA]ac** and **$M1_{15}C_3$[Gd-GA]ac** particles and least for the **$M1_{130}C_3$[Gd-BA]ac** and **$M1_{130}C_3$[Gd-GA]ac** materials. In medium the interaction of present ions with amino groups already manipulates the interaction between the opposed charged groups on the particle surface. Therefore protection of the amino groups in medium has not such a high influence as in water. The difference is especially apparent in the case of the **$M1_{15}C_3$[BA]ac** and **$M1_{15}C_3$[GA]ac** modified particles, where this may depend on the larger amount of amino groups on their surface. Thus a further gain of relaxivity arises by protection of the amino groups.

The determined values among all SNPs show the highest efficiency in relaxivity for the **$M1_{130}$** series. The determined relaxivities emphasize the much stronger sensitivity of the smaller particles of the **$M1_{15}$** and **$M1_{50}$** series in dependency of the medium, the bound complex and the surface charges. Conversely, for the larger particles of the **$M1_{130}$** series, the influence of the molecular properties of the immobilized compounds and the surface charge have less influence on the resulting relaxivity.

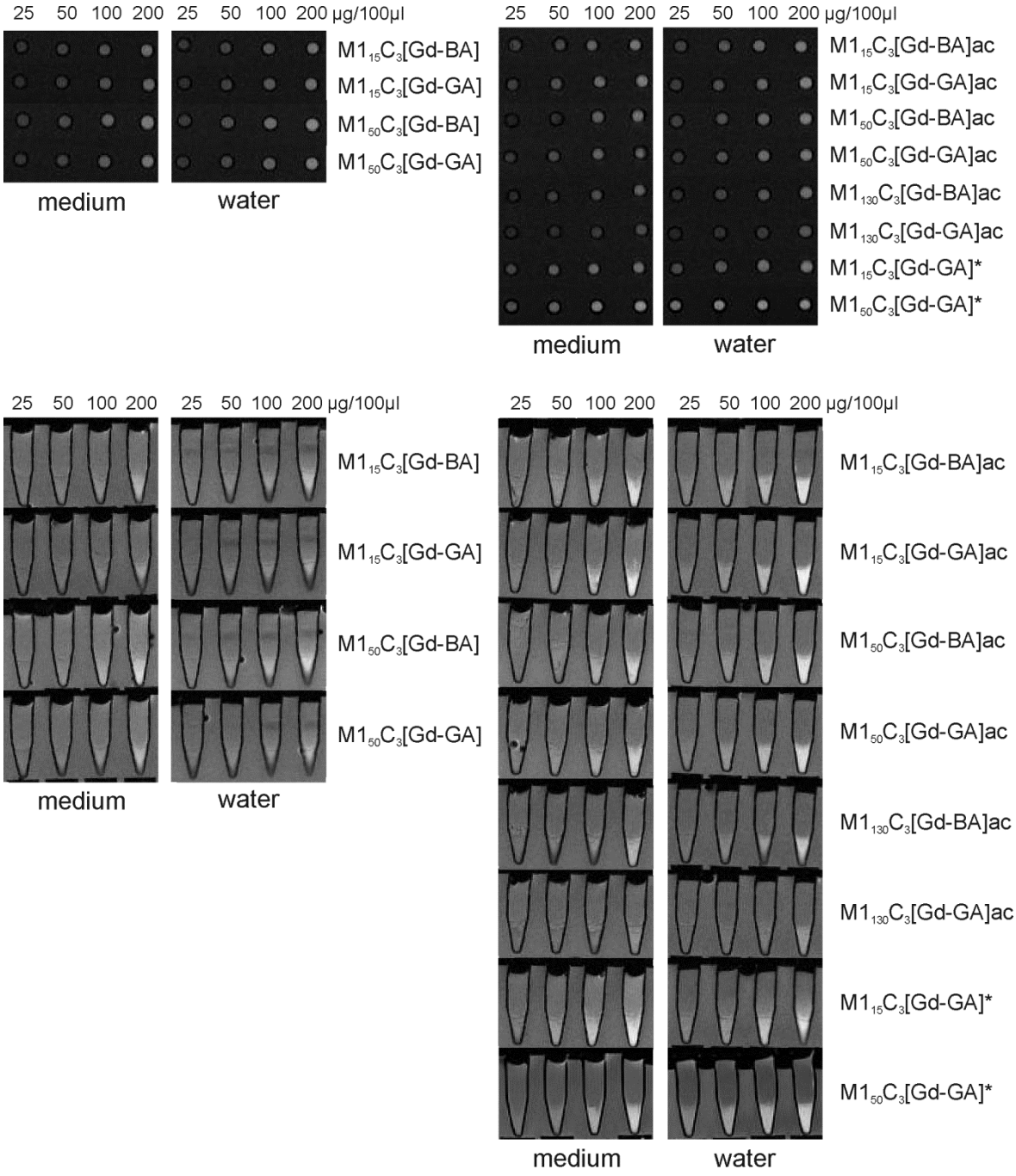

Figure 55: Sagittal and axial T_1-weighted MR images of **M1$_{15/50/130}$C$_3$[Gd-BA]** and **M1$_{15/50/130}$C$_3$[Gd-GA]** particles, as well as twice with **[Gd-GA]** reacted materials **M1$_{15}$C$_3$[Gd-GA]*** and **M1$_{50}$C$_3$[Gd-GA]***. Given concentrations are µg SNPs per 100 µl agar solution.

4.2.11 Stability Test

For *in vivo* application the stability of Gd(III) complex based CAs is very important with respect to their release of toxic Gd(III) ions. Since the Gd(III) loadings of the re-conjugated SNPs **M1$_{15}$C$_3$[Gd-GA]*** and **M1$_{50}$C$_3$[Gd-GA]*** are remarkably high, their stability against leaching was investigated. Therefore the materials were stirred in PBS (pH 7.4) in Eppendorf vials at 37 °C over a period of time from 0.5 h to 72 h. Each of the samples was tested after stirring for free Gd(III) ions (by the xylenol test) and the potential cleavage of complete Gd(III) complexes from the silica surface by relaxometry measurements of the SNPs in agar phantoms and the corresponding supernatants.

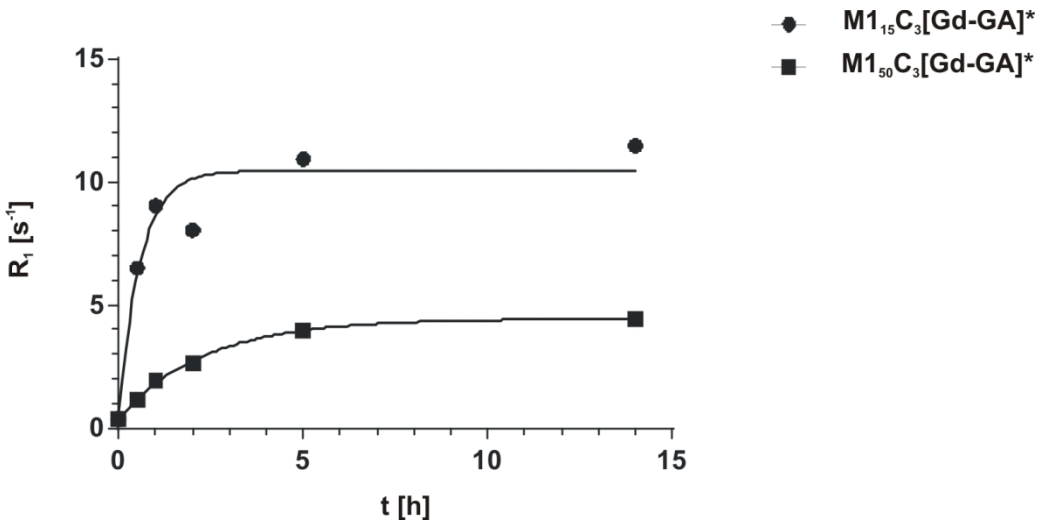

Figure 56: Leaching curves with increasing proportion of released ligands in supernatants from **M1$_{15}$C$_3$[Gd-GA]*** and **M1$_{50}$C$_3$[Gd-GA]*** particle suspensions.

For each of the materials the xylenol test was negative even after 72 h, demonstrating that no release of Gd(III) from the macrocycle takes place under the chosen conditions. However, for the first period from 0.5 h to 14 h changes of the longitudinal relaxation rate (R_1) were found for the SNPs, as well as in the supernatant (Table 24). For extended leaching periods (24 h to 72 h) a further considerably slower change in the values was detected (data not shown). It can be assumed that a significantly decelerated hydrolysis of the complexes causes further changes in the values. The measurements show an initial fast leaching of chelate complexes from the silica surface of the SNPs (Table 24, Figure 56). Interestingly, this phenomenon occurs for both materials only down to 80 % of the original R_1 values of the SNPs. After that, R_1 remains rather stable (Table 24). Similarily, the

observed R_1 values of the corresponding supernatants reach a plateau for both types of SNPs, though at very different levels (Figure 57). However, the rate of reaching this plateau seems to depend strongly on the particle size, being much faster for the material with smaller size, **M1$_{15}$C$_3$[Gd-GA]***.

Table 24: Relaxation rate (R_1) measurements of leaching samples **M1$_{15}$C$_3$[Gd-GA]*** and **M1$_{50}$C$_3$[Gd-GA]*** after stirring in PBS (pH 7.4, 37 °C).

sample	time of exposure [h]	Particle R_1 [% t_0]	Supernatant R_1 [1/s]
M1$_{15}$C$_3$[Gd-GA]*			
R_{1,t_0} = 1.298	0	100	0.366
(100 µg/100µL,	0.5	91	6.497
99.84 µM)	1	86	9.029
R_{1,t_0} = 1.757	2	79	8.049
(200 µg/100µL,	5	81	10.927
199.68 µM)	14	79	11.474
M1$_{50}$C$_3$[Gd-GA]*			
R_{1,t_0} = 1.406	0	100	0.366
(100 µg/100µL,	0.5	104	1.166
94.75 µM)	1	99	1.934
R_{1,t_0} = 2.107	2	102	2.655
(200 µg/100µL,	5	102	3.947
189.50 µM)	14	82	4.445

New synthesized batches of **M1$_{15}$C$_3$[Gd-GA]*** and **M1$_{50}$C$_3$[Gd-GA]*** for leaching experiments. Relaxivities measured in agar phantoms.

Furthermore, the supernantants of the leaching samples were analysed by mass spectrometry to identify the molecular species that is cleaved from the SNPs. Each supernatant of the samples listed in Table 24 shows a peak at -749 m/z with a characteristic isotope pattern for Gadolinium, which can be assigned to the cleavage product **(OH)$_3$SiC$_3$[Gd-GA]$^-$** with one silica unit. No peaks that could be assigned to uncomplexed ligand could be detected further confirming the stable complexation of Gd(III) (data not shown). Thus no elevated toxicity is expected due to free Gd(III) as well as to the cleaved off complex, because this small molecule should be quickly excreted *via* the kidneys.

The found main hydrolysis product **$(OH)_3SiC_3$[Gd-GA]$^-$** correlates well with the leaching behavior observed by relaxometry. For both materials, the initial fast hydrolysis takes place mainly at chelate complexes linked *via* only one siloxane function bound to the surface of the silica core. The quantity of this type of surface bound complexes is most likely higher for **$M1_{15}C_3$[Gd-GA]*** particles than for **$M1_{50}C_3$[Gd-GA]*** due to their smaller size and less spherical shape. In silanisation reactions the alkoxysilanes react with the SNP surfaces by forming mainly one or two, rarely three siloxane bonds. In addition, the size and shape of **$M1_{15}C_3$[Gd-GA]*** particles result in a larger attackable surface area. Because the hydrolysis rate correlates with the level of crosslinking of the siloxane to the SNP surface the initial hydrolysis slows down after the release of these singly connected ligands. Hence, further leaching times from 24 to 72 h generate only minor changes in the determined R_1 values.

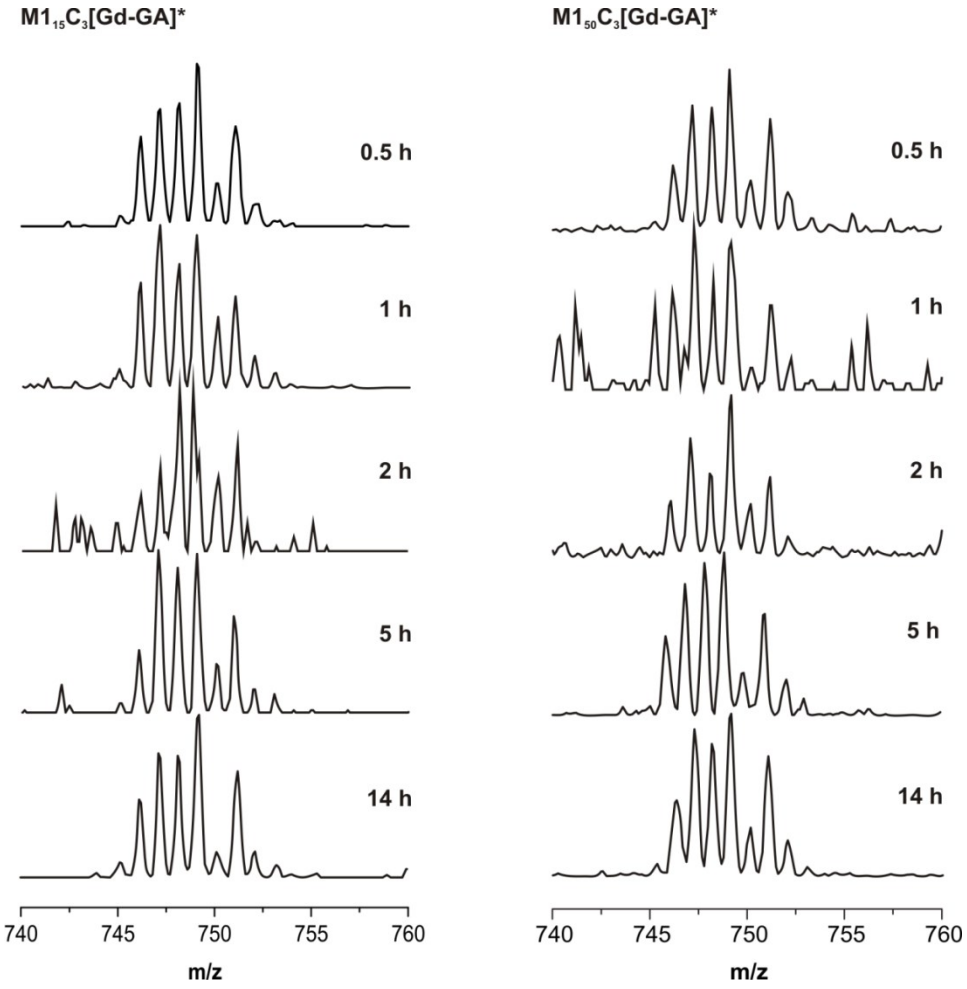

Figure 57: Mass spectra of supernatants from **$M1_{15}C_3$[Gd-GA]*** (left) and **$M1_{50}C_3$[Gd-GA]*** (right) particle suspensions at various leaching times.

4.2.12 Twofold Reaction with [Gd-GA]

After the reaction of the Gd(III) chelate functionalized SNPs **$M1_{15}C_3$[Gd-GA]** and **$M1_{50}C_3$[Gd-GA]**, a reloading with **[Gd-GA]** was implemented. Therefore the existing amino functions of **$M1_{15}C_3NH_2$** were calculated under geometrical considerations and 50 % from this amount were assumed as residual free amino functions. For **$M1_{50}C_3NH_2$** the amount of residual free amino groups (54 %) was calculated and due to geometrical considerations half of it is considered to be able to react with **[Gd-GA]**. Looking at the aspect of higher surface loading after the twofold reaction, the question arises why the Gd(III) chelate complex does not react with all geometrical possible surface amino functions at first attempt. Amine groups have the property to catalyse inter- and intramolecular reactions between silane molecules and surface silanol groups to form siloxane bonds.[151,174,175] Besides, the amino group of the APTES linker can form hydrogen bonds to the surface silanol groups which results in vertically as well as horizontally positioned APTES groups.[174,175] This fact shows the restricted accessibility of the amino groups for further reactions with Gd(III) chelate complexes. Another important issue in relation to the accessibility of the functional group on the silica surface is given by the formation of a cyclic intermediate by intraparticle interaction.[176] It could be assumed that some of the present APTES functions are not available for reaction by forming a five-membered ring by nucleophilic attack of the nitrogen at the silicon atom (Figure 58). This supposed stabilized transition state by forming the five-membered ring on the silica particle surface is similar to already characterized reactions of aminopropyl functionalized silsesquioxanes.[61]

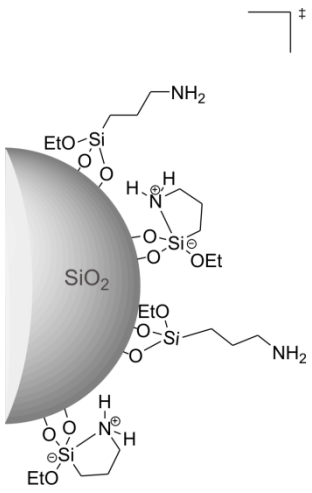

Figure 58: Intraparticle interactions of amino groups on the silica surface.

Two different pathways were proposed for the decomposition of the octaamine silsesquioxane, while for one the presence of water is essential and the decomposition starts by formation of hydroxide ions *via* reaction of the amino groups with water. The second pathway which justifies decomposition without water in dry solvents like DMSO is proposed by the nucleophilic attack of the amino nitrogen at the silicon. In the case of the particle the amino group is probably protonated again after the treatment by water, in the washing process.

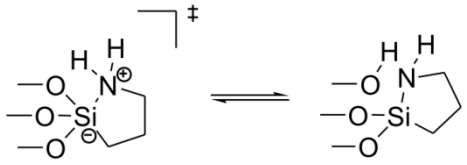

Figure 59: Nucleophilic attack of the APTES nitrogen at the silicon atom favored by forming a five-membered ring.

The presence of Gd(III) chelate complexes as well as particle particle interactions in solution lead to a spatial orientation of the amino propyl functions, which improves the opportunity of reaction with the second charge of **[Gd-GA]** complex (Figure 60). This may be one possible explanation for the higher surface loading by twofold reaction. The surface loading of **$M1_{15}C_3$[Gd-GA]*** is remarkably high with a Gd loading of 125 µmol/g (+125 % in relation to **$M1_{15}C_3$[Gd-GA]**). In comparison, for the **$M1_{50}C_3$[Gd-GA]*** a surface loading of 71.5 µmol/g (+35 % in relation to **$M1_{50}C_3$[Gd-GA]**) is achieved. Looking at the percentage value of carbon in the elemental analysis (Table 15), it is clear that **$M1_{15}C_3NH_2$** contains most likely a higher number of APTES groups than **$M1_{50}C_3NH_2$**.

Interestingly, studies reported a reduced cytotoxity of nanohydroxyapatite particles by acetylating or carboxylating the APTES amine groups.[177,178] Probably this effect is due to electrostatic interactions between the positively charged particles and the negatively charged cell membranes. By protection of the amine groups improved biocompatibility of APTES modified nanohydroxyapatite particles are additionally reported. From this fact the conclusion may be drawn that charge neutralized and negatively charged nanoparticles interact less with the cell membrane and therefore show probably less toxicity. Even though in the case of Gd(III) chelate functionalized silica particles the total charge of the particles is negative (see chapter 4.2.5, Table 12), the amino group protection might gain an improvement concerning the toxicity and biocompatibility. In this case it must be noted

that toxicity depends on various factors among others like particle size and material, surface charge, stability and other properties.

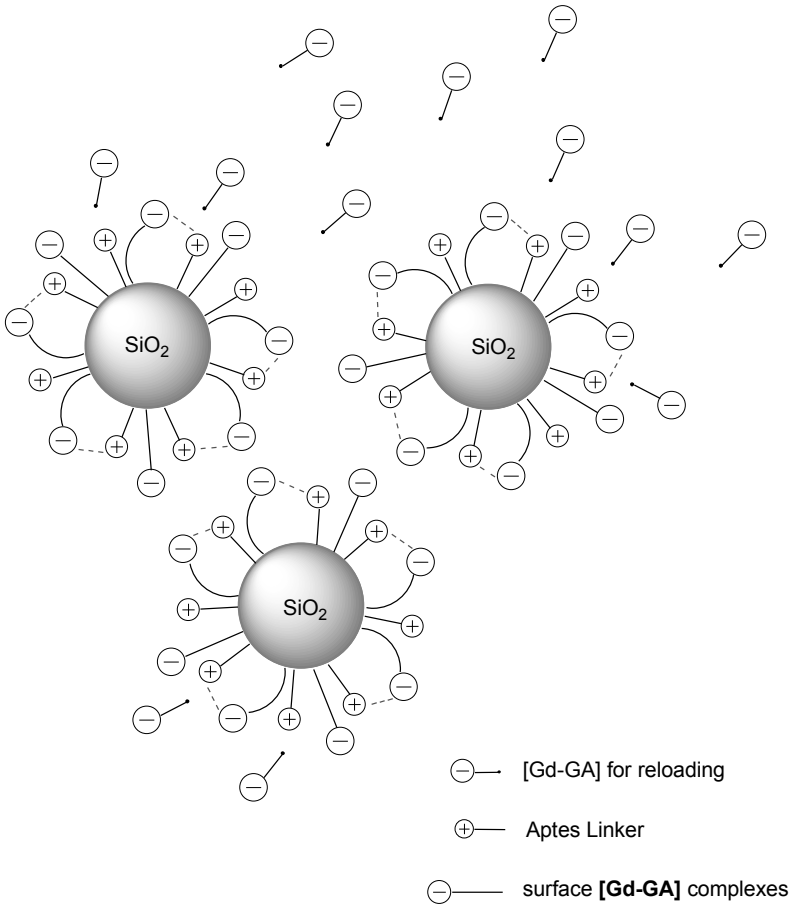

Figure 60: Spatial orientation of the propyl amino functions by Coulomb forces.

5 Experimental Part

5.1 General Remarks

All reactions if not otherwise mentioned were carried out under a dry argon atmosphere using standard Schlenk techniques. Dry solvents (Acetone, acetonitrile, DCM, diethyl ether, ethanol, *n*-hexane, *n*-pentane, toluene and THF) were used from a solvent purification system (SPS 800 MBRAUN) and stored under argon in Schlenk flasks over activated molecular sieve (3 Å or 4 Å). Deuterated solvents DMSO and DCM were stored under argon over activated molecular sieve (3 Å or 4 Å). Chromatographic purifications (silica gel, Amberlite XAD 1600, Sephadex LH-20) were performed under air.

5.2 Materials and Methods

5.2.1 Solvents and Reagents

All reagents were used without further purification, unless otherwise mentioned. 1,4,7,10-tetraazacyclododecane (cyclen, 98 %) was purchased from CheMatch. Azobisisobutyronitrile, 3,5-bis(trifluoromethyl)benzoyl chloride, chelex 100, diisopropylethylamine (99 %), 2,2-dimethoxy-2-phenylacetophenone, 4-(dimethylamino)pyridine, 2-[2-[2-(2-mercaptoethoxy)ethoxy]ethoxy]ethanol, N-(9-fluorenylmethoxycarbonyloxy)succinimide, palladium on carbon (10 %), sodium hydrogen sulfide, triethylene glycol monochlorohydrin, 4,4,4-trifluorobutyric acid, 2,2,2-trifluoroethanethiol, thionylchloride, xylenol orange and yttrium trichloride hexahydrate (99.99 %) were accessible from Sigma-Aldrich. Triethylamine was also acquired from Sigma Aldrich and dried over CaH_2. DMSO (99.8+ %, packed under Argon) and N, N'-dicyclohexylcarbodiimide was used from Alfa Aesar. Benzylbromoacetate and *o*-(benzotriazol-1-yl)-N,N,N',N'-tetramethyl-uronium tetrafluoroborate (TBTU) (> 97 %) was bought from Fluka. Tetra-*n*-butyl-ammonium hydroxide (20 % in water) was aquired from Merck. Acetonitrile (extra dry, over molecular sieves, water < 50 ppm), (3-aminopropyl)-trieethoxysilane (APTES) (99 %) and *tert*-butylbromoacetate was purchased from Acros Organics. Bis(trifluoroethyl)amine, 3,5-bis(trifluoromethyl)benzyl mercaptan, 3,5-bis(trifluoromethyl)benzenethiol, 3,5-bis(trifluoromethyl)pyridine, 3-bromopropyl isothiocyanate, gadolinium trichloride hydrate and 4-trifluoromethylpyridine was obtained from Chempur. Bis(3,3,3-trifluoropropyl)amine was used from Apollo scientifics. $\mathbf{M1_{15}C_3NH_2}$ silica particles (10-20 nm) were purchased from Skyspring Nanomaterials,

Inc. **$M1_{130}C_3$[Gd-BA]** and **$M1_{130}C_3$[Gd-GA]** were previously synthesized and characterized.[25] Octaaminophenyl-POSS and octavinyl-POSS were bought from Hybrid Plastics. 4-Aminophenylacetic acid, 3,5-bis(trifluoromethyl)phenylisothiocyanate, 4-(2-hydroxyethyl)-1-piperazineethanesulfonic acid (HEPES) and 4-nitrophenylacetic acid was purchased from ABCR. Sephadex LH-20 was used from GE Healthcare. Octaaminopropyl-POSS was prepared according to reported procedures.[61] **DO3A** for ligand syntheses of **DOTA-GA** and **DOTA-BA** was prepared according to reported procedures.[179] The lanthanide(III) chloride stock solutions were prepared by dissolving the chloride salt in distilled water. Using xylenol orange as indicator, the exact concentration was determined by complexometric titration with EDTA (disodium salt) in an acetic acid/sodium acetate buffer (pH 5.8). The absence of non-coordinated metal ions in the **Gd[DOTA-BA]** and **Gd[DOTA-GA]** solutions was confirmed by the xylenol test.[153]

5.2.2 Characterization Methods

5.2.2.1 Nuclear Magnetic Resonance (NMR) Spectroscopy

Liquid State NMR Spectroscopy

NMR spectra were measured on a Bruker DRX-250 NMR spectrometer equipped with a 5 mm ATM probe head operating at 250.13 MHz (^{1}H) and 49.69 MHz (^{29}Si) and a Bruker AVII+-400 NMR spectrometer equipped with a 5 mm QNP (quad nucleus) probe head operating at 400.13 MHz (^{1}H), 376.50 MHz (^{19}F) and 100.13 MHz (^{13}C). Further NMR spectra were measured on a Bruker AVII+-500 NMR spectrometer equipped with a 5 mm ATM BBO probe head or a TBO probe head operating at 500.13 MHz (^{1}H), 470.59 (^{19}F), 125.76 (^{13}C) and 99.40 (^{29}Si). All assignments are supported using 2D NMR techniques (^{1}H-^{1}H COSY, ^{1}H-^{13}C HSQC, ^{1}H-^{13}C HMBC, ^{1}H-^{29}Si HSQC, ^{1}H-^{29}Si HMBC, ^{1}H-^{29}Si HMQC). The measurements were performed at room temperature, unless specified otherwise. The chemical shifts are reported in δ values in ppm relative to the external standard $SiMe_4$ (^{1}H, ^{13}C, ^{29} Si) and $CFCl_3$ (^{19}F).

^{1}H NMR Diffusion Spectroscopy (DOSY)

The ^{1}H DOSY experiments were performed using a Bruker AVII+-500 NMR spectrometer operating at 500.13 MHz (^{1}H) using a 5 mm ATM BBO, or a TBO probe head both

equipped with a Z-gradient coil. The samples were dissolved in deuterated dichloromethane, chloroform or dimethyl sulfoxide. The temperature during the measurements was kept at 25 °C using a variable temperature unit and the sample was not spun. The experiments were performed with a 2D sequence for diffusion measurements using stimulated echo with 1 spoil gradient, as implemented in the Bruker TopSpin 2.1 software. Initially the 90° pulse length for the ^{1}H nuclei of the samples was determined and subsequently used to perform the T_1 measurement of each sample as well as to set the recycle delay (longest $T_1 \times 5$) for the ^{1}H DOSY experiments for the relevant ^{1}H nuclei. The sinusoidal gradient pulse lengths (p30) applied on the ^{1}H DOSY experiment were in the range of 1.5 to 3.8 ms. Diffusion delays (d20) utilized in the ^{1}H DOSY experiments were in the range of 75 to 100 ms. Prior to the ^{1}H DOSY experiment, the samples were thermalized for at least 10 min.

Diffusion NMR experiments of the hydrolysis samples were performed according to the sample solubility in different ratios of a DMSO-d6/D_2O-HEPES buffer mixture (pD 7.4). Each ^{1}H DOSY, ^{29}Si HSQC or HMQC and ^{19}F NMR spectra was performed at 37 °C. The parameters for the DOSY NMR spectra were optimized for the starting sample and were not re-optimized during hydrolysis.

^{19}F NMR Experiments for Relaxation Time Determination (T_1/T_2)

All samples were dissolved in DMSO-d6 to obtain a concentration of 5 mM related to the amount of present fluorine. The measurements were performed at a Bruker Avance 300 MHz spectrometer operating at 282.42 MHz for the ^{19}F nucleus. The $^{19}F\{^{1}H\}$ spectra were measured using a CPD sequence. From these experiments the 90° pulse length and the respective O1 value were determined. The T_1 values were obtained by an inversion recovery sequence (24 points). For the determination of the T_2 relaxation time a CPMG sequence was applied (12 points). The T_1/T_2 curves were fitted using the T_1/T_2 analysis module as implemented in the TopSpin NMR software. The measurements were performed at 25 °C. For each sample the measurement was repeated for at least three times. The given values are the average values. For the samples **18** and **19** the T_1 and T_2 were determined by integration of the middle signal of the generated triplet. For the PF-POSS **10**, **11** and **12** a single measurement of T_1/T_2 relaxation times was performed.

Solid State NMR Spectroscopy

^{29}Si CP/MAS and ^{29}Si HP/DEC NMR experiments were measured in 4 mm and 7 mm ZrO_2 rotors, respectively on a Bruker ASX 300 spectrometer, operating at 59.6 MHz. Q_8M_8 was used as external standard. ^{13}C CP/MAS NMR experiments were performed in 4 mm ZrO_2 rotors on a Bruker ASX 200 NMR spectrometer operating at 50.3 MHz. Magic angle spinning was performed at 4 kHz for the ^{29}Si NMR spectra and at 10 kHz for the ^{13}C NMR spectra.

5.2.2.2 Diffuse Reflectance Infrared Fourier Transform (DRIFT) Spectroscopy

DRIFT experiments were recorded on a Bruker Vertex 70 FTIR Spectrometer. The samples were measured in KBr in a ratio of 1 : 5 (sample : KBr) and a resolution of 4 cm^{-1} with 16 scans from 4000 to 500 cm^{-1}.

5.2.2.3 Elemental Analysis

Elemental analysis was performed on an Elementar VarioMICRO V1.9.2 cube, in the CHNS mode.

5.2.2.4 Mass Spectrometry

ESI mass spectra were recorded on a Bruker Daltonics esquire3000plus mass spectrometer (quadrupolar ion trap) with an ESI interface.

HR ESI-TOF MS spectra were recorded on a Bruker Daltonics 3 maXis 4G mass spectrometer.

5.2.2.5 Dynamic Light Scattering (DLS)

DLS-measurements were recorded on a Zetasizer Nano ZS from Malvern instruments. The given Z average is the intensity weighted mean hydrodynamic size of the ensemble collection of particles measured by DLS. The Z average is derived from a cumulants analysis of the measured correlation curve, wherein a single particle size is assumed and a single exponential fit is applied to the autocorrelation function.[69] DLS size distributions by intensity can be converted, using Mie theory, to a volume distribution and further to a number distribution.[69] For measurements the nanoparticles were suspended in water and in a PBS solution (at pH 7.4), respectively. The PBS solution was diluted 1 : 100 from a 12

mM stock solution. The samples were ultrasonicated for 40 min and filtered through a 0.25 µm nylon filter before measurement to remove bigger agglomerates. The particle size was determined from a scattering angle of 173° in 12 mm square polystyrene cuvettes. The After 3 min of temperature equilibration 5 measurements (á 15 runs) were performed at 25 °C.

5.2.2.6 Zeta Potential Measurements

Zeta potentials were recorded with the Zetasizer Nano ZS from Malvern instruments. The silica particles were suspended in a PBS solution and a solution of cell culture medium with 10 % serum, respectively. For obtaining a conductivity between 0.1 and 0.5 mS/cm, the stock solution of PBS (12 mM of PO_4^{3-}) was diluted 1 : 100 with bidistilled water to reach a conductivity of 0.2 mS/cm. The medium with 10 % serum was diluted 1 : 100 with bidistilled water for a conductivity of 0.17 mS/cm, the pH of both solutions was adjusted to 7.4. The silica particle suspensions (0.15 mg/ml) were ultrasonicated for 1 h. Before measurement the suspensions were filtered through 0.25 µm nylon filters and transferred into disposable capillary cells. After three minutes of equilibration of temperature (25 °C) four measurements were recorded. For evaluating the average zeta potential the first measurement was discarded.

5.2.2.7 Scanning Electron Microscopy (SEM)

For SEM images the nanoparticles were suspended in ethanol and ultrasonicated for 30 minutes (1 mg/ml). A drop (20 µl) of the suspension was placed on a silicon wafer and rotated for 3 minutes to remove the solvent. The images were measured with a field emission high resolution scanning electron microscope SU8030 from Hitachi and XL 30-FEG from Philips. Size determinations of the particles were obtained by measuring 50-100 particles with the ImageJ Launcher 1.4.3.67.

5.2.2.8 Scanning Transmission Electron Spectroscopy (STEM)

For STEM images the nanoparticles were suspended in ethanol and ultrasonicated for 30 minutes (1 mg/ml). For sample preparation a drop (20 µl) of the suspension was placed on a 200 mesh holey carbon grip.

The images were measured with a field emission high resolution scanning electron microscope SU8030 from Hitachi. In DF-STEM imaging the detection angle was varied by

changing the size hole of the DF-STEM holder to optimize the Z (atomic number) contrast.

5.2.2.9 Brunauer-Emmet-Teller (BET) Measurements

Adsorption and desorption isotherms were measured with nitrogen at 77.35 K on an ASAP 2020 instrument (Fa. Micromeritics). Before measurement the samples were degassed at 100 °C at 1 mPa for 150 min.

5.2.2.10 ICP Atomic Emission Spectrometry (ICP-AES)

ICP-AES measurements were performed by the Mikroanalytisches Labor Pascher. Samples were dried at 30 °C *in vacuo* and treated with HNO_3/HCl at 180 °C. Using yttrium as internal standard gadolinium was detected with a Thermo ICAP 6500.

5.2.2.11 Thermogravimetric (TGA) Measurements

TG measurements were carried out with the STA 499 F3 Jupiter (Fa. Netzsch). The samples were heated under Argon flow from rt to 1250 °C in Al_2O_3-crucibles with a heating rate of 2 K/min and a gas flow of 20 ml/min.

5.2.2.12 MR Imaging in Agar Phantoms

MRI measurements were performed in 1.5 % agar to stabilize the dispersion of the sample throughout the measurement. A stock solution of 10 mg/ml was thoroughly dispersed by ultrasonication, of which dilutions between 500 and 4,000 µg/ml were prepared in water or cell culture medium with 10 % serum. Each of the solutions (50 µl) was immediately mixed with 1.5 % agar (50 µl), filled into 0.6 ml tubes and subsequently gelled in ice. The agar gel of each sample was overlayed with 300 µl water and cell culture medium, respectively. Accordingly, samples containing 25-200 µg material per 100 µl were prepared, resulting in the different materials in Gd concentrations as given in Table 25. The samples were measured at 3 T (123 MHz) and at room temperature. Determinations of the longitudinal and transverse relaxation rates of the agar layer and the supernatant containing samples were performed by axial slices of 1 mm thickness for each sample.

Table 25: Gd concentrations ($\mathbf{c_{Gd}}$) of MR imaging samples.

sample	$\Gamma_{Gd(III)}$ [µmol/g]	c_{Gd} [µmol/g]
$M1_{15}C_3$[Gd-BA]	47.4	11.9-94.8
$M1_{15}C_3$[Gd-GA]	55.6	13.9-111.2
$M1_{15}C_3$[Gd-GA]*	125.0	31.3-250.0
$M1_{50}C_3$[Gd-BA]	63.0	15.8-126.0
$M1_{50}C_3$[Gd-GA]	54.4	13.6-108.8
$M1_{50}C_3$[Gd-GA]*[(1)]	71.5	17.9-143.0
$M1_{130}C_3$[Gd-BA]	27.0	6.8-54.0
$M1_{130}C_3$[Gd-GA]	10.7	2.7-21.4
$M1_{15}C_3$[Gd-BA]ac	47.7	11.9-95.4
$M1_{15}C_3$[Gd-GA]ac	51.8	13.0-103.6
$M1_{50}C_3$[Gd-BA]ac	59.5	14.9-119.0
$M1_{50}C_3$[Gd-GA]ac	52.2	13.1-104.4
$M1_{130}C_3$[Gd-BA]ac	26.7	6.7-53.4
$M1_{130}C_3$[Gd-GA]ac	10.8	2.7-21.6

$\Gamma_{Gd(III)}$, surface concentration of Gd complexes per gram NP, determined by ICP-MS.
[1] different batch of particles **$M1_{50}C_3$[Gd-GA]** ($\Gamma_{Gd(III)}$ = 52.8 µmol/g) doubly reacted with **[Gd-GA]**.

An inversion recovery experiment was used for T_1 measurements, with an adiabatic inversion pulse, followed by a turbo-spin-echo readout. The time between inversion and readout was varied from 23 ms to 3000 ms. In this way 10-15 images were taken. The repetition time amounts to 10 s, while 15 echoes were acquired by scan and averaged six times. For T_2, a spin echo sequence was used with echo times varying from 25 ms to 275 ms in 10 equidistant steps. By minimizing the crusher gradients around the refocusing pulse the diffusion sensitivity was reduced. All experiments scanned 256^2 voxels in a field of view of 110 mm in both directions, hence following in a voxel volume of 0.43 × 0.43 × 1 mm^3.

For fitting the relaxation curves self-written routines under Matlab 7.1 R14 (The Matchworks Inc., United States) were used. For data analysis the series of T_1 and T_2 relaxation data were fitted according to the following equations:

a) T_1 series with varying t = TI

$$S = S_0\left(1 - \exp\left(\frac{-t}{T_1}\right)\right) + S_{(TI=0)}$$

b) T_2 series with varying t = TE

$$S = S_0\, exp\left(\frac{-t}{T_2}\right)$$

The Trust-Region Reflective Newton algorithm was performed with MATLAB and used for nonlinear least-squares fitting of the parameters S_0, $S_{(TI\,=\,0)}$ and the (T_1/T_2) rate. Therefore manually selected relevant regions were chosen and by mean errors and residual

calculation, as well as visual inspection, the quality of the fit was ensured.

For T_1-weighted MR images (sagittal and axial) imaging sequences, IR-RARE and FLASH were used.
Image intensities in the axial images were evaluated with ImageJ 1.44c (http://rsb.info.nih.gov.ij) and a circular region of interest of 82 voxels was used.

5.2.2.13 Leaching Test

Re-conjugated SNPs **$M1_{15}C_3$[Gd-GA]*** and **$M1_{50}C_3$[Gd-GA]*** were dissolved in PBS (pH 7.4) and carefully stirred in Eppendorfer vials at 37 °C. The concentrations of the NP samples and the resulting Gd(III) concentrations are given in Table 26. After suspending the SNPs in PBS, each sample was ultrasonicated for 15 min and the absence of free gadolinium ions was confirmed by the xylenol test. [153] After the respective exposure time the SNPs were separated from the supernatants by centrifugation. One part of the isolated supernatant was used for the xylenol test, the other part for the supernantant relaxometry measurements. The SNPs were washed subsequently with water, ethanol and *n*-hexane and dried *in vacuo* at room temperature for 24 h prior to relaxometric evaluation.

Table 26: SNP concentration of the leaching suspensions and resulting concentrations of Gd(III) ion.

sample	exposure time [h]	NP concentration [µg/µl]	concentration of Gd^{3+} [µM]
$M1_{15}C_3$[Gd-GA]*	0.5	3000/300	998[(1)]
$M1_{15}C_3$[Gd-GA]*	1	3000/300	998
$M1_{15}C_3$[Gd-GA]*	2	3000/300	998
$M1_{15}C_3$[Gd-GA]*	5	3000/300	998
$M1_{15}C_3$[Gd-GA]*	14	3000/300	998
$M1_{15}C_3$[Gd-GA]*	24	1000/300	417[(2)]
$M1_{15}C_3$[Gd-GA]*	48	1000/300	417
$M1_{15}C_3$[Gd-GA]*	72	1000/300	417
$M1_{50}C_3$[Gd-GA]*	0.5	3000/300	948[(3)]
$M1_{50}C_3$[Gd-GA]*	1	3000/300	948
$M1_{50}C_3$[Gd-GA]*	2	3000/300	948
$M1_{50}C_3$[Gd-GA]*	5	3000/300	948
$M1_{50}C_3$[Gd-GA]*	14	3000/300	948
$M1_{50}C_3$[Gd-GA]*	24	6000/300	1431[(4)]
$M1_{50}C_3$[Gd-GA]*	48	6000/300	1431
$M1_{50}C_3$[Gd-GA]*	72	6000/300	1431

calculated from Gd(III) concentrations determined by ICP-AES (Gd [µmol/g])
[1] 99.84 µmol/g; [2] 124.96 µmol/g; [3] 94.75 µmol/g; [4] 71.54 µmol/g.

5.2.2.14 Centrifugation

Materials were separated using a Beckmann L80 ultracentrifuge with a 70 Ti rotor. Appropriate tubes were used at 40,000 rpm for 30 min.

5.2.2.15 Microwave reactions

Reaction solutions were irradiated in a CEM MARS MW apparatus with a pressure-resistant test tube equipped with an infrared pyrometer for the control of the temperature. The reactions were carried out in sealed microwave vials. All reactions were performed according to a temperature-time sequence (20 min at 150 °C), operating at a maximum power of 300 W.

5.3 Syntheses

5.3.1 Synthesis of PF-POSS 3

Under argon atmosphere OAP-POSS (200 mg, 1.70×10^{-4} mol, 1 eq.) and 3,5-bis(trifluoromethyl)phenylisothiocyanate (467 µl, 2.56×10^{-4} mol, 15 eq.) were dissolved in dry DMSO (2 ml). Dry triethylamine (284 µl, 12 eq.) was added and the mixture stirred at rt for 16 h. The solvent was evaporated. The residue was dissolved in methanol and the precipitations were removed. The solvent was evaporated under reduced pressure and the residue was dissolved in acetone. Formed precipitations were again removed. The solvent was evaporated and the residue was purified by silica gel chromatography starting with DCM (100 %). After eluation of the first fraction, the remaining compound was eluted from the column with MeOH (100 %).

^{1}H NMR (400.13 MHz, MeOD): δ = 0.82 (m, 16H, SiC*H*$_2$CH$_2$CH$_2$), 1.84 (m, 16H, SiCH$_2$C*H*$_2$CH$_2$), 3.62 (m, 16H, SiCH$_2$CH$_2$C*H*$_2$), 7.51 (s, 8H, Ar-C*H*), 8.18 (s, 16H, Ar-C*H*). **^{13}C{^{1}H} NMR** (100.61 MHz, MeOD): δ = 10.1 (Si*C*H$_2$CH$_2$CH$_2$), 23.4 (SiCH$_2$*C*H$_2$CH$_2$), 47.6 (SiCH$_2$CH$_2$*C*H$_2$), 117.5 (NH-*p*-*C*H), 123.2 (NH-*o*-*C*H), 124.7 (q, $^{1}J_{C\text{-}F}$ = 271.9 Hz, Ar-*C*F$_3$), 132.5 (q, $^{2}J_{C\text{-}F}$ = 33.3 Hz, *C*CF$_3$), 143.1 (NH-ipso-*C*), 182.5 (NH*C*SNH). **^{19}F{^{1}H} NMR** (376.50 MHz, MeOD): δ = -64.45 (s). **^{29}Si DEPT-45 NMR** (49.70 MHz, MeOD): δ = -67.8 (s). **IR (KBr, cm^{-1})**: ν (C-H) 2932, ν (C=C)$_{arom.}$ 1620, ν$_{as}$ (C-F) 1384, ν (C=S) 1275, ν$_{as}$ (Si-O-Si) 1127, δ (C-H)$_{arom.}$ 953-683, ν$_{s}$ (Si-O-Si) 557, δ (Si-O-Si) 483.

5.3.2 Synthesis of PF-POSS 5

Under argon atmosphere OAP-POSS (150 mg, 1.28×10^{-4} mol, 1 eq.) was suspended in dry DCM (6 ml). 3,5-Bis(trifluoromethyl)benzoyl chloride (348 µl, 1.92 mmol, 15 eq.) was filled into a dropping funnel and dissolved in DCM (6 ml). Finally triethylamine (762 µl, 5.5 mmol, 43 eq.) was added. Under stirring and cooling with ice, the mixture was added dropwise to the solution in the flask within 25 min. The mixture was then stirred at rt for 16 h. The trietylammonium salt was removed to a large extend by filtration. The solvent was removed under reduced pressure to give a slightly yellowish residue with remaining triethylammonium salt next to the desired PFG-POSS.

^{1}H NMR (400.13 MHz, MeOD): δ = 0.75 (m, 16 H, SiC*H*$_2$CH$_2$CH$_2$N), 1.78 (m, 16 H, SiCH$_2$C*H*$_2$CH$_2$N), 3.39 (m, 16H, SiCH$_2$CH$_2$C*H*$_2$N), 8.00 (m, 8H, NHCO-*p*-C*H*), 8.33 (m,

16H, NHCO-*o*-C*H*). **^{13}C{^{1}H} NMR** (100.61 MHz, MeOD): δ = 10.0 (Si*C*$H_2$$CH_2$$CH_2$N), 23.6 SiCH$_2$*C*H$_2CH_2$N), 43.6 (SiCH$_2CH_2$*C*H$_2$N), 124.3 (q, $^{2}J_{C-F}$ = 272.2 Hz, Ar-*C*F_3), 125.6 (NHCO-p-*C*H), 128.8 (NHCO-o-*C*H), 132.8 (q, $^{1}J_{C-F}$ = 34.1 Hz, *C*CF_3), 143.7 (NHCO-ipso-Ar*C*), 166.4 (CH_2NHCO). **^{19}F{^{1}H} NMR** (376.50 MHz, MeOD): δ = -64.40 (s). **^{29}Si DEPT-45 NMR** (49.7 MHz, MeOD): δ = not observed.

5.3.3 Synthesis of PF-POSS 10

Under argon atmosphere octavinyl-POSS (104 mg, 1.64×10^{-4} mol, 1 eq.) and 3,5-bis(trifluoromethyl)benzyl mercaptan (639 mg, 2.45×10^{-3} mol, 15 eq.) were dissolved in dry toluene (3 ml). AIBN (3 mg) was added and the suspension heated at 80 °C for 24 h. The mixture was cooled to rt. A second portion of AIBN was added and the suspension was again heated at 80 °C for 16 h. Upon completion of the reaction the solvent was removed under reduced pressure and the residue was dissolved in MeOH. The precipitation was removed using a syringe nylon filter and methanol was evaporated to give a yellow resin. The product was dried *in vacuo* at 40 °C for 16 h. Yield: 378 mg (85 %).

^{1}H NMR (400.13 MHz, MeOD): δ = 0.88 (m, 16H, SiC$H_2$$CH_2$S), 2.42 (m, 16H, SiCH$_2CH_2$S), 3.80 (s, 16H, SC$H_2$Ar), 7.78 (s, 8H, SCH$_2$-*p*-C*H*), 7.87 (s, 16H, SCH$_2$-*o*-C*H*). **^{13}C{^{1}H} NMR** (100.61 MHz, MeOD): δ = 12.9 (Si*C*$H_2$$CH_2$S), 26.4 (SiCH$_2$*C*H$_2$S), 36.0 (S*C*H$_2$Ar), 121.5 (sep, $^{3}J_{C-F}$ = 4.8 Hz , SCH$_2$-*p*-*C*H), 124.7 (q, $^{1}J_{C-F}$ = 272.0 Hz, *C*F_3), 130.2 (SCH$_2$-*o*-*C*H), 132.8 (q, $^{2}J_{C-F}$ = 33.1 Hz, *C*CF_3), 143.6 (SCH$_2$*C*). **^{19}F{^{1}H} NMR** (376.50 MHz, MeOD): δ = -64.21 (s). **^{29}Si DEPT-45 NMR** (49.70 MHz, MeOD): δ = -68.5 (s). **MS (ESI)**, m/z: found $[M+Na]^+$ 2734.42 (calc. 2735.01). **IR (KBr, cm^{-1})**: ν (C-H) 2924, ν (C=C)$_{arom.}$(1659), ν_{as} (C-F) 1374, ν_{as} (Si-O-Si) 1133, δ (C-H)$_{arom.}$ 902-756, ν_s (Si-O-Si) 551, δ (Si-O-Si) 471. **Elemental analysis** for $C_{88}H_{72}F_{48}O_{12}S_8Si_8$: found C 39.15, H 2.25, S 9.62 (calc. C 38.93, H 2.67, S 9.45).

5.3.4 Synthesis of PF-POSS 11

In a Schlenk flask octavinyl-POSS (150 mg, 0.24 mmol, 1eq.) and 3,5-bis(trifluoromethyl)benzenethiol (324 µl, 2.37 mmol, 10 eq.) were dissolved in dry toluene (4 ml). AIBN (3 mg) was added and the mixture was stirred at 80 °C for 17 h. After re-addition of 3,5-Bis(trifluoromethyl)benzenethiol (65 µl, 0.47 mmol, 2 eq.) and AIBN (2 mg) the mixture was stirred again at 80 °C for 22 h. The solvent was removed under reduced pressure to give a colorless residue. Dry methanol was added to give a colorless

precipitate of the desired PFG-POSS. The product was dried at 60 °C for 16 h. Yield: 40 mg (9 %).

^{1}H NMR (400.13 MHz, CD_2Cl_2): δ = 1.18 (m, 16 H, SiC*H*$_2$CH$_2$S), 3.11 (m, 16 H, SiCH$_2$C*H*$_2$S), 7.29 (m, A-part of an AA'BB'-system, 16 H, S-*m*-C*H*), 7.45 (m, B-part of an AA'BB'-system, 16 H, S-*o*-C*H*). **^{13}C{^{1}H} NMR** (100.61 MHz, CD_2Cl_2): δ = 12.4 (Si*C*H$_2$CH$_2$S), 27.0 (SiCH$_2$*C*H$_2$S), 124.6 (q, $^1J_{C\text{-}F}$ = 275.1 Hz, *C*F$_3$), 126.1 (q, $^4J_{C\text{-}F}$ = 3.6 Hz, S-*m*-*C*H), 127.5 (S-*o*-*C*H), 127.6 (q, $^2J_{C\text{-}F}$ = 32.6 Hz, *C*CF$_3$), 142.8 (S-*ipso*-Ar*C*). **^{19}F{^{1}H} NMR** (376.50 MHz, CD_2Cl_2): δ = -62.82 (s). **^{29}Si DEPT-45 NMR** (49.70 MHz, CD_2Cl_2): δ = -70.5 (s). **MS (ESI)**, m/z: found $[M+H]^{2+}$ 1029.85 (calc. 1030.23). **IR (KBr, cm^{-1})**: ν (C-H) 2929, ν (C=C) 1609, ν_{as} (C-F) 1330, ν_{as} (Si-O-Si) 1123, δ (C-H)$_{arom.}$ 825-740, ν_s (Si-O-Si) 557, δ (Si-O-Si) 473.

5.3.5 Synthesis of PF-POSS 12

Under argon atmosphere DPAP (13 mg, 5×10^{-5} mol) and 2,2,2-trifluoroethanethiol (422 µl, $4{,}74\times10^{-3}$ mol, 15 eq.) were added to a solution of octavinyl-POSS (200 mg, 3.16×10^{-4} mol, 1 eq.) in dry THF (2 ml) in a quarz Schlenk tube. Under vigorous stirring the solution was irradiated for 3 h using a 700 W medium pressure mercury lamp. The solvent was evaporated and the product was precipitated and subsequently washed four times with MeOH. The off-white solid was dried *in vacuo* at 45 °C for 16 h. Yield: 470 mg (95%).

^{1}H NMR (400.13 MHz, $CDCl_3$): δ = 1.04 (m, 16H, SiC*H*$_2$CH$_2$), 2.77 (m, 16H, SiCH$_2$C*H*$_2$), 3.09 (q, $^3J_{H\text{-}F}$ = 10.0 Hz, 2H, SC*H*$_2$CF$_3$). **^{13}C{^{1}H} NMR** (100.61 MHz, $CDCl_3$): δ = 12.36 (s, Si*C*H$_2$CH$_2$), 27.33 (s, SiCH$_2$*C*H$_2$), 34.42 (q, $^2J_{C\text{-}F}$ = 32.9 Hz, S*C*H$_2$CF$_3$), 126.10 (q, $^1J_{C\text{-}F}$ = 276.3 Hz, *C*F$_3$). **^{19}F NMR** (376.50 MHz, $CDCl_3$): δ = -66.34 (t, $^3J_{F\text{-}H}$ = 10 Hz, F). **^{29}Si DEPT-45 NMR** (49.70 MHz, $CDCl_3$): δ = -70.7 (s). **MS (ESI)**, m/z: found 1582.02 $[M+Na]^+$ (calc.1582.86), found 1598.98 $[M+K]^+$ (calc. 1598.83). **IR (KBr, cm^{-1})**: ν (C-H) 2937, δ (CH_2) 1480, ν_{as} (C-F) 1305, ν_s (C-F) 1251, ν_{as} (Si-O-Si) 1120, ν_s (Si-O-Si) 546, δ (Si-O-Si) 472. **Elemental analysis** for $C_{32}H_{48}F_{24}O_{12}S_8Si_8$: found C 25.05, H 2.46, S 16.30 (calc. C 24.61, H 3.10, S 16.42).

5.3.6 Synthesis of PEG 13

PEG **13** was synthesized similar to procedures reported before.[130] A suspension of sodium hydrogen sulfide (41.65 g, 0.743 mol, 5 eq.) and triethylene glycol monochlorohydrin (25 g, 0.149 mol, 1. eq.) in EtOH (500 ml) was prepared. A solution of hydrochloric acid in

EtOH (50 ml : 250 ml) was added dropwise at 60 °C. The suspension was stirred for 24 h, cooled to rt and hydrochloric acid was added to quench the remaining hydrogen sulfide. The solid was filtered and the solvent was removed under reduced pressure. The residue was dissolved in DCM and the organic layer was extracted with hydrogen carbonate. The organic layer was dried over magnesium sulfate and the solvent was evaporated. The residue was purified by silica flash column chromatography (DCM : MeOH 2 %) to give a yellow oil. Yield: 8.1 g (33 %).

^{1}H NMR (400.13 MHz, $CDCl_3$): δ = 1.48 (t, $^3J_{H-H}$ = 8.2 Hz, 1H, S*H*), 2.54 (td, $^3J_{H-H}$ = 6.4 Hz, $^3J_{H-H}$ = 8.2 Hz, 2H, C*H*$_2$SH), 3.17 (t, $^3J_{H-H}$ = 5.5 Hz, 1H, CH_2O*H*), 3.42-3.52 (m, 8H, C*H*$_2$OC*H*$_2$C*H*$_2$OC*H*$_2$$CH_2OH$), 3.55 (m, 2H, C*H*$_2$OH). **MS (ESI)**, m/z: found 188.82 $[M+Na]^+$ (calc. 189.23). **IR (KBr, cm^{-1})**: ν (C-H) 2868, ν (S-H) 2554, δ (CH_2) 1456, ν_{as} (C-O-C) 1112, ν (CH_2-OH) 1068.

5.3.7 Synthesis of PEG-POSS 15

PEG-POSS **15** was prepared similar to procedures reported before.[99] Under argon a solution of **13** (841 mg, 5.1 mmol, 16 eq.) and DPAP (41 mg) in dry DMF (4 ml) was added to a solution of octavinyl-POSS (200 mg, 0.32 mmol, 1 eq.) in dry THF (2.7 ml) in a quarz Schlenk tube. The mixture was irradiated for 2 h using a 700 W medium pressure mercury lamp. The solvent was removed and the residue purified by Sephadex LH-20 column chromatography (MeOH : H_2O, 1 : 1) to give a slightly yellow oil. Yield: 391 mg (63 %).

^{1}H NMR (400.13 MHz, $CDCl_3$): δ = 1.04 (m, 16H, SiC*H*$_2$$CH_2$), 2.65 (m, 16H, $SiCH_2$C*H*$_2$), 2.74 (m, $^3J_{H-H}$ = 7.0 Hz, 16H, SC*H*$_2$), 2.95 (s, br, 8H, OH), 3.58 (m, 16H, OC*H*$_2$$CH_2OH$), 3.64 (m, 48H, C*H*$_2$OC*H*$_2$C*H*$_2$O), 3.71 (m, 16H, C*H*$_2$OH). **IR (KBr, cm^{-1})**: ν (C-H) 2913, δ (CH_2) 1459, ν_{as} (C-O-C) 1272, ν_s (C-F) 1357, ν_{as} (Si-O-Si) 1110, ν_s (Si-O-Si) 549, δ (Si-O-Si) 470.

5.3.8 Synthesis of PEG-POSS 16

Under argon a solution of 2-[2-[2-(2-mercaptoethoxy)ethoxy]ethoxy]-ethanol (1 g, 4.8 mmol, 16 eq.) and DPAP (38 mg) in dry DMF (4 ml) was added to a solution of octavinyl-POSS (188 mg, 0.3 mmol, 1 eq.) in dry THF (2.7 ml) in a quarz Schlenk tube. The mixture was irradiated for 2 h using a 700W medium pressure mercury lamp. The solvent was removed and the residue purified by Sephadex LH-20 column chromatography (MeOH :

H_2O, 1 : 1) to give a yellow oil. Yield: 505 mg (73 %).

^{1}H NMR (400.13 MHz, CD_2Cl_2): δ = 1.06 (m, 16H, SiC*H*$_2$), 2.67 (m, 16H, SiCH$_2$C*H*$_2$), 2.74 (t, $^3J_{H-H}$ = 7.0 Hz, 16H, SiCH$_2$CH$_2$SC*H*$_2$), 2.83 (s, 8H, OH), 3.58 (m, 16H, OC*H*$_2$CH$_2$OH), 3.62-3.66 (m, 80H, C*H*$_2$OC*H*$_2$C*H*$_2$OC*H*$_2$C*H*$_2$O), 3.69 (m, 16H, C*H*$_2$OH). **^{13}C{^{1}H} NMR** (100.61 MHz, CD_2Cl_2): δ = 13.6 (Si*C*H$_2$), 26.8 (SiCH$_2$*C*H$_2$), 31.6 (SiCH$_2$CH$_2$S*C*H$_2$), 73.0 (O*C*H$_2$CH$_2$OH), 70.7, 70.7, 70.9, 71.0, 71.1 (*C*H$_2$O*C*H$_2$*C*H$_2$O*C*H$_2$*C*H$_2$O), 62.0 (*C*H$_2$OH). **^{29}Si DEPT-45 NMR** (49.70 MHz, CD_2Cl_2): δ = -68.6 (s). **HR ESI-TOF MS**, m/z: found 1179.32902 $[M+2Na]^{2+}$ (calc. 1179.33064) **IR (KBr, cm^{-1})**: ν (C-H) 2912, δ (CH_2) 1455, ν_{as} (C-O-C) 1282, ν_{as} (Si-O-Si) 1113, ν_s (Si-O-Si) 549, δ (Si-O-Si) 473.

5.3.9 Synthesis of PF-POSS 18

15 (195 mg, 0.1 mmol, 1 eq.), 4,4,4-trifluorobutyric acid (226 mg, 1.6 mmol, 16 eq.), DCC (328 mg, 1.6 mmol, 16 eq.) and DMAP (19.4 mg, 0.16 mmol, 1.6 eq) were dissolved in dry DCM (30 ml). The mixture was stirred for 3 min and placed in a CEM micro wave apparatus. The mixture was irradiated at 150 °C for 20 min. After reaction the mixture was cooled down to rt and the solvent was filtered by a glass funnel to remove the solid. The solvent was removed under reduced pressure to give a yellow oil. The residue was dissolved in dry DEE and stored at 4 °C for 16 h. The formed solid was removed by filtration over a glass funnel and the solvent was removed. The crude product was purified by Sephadex LH-20 column chromatography (MeOH). The product was dried at 40 °C. Yield: 258 mg (88 %).

^{1}H NMR (400.13 MHz, (CD_2Cl_2): δ = 1.02 (m, 16H, SiC*H*$_2$), 2.42-2.55 (m, 16H, CH$_2$C*H*$_2$CF$_3$), 2.62 (m, 16H, C*H*$_2$CH$_2$CF$_3$), 2.64 (m, 16H, SiCH$_2$C*H*$_2$), 2.70 (t, $^3J_{H-H}$ = 6.9 Hz, 16H, SiCH$_2$CH$_2$SC*H*$_2$), 3.56-3.64 (m, 48H, SCH$_2$C*H*$_2$OC*H*$_2$C*H*$_2$), 3.67 (m, 16H, C*H2*CH2COO), 4.24 (m, 16H, CH$_2$C*H*$_2$COO). **^{13}C{^{1}H} NMR** (100.61 MHz, (CD_2Cl_2): δ = 13.1 (SiCH$_2$), 26.3 (SiCH$_2$C*H*$_2$), 26.9 (q, $^3J_{C-F}$ = 3.3 Hz, *C*H$_2$CH$_2$CF$_3$), 29.2 (q, $^2J_{C-F}$ = 29.8 Hz, *C*H$_2$CF$_3$), 31.3 (CH$_2$S*C*H$_2$), 64.1 (CH$_2$*C*H$_2$COO), 68.9 (*C*H$_2$CH$_2$COO), 70.2, 70.5, 70.6 (SCH$_2$*C*H$_2$O*C*H$_2$*C*H$_2$), 126.7 (q, $^1J_{C-F}$ = 275.9 Hz, *C*F$_3$), 170.8 (*C*OO). **^{19}F{^{1}H} NMR** (376.50 MHz, (CD_2Cl_2): δ = -67.30 (s). **^{29}Si DEPT-45 NMR** (49.70 MHz, CD_2Cl_2): δ = -68.6 (s). **HR ESI-TOF MS**, m/z: found 1499.27967 $[M+2Na]^{2+}$ (calc. 1499.28017). **IR (KBr, cm^{-1})**: ν (C-H) 2913, ν (C=O) 1742, δ (CH_2) 1443, ν_{as} (C-F) 1327, ν_{as} (C-O-C) 1265, ν_s (C-F) 1188, ν_{as} (Si-O-Si) 1136, ν_s (Si-O-Si) 551, δ (Si-O-Si) 472.

5.3.10 Synthesis of PF-POSS 19

16 (520 mg, 0.23 mmol, 1 eq.), 4,4,4-trifluorobutyric acid (512 mg, 3.6 mmol, 16 eq.), DCC (206 mg, 3.6 mmol, 16 eq.) and DMAP (44 mg, 0.36 mmol, 1.6 eq) were dissolved in dry DCM (40 ml). The mixture was stirred for 5 min and placed in a CEM micro wave machine to irradiate at 150 °C for 20 min. The formed solid was removed by a glass funnel and the solvent was evaporated to give a yellow oil. The residue was dissolved in dry DEE and stored for 16 h. The formed solid was again removed by filtration and the solvent was removed under reduced pressure. The crude product was purified by column chromatography with Sephadex LH-20 to give a slightly yellow oil. Yield: 553 mg (74 %).
^{1}H NMR (400.13 MHz, CD_2Cl_2): δ = 1.05 (m, 16H, SiC*H*$_2$), 2.45-2.57 (m, 16H, $CH_2CH_2CF_3$), 2.63 (m, 16H, $CH_2CH_2CF_3$), 2.65 (m, 16H, $SiCH_2CH_2$), 2.73 (t, $^{3}J_{H-H}$ = 6.9 Hz, 16H, $SiCH_2CH_2SCH_2$), 3.61-3.65 (m, 80H, $SCH_2CH_2OCH_2CH_2OCH_2CH_2$), 3.67 (m, 16H, CH_2CH_2COO), 4.27 (m, 16H, CH_2CH_2COO). **^{13}C{^{1}H} NMR** (100.61 MHz, CD_2Cl_2): δ = 13.5 ($SiCH_2$), 26.8 ($SiCH_2CH_2$), 27.4 (q, $^{3}J_{C-F}$ = 3.2 Hz, $CH_2CH_2CF_3$), 29.6 (q, $^{2}J_{C-F}$ = 29.9 Hz, CH_2CF_3), 31.7 (CH_2SCH_2), 64.6 (CH_2CH_2COO), 69.3 (CH_2CH_2COO), 70.7, 70.9, 70.9, 71.0, 71.0 ($SCH_2CH_2OCH_2CH_2OCH_2CH_2$), 127.1 (q, $^{1}J_{C-F}$ = 275.9 Hz, CF_3), 171.2 (COO). **^{19}F{^{1}H} NMR** (376.50 MHz, CD_2Cl_2): δ = 67.30 (s). **^{29}Si DEPT-45 NMR** (49.7 MHz, CD_2Cl_2): δ = -68.7 (s). **HR ESI-TOF MS**, m/z: found 1675.38342 $[M+2Na]^{2+}$ (calc. 1675.38503). **IR (KBr, cm^{-1})**: ν (C-H) 2872, ν (C=O) 1742, δ (CH_2) 1444, ν_{as} (C-F) 1325, ν_{s} (C-F) 1188, ν_{as} (C-O-C) 1263, ν_{as} (Si-O-Si) 1111, ν_{s} (Si-O-Si) 551, ν (Si-O-Si) 472.

5.3.11 Synthesis of PFG 24

Under argon bis(3,3,3-trifluoropropyl)amine (647 µl, 3.83 mmol, 1 eq.) and 3-bromopropyl isothiocyanate (895 µl, 7.65 mmol, 2 eq.) were dissolved in dry ACN (45 ml). The mixture was refluxed at 90 °C for 22 h. The solvent was evaporated under reduced pressure and the residue was suspended in toluene. A white precipitate was formed, which was separated by centrifugation and washed thereafter four times with toluene. The white powder was dried at 40 °C for 2 d. Yield: 1.3 g of a fluffy white powder (89 %).
^{1}H NMR (400.13 MHz, $(CD_3)_2SO$): δ = 2.04 (m, 2H, $NHCH_2CH_2CH_2N^+$), 2.77 (m, 4H, CH_2CF_3), 3.33 (m, 2H, $NHCH_2CH_2CH_2N^+$), 3.49 (m, 2H, $NHCH_2CH_2CH_2$), 3.79 (m, 4H, $CH_2CH_2CF_3$), CH_2NH (s, 1H, 9.77). **^{13}C{^{1}H} NMR** (100.61 MHz, $(CD_3)_2SO$): δ = 20.1 ($NHCH_2CH_2CH_2N^+$), 27.2 ($NHCH_2CH_2CH_2N^+$), 30.1 (q, $^{2}J_{C-F}$ = 28.0 Hz, CH_2CF_3), 41.9

(NH*C*H_2CH$_2$), 43.4 (br, C*H*$_2$CH$_2$CF$_3$), 165.3 (NH*C*S), 126.1 (q, $^1J_{C-F}$ = 277.2 Hz, CH$_2$*C*F$_3$). **^{19}F{^{1}H} NMR** (376.50 MHz, (CD$_3$)$_2$SO): δ = -63.46 (s). **MS (FAB)**, m/z: found 309.2 [M]$^+$ (calc. 309.1). **IR (KBr, cm^{-1})**: ν (C-H) 2935, δ (CH$_2$) 1607, ν_{as} (C-F) 1395, ν_s (C-F) 1195, ν (C=S) 1024. **Elemental analysis** for $C_{10}H_{15}BrF_6N_2S$: C 30.98, H 3.79, N 7.31, S 8.20 (calc. C 30.86, H 3.88, N 7.20, S 8.24).

5.3.12 Synthesis of Bromo-POSS 26

OAPh-POSS (100 mg, 8.7×10^{-5} mol, 1 eq.) was dissolved in dry DMSO (4 ml) and 3-bromopropyl isothiocyanate was added. The mixture was stirred at rt for 24 h. Upon completion of the reaction the solvent was removed under reduced pressure. The product was precipitated with dry acetone. The slightly yellowish powder was washed two times with water and dried at 80 °C for 2 d. Yield: 187 mg (84 %).

^{1}H NMR (400.13 MHz, (CD$_3$)$_2$SO): δ = 2.08 (m, 16H, NHCH$_2$C*H*$_2$), 3.28 (m, 16H, CH$_2$C*H*$_2$Br), 3.45 (m, 16H, NHC*H*$_2$CH$_2$), 7.45 (m, A-part of an AA'BB'-system, 16H, Si-*o*-C*H*), 7.83 (m, B-part of an AA'BB'-system, 16H, Si-*m*-C*H*), 9.94 (s, 8H, N*H*CH$_2$CH$_2$), 11.29 (s, 8H, N*H*CSNHCH$_2$). **^{13}C{^{1}H} NMR** (100.61 MHz, (CD$_3$)$_2$SO): δ = 20.4 (NHCH$_2$*C*H$_2$), 26.6 (CH$_2$*C*H$_2$Br), 41.4 (NH*C*H$_2$CH$_2$), 124.8 (Si-*o*-*C*H), 127.6 (NH-*ipso*-Ar*C*), 135.3 (Si-*m*-*C*H), 138.0 (Si-*p*-Ar*C*), (C=S) not observed. **^{29}Si DEPT-45 NMR** (49.70 MHz, (CD$_3$)$_2$SO): δ = -78.4 (s). **MS (ESI)**, m/z: found 649.55 [M+4H]$^{4+}$ 649.85 (calc. 649.55), 324.86 [M+8H]$^{8+}$ (calc. 325.28). **IR (KBr, cm^{-1})**: ν (C-H) 2935, δ (CH$_2$) 1619, δ (N-H) 1592, ν (C=S)/ν_{as} (Si-O-Si) 1125, ν_s (Si-O-Si) 530, δ (Si-O-Si) 494.

5.3.13 Synthesis of PFG 28

Under argon atmosphere 3,5-bis(trifluoromethyl)pyridine (1 g, 4.65 mmol, 1 eq.) and two equal portions of 3-bromopropyl isothiocyanate (3.35 g, 18.6 mmol, 4 eq.) were refluxed in dry ACN (50 ml) for 4 d. The second portion of 3-bromopropyl isothiocyanate was added on the second day. The solvent was evaporated and the product was precipitated from toluene. The slightly yellowish powder was washed two times with toluene. Yield: 37 mg (2 %).

^{1}H NMR (400.13 MHz, (CD$_3$)$_2$SO): δ = 2.43 (m, 2H, NCSCH$_2$C*H*$_2$CH$_2$), 3.89 (t, $^3J_{H-H}$ = 6.5 Hz, 2H, NCSC*H*$_2$CH$_2$), 4.86 (t, $^3J_{H-H}$ = 7.3 Hz, 2H, C*H*$_2$N$_{Py}^+$), 9.73 (s, 1H, CH$_2$NPy$^+$-p-C*H*), 10.09 (s, 2H, CH$_2$NPy$^+$-*o*-C*H*). **^{13}C{^{1}H} NMR** (100.61 MHz, (CD$_3$)$_2$SO): δ = 29.7 (NCSCH$_2$*C*H$_2$CH$_2$), 41.9 (NCS*C*H$_2$CH$_2$), 59.9 (*C*H$_2$N$_{Py}^+$), 119.8 (br, *C*CF$_3$), (q, $^1J_{C-F}$ = 277

Hz, *C*F_3), 140.7 ($CH_2N_{Py}^+$-*p*-*C*H), 147.4 ($CH_2N_{Py}^+$-*m*-C*H*), (N*C*S) not observed. **^{19}F{^{1}H} NMR** (376.50 MHz, $(CD_3)_2SO$): δ = -61.05 (s). **MS (ESI)**, m/z: found 430.24 $[M+8K]^{8+}$ (calc. 430.56). **IR (KBr, cm^{-1})**: ν (C-H) 2921, ν (NCS) 2186-2126, δ (CH_2) 1468, ν_{as} (C-F) 1362, ν (C=S) 1159.

5.3.14 Synthesis of PFG 30

4-Trifluoromethylpyridine (1 g, 6.8 mmol, 1 eq.) was dissolved in dry acetonitrile (50 ml) and two equal portions of 3-bromopropyl isothiocyanate (4.90 g, 27.2 mmol, 4 eq.) were added over 4 days. The solution was refluxed at 105 °C for 2 days. After 2 days the second portion of 3-bromopropyl isothiocyanate (2.45 g) was added and the mixture was refluxed for another 2 days. The solvent was evaporated and the product was precipitated with toluene. The substance was dried at 70 °C for 3 d. Yield: 2.1 g of a slightly yellowish powder (94 %).

^{1}H NMR (400.13 MHz, CD_3CN): δ = 2.42 (m, 2H, $NCSCH_2C\mathit{H}_2CH_2$), 3.85 (t, $^3J_{H\text{-}H}$ = 6.3 Hz, 2H, $NCSC\mathit{H}_2CH_2$), 4.95 (t, $^3J_{H\text{-}H}$ = 7.4 Hz, 2H, $C\mathit{H}_2N_{Py}^+$), 8.40 (m, A-part of an AA'XX'-system, 2H, $CH_2N_{Py}^+$-*m*-C*H*), 9.40 (d, X-part of an AA'XX'-system, 2H, $CH_2N_{Py}^+$-*o*-C*H*). **^{13}C{^{1}H} NMR** (100.61 MHz, CD_3CN): δ = 31.4 ($NCSCH_2\mathit{C}H_2CH_2$), 43.0 ($NCS\mathit{C}H_2CH_2$), 60.6 ($\mathit{C}H_2N_{Py}^+$), 120.9 (s, br, *C*CF_3), 122.2 (q, $^1J_{C\text{-}F}$ = 277 Hz, *C*F_3), 126.3 (q, $^3J_{C\text{-}F}$ = 3.3 Hz, $CH_2N_{Py}^+$-*m*-C*H*), 127.8 (N*C*S), 148.2 (s, br, N_{Py}^+-*o*-*C*H). **^{19}F{^{1}H} NMR** (376.50 MHz, CD_3CN): δ = -66.00 (s). **MS (ESI)**, m/z: found 246.76 $[M]^+$ (calc. 247.05). **IR (KBr, cm^{-1})**: ν (C-H) 2993, ν (NCS) 2194-2131, δ (CH_2) 1457, ν_{as} (C-F) 1333, ν (C=S) 1185-1147. **Elemental analysis** for $C_{10}H_{10}F_3N_2S^+Br^-$: found C 36.40, H 2.90, N 8.66, S 9.43 (calc. C 36.71, H 3.08, N 8.56, S 9.80).

5.3.15 Synthesis of PF-POSS 31

A solution of octaaminophenyl-POSS (56 mg, 4.84×10^{-5} mol, 1 eq.) in dry ACN (30 ml) was prepared. **30** (190 mg, 5.80×10^{-4} mol, 12 eq.) dissolved in dry THF (13 ml) was added dropwise over a period of 3 h. The mixture was stirred at rt for 24 h, then refluxed at 80 °C for 24 h and subsequently refluxed at 98 °C for 16 h. A yellow precipitate was formed which was collected after decanting the solvent. The solid was washed four times with ACN/THF (1 : 1) and once with DEE to give an yellowish powder. The product was dried at rt for 24 h *in vacuo*. Yield: 110 mg, (86 %).

^{1}H NMR (400.13 MHz, $(CD_3)_2SO$): δ = 2.27 (m, 16H, $C\mathit{H}_2CH_2N_{Py}^+$), 3.56 (m, 16H,

NHC*H*$_2$CH$_2$CH$_2$N$_{Py}^+$), 4.80 (t, br, $^3J_{H-H}$ = 6.9 Hz, 16H, C*H*$_2$N$_{Py}^+$), 7.59 (m, A-part of an AA'BB'-system, 16H, Si-*o*-C*H*), 7.64 (m, B-part of an AA'BB'-system 16H, Si-*m*-C*H*), 8.24 (s, 8H, N*H*CH$_2$CH$_2$), 8.68 (m, X-part of an AA'XX'-system, 16H, CH$_2$N$_{Py}^+$-*m*-C*H*), 9.49 (m, X-part of an AA'XX'-system, 16H, CH$_2$N$_{Py}^+$-*o*-C*H*, 9.96 (s, 8H, SiAr-N*H*CS). **^{13}C{^{1}H} NMR** (100.61 MHz, (CD$_3$)$_2$SO): δ = 30.0 (*C*H$_2$CH$_2$N$_{Py}^+$), 40.3 (NH*C*H$_2$CH$_2$), 59.6 (*C*H$_2$N$_{Py}^+$), 121.4 (q, $^1J_{C-F}$ = 274.5 Hz, *C*F$_3$), 121.6 (Si-*o*-*C*H), 124.9 (N$_{Py}^+$-*m*-*C*H), 134.2 (Si-*m*-*C*H), 134.8 (Si-*ipso*-Ar*C*), 142.2 (NH-*ipso*-Ar*C*), 142.7 (q, $^2J_{C-F}$ = 34.0 Hz, *C*CF$_3$), 147.3 (N$_{Py}^+$-*o*-*C*H), (*C*S) not observed. **^{19}F{^{1}H} NMR** (376.50 MHz, (CD$_3$)$_2$SO): δ = -63.86 (s). **^{1}H-^{29}Si HMQC NMR** (99.36 MHz, (CD$_3$)$_2$SO): δ = -65.0 (s). **MS (ESI)**, m/z: found 430.24 $[M+8K]^{8+}$ (calc. 430.56). **IR (KBr, cm^{-1})**: ν (C-H) 3045, ν (CH$_2$)/ν (NH-C=S) 1599-1464, ν_{as} (C-F) 1323, ν_{as} (Si-O-Si) 1124, ν (C=S) 1094, ν_s (Si-O-Si) 523, δ (Si-O-Si) 429. **Elemental analysis** for C$_{128}$H$_{128}$Br$_8$F$_{24}$N$_{24}$O$_{12}$S$_8$Si$_8$: C 40.78, H 3.64, N 8.48, S 6.47 (calc. C 40.77, H 3.42, N 8.91, S 6.8).

5.3.16 Synthesis of Ln[DOTA-BA] and Ln[DOTA-GA]

The corresponding ligand (**DOTA-BA**, **DOTA-GA**) was dissolved in distilled water (0.5 ml) and a stock solution of LnCl$_3$ (1.1 eq.) was added. The pH of the solution was adjusted to 6-7 with (*n*-Bu)$_4$NOH (20 %). The solution was stirred at 60 °C for 16 h for GdCl$_3$ and 3 h for YCl$_3$. An excess of non-coordinated Gd(III) or Y(III) ions was removed by the addition of a cation exchange resin (Chelex 100) and stirring for 2 h. The solution was separated from the chelex and the solvent was evaporated *in vacuo* at 40 °C. The absence of free Gd(III) ions was certified by the xylenol test.[153]

5.3.17 Synthesis of 50 nm silica particles M0$_{50}$

Ethanol (300 ml) was warmed to 35 °C. After 30 min an aqueous NH$_4$OH solution (7.6 ml, 101 mmol) and TEOS (11.00 ml, 33.60 mmol) were added under strong stirring. After 20 h the mixture was cooled to room temperature and the particles were separated by centrifugation. The particles were dispersed in water/ethanol (3 : 1) and centrifugated again. This washing step was repeated with water/ethanol (1 : 3) and ethanol. After each washing step the particles were ultrasonicated for 5 min. The particles were dried *in vacuo* at 100 °C for 16 h.

5.3.18 Synthesis of amino terminated nanoparticles $M1_{50}C_3NH_2$

Under argon **$M0_{50}$** (1.8 g) was suspended in dry toluene (15 ml) and APTES (530 µl) was added to the mixture. After refluxing the suspension of the particles for 23 h they were separated by centrifugation and washed twice with toluene and *n*-hexane. After each washing step the particles were ultrasonicated for 5 min. The particles were dried *in vacuo* at 100 °C for 2 d. Yield: 1.5 g of a colorless powder.

5.3.19 Gd(III) chelate modified silica nanoparticles $M1_{50}C_3$[Gd-BA] and $M1_{50}C_3$[Gd-GA]

To a solution of **[Gd-BA](*n*-Bu)$_4$N** or **[Gd-GA](*n*-Bu)$_4$N** (50.4 µmol, 1.1 eq.) in dry DMSO (1 ml), TBTU (24.27 mg, 75.6 µmol, 1.65 eq.) and DIPEA (86 µl, 0.504 mmol, 11 eq.) were added and stirred. **$M1_{50}C_3NH_2$** (100 mg, estimated 45.8 µmol of $-NH_2$, 1 eq.) was suspended in dry DMSO (2 ml). The silica particle suspension was added after 5 min and the mixture was stirred for 3 h. After separation by centrifugation the particles were consecutively washed with DMF, water, ethanol and *n*-hexane. The particles were ultrasonicated for 5 min after each washing step. The particles were dried *in vacuo* at 60 °C for 3 d.

5.3.20 Gd(III) chelate modified silica nanoparticles $M1_{15}C_3$[Gd-BA] and $M1_{15}C_3$[Gd-GA]

The commercially available particles **$M1_{15}C_3NH_2$** (150 mg, estimated 0.172 mmol of $-NH_2$, 1 eq.) were suspended in dry DMSO (2 ml). To a solution of **[Gd-BA](*n*-Bu)$_4$N** and **[Gd-GA](*n*-Bu)$_4$N** (0.189 mmol, 1.1 eq.), respectively, in dry DMSO (1 ml), TBTU (91.01 mg, 28.4 µmol, 1.65 eq) and DIPEA (321 µl, 1.89 mmol, 11 eq.) were added and stirred. After 5 min the nanoparticle suspension was added and the mixture was stirred for 3 h. The particles were separated by centrifugation and consecutively washed with DMF, water, ethanol and *n*-hexane. After each washing step the particles were ultrasonicated for 5 min. The particles were dried *in vacuo* at 60 °C for 3 d.

5.3.21 Synthesis of acetylated Gd(III) chelate modified silica nanoparticles $M1_{15/50/130}C_3$[Gd-BA]ac and $M1_{15/50/130}C_3$[Gd-GA]ac

$M1_{15/50/130}C_3$[Gd-BA] and **$M1_{15/50/130}C_3$[Gd-GA]** silica nanoparticles (20 mg) were suspended in 4 ml of DMF, respectively. Acetic anhydride (2 ml) was added and each

mixture was first stirred for 2.5 h, then ultrasonicated for 30 min. Each of the materials obtained was separated by centrifugation and washed with water, water/ethanol (1 : 1), ethanol and *n*-hexane. After each washing step the particles were ultrasonicated for 5 min. The particles were dried at 60 °C for 16 h.

5.3.22 Repeated conjugation of $M1_{15}C_3$[Gd-GA] with [Gd-GA]

$M1_{15}C_3$[Gd-GA] (30 mg, estimated 16.2 µmol of $-NH_2$, 1 eq.) was suspended in DMSO (1 ml). To a solution of **Gd[DOTA-GA](*n*-Bu)$_4$N** (10 mg, 21.0 µmol, 1.3 eq) in dry DMSO (1 ml), TBTU (10.1 mg, 32.0 µmol, 2 eq.) and DIPEA (36 µl, 0.21 mmol, 13 eq.) were added and stirred for 5 min. The nanoparticle suspension was added and the mixture was ultrasonicated for 1 h. After separation by centrifugation the particles were washed with DMF, water, ethanol and *n*-hexane, ultrasonicated between the washing steps and dried at 60 °C for 1 d.

5.3.23 Repeated conjugation of $M1_{50}C_3$[Gd-GA] with [Gd-GA]

$M1_{50}C_3$[Gd-GA] (60 mg, estimated 13.7 µmol of $-NH_2$, 1 eq.) was suspended in DMSO (1.5 ml). To a solution of **[Gd-GA](*n*-Bu)$_4$N** (8.51 mg, 17.8 µmol, 1.3 eq) in dry DMSO (1 ml), TBTU (8.6 mg, 26.8 µmol, 2 eq.) and DIPEA (31 µl, 0.18 mmol, 13 eq.) were added and stirred for 5 min. After adding the nanoparticle suspension the mixture was ultrasonicated for 1.5 h. By centrifugation separated particles were washed with DMF, water, ethanol and *n*-hexane, ultrasonicated between the washing steps and dried at 60 °C for 1 d.

References

[1] P. Caravan, J. J. Ellison, T. J. McMurry, R. B. Lauffer, *Chem. Rev.* **1999**, *99*, 2293–2352.

[2] A. S. Merbach, L. Helm, É. Tóth, *The Chemistry of Contrast Agents in Medical Magnetic Resonance Imaging*, John Wiley & Sons, **2013**.

[3] G. Paul, Y. Prado, N. Dia, E. Rivière, S. Laurent, M. Roch, L. V. Elst, R. N. Muller, L. Sancey, P. Perriat, et al., *Chem. Commun.* **2014**, *50*, 6740–6743.

[4] G. H. Im, S. M. Kim, D.-G. Lee, W. J. Lee, J. H. Lee, I. S. Lee, *Biomaterials* **2013**, *34*, 2069–2076.

[5] B. Drahoš, I. Lukeš, É. Tóth, *Eur. J. Inorg. Chem.* **2012**, *2012*, 1975–1986.

[6] J. W. M. Bulte, D. L. Kraitchman, *NMR Biomed.* **2004**, *17*, 484–499.

[7] R. Weissleder, G. Elizondo, J. Wittenberg, C. A. Rabito, H. H. Bengele, L. Josephson, *Radiology* **1990**, *175*, 489–493.

[8] L. Telgmann, M. Sperling, U. Karst, *Anal. Chim. Acta* **2013**, *764*, 1–16.

[9] S. Laurent, D. Forge, M. Port, A. Roch, C. Robic, L. Vander Elst, R. N. Muller, *Chem. Rev.* **2008**, *108*, 2064–2110.

[10] E. Kanal, K. Maravilla, H. A. Rowley, *Am. J. Neuroradiol.* **2014**.

[11] V. Kubíček, É. Tóth, in *Adv. Inorg. Chem.* (Ed.: Rudi van Eldik and Colin D. Hubbard), Academic Press, **2009**, pp. 63–129.

[12] I. Tirotta, V. Dichiarante, C. Pigliacelli, G. Cavallo, G. Terraneo, F. B. Bombelli, P. Metrangolo, G. Resnati, *Chem. Rev.* **2014**.

[13] I. Tirotta, A. Mastropietro, C. Cordiglieri, L. Gazzera, F. Baggi, G. Baselli, M. G. Bruzzone, I. Zucca, G. Cavallo, G. Terraneo, et al., *J. Am. Chem. Soc.* **2014**, *136*, 8524–8527.

[14] U. Flögel, Z. Ding, H. Hardung, S. Jander, G. Reichmann, C. Jacoby, R. Schubert, J. Schrader, *Circulation* **2008**, *118*, 140–148.

[15] D. Bartusik, D. Aebisher, *Biomed. Pharmacother.* **2014**, *68*, 813–817.

[16] M. J. Couch, I. K. Ball, T. Li, M. S. Fox, A. V. Ouriadov, B. Biman, M. S. Albert, *NMR Biomed.* **2014**.

[17] C. Jacoby, S. Temme, F. Mayenfels, N. Benoit, M. P. Krafft, R. Schubert, J. Schrader, U. Flögel, *NMR Biomed.* **2014**, *27*, 261–271.

[18] M. Srinivas, P. Boehm-Sturm, M. Aswendt, E. D. Pracht, C. G. Figdor, I. J. de Vries, M. Hoehn, *J. Vis. Exp. JoVE* **2013**, e50802.

[19] M. A. Hahn, A. K. Singh, P. Sharma, S. C. Brown, B. M. Moudgil, *Anal. Bioanal. Chem.* **2011**, *399*, 3–27.

[20] Z. Zhou, L. Wang, X. Chi, J. Bao, L. Yang, W. Zhao, Z. Chen, X. Wang, X. Chen, J. Gao, *ACS Nano* **2013**, *7*, 3287–3296.

[21] A. W. H. Lin, N. A. Lewinski, J. L. West, N. J. Halas, R. A. Drezek, *J. Biomed. Opt.* **2005**, *10*, 064035–064035–10.

[22] H. B. Na, I. C. Song, T. Hyeon, *Adv. Mater.* **2009**, *21*, 2133–2148.

[23] A. Z. Wilczewska, K. Niemirowicz, K. H. Markiewicz, H. Car, *Pharmacol. Rep. PR* **2012**, *64*, 1020–1037.

[24] R. Joshi, V. Feldmann, W. Koestner, C. Detje, S. Gottschalk, H. A. Mayer, M. G. Sauer, J. Engelmann, *Biol. Chem.* **2013**, *394*, 125–135.

[25] V. Feldmann, Dissertation, University of Tübingen, **2011**.

[26] J.-L. Bridot, A.-C. Faure, S. Laurent, C. Rivière, C. Billotey, B. Hiba, M. Janier,

V. Josserand, J.-L. Coll, L. Vander Elst, et al., *J. Am. Chem. Soc.* **2007**, *129*, 5076–5084.
[27] J. Key, J. F. Leary, *Int. J. Nanomedicine* **2014**, *9*, 711–726.
[28] J. Henig, E. Tóth, J. Engelmann, S. Gottschalk, H. A. Mayer, *Inorg. Chem.* **2010**, *49*, 6124–6138.
[29] M. P. Lowe, *Aust. J. Chem.* **2002**, *55*, 551–556.
[30] Y. Jin, C. Jia, S.-W. Huang, M. O'Donnell, X. Gao, *Nat. Commun.* **2010**, *1*, 41.
[31] A. Keliris, I. Mamedov, G. E. Hagberg, N. K. Logothetis, K. Scheffler, J. Engelmann, *Contrast Media Mol. Imaging* **2012**, *7*, 478–483.
[32] B. E. Rolfe, I. Blakey, O. Squires, H. Peng, N. R. B. Boase, C. Alexander, P. G. Parsons, G. M. Boyle, A. K. Whittaker, K. J. Thurecht, *J. Am. Chem. Soc.* **2014**, *136*, 2413–2419.
[33] X. Yang, Y. Sun, S. Kootala, J. Hilborn, A. Heerschap, D. Ossipov, *Carbohydr. Polym.* **2014**, *110*, 95–99.
[34] G. Bhakta, R. K. Sharma, N. Gupta, S. Cool, V. Nurcombe, A. Maitra, *Nanomedicine Nanotechnol. Biol. Med.* **2011**, *7*, 472–479.
[35] T.-H. Chung, S.-H. Wu, M. Yao, C.-W. Lu, Y.-S. Lin, Y. Hung, C.-Y. Mou, Y.-C. Chen, D.-M. Huang, *Biomaterials* **2007**, *28*, 2959–2966.
[36] X. Li, L. Wang, Y. Fan, Q. Feng, F. Cui, *J. Nanomater.* **2012**, *2012*, e548389.
[37] W. J. Rieter, J. S. Kim, K. M. L. Taylor, H. An, W. Lin, T. Tarrant, W. Lin, *Angew. Chem. Int. Ed.* **2007**, *46*, 3680–3682.
[38] K. M. L. Taylor-Pashow, J. D. Rocca, R. C. Huxford, W. Lin, *Chem. Commun.* **2010**, *46*, 5832–5849.
[39] F. Carniato, L. Tei, W. Dastrù, L. Marchese, M. Botta, *Chem. Commun.* **2009**, 1246–1248.
[40] F. Carniato, L. Tei, M. Cossi, L. Marchese, M. Botta, *Chem. – Eur. J.* **2010**, *16*, 10727–10734.
[41] S.-H. Wu, Y. Hung, C.-Y. Mou, *Chem. Commun. Camb. U. K.* **2011**, *47*, 9972–9985.
[42] W.-Y. Huang, G.-L. Davies, J. J. Davis, *Chem. Commun. Camb. U. K.* **2013**, *49*, 60–62.
[43] K. M. L. Taylor-Pashow, R. Della, W. Lin, *Nanomaterials* **2012**, *2*, 1–14.
[44] H. Skår, Y. Liang, E. S. Erichsen, R. Anwander, J. G. Seland, *Microporous Mesoporous Mater.* **2013**, *175*, 125–133.
[45] C. Platas-Iglesias, L. Vander Elst, W. Zhou, R. N. Muller, C. F. G. C. Geraldes, T. Maschmeyer, J. A. Peters, *Chem. – Eur. J.* **2002**, *8*, 5121–5131.
[46] P. Caravan, *Chem. Soc. Rev.* **2006**, *35*, 512.
[47] D. W. Scott, *J. Am. Chem. Soc.* **1946**, *68*, 356–358.
[48] R. H. Baney, M. Itoh, A. Sakakibara, T. Suzuki, *Chem. Rev.* **1995**, *95*, 1409–1430.
[49] P. P. Pescarmona, T. Maschmeyer, *Aust. J. Chem.* **2001**, *54*, 583–596.
[50] G. Li, L. Wang, H. Ni, C. U. P. Jr, *J. Inorg. Organomet. Polym.* **2001**, *11*, 123–154.
[51] E. Lindner, T. Schneller, F. Auer, H. A. Mayer, *Angew. Chem. Int. Ed.* **1999**, *38*, 2154–2174.
[52] Y. Chujo, K. Tanaka, *J. Netw. Polym.* **2011**, *32*, 233–244.
[53] D. A. Loy, K. J. Shea, *Chem. Rev.* **1995**, *95*, 1431–1442.
[54] R. M. Laine, C. Zhang, A. Sellinger, L. Viculis, *Appl. Organomet. Chem.* **1998**, *12*, 715–723.
[55] T. K. Jain, I. Roy, T. K. De, A. Maitra, *J. Am. Chem. Soc.* **1998**, *120*, 11092–11095.

[56] L. E. Euliss, J. A. DuPont, S. Gratton, J. DeSimone, *Chem. Soc. Rev.* **2006**, *35*, 1095–1104.
[57] C. Barbé, J. Bartlett, L. Kong, K. Finnie, H. Q. Lin, M. Larkin, S. Calleja, A. Bush, G. Calleja, *Adv. Mater.* **2004**, *16*, 1959–1966.
[58] R. K. Iler, *The Chemistry of Silica: Solubility, Polymerization, Colloid and Surface Properties and Biochemistry of Silica*, John Wiley & Sons, New York, **1979**.
[59] Y. Kaneko, E. B. Coughlin, T. Gunji, M. Itoh, K. Matsukawa, K. Naka, *Int. J. Polym. Sci.* **2012**, *2012*, e453821.
[60] F. Kocak, Diploma thesis, University of Tübingen, **2011**.
[61] J. Henig, Dissertation, University of Tübingen, **2010**.
[62] M. Herrero, B. Alonso, J. Losada, P. García-Armada, C. M. Casado, *Organometallics* **2012**, *31*, 6344–6350.
[63] Y. El Aziz, A. R. Bassindale, P. G. Taylor, P. N. Horton, R. A. Stephenson, M. B. Hursthouse, *Organometallics* **2012**, *31*, 6032–6040.
[64] W. Stöber, A. Fink, E. Bohn, *J. Colloid Interface Sci.* **1968**, *26*, 62–69.
[65] F. D. Osterholtz, E. R. Pohl, *J. Adhes. Sci. Technol.* **1992**, *6*, 127–149.
[66] C. J. Brinker, G. W. Scherer, *J. Non-Cryst. Solids* **1985**, *70*, 301–322.
[67] N. Plumeré, A. Ruff, B. Speiser, V. Feldmann, H. A. Mayer, *J. Colloid Interface Sci.* **2012**, *368*, 208–219.
[68] B. Chu, in *Soft Matter Charact.* (Eds.: R. Borsali, R. Pecora), Springer Netherlands, **2008**, pp. 335–372.
[69] Malvern Instruments, *Zetasizer Nano User Manual*, **2013**.
[70] T. Wriedt, in *Mie Theory* (Eds.: W. Hergert, T. Wriedt), Springer Berlin Heidelberg, **2012**, pp. 53–71.
[71] A. Berger, *BMJ* **2002**, *324*, 35.
[72] R. B. Lauffer, *Chem. Rev.* **1987**, *87*, 901–927.
[73] R. V. Southwood-Jones, W. L. Earl, K. E. Newman, A. E. Merbach, *J. Chem. Phys.* **1980**, *73*, 5909–5918.
[74] J.-M. Idée, M. Port, I. Raynal, M. Schaefer, S. Le Greneur, C. Corot, *Fundam. Clin. Pharmacol.* **2006**, *20*, 563–576.
[75] M. Port, J.-M. Idée, C. Medina, C. Robic, M. Sabatou, C. Corot, *BioMetals* **2008**, *21*, 469–490.
[76] Y.-M. Wang, C.-H. Lee, G.-C. Liu, R.-S. Sheu, *J. Chem. Soc. Dalton Trans.* **1998**, 4113–4118.
[77] M. F. Tweedle, J. J. Hagan, K. Kumar, S. Mantha, C. A. Chang, *Magn. Reson. Imaging* **1991**, *9*, 409–415.
[78] S. Aime, M. Botta, E. Terreno, in *Adv. Inorg. Chem.*, Academic Press, **2005**, pp. 173–237.
[79] J. Kowalewski, D. Kruk, G. Parigi, in *Adv. Inorg. Chem.*, Academic Press, **2005**, pp. 41–104.
[80] S. Aime, M. Fasano, E. Terreno, *Chem. Soc. Rev.* **1998**, *27*, 19.
[81] P. Caravan, C. T. Farrar, L. Frullano, R. Uppal, *Contrast Media Mol. Imaging* **2009**, *4*, 89–100.
[82] R. Díaz-López, N. Tsapis, E. Fattal, *Pharm. Res.* **2010**, *27*, 1–16.
[83] J. Chen, G. M. Lanza, S. A. Wickline, *Wiley Interdiscip. Rev. Nanomed. Nanobiotechnol.* **2010**, *2*, 431–440.
[84] H. Matsushita, S. Mizukami, F. Sugihara, Y. Nakanishi, Y. Yoshioka, K. Kikuchi, *Angew. Chem. Int. Ed.* **2014**, *53*, 1008–1011.

[85] G. N. Holland, P. A. Bottomley, W. S. Hinshaw, *J. Magn. Reson. 1969* **1977**, *28*, 133–136.
[86] J. Wang, M. Sánchez-Roselló, J. L. Aceña, C. del Pozo, A. E. Sorochinsky, S. Fustero, V. A. Soloshonok, H. Liu, *Chem. Rev.* **2014**, *114*, 2432–2506.
[87] B. Z. Gong, M. Gill, D. B. Washburn, W. C. Davenport, D. Adams, L. Kwock, *Magn. Reson. Imaging* **1991**, *9*, 101–106.
[88] J. Yu, V. D. Kodibagkar, W. Cui, R. P. Mason, *Curr. Med. Chem.* **2005**, *12*, 819–848.
[89] J. W. M. Bulte, *Nat. Biotechnol.* **2005**, *23*, 945–946.
[90] J. Ruiz-Cabello, B. P. Barnett, P. A. Bottomley, J. W. M. Bulte, *NMR Biomed.* **2011**, *24*, 114–129.
[91] J. M. Pérez-Sánchez, R. Pérez de Alejo, I. Rodríguez, M. Cortijo, G. Peces-Barba, J. Ruiz-Cabello, *Magn. Reson. Med. Off. J. Soc. Magn. Reson. Med. Soc. Magn. Reson. Med.* **2005**, *54*, 460–463.
[92] R. P. Mason, *Artif. Cells Blood Substit. Biotechnol.* **1994**, *22*, 1141–1153.
[93] A. Mastropietro, E. De Bernardi, G. L. Breschi, I. Zucca, M. Cametti, C. D. Soffientini, M. de Curtis, G. Terraneo, P. Metrangolo, R. Spreafico, et al., *J. Magn. Reson. Imaging* **2014**, *40*, 162–170.
[94] J. Hennig, A. Nauerth, H. Friedburg, *Magn. Reson. Med.* **1986**, *3*, 823–833.
[95] A. Oppelt, R. Graumann, H. Barfuss, H. Fischer, W. Hartl, W. Schajor, *Electromedica* **1986**, 15–18.
[96] A. Haase, J. Frahm, D. Matthaei, W. Hanicke, K.-D. Merboldt, *J. Magn. Reson. 1969* **1986**, *67*, 258–266.
[97] F. J. Feher, K. D. Wyndham, D. Soulivong, F. Nguyen, *J. Chem. Soc. Dalton Trans.* **1999**, 1491.
[98] Y. Li, W.-B. Zhang, I.-F. Hsieh, G. Zhang, Y. Cao, X. Li, C. Wesdemiotis, B. Lotz, H. Xiong, S. Z. D. Cheng, *J. Am. Chem. Soc.* **2011**, *133*, 10712–10715.
[99] M. L. Conte, S. Staderini, A. Chambery, N. Berthet, P. Dumy, O. Renaudet, A. Marra, A. Dondoni, *Org. Biomol. Chem.* **2012**, *10*, 3269–3277.
[100] M. L. Conte, M. J. Robb, Y. Hed, A. Marra, M. Malkoch, C. J. Hawker, A. Dondoni, *J. Polym. Sci. Part Polym. Chem.* **2011**, *49*, 4468–4475.
[101] J. Xu, X. Li, C. M. Cho, C. L. Toh, L. Shen, K. Y. Mya, X. Lu, C. He, *J. Mater. Chem.* **2009**, *19*, 4740–4745.
[102] H. J. Konig, H. C. Marsmann, M. C. Letzel, in *Organosilicon Chem. Set* (Eds.: N. Auner, J. Weis), Wiley-VCH Verlag GmbH, **2008**, pp. 425–428.
[103] X. Yu, S. Zhong, X. Li, Y. Tu, S. Yang, R. M. Van Horn, C. Ni, D. J. Pochan, R. P. Quirk, C. Wesdemiotis, et al., *J. Am. Chem. Soc.* **2010**, *132*, 16741–16744.
[104] W.-B. Zhang, Y. Li, X. Li, X. Dong, X. Yu, C.-L. Wang, C. Wesdemiotis, R. P. Quirk, S. Z. D. Cheng, *Macromolecules* **2011**, *44*, 2589–2596.
[105] Y. Gao, A. Eguchi, K. Kakehi, Y. C. Lee, *Org. Lett.* **2004**, *6*, 3457–3460.
[106] L. Li, R. Liang, Y. Li, H. Liu, S. Feng, *J. Colloid Interface Sci.* **2013**, *406*, 30–36.
[107] A. Luo, X. Jiang, H. Lin, J. Yin, *J. Mater. Chem.* **2011**, *21*, 12753–12760.
[108] S. Shen, F. Ye, C. Zhang, Y. Xiong, L. Su, S. Zhao, *Analyst* **2014**.
[109] Y. Li, K. Guo, H. Su, X. Li, X. Feng, Z. Wang, W. Zhang, S. Zhu, C. Wesdemiotis, S. Z. D. Cheng, et al., *Chem. Sci.* **2014**, *5*, 1046–1053.
[110] K. Rózga-Wijas, J. Chojnowski, *J. Inorg. Organomet. Polym. Mater.* **2012**, *22*, 588–594.
[111] X. Wang, J. M. Chin, C. He, J. Xu, *Sci. Adv. Mater.* **2014**, *6*, 1553–1561.
[112] T. Fukuyama, M. T. Rahman, N. Kamata, I. Ryu, *Beilstein J. Org. Chem.* **2009**, *5*.
[113] J. Brandrup, E. H. Immergut, E. A. Grulke, Eds. , *Polymer Handbook, 4th Edition*,

Wiley-Interscience, New York ; Chichester, **2003**.
[114] R. A. Newmark, J. R. Hill, *Org. Magn. Reson.* **1977**, *9*, 589–592.
[115] R. A. Newmark, J. R. Hill, G. V. D. Tiers, *Magn. Reson. Chem.* **1988**, *26*, 612–614.
[116] T. Yamaoka, Y. Tabata, Y. Ikada, *J. Pharm. Sci.* **1994**, *83*, 601–606.
[117] S. S. Banerjee, N. Aher, R. Patil, J. Khandare, *J. Drug Deliv.* **2012**, *2012*, e103973.
[118] J. M. Harris, N. E. Martin, M. Modi, *Clin. Pharmacokinet.* **2001**, *40*, 539–551.
[119] S. Zalipsky, *Adv. Drug Deliv. Rev.* **1995**, *16*, 157–182.
[120] P. Calvo, B. Gouritin, H. Chacun, D. Desmaële, J. D'Angelo, J.-P. Noel, D. Georgin, E. Fattal, J. P. Andreux, P. Couvreur, *Pharm. Res.* **2001**, *18*, 1157–1166.
[121] J. V. Jokerst, T. Lobovkina, R. N. Zare, S. S. Gambhir, *Nanomed.* **2011**, *6*, 715–728.
[122] E. A. Nance, G. F. Woodworth, K. A. Sailor, T.-Y. Shih, Q. Xu, G. Swaminathan, D. Xiang, C. Eberhart, J. Hanes, *Sci. Transl. Med.* **2012**, *4*, 149ra119–149ra119.
[123] A. Ardana, A. K. Whittaker, K. J. Thurecht, *Macromolecules* **2014**, *47*, 5211–5219.
[124] M. Hamidi, A. Azadi, P. Rafiei, *Drug Deliv.* **2006**, *13*, 399–409.
[125] J. M. Harris, R. B. Chess, *Nat. Rev. Drug Discov.* **2003**, *2*, 214–221.
[126] C. Monfardini, O. Schiavon, P. Caliceti, M. Morpurgo, J. M. Harris, F. M. Veronese, *Bioconjug. Chem.* **1995**, *6*, 62–69.
[127] G. S. Kwon, *Crit. Rev. Ther. Drug Carrier Syst.* **2003**, *20*, 357–403.
[128] A. G. Kanaras, F. S. Kamounah, K. Schaumburg, C. J. Kiely, M. Brust, *Chem. Commun.* **2002**, 2294–2295.
[129] A. Dondoni, A. Marra, *Chem. Soc. Rev.* **2012**, *41*, 573.
[130] H. Lang, C. Duschl, H. Vogel, *Langmuir* **1994**, *10*, 197–210.
[131] P.-T. Lin, D. B. Salunke, L.-H. Chen, C.-M. Sun, *Org. Biomol. Chem.* **2011**, *9*, 2925–2937.
[132] M. P. Krafft, J. G. Riess, *J. Polym. Sci. Part Polym. Chem.* **2007**, *45*, 1185–1198.
[133] M. Ogawa, S. Nitahara, H. Aoki, S. Ito, M. Narazaki, T. Matsuda, *Macromol. Chem. Phys.* **2010**, *211*, 1602–1609.
[134] Y. B. Yu, *Wiley Interdiscip. Rev. Nanomed. Nanobiotechnol.* **2013**.
[135] S. A. Holmes, T. D. Thomas, *J. Am. Chem. Soc.* **1975**, *97*, 2337–2341.
[136] M. Longmire, P. L. Choyke, H. Kobayashi, *Nanomed.* **2008**, *3*, 703–717.
[137] R. Delgado, J. J. R. Frausto Da Silva, M. T. S. Amorim, M. F. Cabral, S. Chaves, J. Costa, *Anal. Chim. Acta* **1991**, *245*, 271–282.
[138] L. T. Zhuravlev, *Colloids Surf. Physicochem. Eng. Asp.* **2000**, *173*, 1–38.
[139] F. Novak, N. Plumeré, B. Schetter, B. Speiser, D. Straub, H. A. Mayer, M. Reginek, K. Albert, G. Fischer, C. Meyer, et al., *J. Solid State Electrochem.* **2010**, *14*, 289–303.
[140] H. Giesche, *J. Eur. Ceram. Soc.* **1994**, *14*, 189–204.
[141] V. Feldmann, J. Engelmann, S. Gottschalk, H. A. Mayer, *J. Colloid Interface Sci.* **2012**, *366*, 70–79.
[142] Y. Jin, A. Li, S. G. Hazelton, S. Liang, C. L. John, P. D. Selid, D. T. Pierce, J. X. Zhao, *Coord. Chem. Rev.* **2009**, *253*, 2998–3014.
[143] A. Krysztafkiewicz, S. Binkowski, *Pigment Resin Technol.* **1999**, *28*, 270–281.
[144] A. Krysztafkiewicz, T. Jesionowski, S. Binkowski, *Colloids Surf. Physicochem. Eng. Asp.* **2000**, *173*, 73–84.
[145] L. Wang, M.-C. Estevez, M. O'Donoghu, W. Tan, *Langmuir* **2008**, *24*, 1635–1639.

[146] J. E. Sandoval, J. J. Pesek, *Anal. Chem.* **1991**, *63*, 2634–2641.
[147] A. Budny, F. Novak, N. Plumeré, B. Schetter, B. Speiser, D. Straub, H. A. Mayer, M. Reginek, *Langmuir* **2006**, *22*, 10605–10611.
[148] J. Kim, J. Cho, P. M. Seidler, N. E. Kurland, V. K. Yadavalli, *Langmuir* **2010**, *26*, 2599–2608.
[149] R. M. Pasternack, S. Rivillon Amy, Y. J. Chabal, *Langmuir* **2008**, *24*, 12963–12971.
[150] K. K. Unger, N. Becker, P. Roumeliotis, *J. Chromatogr. A* **1976**, *125*, 115–127.
[151] P. V. Der Voort, E. F. Vansant, *J. Liq. Chromatogr. Relat. Technol.* **1996**, *19*, 2723–2752.
[152] R. G. Acres, A. V. Ellis, J. Alvino, C. E. Lenahan, D. A. Khodakov, G. F. Metha, G. G. Andersson, *J. Phys. Chem. C* **2012**, *116*, 6289–6297.
[153] A. Barge, G. Cravotto, E. Gianolio, F. Fedeli, *Contrast Media Mol. Imaging* **2006**, *1*, 184–188.
[154] F. Carniato, L. Tei, A. Arrais, L. Marchese, M. Botta, *Chem. - Eur. J.* **2013**, *19*, 1421–1428.
[155] M. Pálmai, L. N. Nagy, J. Mihály, Z. Varga, G. Tárkányi, R. Mizsei, I. C. Szigyártó, T. Kiss, T. Kremmer, A. Bóta, *J. Colloid Interface Sci.* **2013**, *390*, 34–40.
[156] J. B. Lambert, *Organic Structural Spectroscopy*, Alpha Books, **2010**.
[157] R. Peña-Alonso, F. Rubio, J. Rubio, J. L. Oteo, *J. Mater. Sci.* **2007**, *42*, 595–603.
[158] R. Sethi, J. S. Ananta, C. Karmonik, M. Zhong, S. H. Fung, X. Liu, K. Li, M. Ferrari, L. J. Wilson, P. Decuzzi, *Contrast Media Mol. Imaging* **2012**, *7*, 501–508.
[159] J. Wagner, *Chem. Ing. Tech.* **1986**, *58*, 578–583.
[160] R. C. Murdock, L. Braydich-Stolle, A. M. Schrand, J. J. Schlager, S. M. Hussain, *Toxicol. Sci.* **2008**, *101*, 239–253.
[161] P. Bihari, M. Vippola, S. Schultes, M. Praetner, A. G. Khandoga, C. A. Reichel, C. Coester, T. Tuomi, M. Rehberg, F. Krombach, *Part. Fibre Toxicol.* **2008**, *5*, 14.
[162] M. A. Piechowiak, A. Videcoq, F. Rossignol, C. Pagnoux, C. Carrion, M. Cerbelaud, R. Ferrando, *Langmuir* **2010**, *26*, 12540–12547.
[163] J. A. Lewis, *J. Am. Ceram. Soc.* **2000**, *83*, 2342.
[164] S. Jenkins, S. R. Kirk, M. Persson, J. Carlen, Z. Abbas, *J. Chem. Phys.* **2009**, *130*, 134702–134702–13.
[165] J. D. Clogston, A. K. Patri, *Methods Mol. Biol. Clifton NJ* **2011**, *697*, 63–70.
[166] M. Kobayashi, M. Skarba, P. Galletto, D. Cakara, M. Borkovec, *J. Colloid Interface Sci.* **2005**, *292*, 139–147.
[167] M. Kobayashi, F. Juillerat, P. Galletto, P. Bowen, M. Borkovec, *Langmuir* **2005**, *21*, 5761–5769.
[168] K. Higashitani, M. Kondo, S. Hatade, *J. Colloid Interface Sci.* **1991**, *142*, 204–213.
[169] T. L. Doane, C.-H. Chuang, R. J. Hill, C. Burda, *Acc. Chem. Res.* **2012**, *45*, 317–326.
[170] P. Voisin, E. J. Ribot, S. Miraux, A.-K. Bouzier-Sore, J.-F. Lahitte, V. Bouchaud, S. Mornet, E. Thiaudière, J.-M. Franconi, L. Raison, et al., *Bioconjug. Chem.* **2007**, *18*, 1053–1063.
[171] S. Brunauer, P. H. Emmett, E. Teller, *J. Am. Chem. Soc.* **1938**, *60*, 309–319.
[172] S. J. Gregg, K. S. W. Sing, *Adsorption, Surface Area, and Porosity*, Academic Press, **1991**.
[173] P. C. Hiemenz, R. Rajagopalan, *Principles of Colloid and Surface Chemistry, Third Edition, Revised and Expanded*, CRC Press, **1997**.
[174] S. M. Kanan, W. T. Y. Tze, C. P. Tripp, *Langmuir* **2002**, *18*, 6623–6627.
[175] E. Asenath Smith, W. Chen, *Langmuir ACS J. Surf. Colloids* **2008**, *24*, 12405–

12409.
[176] M. Etienne, A. Walcarius, *Talanta* **2003**, *59*, 1173–1188.
[177] S. Wang, S. Wen, M. Shen, R. Guo, X. Cao, J. Wang, X. Shi, *Int. J. Nanomedicine* **2011**, *6*, 3449–3459.
[178] M. Shen, S. H. Wang, X. Shi, X. Chen, Q. Huang, E. J. Petersen, R. A. Pinto, J. R. Baker, W. J. Weber, *J. Phys. Chem. C* **2009**, *113*, 3150–3156.
[179] A. Dadabhoy, S. Faulkner, P. G. Sammes, *J. Chem. Soc. Perkin Trans. 2* **2002**, 348–357.

Summary

Magnetic resonance imaging (MRI) is an important diagnostic tool for the imaging of soft tissues. The measuring principles of MRI are based on the nuclear magnetic resonance (NMR). The non-invasive technique of MRI allows for the detection of tumors, infections and injuries at an early stage. New opportunities for medical diagnosis and magnetic resonance (MR) imaging techniques are offered with the use of hybrid nanomaterials. The anchoring of functional organic compounds to hybrid nanoparticles as inorganic matrix materials makes it possible to create long-term tracking materials, carriers for drugs and multifunctional imaging agents. The functionalization of a nano-sized material, *e.g.* with paramagnetic Gd(III) chelate complexes for ^{1}H imaging or with ^{19}F containing molecules for ^{19}F imaging leads to a high concentration of contrast agents, which can be obtained at low volumes. In this way increased local concentrations lead to higher resolutions in ^{1}H or ^{19}F MRI images, respectively. Furthermore, the lowered rotational tumbling of the nanoparticular CA influences the relaxation times in the human body which leads to a high contrast in the ^{1}H MRI images.

The ^{19}F imaging is an important alternative imaging technique to ^{1}H MRI. To achieve a high resolution and a good contrast an intense sharp singlet in the ^{19}F NMR spectrum has to be generated. The T_8-silsesquioxane (POSS) offers due to its cubic symmetry an ideal core and can serve therefore as a multiplier for ^{19}F signals.

In the first part of this work T_8-silsesquioxanes were functionalized with polyorganofluorinated groups (PFG). By different synthetic pathways highly symmetrical polyorganofluorinated POSS cubes (PF-POSS) which generate a sharp singlet in the ^{19}F spectrum were obtained (Scheme 1). The properties of the PF-POSS cubes in dependency of their PFG structures, the resulting solubility and their hydrolysis stability were investigated. The hydrolysis process was studied by ^{1}H, ^{19}F, ^{29}Si NMR and DOSY NMR spectroscopy as well as MS-ESI spectrometry. Furthermore, the hydrodynamic radii of the obtained PF-POSS were determined by ^{1}H DOSY NMR spectroscopy. The T_1 and T_2 relaxation time for the ^{19}F nuclei of the respective PF-POSS was determined for the most hydrophobic PF-POSS structures **3**-**5**, two different polyethylene glycol functionalized PF-POSS cubes **6** and **7** as well as for a polar, charged and water soluble PF-POSS **8** (Scheme 1). Additionally, *in vitro* measurements were performed for the PF-POSS cubes **3**-**5**.

Furthermore, a *post mortem* imaging was implemented to study the behavior of the nonpolar PF-POSS **5** in rat brain tissue.

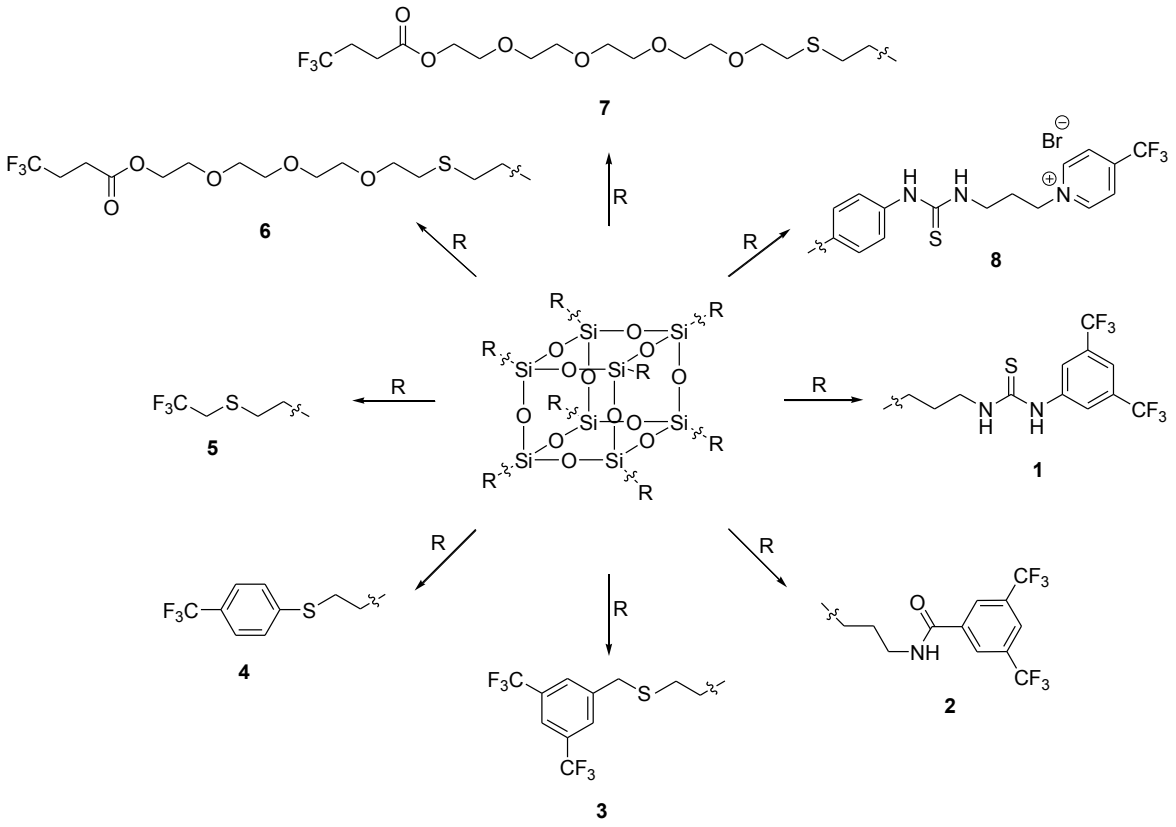

Scheme 1

As a result of this work the desired range of PF-POSS cubes of different polarities was successfully synthesized. For each of the PF-POSS cubes a sharp ^{19}F NMR signal could be realized by simple synthetic steps. The evaluation of the hydrodynamic radii determined by ^{1}H DOSY NMR experiments delivered sizes in the range of 0.53 to 1.61 nm. From this it could be concluded that no outwardly stretched linker structures are present in solution. Since the sizes of all PF-POSS cubes were determined as significantly smaller than the kidney pores it could be assumed, that an excretion *via* the kidneys is possible in the case of an application in animal tissue. In addition, long-term hydrolysis studies during several weeks were performed to characterize final hydrolysis fragments of PF-POSS **3**-**8**. The hydrodynamic radii were specified in the range of 200 pm to 470 pm. Besides, the formation of siloxane trimers and dimers could be emphasized by characteristic signals in time dependent measured ^{29}Si NMR spectra and in MS-ESI spectra. From the series of the

hydrolyzed PF-POSS cubes **3**, **5**, **6**, **7** and **8** it could be concluded, that the anchoring of PFGs to POSS cages decelerates the hydrolysis very strongly in dependency of the sterical demand of the PFG. This occurs by the shielding effect of the fluorine, which prevents the nucleophilic attack of water at the silicon core. Consequently, this leads to the high hydrolysis stability with a stable ^{19}F signal within the required MRI experiment time (4 h). Prior to the ^{19}F *in vitro* measurements the ^{19}F relaxivities of the PF-POSS **3**-**5** were determined. The shortest T_1 relaxation time was obtained for **5** by 853.6 ms, while the longest T_1 relaxation time of 999.6 ms was determined for **4**. The ^{19}F MR images of **3**-**5** showed a good contrast with solutions of 260 mM concentration related to the fluorine amount. The best contrast within these PF-POSS cubes was obtained for **5**. The *post mortem* images of **5** in rat brain showed a good contrast, while the insufficient solubility of **5** caused two spots. Despite, the PF-POSS cube **5** shows the potential as basic structure for imaging in brain tissue, the effect of further decreased polarity could be a solution for the solubility properties. Since the blood tissue barriers are permeable for either lipophilic or hydrophilic drugs depending on the location in the human body, PF-POSS cubes with higher polarity were investigated additionally. The syntheses of two partially water soluble PEGylated PF-POSS cubes **6** and **7** as well as the synthesis of the fully water soluble PF-POSS **8** were achieved successfully. The T_1 relaxation time for the ^{19}F nucleus was determined to be the longest for the PEGylated PF-POSS **6** with 1864.3 ms and the shortest for the charged PF-POSS **8** with 1011.3 ms. While the long T_1 times of the PEGylated PF-POSS are the major drawback for T_1 weighted images, the successful synthesis of the fully water soluble PF-POSS **8** offers great advantages compared to commercial ^{19}F agents which are not soluble in water and have to be injected as emulsions. This study revealed that the best way to obtain a full water solubility is achieved by the construction of a charged PF-POSS species, without a strong lengthening of the T_1 relaxation times.

In the second part of this work the size dependent properties of spherical and monodisperse silica nanoparticles (SNPs) with diameters of about 15, 50 and 130 nm were examined for their application as potential contrast agents (CAs) for magnetic resonance imaging (MRI). Therefore the SNPs were covalently functionalized with two different lanthanoid(III) (Ln = Gd) DOTA chelate complexes *via* an aminopropyl linker (Figure 1).

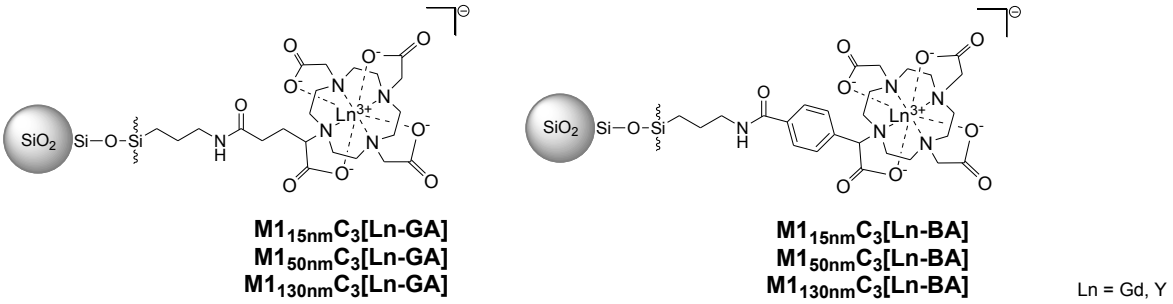

Figure 1

Analogous materials which were functionalized with yttrium complexes served for the analysis of the materials by solid state NMR spectroscopy. Measurements, like dynamic light scattering (DLS), zeta potential and scanning electron microscopy (SEM) were carried out to investigate surface interparticle interactions and the influence of surface charges. Moreover DRIFT, thermogravimetric analyses (TGA), scanning electron transmission microscopy (STEM) and elemental analyses (EA) were performed to characterize the materials. The specific surface area (A_{BET}) and pore sizes (d_P) were determined by nitrogen adsorption isotherms by means of the Brunauer-Emmet-Teller (BET) model. In order to evaluate an optimal particle size, the expected increase in relaxivity due to the Gd(III) surface payload was examined. The longitudinal and transverse relaxation rates (r_1 and r_2) of the SNPs were investigated by MRI at 3 Tesla in agar phantoms.

The highest relaxivities are obtained for the largest particles **$M1_{130nm}C_3$[Gd-BA]** and -**[Gd-GA]**, respectively, with values up to 3.30×10^5 $mM^{-1}s^{-1}$ in medium. The smaller SNPs display lower relaxivities [per Gd(III)] due to agglomeration and consequently reduced number of freely available Gd(III) complexes and restricted access for water exchange. Consequently, the final relaxivity of the smaller SNPs results from the average of opposed effects of higher surface coverage and agglomeration behavior. The surface loading with Gd(III)-chelates was varied for the smaller SNPs by repeating the coupling procedure resulting in high Gd(III)-loadings of up to 125 µmol per gram of NPs. Subsequently, stability studies for the re-conjugated NPs with high payloads of Gd complexes were carried out with respect to the leaching of complexes from the surface and release of free gadolinium from the complexes. It could be shown that no free Gd was released during the leaching tests. Furthermore, the surface charge of all SNPs was modified by acetylation of remaining amino groups following the primary coupling

reaction with Gd(III)-chelates. The enhancement of the relaxivities (r_1 and r_2) was achieved after the modification by repeated conjugation with the Gd(III) complex and the acetyl protection of residual surface amino groups, respectively, resulting in high r_1 values up to 4.49×10^5 $mM^{-1}s^{-1}$ per NP. A significant strong increase was detected in the transverse relaxivities r_2 of the materials as well. The acetyl protected SNPs exhibit higher relaxivities by reducing the positive NP surface charge of the free amino groups and their interaction with negatively charged complex species. A similar effect is observed for the re-reacted SNPs, with up to more than 300 % of the initial r_1 relaxivities per NP compared to their once reacted counterparts. Thus, the increase of r_1 and r_2 is stronger the bigger the particles are and the more primary amino groups can be acetylated.

Zusammenfassung

Die Magnetresonanz-Tomographie (MRT) stellt ein wichtiges diagnostisches Verfahren zur Bildgebung von Weichgewebe dar. Die Messprinzipien der MRT basieren auf der magnetischen Kernresonanz (NMR). Die nicht-invasive Technik der MRT erlaubt die Detektion von Tumoren, Infekten und Verletzungen im frühen Stadium. Neue Möglichkeiten zur Anwendung in der medizinischen Diagnostik und in der Magnetresonanzbildgebung (MR-Bildgebung) werden durch die Verwendung von hybriden Nanomaterialien ermöglicht. Die Verankerung von funktionellen organischen Komponenten an hybriden Nanomaterialien als anorganisches Matrixmaterial macht es möglich Langzeit-tracking-Materialien, Träger für Wirkstoffe und multifunktionale bildgebende Wirkstoffe zu erzeugen. Die Funktionalisierung von Materialien in Nanogröße, beispielsweise mit paramagnetischen Gd(III)-Chelatkomplexen für die ^{1}H- oder mit ^{19}F-enthaltenden Molekülen für die ^{19}F-Bildgebung, führt zu hohen Konzentrationen an Kontrastmitteln (KM), die in einem kleinen Volumen erhalten werden können. Die auf diese Weise erzeugten hohen lokalen Konzentrationen führen in den ^{1}H- bzw. ^{19}F-Bildern zu höheren Auflösungen. Weiterhin beeinflusst die erniedrigte Taumelbewegung der nanopartikulären KM die Relaxationszeiten im menschlichen Körper und erzeugt einen intensiven Kontrast in den ^{1}H-MRT-Bildern.

Die ^{19}F-Bildgebung stellt eine wichtige alternative Technik zur ^{1}H-Bildgebung dar. Um eine gute Auflösung zu erreichen und einen guten Kontrast zu erzeugen, muss ein intensives, scharfes Singulett im ^{19}F-NMR-Spektrum erzeugt werden. Das T_8-Silsesquioxan (POSS) bietet dank seiner kubischen Symmetrie einen idealen Kern und kann deshalb als Multiplikator für ^{19}F-Signale dienen.

Im ersten Teil dieser Arbeit werden T_8-Silsesquioxane mit polyorganofluorierten Gruppen (PFG) funktionalisiert. Über verschiedene Synthesewege wurden hochsymmetrische polyorganofluorierte POSS-Würfel (PF-POSS) erhalten, welche ein scharfes Singulett im ^{19}F-NMR-Spektrum generieren (Schema 1). Die Eigenschaften der PF-POSS-Würfel in Abhängigkeit von ihren PFG-Strukturen, die resultierenden Löslichkeiten und ihre Hydrolysestabilitäten wurden untersucht. Der Hydrolyseprozess wurde mittels ^{1}H-, ^{19}F-, ^{29}Si-NMR- und DOSY-NMR-Spektroskopie, als auch mit der MS-ESI-Spektrometrie untersucht. Weiterhin wurden die hydrodynamischen Radien der erhaltenen PF-POSS über

^{1}H-DOSY-NMR-Spektroskopie bestimmt. Die T_1- und T_2-Relaxationzeiten des ^{19}F-Kerns des jeweiligen PF-POSS wurden für die am stärksten hydrophoben PF-POSS **3-5**, zwei verschiedene Polyethylengykol funktionalisierte PF-POSS Würfel **6** und **7** als auch für einen polaren sowie wasserlöslichen PF-POSS **8** bestimmt (Schema 1). Zusätzlich wurden *in vitro* Messungen für die PF-POSS-Würfel **3-5** vollzogen. Weiterhin wurde für die PF-POSS **3-5** eine *ex vivo* Tomographie durchgeführt um das Verhalten des unpolaren PF-POSS **5** im Gehirngewebe einer Ratte zu untersuchen.

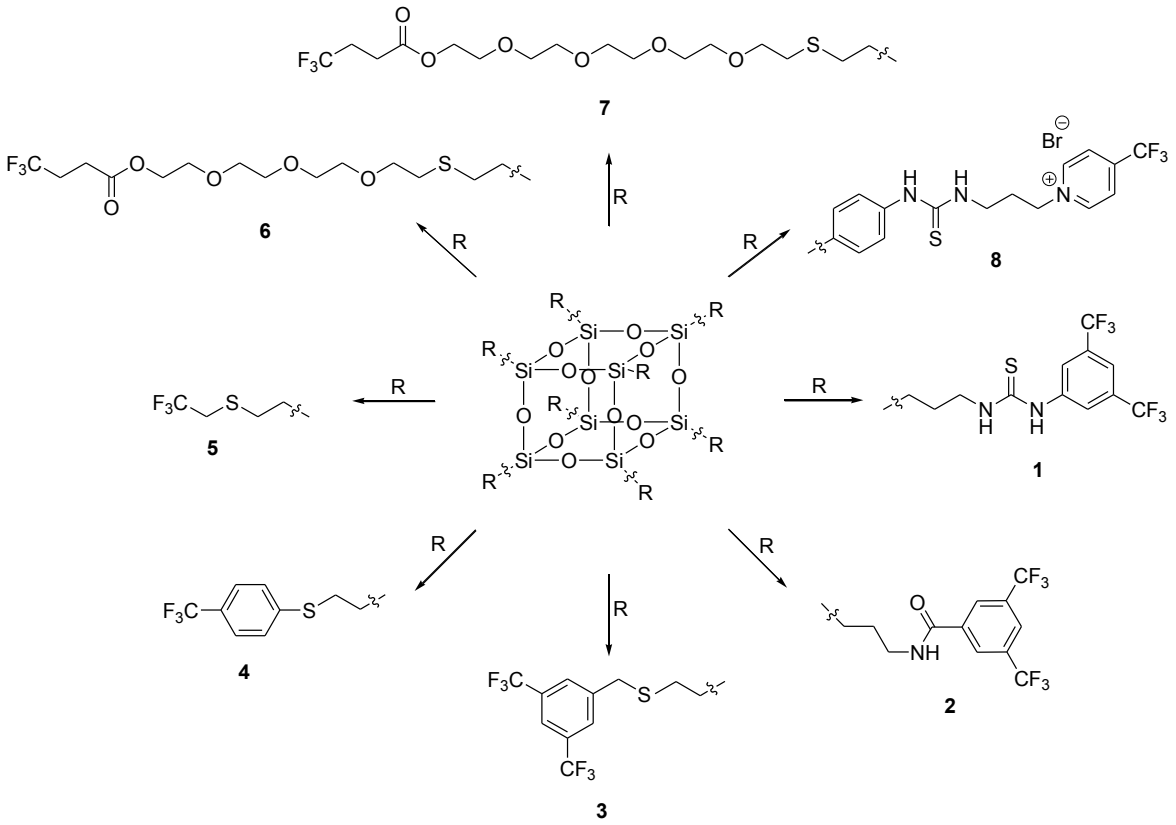

Schema 1

Als Ergebnis dieser Arbeit wurde die gewünschte Bandbreite an PF-POSS-Würfeln verschiedener Polaritäten erfolgreich synthetisiert. Für jeden der PF-POSS-Würfel wurde ein scharfes ^{19}F-NMR-Signal über einfache synthetische Schritte erzielt. Die Auswertung der über ^{1}H-DOSY-NMR-Experimente bestimmten hydrodynamischen Radien ergab Größen im Bereich von 0,53 bis 1,61 nm. Durch diese Ergebnisse konnte davon ausgegangen werden, dass in Lösung keine nach außen gestreckten Linker vorhanden sind. Da die Größen aller PF-POSS-Würfel als signifikant kleiner als die Nierenporen bestimmt wurden, kann angenommen werden, dass eine Ausscheidung über die Nieren im Falle einer

Anwendung in tierischem Gewebe möglich ist. Zusätzlich wurden Langzeit-Hydrolysestudien über mehrere Wochen durchgeführt, um endgültige Hydrolysefragmente der PF-POSS-Würfel **3**-**8** zu charakterisieren. Hierbei wurden hydrodynamische Radien im Bereich von 200 pm bis 470 pm bestimmt. Desweiteren konnte die Bildung von Siloxan-Dimeren und -Trimeren durch charakteristische Signale in zeitabhängig gemessenen ^{29}Si-NMR-Spektren und in ESI-MS-Spektren belegt werden. Aus der Serie der hydrolysierten PF-POSS-Würfel **3**, **5**, **6**, **7** und **8** konnte geschlussfolgert werden, dass die Verankerung der PFGs am POSS-Käfig die Hydrolyse in Abhängigkeit vom sterischen Anspruch der PFG stark verlangsamt. Dies geschieht über den abschirmenden Effekt des Fluors, welches den nukleophilen Angriff von Wasser am Siliziumkern verhindert. Folglich führt dies zu einer hohen Hydrolysestabilität mit einem konstanten ^{19}F-Signal innerhalb der für ein MRT-Experiment benötigten Zeit (4 h). Die ^{19}F-Relaxivitäten der PF-POSS **3**-**5** wurden vor der jeweiligen *in vitro* ^{19}F-Messung bestimmt. Die kürzeste T_1-Relaxationszeit wurde für **5** mit 853.6 ms erhalten, während die längste T_1-Relaxationszeit auf 999.6 ms für **4** bestimmt wurde. Die ^{19}F-MR-Aufnahmen von **3**-**5** zeigten einen guten Kontrast für Lösungen von einer Konzentration von 260 mM bezogen auf den Fluorgehalt. Der beste Kontrast innerhalb dieser PF-POSS Würfel wurde für **5** erhalten. Die MR-Aufnahmen von **5** im Rattengehirn zeigten einen guten Kontrast, wobei die ungenügende Löslichkeit von **5** zu zwei Spots führte. Trotz des gezeigten hohen Potentials von **5** als Basisstruktur für die Tomographie im Gehirngewebe, könnte eine weitere Erniedrigung der Polarität eine Lösung für die Löslichkeitseigenschaften darstellen. Da die Blut-Gewebe-Schranken abhängig von ihrer Lokalisation im menschlichen Körper für lipophile oder hydrophile Wirkstoffe durchgängig sind, wurden zusätzlich Untersuchungen von hydrophilen PF-POSS Würfeln durchgeführt. Die erfolgreiche Synthese zweier teilweise wasserlöslichen PEGylierten PF-POSS Würfel **6** und **7** als auch die Synthese des vollständig wasserlöslichen PF-POSS **8** wurde erfolgreich erzielt. Die T_1-Relaxationszeit für den ^{19}F-Kern wurden als längste für den PEGylierten PF-POSS-Würfel **6** mit 1864,3 ms und als kürzeste für den geladenen PF-POSS **8** mit 1011,3 ms bestimmt. Während die langen T_1-Zeiten den Hauptnachteil für T_1-gewichtete Aufnahmen bilden, bietet die Synthese des wasserlöslichen PF-POSS **8** große Vorteile im Vergleich zu kommerziellen ^{19}F-Agenzien, die nicht wasserlöslich sind und als Emulsionen injiziert werden müssen. Diese Studie zeigte, dass der beste Weg eine Wasserlöslichkeit zu erhalten durch die Konstruktion einer

geladenen PF-POSS Spezies gelingt, ohne dabei zu einer erheblichen Verlängerung der T_1-Relaxationszeiten zu führen.

Im zweiten Teil dieser Arbeit wurden die größenabhängigen Eigenschaften von sphärischen, nichtporösen und monodispersen Silika-Nanopartikeln (SNPs) mit Durchmessern von 15, 50 und 130 nm für ihre Anwendung als potentielle Kontrastmittel (KM) in der Magnetresonanztomographie (MRT) untersucht. Hierfür wurden die SNPs kovalent mit zwei verschiedenen Lanthanoid(III) (Ln = Gd) DOTA-Chelatkomplexen über einen Aminopropyllinker funktionalisiert.

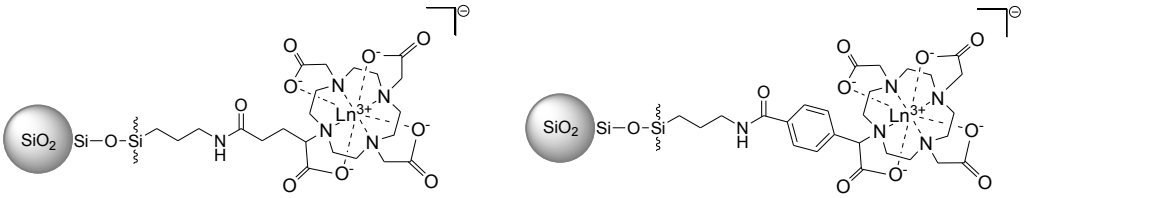

Abbildung 1

Analoge Materialien, die mit Yttrium(III)komplexen funktionalisiert wurden, dienten zur Analyse der Materialien mittels Festkörper-NMR-Spektroskopie. Messungen wie die dynamische Lichtstreuung (DLS), das Zeta-Potential und die Rasterelektronenmikroskopie (REM) wurden durchgeführt um die Wechselwirkung zwischen den Partikeloberflächen und den Einfluss der Oberflächenladungen zu untersuchen. Weiterhin wurden DRIFT, thermogravimetrische Messungen (TGA), Rastertransmissionselektronenmikroskopie (RTEM) und Elementaranalysen durchgeführt um die Materialien zu charakterisieren. Die spezifische Oberfläche (A_{BET}) und die Porengrößen (d_P) wurden über Stickstoffabsorptionsisothermen anhand des Brunauer-Emmet-Teller (BET)-Modells bestimmt. Um eine optimale Partikelgröße zu evaluieren, wurde der erwartete Anstieg an Relaxivität durch eine höhere Gd(III)-Oberflächenladung geprüft. Die longitudinalen und transversalen Relaxationsraten (r_1 und r_2) der SNPs wurden mittels MRT bei 3 Tesla in Agarphantomen untersucht.

Die höchsten Relaxivitäten wurden für die größten Partikel **M1$_{130nm}$C$_3$[Gd-BA]** beziehungsweise -**[Gd-GA]**, mit Werten von bis zu 3.30×10^5 $mM^{-1}s^{-1}$ in Medium erhalten. Die kleineren SNPs zeigen geringere Relaxivitäten [pro Gd(III)] aufgrund von Agglomeration und einer dadurch reduzierten Menge an frei zugänglichen Gd(III)-Komplexen und einem dabei auftretenden eingeschränkten Zugang für einen Wasseraustausch. Folglich resultiert die endgültige Relaxivität der kleineren Partikel aus dem Mittel der entgegengesetzten Effekte von höherer Oberflächenbeladung und dem Agglomerationsverhalten. Die Oberflächenbeladung mit Gd(III)-Chelaten wurde für die kleineren Partikel durch die Wiederholung des Kopplungsvorganges variiert, wodurch hohe Gd(III)-Beladungen von bis zu 125 μmol pro Gramm NP resultierten. Des Weiteren wurden Stabilitätsstudien der re-konjugierten NPs mit hohen Gd(III)-Beladungen hinsichtlich eines Leachings von Komplexen von der Partikeloberfläche und einer Freisetzung des Gd aus den Komplexen vollzogen. Es konnte gezeigt werden, dass während der Leachingversuche kein Gd freigesetzt wurde. Weiterhin wurde eine Modifizierung der Oberflächenladung aller NPs durch Acetylierung der nach einmaliger Kupplungsreaktion mit Gd(III)-Chelaten verbliebenen Aminofunktionen durchgeführt. Es wurde eine Erhöhung der Relaxivitäten (r_1 und r_2) nach der Modifizierung durch wiederholte Konjugation mit dem Gd(III)-Komplex, beziehungsweise nach der Acetyl-Schützung der verbliebenen Aminogruppen erhalten, aus welcher sich hohe r_1-Werte von bis zu 4.49×10^5 $mM^{-1}s^{-1}$ pro NP ergaben. Eine ebenfalls signifikante Steigerung in den r_2-Werten wurde ebenso festgestellt. Durch die Reduzierung der positiven NP-Oberflächenladung durch freie Aminogruppen und deren Interaktion mit negativ geladenen Komplex-Spezies weisen die acetylgeschützten SNPs höhere Relaxivitäten auf. Ein ähnlicher Effekt wird für die wiederholt reagierten SNPs beobachtet, die eine mehr als 300 % höhere Relaxivität gegenüber ihren ungeschützen Analogen aufweisen. Demnach ist die Zunahme von r_1 und r_2 umso stärker je größer die Partikel sind und je mehr der anfänglichen Aminogruppen geschützt werden können.

Meine akademische Ausbildung verdanke ich:

K. Albert; T. Chassé; D. Christen; H.-J. Egelhaaf; O. Eibl; H. Eckstein; K. Eichele; G. Gauglitz; N. Kuhn; W. Jäger; N. Kuhn; S. Lauffer; H.-G. Mack; M. E. Maier; H. A. Mayer; A. J. Meixner; H.-J. Meyer; U. Nagel; C. Ochsenfeld; H. Oberhammer; H. Pommer; V. Schurig; E. Schweda; B. Speiser; J. Strähle; L. Wesemann; D. Wistuba; K.-P. Zeller; T. Ziegler.